

University of Windsor

Scholarship at UWindor

Electronic Theses and Dissertations

Theses, Dissertations, and Major Papers

1-1-2006

Modeling of subsurface deformation and damage in an aluminum -silicon alloy subjected to sliding contact.

S. Subutay Akarca
University of Windsor

Follow this and additional works at: <https://scholar.uwindsor.ca/etd>

Recommended Citation

Akarca, S. Subutay, "Modeling of subsurface deformation and damage in an aluminum -silicon alloy subjected to sliding contact." (2006). *Electronic Theses and Dissertations*. 7200.
<https://scholar.uwindsor.ca/etd/7200>

This online database contains the full-text of PhD dissertations and Masters' theses of University of Windsor students from 1954 forward. These documents are made available for personal study and research purposes only, in accordance with the Canadian Copyright Act and the Creative Commons license—CC BY-NC-ND (Attribution, Non-Commercial, No Derivative Works). Under this license, works must always be attributed to the copyright holder (original author), cannot be used for any commercial purposes, and may not be altered. Any other use would require the permission of the copyright holder. Students may inquire about withdrawing their dissertation and/or thesis from this database. For additional inquiries, please contact the repository administrator via email (scholarship@uwindsor.ca) or by telephone at 519-253-3000ext. 3208.

**MODELING OF SUBSURFACE DEFORMATION AND DAMAGE IN
AN ALUMINUM-SILICON ALLOY SUBJECTED TO SLIDING
CONTACT**

by

S. Subutay Akarca

A Dissertation

**Submitted to the Faculty of Graduate Studies and Research
through Engineering Materials
in Partial Fulfillment of the Requirements for
the Degree of Doctor of Philosophy at the
University of Windsor**

Windsor, Ontario, Canada

2006

© 2006 S. Subutay Akarca



Library and
Archives Canada

Bibliothèque et
Archives Canada

Published Heritage
Branch

Direction du
Patrimoine de l'édition

395 Wellington Street
Ottawa ON K1A 0N4
Canada

395, rue Wellington
Ottawa ON K1A 0N4
Canada

Your file *Votre référence*
ISBN: 978-0-494-35072-0
Our file *Notre référence*
ISBN: 978-0-494-35072-0

NOTICE:

The author has granted a non-exclusive license allowing Library and Archives Canada to reproduce, publish, archive, preserve, conserve, communicate to the public by telecommunication or on the Internet, loan, distribute and sell theses worldwide, for commercial or non-commercial purposes, in microform, paper, electronic and/or any other formats.

The author retains copyright ownership and moral rights in this thesis. Neither the thesis nor substantial extracts from it may be printed or otherwise reproduced without the author's permission.

AVIS:

L'auteur a accordé une licence non exclusive permettant à la Bibliothèque et Archives Canada de reproduire, publier, archiver, sauvegarder, conserver, transmettre au public par télécommunication ou par l'Internet, prêter, distribuer et vendre des thèses partout dans le monde, à des fins commerciales ou autres, sur support microforme, papier, électronique et/ou autres formats.

L'auteur conserve la propriété du droit d'auteur et des droits moraux qui protègent cette thèse. Ni la thèse ni des extraits substantiels de celle-ci ne doivent être imprimés ou autrement reproduits sans son autorisation.

In compliance with the Canadian Privacy Act some supporting forms may have been removed from this thesis.

Conformément à la loi canadienne sur la protection de la vie privée, quelques formulaires secondaires ont été enlevés de cette thèse.

While these forms may be included in the document page count, their removal does not represent any loss of content from the thesis.

Bien que ces formulaires aient inclus dans la pagination, il n'y aura aucun contenu manquant.


Canada

ABSTRACT

The sliding wear encountered by aluminum alloys tends to induce plastic deformation below the contact surfaces, even at light loads. There is experimental evidence of damage accumulation in the form of nucleation of voids and microcracks around second phase particles in the material layers adjacent to the contact surface. The crack propagation found at a certain depth below the surface may lead to the creation of long, thin plate-like wear debris particles. The objective of this work was to study the deformation and damage accumulation processes experienced by aluminum alloys during sliding wear. The explicit finite element program LS-DYNA was used to model sliding contacts. The material model used in the finite element analysis was based on the stress/strain behavior of a 356 Al (Al-7 % Si) alloy, and determined directly from the analysis of the subsurface deformation generated during the sliding wear tests. Strain rate and thermal effects were also considered by a coupled thermal and mechanical analysis. Rigid cylindrical asperities were loaded and moved, at a constant sliding velocity, over a three-dimensional 356 Al structure. Both Eulerian and Lagrangian finite element formulations were used, and the accumulation of stresses and strains was studied as a function of the asperity contact cycle number. The finite element model was validated by comparing its results with the normal and sliding contact experiment observations.

Initially, the von Mises stress in the aluminum subsurface layers increased rapidly. With a loading condition of 10 m/s sliding velocity and 150 N/mm normal load, the von Mises stress and the equivalent plastic strain at the contact surface were 514 MPa and 0.19, respectively after the first asperity contact. After the fourth asperity passage, the stress and the plastic strain at the contact surface increased to 586 MPa and 0.78. During the subsequent sliding contacts, the subsurface stresses attained a constant value with only a 2% increase in the stress between the fourth and the seventh asperity contacts. Variations in hydrostatic pressure, strain rate and temperature values at the surface and subsurface regions were also determined, based on different loading conditions, as a function of the sliding contact numbers. The hydrostatic pressure at the surface increased from 1150 MPa to 1300 MPa as the sliding process progressed from the first to the seventh asperity contacts. A total temperature increase of 45 K occurred

at the surface after the seventh sliding contact, compared to the 300 K initial surface temperature.

A model of the subsurface damage accumulation process was proposed based on the Rice and Tracey void growth model, which considered the presence of a damage gradient that reached a maximum at a critical depth. For a sliding velocity of 10 m/s and a normal load of 150 N/mm, the location of material where the maximum rate of damage occurred corresponded to a normalized depth (depth/asperity diameter) of 0.060. Increasing the load to 250 N/mm caused an increase in the critical depth of damage to a normalized depth of 0.085. An increase of the sliding velocity from 5 m/s to 10 m/s moved the location of maximum damage from 0.050 to 0.060. Friction (coefficient of friction ≥ 0.3) changed the subsurface damage gradient distribution completely, moving the location of the maximum damage rate to the surface. The effects of hard particles on the distribution of subsurface stresses, strains and the damage gradient were also investigated. Si particles in different shapes (square, rectangular and circular) embedded in the aluminum matrix helped to resist the penetration of deformation below the surface of the 356 Al matrix. However, an increase in the stresses and plastic strains prompted an increase in the damage gradient in some locations adjacent to the Si particles.

To
my wife Arzu Akarca
and to
my family

ACKNOWLEDGEMENT

I would like to express my sincere gratitude to Dr. A. T. Alpas and Dr. W. J. Altenhof for their supervision and support. Their guidance and encouragement were always great sources of motivation for me during my studies.

I would like to thank to Mr. J. Robinson for his technical assistance; Ms. B. Denomey for her administrative assistance. I also would like to thank my friends and colleagues in NSERC/GM IRC for their support and friendship. In addition, I would like to express my gratitude to my dissertation committee for their revisions and suggestions.

Finally, I would like to thank my wife, Arzu, for her endless support, encouragement and patience throughout the journey we took together.

TABLE OF CONTENTS

ABSTRACT	iii
DEDICATION	v
ACKNOWLEDGEMENTS	vi
LIST OF TABLES	xii
LIST OF FIGURES	xiv
NOMENCLATURE	xxix
LIST OF ABBREVIATIONS	xxxix

CHAPTER 1:

INTRODUCTION	1
---------------------------	----------

CHAPTER 2:

LITERATURE REVIEW	6
--------------------------------	----------

2.1. WEAR	6
2.1.1. DEFINITION AND MECHANISMS	6
2.1.2. SUBSURFACE MICROSTRUCTURES OF THE WORN SURFACES	11
2.1.3. SUBSURFACE DAMAGE MECHANISMS DURING DELAMINATION.....	14

2.2. ANALYTICAL AND NUMERICAL SOLUTIONS OF CONTACT STRESS FIELDS	21
2.2.1. ANALYTICAL SOLUTIONS OF CONTACT PROBLEMS.....	21
2.2.2. FINITE ELEMENT ANALYSES APPLIED TO SLIDING CONTACT PROBLEMS	38

2.3. CONSTITUTIVE EQUATIONS FOR ALUMINUM ALLOYS	50
2.3.1. THE EFFECT OF HYDROSTATIC PRESSURE ON THE MECHANICAL PROPERTIES	56
2.3.2. STRAIN RATE SENSITIVITY OF ALUMINUM ALLOYS	56
2.3.3. THERMAL SOFTENING OF ALUMINUM ALLOYS	63

CHAPTER 3:

SCOPE OF THE PRESENT RESEARCH	69
--	-----------

CHAPTER 4:	
FINITE ELEMENT PROCEDURES	71
4.1. ANALYSIS OF NORMAL CONTACT BETWEEN SOLIDS	71
4.1.1. FE MODEL GEOMETRY	71
4.1.2. ELEMENT FORMULATION AND PROPERTIES.....	71
4.1.3. MATERIAL MODEL	72
4.1.4. LOADING AND BOUNDARY CONDITIONS.....	73
4.1.5. CONTACT ALGORITHM.....	73
4.1.6. HOURGLASS MODES	78
4.1.7. MASS SCALING	78
4.2. ANALYSIS OF SLIDING CONTACT BETWEEN SOLIDS	78
4.2.1. FE MODEL GEOMETRY	79
4.2.2. ELEMENT FORMULATION AND PROPERTIES.....	80
4.2.3. MATERIAL MODEL	80
4.2.4. LOADING AND BOUNDARY CONDITIONS.....	86
4.2.5. CONTACT ALGORITHM.....	86
4.3. EFFECTS OF TEMPERATURE AND STRAIN RATE ON THE SUBSURFACE DAMAGE	87
4.3.1. FE MODEL GEOMETRY	89
4.3.2. ELEMENT FORMULATION AND PROPERTIES.....	89
4.3.3. MATERIAL MODEL	89
4.3.4. LOADING AND BOUNDARY CONDITIONS.....	94
4.3.5. CONTACT ALGORITHM.....	95
4.4. EFFECTS OF SECONDARY HARD PARTICLES ON THE SUBSURFACE DAMAGE	95
4.4.1. FE MODEL GEOMETRY	96
4.4.2. ELEMENT FORMULATION AND PROPERTIES.....	96
4.4.3. MATERIAL MODEL	97
4.4.4. LOADING AND BOUNDARY CONDITIONS.....	97
CHAPTER 5:	
EXPERIMENTAL PROCEDURES.....	101
5.1. NORMAL AND SLIDING CONTACT EXPERIMENTS	101
5.1.1. SAMPLE MATERIALS	101
5.1.2. EXPERIMENTAL SET UP.....	102
5.2. TEMPERATURE MEASUREMENT DURING SLIDING	109
5.2.1. SAMPLE MATERIALS	109
5.2.2. EXPERIMENTAL SET UP.....	109

CHAPTER 6:	
VALIDATION OF NUMERICAL MODELS	112
6.1. ENERGY AND EXTERNAL WORK ANALYSIS FOR THE FINITE ELEMENT MODELS.....	112
6.1.1. ANALYSIS OF NORMAL CONTACT BETWEEN SOLIDS.....	112
6.1.2. ANALYSIS OF SLIDING CONTACT BETWEEN SOLIDS.....	113
6.1.3. EFFECTS OF TEMPERATURE AND STRAIN RATE ON THE SUBSURFACE DAMAGE	113
6.1.4. EFFECTS OF SECONDARY HARD PARTICLES ON THE SUBSURFACE DAMAGE	114
6.2. TIME-HISTORY DATA.....	114
6.2.1. ANALYSIS OF NORMAL CONTACT BETWEEN SOLIDS.....	114
6.2.2. ANALYSIS OF SLIDING CONTACT BETWEEN SOLIDS.....	115
6.2.3. EFFECTS OF TEMPERATURE AND STRAIN RATE ON THE SUBSURFACE DAMAGE	122
6.2.4. EFFECTS OF SECONDARY HARD PARTICLES ON THE SUBSURFACE DAMAGE	122
6.3. HERTZ THEORY COMPARISONS	122
6.4. COMPARISON OF THE EXPERIMENTAL AND NUMERICAL RESULTS	123
6.4.1. NORMAL CONTACT	131
6.4.2. SLIDING CONTACT	135
6.5. COMPARISON OF THE EXPERIMENTAL OBSERVATIONS AND THERMAL SOFTENING MODEL.....	136
CHAPTER 7:	
RESULTS AND DISCUSSION	148
7.1. SLIDING CONTACT BETWEEN SOLIDS.....	148
7.1.1. VARIATIONS OF STRESSES AND STRAINS WITH NUMBER OF SLIDING CONTACTS	148
7.1.2. VARIATIONS OF HYDROSTATIC PRESSURE WITH NUMBER OF SLIDING CONTACTS	149
7.1.3. SUBSURFACE STRAIN RATE DISTRIBUTION.....	156
7.1.4. EFFECT OF NORMAL LOAD	156
7.1.5. EFFECT OF FRICTION	156
7.1.6. EFFECT OF SLIDING VELOCITY.....	161
7.1.7. EFFECT OF DISTANCE BETWEEN ASPERITIES.....	161
7.2. EFFECTS OF TEMPERATURE AND STRAIN RATE ON THE SUBSURFACE DAMAGE	162
7.2.1. VARIATIONS OF SUBSURFACE STRESSES AND STRAINS WITH NUMBER OF SLIDING CONTACTS.....	162
7.2.2. VARIATION OF HYDROSTATIC PRESSURE WITH NUMBER OF SLIDING CONTACTS	166
7.2.3. VARIATION OF THE DEFORMATION INDUCED SUBSURFACE TEMPERATURES WITH NUMBER OF SLIDING CONTACTS	173

7.2.4. SUBSURFACE STRAIN RATE DISTRIBUTION WITH THE INCREASE IN THE NUMBER OF SLIDING CONTACTS.....	173
7.2.5. EFFECT OF MATERIAL MODEL ON THE PREDICTION OF SUBSURFACE DEFORMATION.....	177
7.2.6. EFFECT OF NORMAL LOAD	178
7.2.7. EFFECT OF FRICTION	178
7.2.8. EFFECT OF SLIDING VELOCITY.....	179
7.3. COMPARISON OF EULERIAN AND LAGRANGIAN SLIDING MODELS	179
7.4. EFFECTS OF SECONDARY HARD PARTICLES ON THE SUBSURFACE DAMAGE	190
7.5. ANALYSIS OF SUBSURFACE DAMAGE ACCUMULATION PROCESS	207
7.5.1. NUMERICAL SUBSURFACE DAMAGE.....	207
7.5.2. INFLUENCE OF Si PARTICLES ON SUBSURFACE DAMAGE GRADIENT.....	216
7.5.3. EXPERIMENTAL SUBSURFACE CRACK GROWTH OBSERVATIONS AND COMPARISON WITH NUMERICAL DAMAGE GRADIENT.....	222
 CHAPTER 8:	
SUMMARY AND CONCLUSIONS	230
 CHAPTER 9:	
SUGGESTIONS FOR FUTURE WORK	234
 REFERENCES	235
 APPENDIX A:	
FINITE ELEMENT ANALYSIS BASICS.....	245
 A.1. TIME INTEGRATION METHODS	246
A.2. ELEMENT FORMULATIONS	249
A.3. CONTACT ALGORITHMS.....	250
A.4. ENERGIES AND EXTERNAL WORK.....	252
 APPENDIX B:	
SAMPLE NORMAL CONTACT ANALYSIS INPUT FILE	254

APPENDIX C:	
SAMPLE SLIDING CONTACT ANALYSIS INPUT FILE	258
APPENDIX D:	
EOS ANALYSIS	268
APPENDIX E:	
SAMPLE COUPLED THERHAL AND MECHANICAL SLIDING CONTACT ANALYSIS INPUT FILE	272
APPENDIX F:	
SAMPLE INPUT FILE FOR MODELING THE INFULENCE OF SECONDARY HARD PARTICLES	283
APPENDIX G:	
DIMENSIONAL ANALYSIS.....	295
G.1. INTRODUCTION TO DIMENSIONAL ANALYSIS AND BUCKINGHAM π THEOREM	295
G.2. SLIDING OF AN ASPERITY OVER A DEFORMABLE MATERIAL.....	298
G.3. STRAIN RATE AND THERMAL SOFTENING EFFECTS.....	301
VITA AUCTORIS	302

LIST OF TABLES

Chapter 2

Table 2.1:	Flow stress-plastic strain curve constants for different materials represented by Equation 2.57 [129].	55
------------	--	----

Chapter 4

Table 4.1:	Comparison of the different meshed elastic normal contact models.	76
Table 4.2:	Data points used to discretize the experimentally determined stress/strain relationship of the 356 Al alloy.	85
Table 4.3:	EOS parameters for the 356 Al alloy obtained from Steinberg [96].	87
Table 4.4:	Total number of elements and nodes used in the discretization of the finite element models.	98

Chapter 6

Table 6.1:	Maximum values of energies obtained from a typical normal contact simulation.	116
Table 6.2:	Maximum values of energies obtained from a typical sliding contact simulation (Eulerian model).	117
Table 6.3:	Maximum values of energies obtained from a typical sliding contact simulation using Lagrangian thermo-mechanical model.	118
Table 6.4:	Maximum values of energies obtained from a typical sliding contact simulation with hard particles.	119
Table 6.5:	Comparison of the elastic normal contact model results and the Hertz theory calculations for normal load of 3.3N/mm.	130
Table 6.6:	Comparison of penetration depths and element numbers in the contact line for elastic numerical models for normal load of 3.3N/mm.	130

Table 6.7:	Comparison of the experimentally and numerically determined indentation contact depth on the 356 Al material.....	134
Table 6.8:	Comparison of the experimentally and numerically determined indentation contact length on the 356 Al material.....	134
Table 6.9:	Comparison of the experimentally and numerically determined plastic zone depth.....	137
Table 6.10:	Comparison of the experimentally and numerically determined plastic zone width.....	137
Table 6.11:	Coefficients <i>A</i> , <i>B</i> and <i>C</i> in the Equation 6.1 for the 356 Al alloy (sliding velocity: 0.15 m/s, normal load: 300 N/mm).....	138
Table 6.12:	Coefficients <i>A</i> , <i>B</i> and <i>C</i> in the Equation 6.1 for the 1100 Al.....	142
Table 6.13:	Flow stress-plastic strain curve constants of the 1100 Al material for two different loads.....	145

Chapter 7

Table 7.1:	Change in the subsurface characteristics with the implementation of a square shaped Si particle in the 356 Al matrix for a sliding velocity of 10 m/s and normal load of 250 N/mm (↑ : increase, ↓: decrease).....	204
Table 7.2:	Change in the subsurface characteristics with the implementation of a rectangular shaped Si particle in the 356 Al matrix for a sliding velocity of 10 m/s and normal load of 250 N/mm (↑ : increase, ↓: decrease).....	205
Table 7.3:	Change in the subsurface characteristics with the implementation of a circular shaped Si particle in the 356 Al matrix for a sliding velocity of 10 m/s and normal load of 250 N/mm (↑ : increase, ↓: decrease).....	206
Table 7.4:	Pre-exponential and exponential coefficients in Equations 7.1 to 7.4 (Sliding velocity: 10 m/s, Normal load: 150 N/mm).....	211

LIST OF FIGURES

Chapter 1

- Figure 1.1: Subsurface crack propagation observed in a 356 Al alloy during dry sliding wear [17].....5
- Figure 1.2: Distributions of the hydrostatic pressure (σ_H) and the flow stress (σ_F) that create a subsurface damage gradient (z_C is the location of the highest damage).....5

Chapter 2

- Figure 2.1: Apparent and real area of contact [5]. 9
- Figure 2.2: Formation of wear sheets due to delamination: (a) Smoothing of the softer surface, (b) Strain accumulation below the surface, (c) Initiation of subsurface cracks and (d) Formation of sheet-like wear particles [5]. 10
- Figure 2.3: Subsurface crack under a moving asperity [118]..... 10
- Figure 2.4: Void formation around inclusions and crack propagation from these voids near the surface in annealed Fe-1.3 % Mo [118]..... 12
- Figure 2.5: Schematic diagram showing how the severity of plastic deformation is distributed beneath a worn metal surface in the severe wear regime [29]. 13
- Figure 2.6: Stages in the cup-and-cone fracture (a) Initial necking, (b) Small cavity formation, (c) Coalescence of cavities to form a crack, (d) crack propagation and (e) Final shear fracture at a 45 ° angle relative to the tensile direction [36]. 16
- Figure 2.7: The void nucleation strains for various hydrostatic stresses in a spheroidised 1045 steel [124]. 18
- Figure 2.8: A spherical void subjected to remote stress and strain rate fields [25, 37]. 22

Figure 2.9:	Contact between cylindrical surfaces: (a) Area of contact in Hertz theory, (b) Maximum contact pressure and axes.....	25
Figure 2.10:	Hertz theory (a) Subsurface stresses along the axis of symmetry, (b) Contours of maximum shear stress [43].....	25
Figure 2.11:	Geometry of the single point contact problem by Boussinesq and Cerruti [43].....	26
Figure 2.12:	Schematic view of sliding contact from Hamilton and Goodman [50].....	30
Figure 2.13:	Lines of constant von Mises stress normalized by maximum contact pressure (P_0) on plane $y = 0$ beneath circular contact [42].	30
Figure 2.14:	Lines of constant von Mises stress normalized by maximum contact pressure (P_0) on plane $y = 0$ beneath circular contact, $\mu = 0.25$ [42].	31
Figure 2.15:	Lines of constant von Mises stress normalized by maximum contact pressure (P_0) on plane $y = 0$ beneath circular contact, $\mu = 0.50$ [42].	31
Figure 2.16:	Lines of constant von Mises stress normalized by maximum contact pressure (P_0) beneath contact between normally loaded cylinders [42]..	33
Figure 2.17:	Lines of constant von Mises stress normalized by maximum contact pressure (P_0) beneath contact between cylinders, $\mu = 0.25$ [42].....	33
Figure 2.18:	Lines of constant von Mises stress normalized by maximum contact pressure (P_0) beneath contact between cylinders, $\mu = 0.50$ [42].....	34
Figure 2.19:	Sliding contact by Johnson [43] P is the normal load and Q is the tangential traction.....	34
Figure 2.20:	Contours of the principal shear stress beneath a sliding contact ($\mu = 0.2$) [43].....	36
Figure 2.21:	Model of a contact between a stationary rigid asperity and a sliding elastic-perfectly plastic plane (U : sliding velocity) [118].	37
Figure 2.22:	Steady state plastic deformation regions in an elastic-perfectly plastic material under a sliding contact, for a maximum applied normal stress $p_0 = 4k$ and different coefficients of friction [118].....	37
Figure 2.23:	Finite element mesh around a crack tip by Sin and Suh [45].	40

Figure 2.24:	Comparison of contours of von Mises stress values normalized by P_0 ; sharp lines: finite element analysis, smooth lines: theoretical values [46].	40
Figure 2.25:	von Mises stress contours after penetration and sliding of a half-space surface: (a) $\mu=0.1$, (b) $\mu=0.5$, von Mises stress contours after penetration and sliding of a layered surface for $\mu=0.1$, $E(\text{layer})/E(\text{substrate})= 4$: (c) $h/R= 0.0356$ (d) $h/R= 0.142$ (Stresses are in GPa, h: height of layer, R: radius of cylinder, E: elastic modulus) [52].	44
Figure 2.26:	Pressure profiles under the indenter for a layered medium [53].	45
Figure 2.27:	Schematic view of sliding contact of a two-layer half-space by Tian and Saka [54].	45
Figure 2.28:	Distribution of contact pressure and subsurface principal shear stress for simulated elastic contact of surfaces: (a) Contact geometry and surface pressure distribution, (b) Contour plot of principle shear stress distribution normalized by maximum contact pressure, (c) Effect of friction, $\mu=0.1$, on stress distribution shown in (b) (Due to the effect of rough engineering surface, the maximum principle shear stress is observed very close to the surface, even when frictionless conditions are considered) [15].	46
Figure 2.29:	Schematic diagram of the geometry of an interface crack by Tian and Saka [56].	47
Figure 2.30:	(a) Schematic representation of a horizontal subsurface crack in a two-dimensional half-space subjected to an array of moving asperity contacts, (b) A representative single-asperity and the contact related nomenclature [59].	51
Figure 2.31:	Wear profile of the punch after 20000 blanking cycles (a) FEM calculation, (b) Experiment [61].	52
Figure 2.32:	Tension testing apparatus under hydrostatic pressure [66].	58
Figure 2.33:	The effect of pressure on the ductility of aluminum subjected to tensile test [66].	59

Figure 2.34:	Dynamic uniaxial compressive tests on work hardened aluminum at various constant strains (o: $\epsilon=0.01$, \square : $\epsilon=0.02$ Δ : $\epsilon=0.04$, ∇ : $\epsilon=0.08$, $+$: $\epsilon=0.16$) [67].	60
Figure 2.35:	Dynamic shear stress-shear strain curves for commercially pure aluminum at various strain rates (the nominal shear strain rates are given by the following symbols: $+$: $\dot{\gamma}=2800 \text{ s}^{-1}$; Δ : $\dot{\gamma}=2200 \text{ s}^{-1}$; \square : $\dot{\gamma}=1600 \text{ s}^{-1}$; \bullet : $\dot{\gamma}=1450 \text{ s}^{-1}$; x : $\dot{\gamma}=800 \text{ s}^{-1}$; ∇ : $\dot{\gamma}=600 \text{ s}^{-1}$; o: $\dot{\gamma}=0.002 \text{ s}^{-1}$,) [68].	60
Figure 2.36:	Comparison of static and dynamic yield stresses for 6061-T6 aluminum obtained by biaxial tensile test (o: dynamic yield point (40 s^{-1} strain rate), \square : static yield point) [69].	61
Figure 2.37:	Stress-strain relationships obtained by torsion tests and dynamic Hopkinson bar tensile tests for (a) 2024-T351 Aluminum, (b) 7039 Aluminum [73, 74].	62
Figure 2.38:	Spall strength versus strain rate for 6061-T6 Al alloy (\bullet) and 99.0 % pure aluminum (\square) [133, 134].	66
Figure 2.39:	Change of flow stress for some aluminum alloys with temperature [75, 76] (True stresses are given at 0.2 true plastic strain).	67
Figure 2.40:	Change of the Johnson-Cook thermal material parameter (m) with temperature for some aluminum alloys calculated using stress-strain curves from Figure 2.39.	67
Figure 2.41:	Strain and temperature dependence of the strain rate sensitivity for (a) Al-Mg-Si alloy, (b) pure aluminum [77].	68

Chapter 4

Figure 4.1:	General view of the normal contact finite element models, loading (F: distributed normal load) and boundary conditions (restriction of the bottom nodes from the motion): (a) Model A and (b) Model B.	74
-------------	--	----

Figure 4.2:	General view of the normal contact finite element models, loading (F: distributed normal load) and boundary conditions (restriction of the bottom nodes from the motion): (a) Models C, D, E and (b) Model F.....	75
Figure 4.3:	Normal load application curve for the simulations using: (a) the explicit solution scheme and (b) the implicit solution scheme.....	77
Figure 4.4:	General view of the multiple asperity contacts model (The first asperity is shown during sliding while the following asperity is at rest).	83
Figure 4.5:	Mesh generated for the finite element model: (a) the complete mesh, (b) the asperity and (c) part of the 356 Al structure closer to the contact surface.....	84
Figure 4.6:	Experimentally determined stress/strain behaviour of the 356 Al alloy and the data points used to discretize it in the finite element material model.	85
Figure 4.7:	Distribution of the normal load equally on each node located at the top layer of the asperity.....	88
Figure 4.8:	Boundary conditions and symmetry axes.	88
Figure 4.9:	Geometry of the finite element model ((1) is the 356 Al half-space and (2) is the steel counterface), loading (F: Distributed normal load, V: Sliding velocity) and boundary conditions (restriction of the bottom nodes from the motion).	92
Figure 4.10:	The relationship among stress, strain, strain rate and temperatures according to Equation 4.5.	93
Figure 4.11:	A typical microstructure observed in a 356 Al alloy after T6 heat treatment.....	99
Figure 4.12:	General view of the finite element model developed for the investigation of influence of the hard particles.	99
Figure 4.13:	Geometric details of the finite element model for the hard particles: (a) square shaped Si particle, (b) rectangular shaped Si particle and (c) circular shaped Si particle.	100

Chapter 5

- Figure 5.1: Microstructure of the 356 Al samples: (a) after a solution treatment of 12 hours at 813 K, (b) after a solution treatment of 24 hours at 813 K, (c) after a solution treatment of 36 hours at 813 K (35.0 ± 2.5 HRB, 74.5 ± 6.0 Vickers hardness) and (d) after a solution treatment of 36 hours at 813 K and an aging heat treatment of 5 hours at 428 K (50.6 ± 2.0 HRB, 84.1 ± 1.5 Vickers hardness)..... 103
- Figure 5.2: Views of the normal contact samples: (a) 2mm diameter M2 tool steel cylinder and (b) the 356 Al sample after several normal contacts (indentations). 104
- Figure 5.3: (a) Surface profile obtained by optical surface profilometer: Determination of the plastic deformation characteristics (plastic deformation width and depth) from the experimental studies (Load: 335.8 N/mm), 105
(b) Determination of the plastic deformation characteristics (plastic deformation width and depth) from the numerical studies (Load: 335.82 N/mm). 105
- Figure 5.4: (a) Surface profile obtained by optical surface profilometer: Determination of the contact characteristics (contact length and depth) from the experimental studies (Load: 335.82 N/mm), 106
(b) Determination of the plastic deformation characteristics (contact length and depth) from the numerical studies (Load: 335.82 N/mm). 106
- Figure 5.5: Photograph of the reciprocating wear machine with its specimen holders used in sliding contact experiments..... 107
- Figure 5.6: (a) Schematic view of the sliding contact samples: the 356 Al, M2 tool steel cylinders and markers..... 108
(b) Subsurface micrograph showing displacement of the marker after multiple sliding contacts (sliding velocity: 0.15 m/s, normal load: 300 N/mm). 108
- Figure 5.7: Schematic view of the block-on-ring wear test setup. 111

Figure 5.8:	Subsurface micrograph showing the deformation of the reference marker along the direction of sliding (Test result with 1 m/s sliding velocity and 30 N normal load).	111
-------------	--	-----

Chapter 6

Figure 6.1:	Typical energies and external work observed in the normal contact simulations.....	116
Figure 6.2:	Energies and external work typical of the sliding contact modeling simulations (Eulerian model).....	117
Figure 6.3:	Typical energies and external work observed in the sliding contact simulations with Lagrangian thermo-mechanical model..	118
Figure 6.4:	Energies and external work typical of the sliding contact modeling simulations with hard particles.....	119
Figure 6.5:	Interface forces applied to the asperity in the normal contact modeling simulations: (a) Force in the X direction, (b) Force in the Y direction....	120
Figure 6.6:	Variation of the von Mises stress at 0.2 μm depth (Normal load: 3.3 N, Normal contact model).	121
Figure 6.7:	Interface forces applied to the asperity in the sliding contact modeling simulations using the Eulerian model: (a) Force in the X direction, (b) Force in the Y direction.	124
Figure 6.8:	(a) Variation of the von Mises stress at 200 μm depth, (b) Accumulation of the plastic strain at 200 μm depth (Sliding velocity: 10 m/s, Normal load: 300 N/mm, Eulerian model).....	125
Figure 6.9:	Interface forces applied to the asperities in the sliding contact simulations with Lagrangian thermo-mechanical model: (a) Force in the X direction, (b) Force in the Y direction.	126
Figure 6.10:	Variation of interface forces in the X direction with normal load (Sliding velocity: 10 m/s, thermo-mechanical model).	127
Figure 6.11:	Variation of interface forces in the X direction with sliding velocity (Normal load: 250 N/mm, Lagrangian thermo-mechanical model).	128

Figure 6.12:	(a) Variation of the von Mises stress at 25 μm depth, (b) Accumulation of the plastic strain at 25 μm depth (Sliding velocity: 10 m/s, Normal load: 150 N/mm, Lagrangian thermo-mechanical model).....	129
Figure 6.13:	Comparison of the pressure distribution (P) in the contact zone obtained by the elastic finite element models and the analytical solution (x is the distance along the surface).	132
Figure 6.14:	Comparison of the subsurface stresses in the aluminum half-space material along the axis of symmetry obtained by the elastic finite element models and the analytical solution.....	133
Figure 6.15:	Marker position in the 356 Al alloy after four sliding tests with a sliding velocity of 0.15 m/s and normal load of 300 N/mm.....	137
Figure 6.16:	Determination of the deformation angle (θ) to calculate the equivalent plastic strain below the contact surface.....	138
Figure 6.17:	Subsurface equivalent plastic strain distribution in the 356 Al alloy after sliding contacts (sliding velocity: 0.15 m/s and normal load: 300 N/mm).	139
Figure 6.18:	Marker position in the 1100 Al samples after wear tests with 10 N and 30 N normal loads and 1 m/s sliding velocity.....	142
Figure 6.19:	Equivalent plastic strain vs. depth below the worn surfaces at different loads (sliding distance = 1000m, sliding velocity = 1 m/s).	143
Figure 6.20:	Flow stress (Vickers hardness) vs. depth below the worn surface at different loads (sliding distance = 1000m, sliding velocity = 1 m/s).....	144
Figure 6.21:	Cumulative flow stress-strain curve of the 1100 Al material for two different loads.	145
Figure 6.22:	Temperature distribution at the contact surface for two different loads.	146
Figure 6.23:	Experimental cumulative flow stress-strain behaviour of the 1100 Al material (measured) and calculated stress-strain relationship by using thermal softening equation (Equation 4.12).....	147

Chapter 7

- Figure 7.1: von Mises stress (in MPa units) distribution in the 356 Al alloy after multiple sliding contacts: (a) after the first contact, (b) after the fourth contact and (c) after the seventh contact (Sliding velocity: 10 m/s, Normal load: 300 N/mm, Equation 4.1, Eulerian model). 150
- Figure 7.2: Equivalent plastic strain distribution in the 356 Al alloy after multiple sliding contacts: (a) after the first contact, (b) after the fourth contact and (c) after the seventh contact (Sliding velocity: 10 m/s, Normal load: 300 N/mm, Equation 4.1, Eulerian model). 151
- Figure 7.3: Increase in subsurface stresses with increasing number of the asperity contacts at the mid-point of the 356 Al alloy (Sliding velocity: 10 m/s, Normal load: 300 N/mm, Equation 4.1, Eulerian model). (z is the depth beneath the contact surface and a is the asperity diameter)..... 152
- Figure 7.4: Increase in subsurface equivalent plastic strains with increasing number of the asperity contacts at the mid-point of the 356 Al alloy (Sliding velocity: 10 m/s, Normal load: 300 N/mm, Equation 4.1, Eulerian model). (z is the depth beneath the contact surface and a is the asperity diameter)..... 153
- Figure 7.5: Hydrostatic pressure (in MPa units) distribution in the 356 Al alloy after multiple sliding contacts: (a) after the first contact, (b) after the fourth contact and (c) after the seventh contact (Sliding velocity: 10 m/s, Normal load: 300 N/mm, Equation 4.1, Eulerian model). 154
- Figure 7.6: Accumulation of the hydrostatic pressure with increasing number of the asperity contacts at the mid-point of the 356 Al alloy (Sliding velocity: 10 m/s, Normal load: 300 N/mm, Equation 4.1, Eulerian model). (z is the depth beneath the contact surface and a is the asperity diameter)..... 155
- Figure 7.7: Change of the strain rate with multiple sliding contacts at the mid-point of the 356 Al alloy (Sliding velocity: 10 m/s, Normal load: 300 N/mm, Equation 4.1, Eulerian model). 157
- Figure 7.8: Effect of the normal load on the distribution of von Mises stress (Sliding velocity: 10 m/s, Equation 4.1, Eulerian model)..... 158

Figure 7.9:	Effect of the normal load on the distribution of subsurface strains (Sliding velocity: 10 m/s, Equation 4.1, Eulerian model).....	159
Figure 7.10:	The effect of coefficient of friction ($\mu=0.0$ to 0.8) on the maximum stress and strain values. (The order of the asperities, and the resulting stresses and strains are indicated for $\mu=0.0$. The continuous curve is the experimentally defined stress/strain relationship).	160
Figure 7.11:	The hydrostatic pressure and the von Mises stress distributions below the surface of the 356 Al after passage of the seventh asperity for $\mu=0.0$ and $\mu=0.3$ (Sliding velocity: 10 m/s, Normal load: 300 N/mm, Equation 4.1, Eulerian model).....	163
Figure 7.12:	Effect of the sliding velocity on the distribution of equivalent plastic strain under the surface of 356 Al alloy (Normal load: 300 N/mm, Equation 4.1, Eulerian model, values after one asperity contact).	164
Figure 7.13:	Effect of the asperity distance on the distribution of equivalent plastic strain at 100 μm depth (d represents the distance between the asperities and ϕ is the asperity diameter) (Sliding velocity: 10 m/s, Normal load: 300 N/mm, Equation 4.1, Eulerian model).	165
Figure 7.14:	von Mises stress (MPa) distribution in the 356 Al half-space after multiple sliding contacts: (a) after the first contact, (b) after the fourth contact and (c) after the seventh contact (Sliding velocity: 10 m/s, Normal load: 150 N/mm, Equation 4.5, Lagrangian model).	167
Figure 7.15:	Variation of the subsurface stresses with increasing number of sliding contacts at the mid-point of the 356 Al half-space (Sliding velocity: 10 m/s, Normal load: 150 N/mm, Equation 4.5, Lagrangian model). (z is the depth beneath the contact surface and a is the counterface diameter).....	168
Figure 7.16:	Equivalent plastic strain distribution in the 356 Al half-space after multiple sliding contacts: (a) after the first contact, (b) after the fourth contact and (c) after the seventh contact (Sliding velocity: 10 m/s, Normal load: 150 N/mm, Equation 4.5, Lagrangian model).	169

Figure 7.17:	Accumulation of the subsurface equivalent plastic strains with increasing number of the sliding contacts at the mid-point of the 356 Al half-space (Sliding velocity: 10 m/s, Normal load: 150 N/mm, Equation 4.5, Lagrangian model). (z is the depth beneath the contact surface and a is the asperity diameter).....	170
Figure 7.18:	Hydrostatic Pressure (in MPa units) distribution in the 356 Al half-space after multiple sliding contacts: (a) after the first contact, (b) after the fourth contact and (c) after the seventh contact (Sliding velocity: 10 m/s, Normal load: 150 N/mm, Equation 4.5, Lagrangian model).....	171
Figure 7.19:	Distribution of the hydrostatic pressure with increasing number of sliding contacts at the mid-point of the 356 Al half-space (Sliding velocity: 10 m/s, Normal load: 150 N/mm, Equation 4.5, Lagrangian model).....	172
Figure 7.20:	Temperature (in Kelvin) distribution in the 356 Al half-space after multiple sliding contacts: (a) after the first contact, (b) after the fourth contact and (c) after the seventh contact (Sliding velocity: 10 m/s, Normal load: 150 N/mm, Equation 4.5, Lagrangian model).....	174
Figure 7.21:	Increase of the subsurface temperature with multiple sliding contacts at the mid-point of the 356 Al half-space (Sliding velocity: 10 m/s, Normal load: 150 N/mm, Equation 4.5, Lagrangian model).....	175
Figure 7.22:	Change of the strain rate with multiple sliding contacts at the mid-point of the 356 Al half-space (Sliding velocity: 10 m/s, Normal load: 150 N/mm, Equation 4.5, Lagrangian model).....	176
Figure 7.23:	Comparison of the effect of the material model on the subsurface plastic strain distribution in the 356 Al half-space (Results after seventh sliding contact) (Sliding velocity: 10 m/s, Normal load: 150 N/mm, Lagrangian model).....	180
Figure 7.24:	Comparison of the effect of the material model on the subsurface temperature distribution in the 356 Al half-space (Results after seventh sliding contact) (Sliding velocity: 10 m/s, Normal load: 150 N/mm, Lagrangian model).....	181

Figure 7.25:	Effect of the normal load on the distribution of the subsurface strains (Results after the seventh contact) (Sliding velocity: 10 m/s, Lagrangian model).....	182
Figure 7.26:	Effect of the normal load on the accumulation of the stresses, strains and temperature in the 356 Al half-space with increasing number of sliding contacts. (The order of the asperities, the resulting stresses, strains and temperatures are indicated. Results are taken from the mid-point of the 356 Al half-space close to the surface). (Sliding velocity: 10 m/s, Equation 4.5, Lagrangian model).....	183
Figure 7.27:	Effect of the friction on the accumulation of the stresses, strains and temperature in the 356 Al half-space after 3rd sliding contact. (The order of the asperities, the resulting stresses, strains and temperatures are indicated. Results are taken from the mid-point of the 356 Al half-space). (Sliding velocity: 10 m/s, Normal load: 150 N/mm, Equation 4.5, Lagrangian model).....	184
Figure 7.28:	Effect of the sliding velocity on the accumulation of the subsurface stresses, strains and temperature in the 356 Al half-space after seventh sliding contact. (The order of increasing depth, and the resulting stresses, strains and temperatures are indicated. Results are taken from the mid-point of the 356 Al half-space). (Normal load: 150 N/mm, Equation 4.5, Lagrangian model).....	185
Figure 7.29:	Distribution of the equivalent plastic strain at the center of the 356 Al after seventh sliding contact (Sliding velocity: 10 m/s, obtained with strain hardening material model (Equations 4.1 and 4.7)).....	187
Figure 7.30:	Distribution of the von Mises stress at the center of the 356 Al after seventh sliding contact (Sliding velocity: 10 m/s, obtained with strain hardening material model (Equations 4.1 and 4.7)).....	188
Figure 7.31:	Maximum stress-strain values obtained from numerical simulations and comparison to the original experimental stress-strain curve (Results are given after first and seventh contacts at the surface). (Sliding velocity: 10 m/s, obtained with strain hardening material model (Equations 4.1 and 4.7)).	189

Figure 7.32:	von Mises stress (MPa) distribution in the 356 Al half-space after seventh sliding contact (Sliding velocity: 10 m/s, Normal load: 250 N/mm, Equation 4.5).....	191
Figure 7.33:	von Mises stress (MPa) distribution in the 356 Al half-space after seventh sliding contact with the implementation of a square shaped Si particle (Sliding velocity: 10 m/s, Normal load: 250 N/mm, Equation 4.5).....	192
Figure 7.34:	von Mises stress (MPa) distribution in the 356 Al half-space after seventh sliding contact with the implementation of a rectangular shaped Si particle (Sliding velocity: 10 m/s, Normal load: 250 N/mm, Equation 4.5).....	193
Figure 7.35:	von Mises stress (MPa) distribution in the 356 Al half-space after seventh sliding contact with the implementation of a circular shaped Si particle (Sliding velocity: 10 m/s, Normal load: 250 N/mm, Equation 4.5).....	194
Figure 7.36:	Subsurface von Mises stress (MPa) distribution at the mid-point of the 356 Al half-space after seventh sliding contact (Sliding velocity: 10 m/s, Normal load: 250 N/mm, Equation 4.5).....	195
Figure 7.37:	Equivalent plastic strain distribution in the 356 Al half-space after seventh sliding contact (Sliding velocity: 10 m/s, Normal load: 250 N/mm, Equation 4.5): (a) the model not considering a Si particle and (b) the model with square shaped Si particle.....	198
Figure 7.38:	Equivalent plastic strain distribution in the 356 Al half-space after seventh sliding contact (Sliding velocity: 10 m/s, Normal load: 250 N/mm, Equation 4.5): (a) the model with rectangular shaped Si particle and (b) the model with circular shaped Si particle.....	199
Figure 7.39:	Equivalent plastic strain distribution at the mid-point of the 356 Al half-space after seventh sliding contact with and without the implementation of a Si particle (Sliding velocity: 10 m/s, Normal load: 250 N/mm, Equation 4.5).....	200
Figure 7.40:	Hydrostatic pressure (in MPa units) distribution at the mid-point of the 356 Al half-space after seventh sliding contact with and without the implementation of a Si particle (Sliding velocity: 10 m/s, Normal load: 250 N/mm, Equation 4.5).....	201

Figure 7.41:	Change in the subsurface temperature distribution at the mid-point of the 356 Al half-space with the implementation of a Si particle below the surface (Sliding velocity: 10 m/s, Normal load: 250 N/mm, Equation 4.5).....	202
Figure 7.42:	Subsurface regions adjacent to the square shaped Si particle.....	203
Figure 7.43:	Change in the damage rate with the depth below the contact surface with increasing number of sliding contacts (Sliding velocity: 10 m/s and Normal load: 150 N/mm).....	212
Figure 7.44:	Effect of the material model on the damage rate below the contact surface after seventh sliding contact (Sliding velocity: 10 m/s and Normal load: 150 N/mm).....	213
Figure 7.45:	Effect of the normal load and the sliding velocity on the damage rate below the contact surface after seventh sliding contact obtained with Equation 4.5.....	214
Figure 7.46:	Effect of the friction on the damage rate below the contact surface after third sliding contact (Sliding velocity: 10 m/s, Normal load: 150 N/mm, obtained with Equation 4.5).....	215
Figure 7.47:	Position of the subsurface lines used for the damage rate calculations in the 356 Al half-space.....	218
Figure 7.48:	Change in the subsurface damage rate at the mid-point of the 356 Al half-space with the implementation of Si particles (Sliding velocity: 10 m/s, Normal load: 250 N/mm, Results after seventh sliding contact).....	219
Figure 7.49:	Change in the subsurface damage rate at the back edge of the Si particle (Sliding velocity: 10 m/s, Normal load: 250 N/mm, Results after seventh sliding contact).....	220
Figure 7.50:	Change in the subsurface damage rate at the front edge of the Si particle (Sliding velocity: 10 m/s, Normal load: 250 N/mm, Results after seventh sliding contact).....	221
Figure 7.51:	Subsurface crack propagation in the 356 Al alloy after seven sliding contacts with a M2 tool steel (Sliding velocity: 0.15 m/s and Normal load: 250 N/mm) (SEM Back-Scattered Electron Image (BEI)).....	224

Figure 7.52:	Plate-like wear debris formation in the 356 Al alloy after seven sliding contacts with a M2 tool steel (Sliding velocity: 0.15 m/s and Normal load: 250 N/mm) (SEM BEI).....	225
Figure 7.53:	Debris formation in the 356 Al alloy after seven sliding contacts with a M2 tool steel (Sliding velocity: 0.15 m/s and Normal load: 250 N/mm) (SEM Secondary Electron Image (SEI)).....	226
Figure 7.54:	Propagation of a subsurface crack in the 356 Al alloy parallel to the surface (Sliding velocity: 0.15 m/s and Normal load: 250 N/mm) (SEM SEI).....	227
Figure 7.55:	Propagation and joining of surface cracks in the 356 Al alloy (Sliding velocity: 0.15 m/s and Normal load: 250 N/mm) (SEM SEI).....	228
Figure 7.56:	Comparison of the experimental and numerical maximum damage depths (z_c) in the 356 Al alloy for different sliding velocities (Normal load: 250 N/mm).....	229

Appendix D

Figure D.1:	(a) Pressure prediction by the Gruneisen EOS and Linear Polynomial EOS, (b) Pressure prediction difference between the Gruneisen EOS and Linear Polynomial EOS as percentage.....	267
Figure D.2:	Comparison of the predictions two simulations using two different EOS for the 356 Al material: (a) hydrostatic pressure, (b) von Mises stress and (c) equivalent plastic strain (Sliding velocity: 10 m/s, Normal load: 300 N/mm).....	270

Appendix G

Figure G.1:	The change of plastic strain against depth at the mid point of the finite element model.	300
-------------	---	-----

NOMENCLATURE

Chapter 1

R :	radius of a void
\dot{R} :	void growth rate
σ_H :	mean or hydrostatic stress
σ_f :	equivalent flow stress
$\dot{\epsilon}$:	the strain rate

Chapter 2

V :	volume of the wear sheet
S_D :	sliding distance
L :	applied normal load
H :	hardness of the material
K :	proportionality constant
W :	wear rate
P :	applied load
S_V :	sliding speed
f :	mass fraction of oxygen in the oxide
t :	thickness of oxide film
ρ :	material density
A_p :	material constant
Q_p :	activation energy of the oxidation,
R :	gas constant

T :	temperature
ΔL :	contact length
d :	subsurface depth of the crack
λ :	spacing between the asperities
l_c :	spacing between cracks
$\Delta \bar{C}_L$:	average crack propagation rate of the left side of crack
$\Delta \bar{C}_R$:	average crack propagation rate of the right side of crack
N :	number of contact cycles
σ_m :	hydrostatic tension component of the stress
σ_f :	flow stress of the material
σ_{rr} :	maximum interfacial stress
σ_C :	critical value of normal stress for micro-void nucleation
σ_{loc} :	local stress
ρ_{loc} :	local dislocation density
ϵ_N :	void nucleation strain
$d\eta_{zb}$:	damage rate
F_{zb} :	relative growth factor
F_{zb}^f :	critical value of the relative growth factor for fracture
b :	radius of the growing cylindrical cavity
l_b :	mean spacing between the cavities
b^0 :	initial value of the radius
l_b^0 :	mean spacing
$d\bar{\epsilon}$:	equivalent strain

n :	strain hardening coefficient,
$\bar{\sigma}$:	equivalent stress
σ_a :	applied transverse tensile stress
σ_b :	applied transverse tensile stress
$\dot{\epsilon}_i$:	strain rate in the i direction
ν :	Lode variable
\dot{R}_k :	rates of change in the radius of the void in the directions X_1 , X_2 and X_3
$(1+E)$:	factor describing the amplification of the void's growth rate relative to the strain rate of the matrix
D_S :	factor describing the void's growth rate relative to the stresses in the matrix
σ_0 :	the yield stress
\dot{R} :	overall void growth rate
R :	radius
x :	position in the X direction
$P(x)$:	pressure distribution in the X direction
P_0 :	maximum contact pressure
a :	semi-contact width
E^* :	combined modulus
E :	elastic modulus
ν :	Poisson's ratio
σ_x :	first principle stress
σ_y :	second principle stress
σ_z :	third principle stress

τ :	maximum shear stress
\bar{u} :	displacement
$Q(x)$:	shear traction distribution in the X direction
μ :	coefficient of friction
k :	yield strength in shear
h :	height of coating layer
s :	sliding distance
A :	contact area
h :	wear depth
k :	dimensional wear coefficient
γ :	wear coefficient
F_N :	applied normal load
$\bar{\sigma}_f$:	equivalent or flow stress
$\bar{\epsilon}$:	equivalent strain
K_n :	work hardening coefficient
$\bar{\sigma}_0$:	initial yield stress
$\bar{\sigma}_s$:	saturation stress, the stress at which the work hardening rate becomes zero
ϵ_C :	material constant
D :	material constant
q :	material constant
C :	material constant
σ_T :	flow stress at temperature T
σ_{room} :	flow stress at room temperature

T_{room} :	room temperature
T_{melt} :	melting temperature
m :	Johnson-Cook thermal material parameter
n_R :	strain rate sensitivity
$\Delta\sigma'_G$:	stress constant
σ :	plastic flow stress
ε :	plastic strain
$\dot{\varepsilon}$:	strain rate
l :	the average grain diameter
c_j :	material constants

Chapter 4

σ_f :	flow stress
ε :	equivalent plastic strain
σ_0 :	bulk flow strength
σ_S :	saturation stress, the stress at which the work hardening rate becomes zero
ε_C :	material constant
P :	pressure
E :	energy per unit volume
ρ_0 :	initial density
ρ :	density of the material
C_0 :	bulk sound speed

γ_0 :	initial value of Gruneisen's gamma
b :	coefficient of the volume dependence of gamma
S_1 :	linear equation of state coefficient
S_2 :	quadratic equation of state coefficient
S_3 :	cubic equation of state coefficient
ψ :	compression
$\dot{\epsilon}^P$:	plastic strain rate
D :	Cowper and Symond material parameter
q :	Cowper and Symond material parameter
T :	temperature of the contacting material
T_{room} :	room temperature
T_{melt} :	melting temperature
m :	dimensionless Johnson-Cook thermal material parameter
ν :	Poisson's ratio
x_i :	coordinates as a function of time
β :	work rate to heat rate conversion factor
C_P :	specific heat
k_{ij} :	thermal conductivity
Q :	internal heat generation rate per unit volume
μ :	coefficient of friction

Chapter 6

σ_x :	first principle stress
σ_y :	second principle stress

τ :	maximum shear stress
Z :	subsurface depth
D :	position of the marker at a given depth
A :	material constant
B :	material constant
C :	material constant
ε :	equivalent plastic strain
θ :	deformation angle
σ_f :	flow stress
H :	microhardness
C_H :	material constant
m :	dimensionless Johnson-Cook thermal material parameter

Chapter 7

z :	depth beneath the contact surface
a :	asperity diameter
μ :	coefficient of friction
σ_H :	hydrostatic pressure
ε :	plastic strain
$\dot{\varepsilon}$:	strain rate
T :	temperature
\dot{R} :	void growth rate
R :	initial radius of the void

Appendix A

$[M]$:	mass matrix
$\{\ddot{u}\}$:	nodal accelerations vector
$[C]$:	damping matrix
$\{\dot{u}\}$:	nodal velocities vector
$[K]$:	stiffness matrix
$\{u\}$:	nodal displacements vector
$\{F_{external}\}$:	force vector including all forces, pressures, and body loads acting upon the finite element mesh
n :	present time step
$n+1$:	next time step
$n-1$:	previous time step
Δt :	duration of the time step interval
Δt_c :	critical time step
S :	safety factor
l_c :	smallest finite element length
c :	wave propagation velocity
ρ :	material density
E :	Young's Modulus
ν :	Poisson's ratio
β :	empirical coefficient
γ :	empirical coefficient
C_{user} :	user defined scale factor

K :	bulk modulus
A :	face area of the element in contact
V :	volume of the element
D_i :	shell element diagonals
f :	force
p :	penetration depth
k :	spring stiffness
Δt_{sc} :	time step size for the contact springs
m_s :	mass of slave node
m_m :	mass of master segment
E_{sie} :	sliding interface energy

Appendix D

P :	pressure
E :	energy per unit volume
C_i :	polynomial equation coefficients
ψ :	compression
ρ :	density of the material
ρ_0 :	initial density

Appendix G

n :	number of variables
k :	number of independent dimensions
p :	amount of dimensionless numbers

c :	geometric scale factor
L_S :	length in the scaled model
L_0 :	length in the original model
$2R$:	asperity diameter
W :	asperity thickness
F :	applied normal load
V :	sliding velocity
σ_0 :	bulk flow strength
σ_S :	saturation stress, the stress at which the work hardening rate becomes zero
\mathcal{E}_C :	material constant
σ_f :	flow stress of the material
\mathcal{E} :	plastic strain

LIST OF ABBREVIATIONS

FE:	Finite Element
FEA:	Finite Element Analysis
FEM:	Finite Element Method
LS-DYNA:	An explicit finite element program
LSTC:	Livermore Software Technology Corporation
DOF:	Degrees Of Freedom
EOS:	Equation Of State
CPU:	Central Processing Unit
ADINA:	A finite element software
ABAQUS:	A finite element software
PAFEC:	A finite element software
ANSYS:	A finite element software
COF:	Coefficient Of Friction
SEM:	Scanning Electron Microscope
BEI:	Back-scattered Electron Image
SEI:	Secondary Electron Image
ETP:	Electrolytic Tough Pitch
FCC:	Face Centered Cubic
BCC:	Body Centered Cubic

CHAPTER 1

INTRODUCTION

Aluminum-silicon alloys boast a high strength-to-weight ratio and superior castability, which makes them an integral element in many vehicle components. Some of these components such as pistons and cylinder bores, however, are subjected to a considerable amount of sliding motion. Despite their benefits, aluminum-silicon alloys have a relatively low wear resistance when compared to steel—a factor that has restricted the widespread application of these alloys in parts that operate in sliding contact conditions. Sliding wear is complicated, and incorporates several physical, chemical and thermal events. The mechanisms of sliding wear, such as cutting and plowing in the form of abrasive wear, asperity deformation, subsurface crack initiation and growth have left the associated problems open to investigation. This study seeks to better understand and optimize the tribological behaviour of aluminum alloys.

Engineering surfaces are not smooth. They contain peaks and valleys called asperities—sites where contact between two solid surfaces occurs. These asperities are responsible for supporting the applied loads and tractions that are formed when surfaces meet. It follows that understanding the interactions of the asperities between converging surfaces is an essential part of wear studies. While the elastic contact between a sphere or a cylinder and a plane has been studied extensively since the leading work of Hertz [1], plastic deformation of the asperities in aluminum alloys occurs during dry sliding wear—even at low loads—and theoretical contact mechanics solutions are limited in regard to these cases. The finite element method provides a convenient tool for the study of plastic contact problems, and there are a few investigations aimed at studying such contact problems with the goal of modeling wear events using numerical tools. The plastic material models used in these published studies tend to be simple in nature, making it necessary to implement realistic material models. It stands to reason that the distribution and accumulation of subsurface stress and strain within sliding asperity contacts should be investigated in more detail if we are to fully comprehend the sliding contact behaviour of aluminum alloys.

Some examples of experimental work on the topic of subsurface plastic deformation during wear are given in [2-5]. These experimental investigations revealed that, during sliding contact, the nucleation of voids and micro-cracks occurs around the second phase particles, such as silicon [2-5]. Examination of the affect of inclusions and secondary particles on the ductile fracture of alloys, including aluminum alloys containing 7 % and 13 % silicon, revealed that second phase particles are the source of cracks that lead to ductile rupture [6, 7]. The fracture mechanisms of silicon particles in aluminum alloys have been explored by various researchers [8, 9].

Thin, plate-like flake debris formation is commonly observed in sliding wear systems. Suh [10, 11] revealed that in dry or poorly lubricated sliding conditions, cracks initiating from secondary particles or inclusions had a tendency to spread parallel to the surface—forming wear particles that had a thin, flaked shape. This process of delamination was confirmed by both analytical and experimental work [12-16]. The dry sliding behaviour of an Al-7 % Si (A356 Al) alloy was investigated by Zhang and Alpas [17]. Their study also indicated that thin, flake or plate-like debris particles were generated during the process of subsurface delamination—a process that occurred as a result of the formation of cracks which originated from the silicon particles and spread parallel to the surface. Figure 1 shows a micrograph where subsurface crack propagation can be observed under dry sliding contact conditions [17].

The fracture mechanics approach has also been applied in the study of subsurface delamination problems [12, 18-22]. Fleming and Suh [12] made one of the first attempts to model the subsurface crack propagation in sliding contact using linear elastic fracture mechanics. They proved that both the stress intensity factor and, in turn, the crack propagation rate increased in tandem with an increase in the coefficient of friction. Rosenfield [18] calculated the stress intensity associated with a subsurface crack—driven by shear stresses due to an asperity contact—but elastic fracture mechanics models do not provide appropriate solutions for the wear of ductile materials.

A more promising approach argues that delamination cracks are, in fact, ductile plastic shear fractures formed by the linking of voids along high shear planes [22]. Tierlinck et al. [23] have shown that a superimposed hydrostatic compression tends to facilitate shear fractures by suppressing the dilatation of voids that would otherwise lead to tensile failure [24]. The basic need that must be met when modeling the delamination is the ability to define the depth at which cracks initiate and propagate. Ductile void

growth theories provide insight into the damage processes observed in ductile materials and they could be used to study how a void grows under an imposed stress and strain field. Rice and Tracey [25] developed one of the well known relationships used to describe the growth rate of a spherical void in a ductile solid that has been subjected to a triaxial stress and strain rate field. They estimated the growth rate of a void of radius R in a ductile and hardening matrix during shear by using the following relationship:

$$\dot{R} = \left[\frac{5}{3} + \frac{\sqrt{3}}{2} \frac{\sigma_H}{\sigma_f} \right] \dot{\epsilon} R \quad (1.1)$$

where \dot{R} is the void growth rate, σ_H is the mean or hydrostatic stress, σ_f is the equivalent flow stress and $\dot{\epsilon}$ is the strain rate.

In the subsurface layers that lie adjacent to the contact surfaces, the competition between the hydrostatic pressure—which suppresses void growth—and the equivalent stress—which enhances it—is considered to be responsible for the generation of a damage gradient [17]. Figure 1.2 illustrates the formation of a subsurface damage gradient. Working with this concept, debris formation can be attributed to the delamination of the subsurface layers at a certain depth—where the damage accumulation rate is the highest. The distributions of the subsurface stresses and strains must, in turn, be determined in order to quantify the process. Attempting to experimentally determine the subsurface deformation state—hydrostatic stresses and strain rates generated during sliding contact in particular—is a formidable challenge. Numerical analyses are needed to predict the subsurface damage gradients under various loading conditions.

Accordingly, this work studied the deformation and damage accumulation processes observed during the sliding wear of aluminum alloys. It investigated the accumulation of subsurface stresses and strains in an Al-Si alloy that had been subjected to sliding contact cycles, using a finite element model that was built specifically for this purpose. The numerical material model was based on the stress-strain relationship for a 356 grade Al (7 % Si) alloy, which was obtained from the sliding wear tests (not from tensile tests). Finite element models were tested and validated by comparing the results with theoretical elastic contact studies as well as normal and

sliding contact experiments. A model of debris formation was then proposed, using the Rice and Tracey void growth model that considers the presence of a damage gradient that reaches its maximum at a critical depth.

The work presented in this dissertation is compiled into 9 chapters. Chapter 2 provides a description of the sliding wear and its mechanisms, then continues with a review of the theoretical and numerical contact mechanics solutions used in the contact problems. Chapter 2 also contains a summary of constitutive equations for the aluminum alloys. Chapter 3 covers the objectives and scope of the research, while the details of the numerical and experimental procedures utilized are presented in Chapter 4 and 5. Chapter 6 presents the validation studies where accuracy of the numerical model predictions are investigated by using several methods including energy balance analysis, time history data analysis, Hertz theory comparisons and experimental and numerical comparisons. In Chapter 7, the results and discussion on subsurface deformation are given with an analysis of subsurface damage accumulation process during sliding contacts. Chapter 8 summarizes the results and gives the conclusions of the work. Finally, the suggestions for future work are presented in Chapter 9.

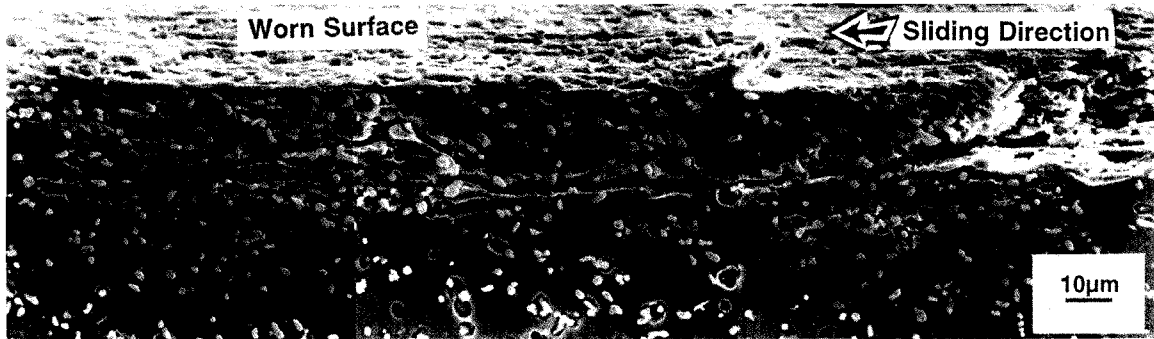


Figure 1.1: Subsurface crack propagation observed in a 356 Al alloy during dry sliding wear [17].

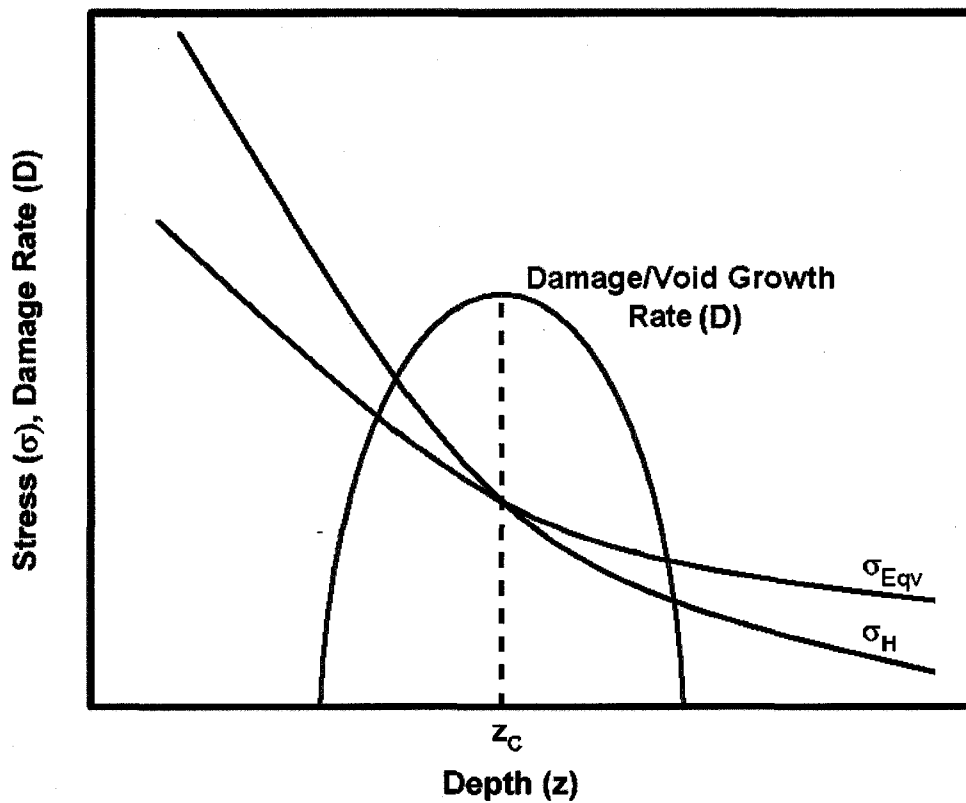


Figure 1.2: Distributions of the hydrostatic pressure (σ_H) and the equivalent stress (σ_{Eqv}) that create a subsurface damage gradient (damage rate is examined in Section 7.5 and presented as normalized void growth rate, \dot{R}/R). (z_c is the location of the highest damage).

CHAPTER 2

LITERATURE REVIEW

This chapter summarizes previous work on the sliding wear of ductile materials and the mechanisms that control the wear, then reviews published literature on the contact mechanics. This section also presents current knowledge of the effects that hydrostatic pressure, strain rate and temperature have on the mechanical behaviour of aluminum alloys. The finite element models developed in this study were built on guidance obtained from this critical literature review, which has also proved the novelty of this study.

2.1. WEAR

2.1.1. DEFINITION AND MECHANISMS

Wear can be defined as damage to a solid surface that generally involves the progressive loss of material, due to relative motion between that surface and a contacting substance or substances [26]. Material can be removed from a solid surface in three ways: by melting, by chemical dissolution or by the physical separation of atoms from the surface [27]. However, wear processes can also occur without the removal of materials. Material displacement and plastic deformation may occur in the surface and subsurface during the sliding process, accompanied by some changes in shape and/or properties [28].

When two nominally plane and parallel surfaces are brought together, contact will initially occur at only a few points. As the normal load is increased, however, the surfaces move closer together and a larger number of the peaks or asperities on the two surfaces come into contact. Since the asperities provide the only points at which the surfaces touch, they are responsible for supporting the normal load on the surface, and transmitting tangential forces (Figure 2.1) [5]. In addition, they are responsible for generating any frictional forces that act between them. A comprehensive understanding

of the way in which the asperities of two surfaces interact under varying loads is crucial to any study of friction and wear [29].

Wear processes may be classified by the type of relative motion to which the surfaces are subjected—sliding wear, rolling wear, oscillation wear, impact wear and erosive wear. Wear processes are called dry, lubricated, two-body and three-body wear related to the interfacial element [5]. Sliding wear occurs when two solid surfaces slide against each other [5, 27, 29]. A simple theoretical analysis of this type of wear was initially proposed by Archard [30,31]. Archard's approach was based on the concept of asperity contacts: that contact between the two surfaces will occur where asperities touch, and the true area of contact will be equal to the sum of the individual asperity contact areas. Asperities that are subjected to high normal loads deform plastically until the areas of contact are large enough to support the load, and the plastically deformed asperities adhere to each other. Large shear forces—localized at these adhesions—cause fractures in one of the materials, and a fragment is removed and transferred to the other. Archard stated that when two materials slide against each other, the wear volume V is linearly proportional to the sliding distance S_D and normal load L , but inversely proportional to the hardness H of the material. This may be expressed as:

$$V = K \frac{LS_D}{3H} \quad (2.1)$$

where K is a dimensionless proportionality constant, commonly known as the wear coefficient. The factor 3 is given by Archard [30] for adhesion. Although Equation 2.1 implies that harder materials wear less, there are many exceptions to this statement. For example, a soft, commercially pure copper can be much more resistant to wear than AISI 1045 steel, which is much harder. In abrasive wear, the surface of a softer metal is plowed by hard abrasive particles, wear particles or hard asperities of the counterface. Abrasive wear follows the relationship given by Equation 2.1 reasonably well; that is, the harder the material the lower the wear rate [32].

Quinn [33] developed an oxidative theory of wear for the dry sliding of steels. He proposed that the frictional heat flux generated at the real contact areas is divided so that part of the heat flows into one specimen, and the remainder flows into the second

specimen. This raises the temperature of the contacting surfaces and, if the heat flux and the temperature are sufficiently great, the asperities of the contacting metals undergo oxidation—forming an oxide film on the contacting surfaces. The oxide film is removed when it reaches a critical thickness and becomes mechanically unstable. He proposed the following equation for the wear rate (W):

$$W = \left(\frac{P}{HS_v f^2 t^2 \rho^2} \right) A_p \exp\left(\frac{-Q_p}{RT} \right) \quad (2.2)$$

where P is the load, H is the hardness of the metal, S_v is the sliding speed, f is the mass fraction of oxygen in the oxide, t is the thickness of oxide film, ρ is the density of the oxide, A_p is a constant, Q_p is the activation energy of the oxidation, R is the gas constant and T is the temperature at the contact. This theory is valid in cases where oxidation is the dominant wear mechanism.

Plate-like wear debris is commonly observed in sliding wear systems. Suh [10,11] developed a delamination wear theory to model the formation of this type of wear particle or debris. Figure 2.2 shows the steps of plate-like wear debris formation, according to the delamination theory [5]. The theory states that during sliding, normal and tangential forces are transmitted through asperities. Each asperity along the softer surface experiences cyclic loading. The harder asperities cause plastic shear deformation on the softer surface, and increasing subsurface deformation leads to the nucleation of cracks below the surface. Crack nucleation cannot occur very near the surface, due to the triaxial state of compressive loading existing just below the contact region. Pre-existing cracks and voids and newly formed cracks grow with further loading and deformation. Then, the cracks propagate parallel to the surface at a specific depth that depends on the loading conditions and material properties. When the cracks are finally able to shear to the surface in certain weak positions, long and thin wear sheets are formed [32]. Fleming and Suh [12,15] developed a wear equation based on this delamination theory for a subsurface crack as shown in Figure 2.3:

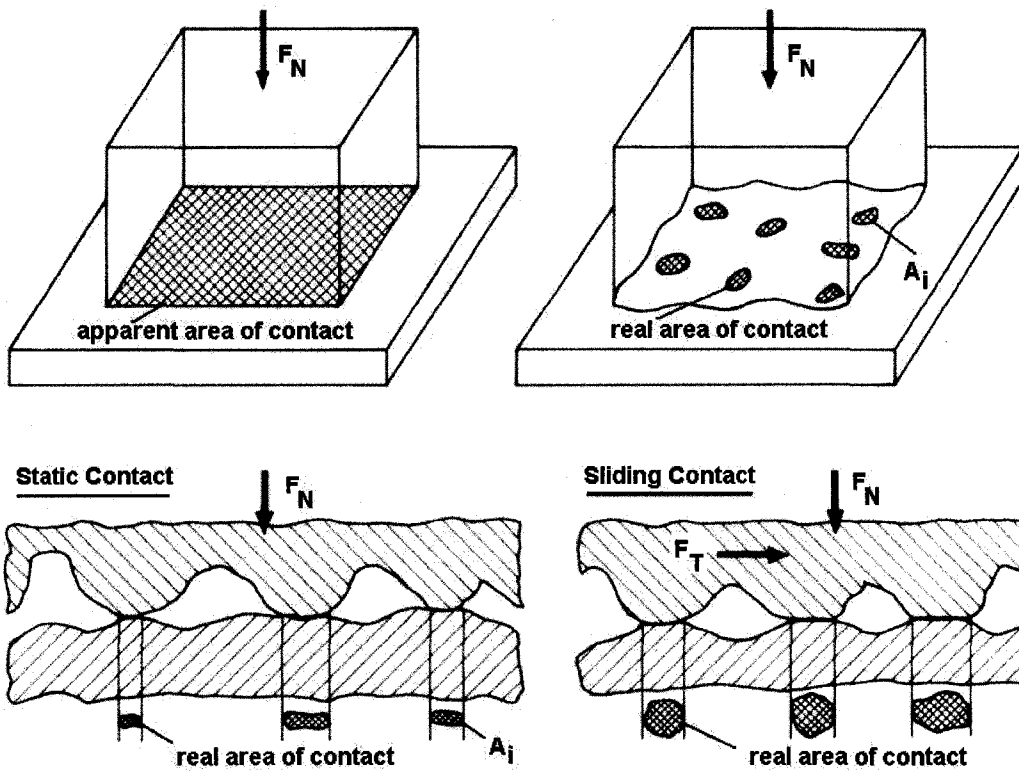


Figure 2.1: Apparent and real area (A_i) of contact (F_N : normal load, F_T : tangential load) [5].

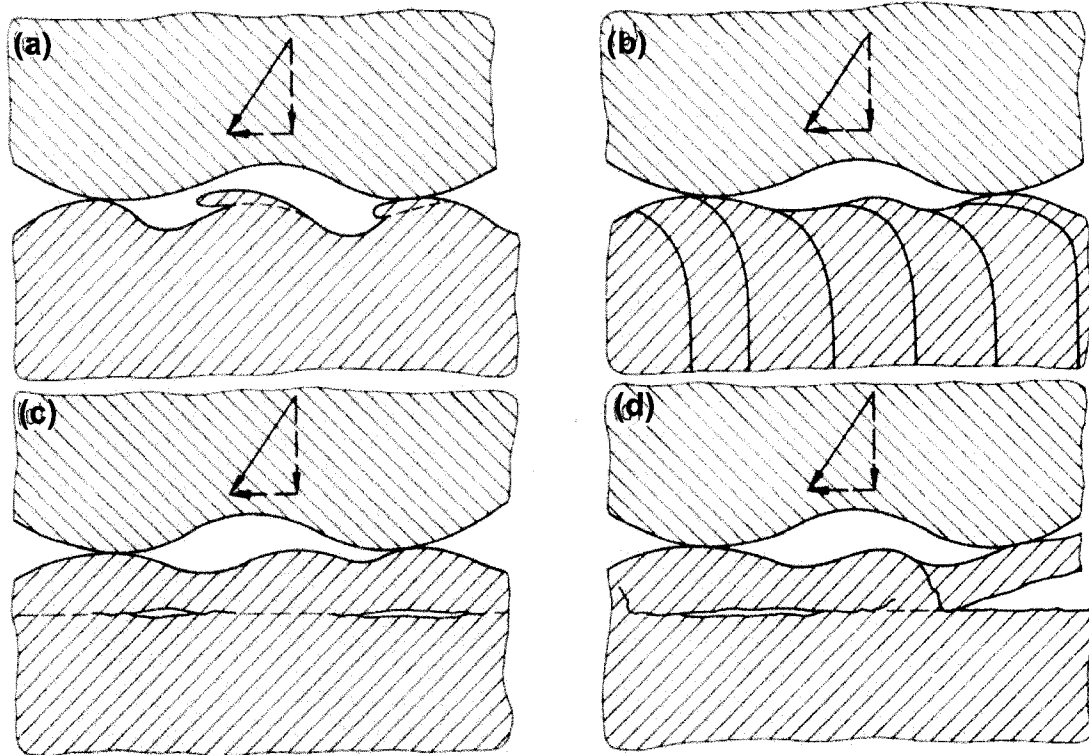


Figure 2.2: Formation of wear sheets due to delamination: (a) Smoothing of the softer surface, (b) Strain accumulation below the surface, (c) Initiation of subsurface cracks and (d) Formation of sheet-like wear particles [5].

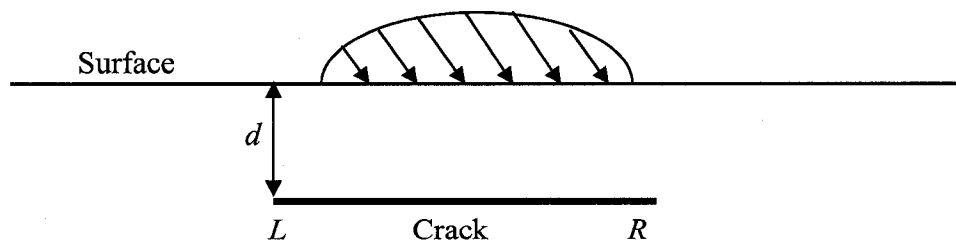


Figure 2.3: Subsurface crack under a moving asperity [32].

$$\frac{V}{S_D} = \frac{\Delta L^2 d (\Delta \bar{C}_L + \Delta \bar{C}_R)}{\lambda l_c} \quad (2.3)$$

where V is the volume of the wear sheet, S_D is the sliding distance, ΔL is the contact length, d is the subsurface depth of the crack, λ is the spacing between the asperities, l_c is the spacing between cracks and $\Delta \bar{C}_L$ and $\Delta \bar{C}_R$ are the average crack propagation rates during N contact cycles of the left (L) and the right (R) sides of crack, respectively (Figure 2.3). Many experimental studies have substantiated the delamination theory, agreeing that the delamination process is initiated when the subsurface plastic deformation causes the nucleation of voids, and that with further deformation, these voids elongate and link up to form long cracks in a direction parallel to the wear surface. Figure 2.4 shows micrographs where void formation around inclusions and crack propagation are shown in an annealed Fe- 1.3 % Mo [32].

2.1.2. SUBSURFACE MICROSTRUCTURES OF THE WORN SURFACES

The subsurface layers below the worn surfaces in samples subjected to sliding wear may show heavily deformed regions adjacent to worn surfaces. Many investigations show that large subsurface strains and plastic deformation can be generated near the worn surfaces, even under light loads [2-5, 28, 29]. Figure 2.5 schematically illustrates the different regions observed in the worn layers [29]. Three distinct regions are generally reported: i) Zone 1 is the region of bulk material that remains undeformed; ii) Zone 2 consists of plastically deformed material, with plastic shear strains increasing towards the surface; iii) In Zone 3, the material closest to the surface—often a mixed structure—is found with very fine grains composed of original bulk material, material from the counterface and oxides (tribolayers). Grain refinement and reorientation may be observed towards the boundary between Zones 2 and 3.

Transmission electron microscopy revealed some important developments in the deformation structures of the worn surfaces. Ohmae et al. [34], Rigney et al. [35] and Heilman et al. [36] found that dislocation density below the wear surface was extremely high, and the formation of a dislocation cell structure was predominant. As the depth

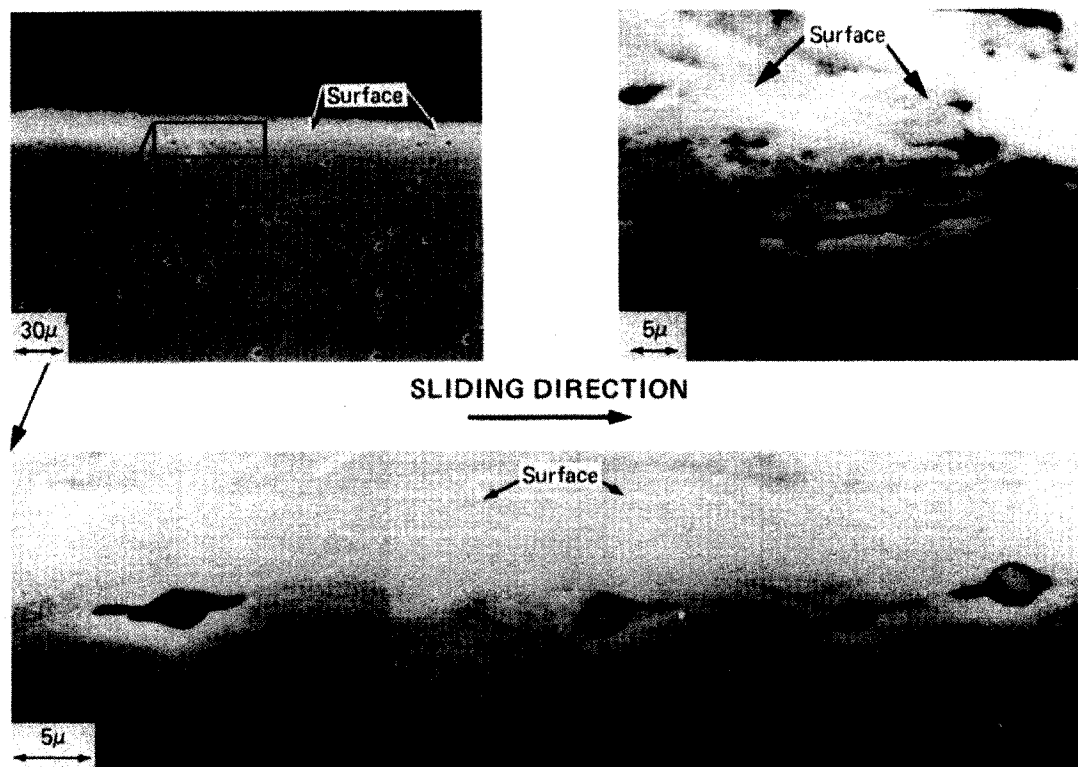


Figure 2.4: Void formation around inclusions and crack propagation from these voids near the surface in annealed Fe-1.3 % Mo [32].

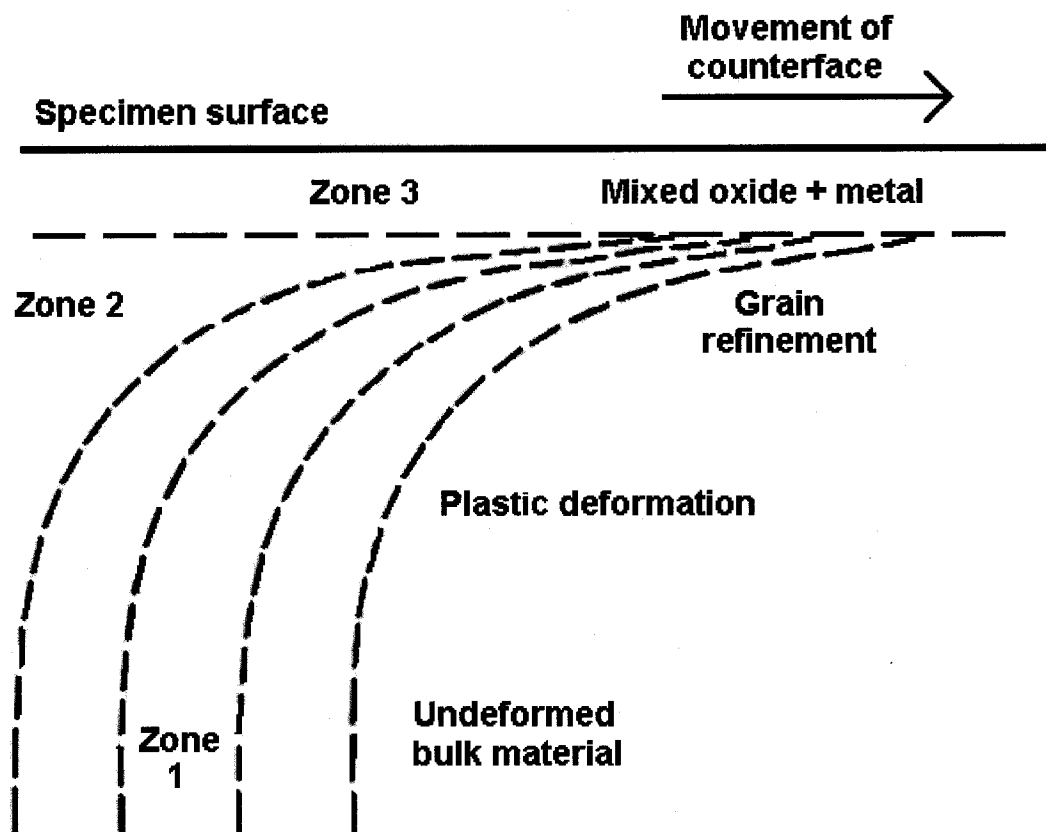


Figure 2.5: Schematic diagram showing how the severity of plastic deformation is distributed beneath a worn metal surface in the severe wear regime [29].

from the surface decreased, the cell size and the misorientation between the cells decreased as well.

2.1.3. SUBSURFACE DAMAGE MECHANISMS DURING DELAMINATION

The process of delamination—the plastic deformation of a subsurface layer, void nucleation and crack propagation below the surface—was shown to be one of the main mechanisms during sliding wear of the metals. Voids around inclusions or hard secondary-phase particles could only nucleate below a certain depth from the surface—due to the large hydrostatic pressure near the asperity contact—and only above other depths—due to the decrease in stress and deformation with distance from the contact [10-15].

Although the state of stress and strain in wear is different from that found in uniaxial testing, void nucleation studies in uniaxial tension and in pure shear testing will be reviewed initially, because of the similarities. The void nucleation process in uniaxial tension and in pure shear testing has been the subject of both theoretical and experimental investigations. The experimental results indicate that voids nucleate from hard particles, either by particle-matrix separation, or by particle fracture. Matrix-particle separation (or interface decohesion) tends to be the case if the particles are equiaxed, while particle fracture is common for elongated particles. The tensile fracture process normally occurs in several stages, which are illustrated in Figure 2.6 [37]. First, after necking begins, small cavities or micro-voids form in the interior of the sample. As deformation continues, these micro-voids enlarge, come together and coalesce to form an elliptical crack, which has its long axis perpendicular to the stress direction. The crack continues to grow in a direction parallel to its major axis via this micro-void coalescence process. Finally, fracture ensues, prompted by the rapid propagation of a crack by shear deformation around the outer perimeter of the neck at an angle of about 45° with the tensile axis where the shear stress is at its maximum. Fractures with these characteristic surface contours are called “cup-and-cone” fractures, because one of the mating surfaces is in the form of a cup, and the other is shaped like a cone [37].

Previous investigations of void formation can be grouped into three categories, according to criterion used for void formation: the energy criterion, the local stress criterion and the local strain criterion [13]. Gurland and Plateau [6] examined the role of

inclusions and secondary particles on the ductile fracture of alloys—including an aluminum 13% silicon casting alloy—and showed that inclusions or precipitates are often the source of the cracks that lead to ductile rupture. They proposed that voids can form at the interface when the locally concentrated elastic strain energy, which could be released upon decohesion, becomes comparable with the energy of the surfaces to be generated. A more detailed analysis by Tanaka et al. [38] revealed that, in a purely elastic situation, the energy criterion is always satisfied for particles larger than 25 nm when the stress almost reaches the yield stress. However, in many instances, much larger particles have been observed to remain attached to the matrix, even at strains much larger than the yield strain [13]. Therefore, the energy criterion is a necessary, but not a sufficient condition.

Since the energy requirement is not a sufficient condition, some local stress or strain criterion must be satisfied before void nucleation. Argon et al. [39-41] analyzed the void nucleation process around rigid inclusions of circular cross sections embedded in an elastic-plastic matrix in plane strain condition, subjected to pure shear and superimposed hydrostatic tension. They suggested that the hydrostatic tension component of the stress (σ_m) could be superimposed on the flow stress of the material (σ_f):

$$\sigma_{rr} = \sigma_f + \sigma_m \quad (2.4)$$

where σ_{rr} is the maximum interfacial stress. Void nucleation was stated as possible if σ_{rr} reaches the particle-matrix bond strength. Equation 2.4 states that voids can nucleate more easily if a hydrostatic tensile stress is present, and that void nucleation can be suppressed in the presence of a hydrostatic compressive stress.

Le Roy et al. [42] suggested a critical value of normal stress (σ_c) for micro-void nucleation, by decohesion of the particle-matrix interface by using Equation 2.4:

$$\sigma_c = \sigma_{loc} + \sigma_m \quad (2.5)$$

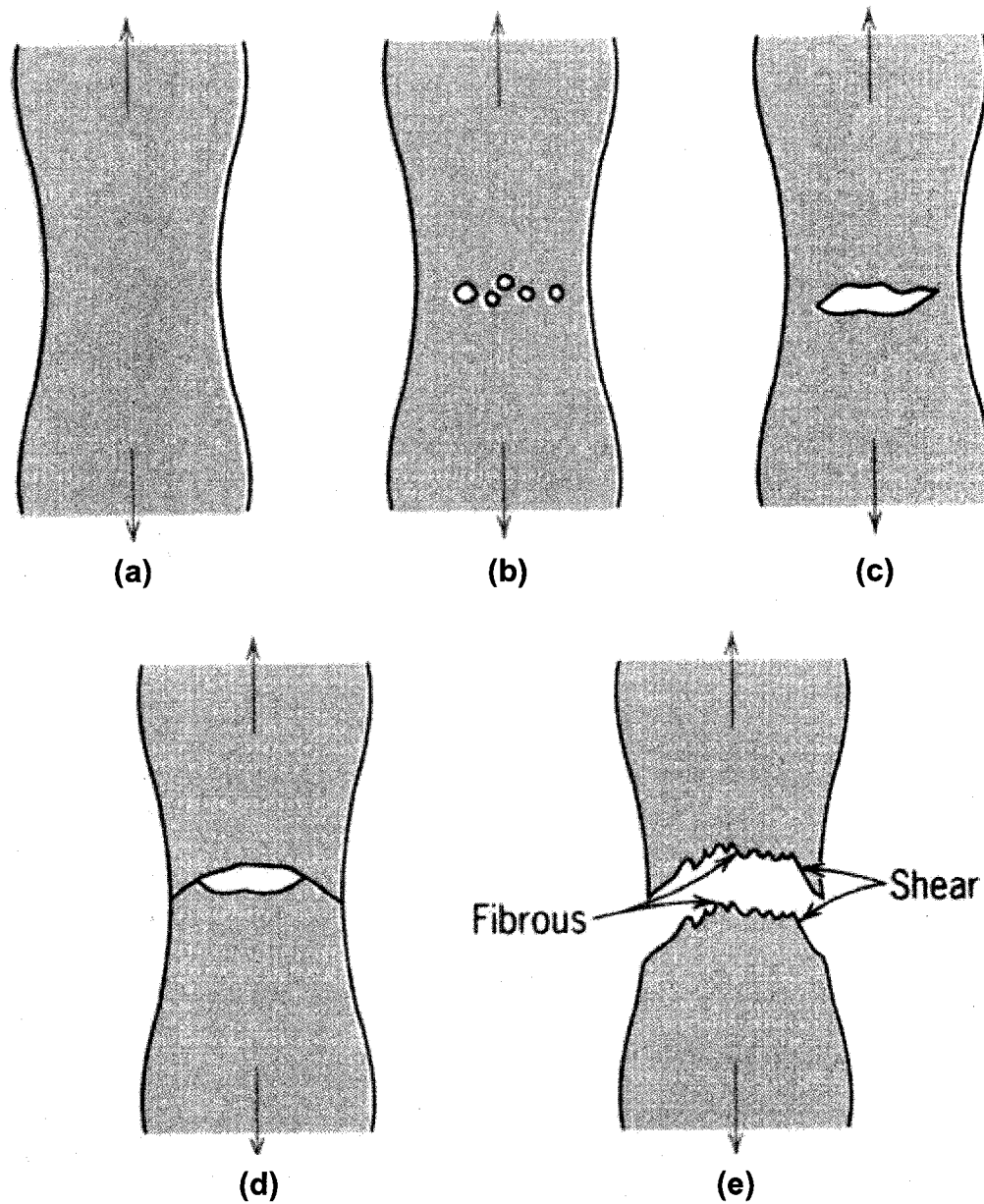


Figure 2.6: Stages in the cup-and-cone fracture (a) Initial necking, (b) Small cavity formation, (c) Coalescence of cavities to form a crack, (d) crack propagation and (e) Final shear fracture at a 45° angle relative to the tensile direction [37].

where σ_{loc} is the local stress. The value of σ_{loc} was determined by the local dislocation density (ρ_{loc}), which has accumulated at the particle. By assuming that the local dislocation density increases linearly with strain and $\sigma_{loc} \propto \sqrt{\rho_{loc}}$, the void nucleation strain (ε_N) was determined as:

$$\varepsilon_N^{1/2} = \frac{(\sigma_C - \sigma_m)}{K} \quad (2.6)$$

where K is a constant. The void nucleation strain obtained from Equation 2.6 as a function of hydrostatic stress is shown in Figure 2.7, where experimental results for 1045 steel is also included [40, 42, 43]. The experimental data is consistent with the form of Equation 2.6. In addition, the intercept value for $\varepsilon_N = 0$ yields an estimate of σ_C equal to 1200 MPa. This value is comparable with the value of 1700 MPa, derived by Argon, and Im [40], as well as with the values of the interfacial strength for various carbides in steel of 1000 to 3000 MPa—derived by other techniques [42].

The fracture of ductile solids was observed to result from the growth and coalescence of microscopic voids [44-46]. Once a micro-void has been nucleated in a plastically deforming matrix—by the debonding or cracking of a second phase particle or inclusion—the resulting stress-free surface of the void causes a localized stress and strain concentration in the adjacent plastic field. With the continuing plastic flow of the matrix, the micro-void will undergo a volumetric growth and shape change that amplifies the distortion imposed by the remote uniform strain rate field [47]. The relation between the growth of a void and imposed stress and strain must be discovered and understood to develop a fracture criterion. McClintock [48] presented an analysis of the expansion of a long, circular cylindrical cavity in a non-hardening material, pulled in the direction of its axis while subjected to transverse tensile stresses. He showed that the relative void expansion per unit applied strain increment increases exponentially with the transverse stresses:

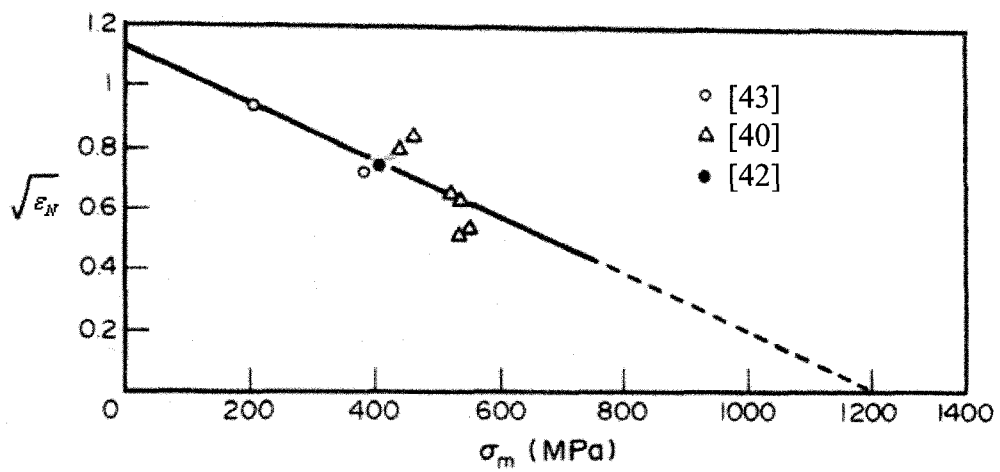


Figure 2.7: The void nucleation strains for various hydrostatic stresses in a spheroidised 1045 steel [42].

$$\frac{d\eta_{zb}}{d\bar{\epsilon}} = \frac{1}{\ln F_{zb}^f} \left[\frac{\sqrt{3}}{2(1-n)} \sinh \left(\frac{\sqrt{3}(1-n)(\sigma_a + \sigma_b)}{2\bar{\sigma}} \right) + \frac{3(\sigma_a - \sigma_b)}{4\bar{\sigma}} \right] \quad (2.7)$$

where $d\eta_{zb}$ is the damage defined as $d\eta_{zb} = d(\ln F_{zb}) / \ln F_{zb}^f$, F_{zb} is the relative growth factor defined as $F_{zb} = (b/l_b) / (b^0/l_b^0)$, F_{zb}^f is the critical value of the relative growth factor for fracture defined as $F_{zb}^f = (1/2) / (b^0/l_b^0)$, b is the radius of the growing cylindrical cavity, l_b is the mean spacing between the cavities, b^0 and l_b^0 are the initial values of the radius and the mean spacing, respectively, $d\bar{\epsilon}$ is the equivalent strain, n is the strain hardening coefficient, $\bar{\sigma}$ is the equivalent stress and σ_a and σ_b are the applied transverse tensile stresses.

Rice and Tracey [25, 47] determined the growth rate of a spherical void in a ductile solid, subjected to remote, uniform triaxial stress and strain rate fields—a more realistic approach than the one-dimensional growth case studied by McClintock [48]. They treated the void growth problem in the domain of continuum plasticity, which considers separation to be a kinematical result of large but localized plastic deformations. Figure 2.8 shows the geometry of the void growth problem. First, a variational principle was established to characterize the flow field in an elastically rigid and incompressible plastic material (either perfectly-plastic or strain hardening) that contained an internal void or voids and had been subjected to a remote uniform stress and strain rate field. Then, a Rayleigh-Ritz procedure was developed and applied to the enlargement of an isolated spherical void for approximate solutions. The strain rate field is characterized, in terms of the principal components $\dot{\epsilon}_1 \geq \dot{\epsilon}_2 \geq \dot{\epsilon}_3$, by the Lode variable v defined by:

$$v = -\frac{3\dot{\epsilon}_2}{\dot{\epsilon}_1 - \dot{\epsilon}_3} \quad (2.8)$$

The results for the rates of change \dot{R}_K in the radius of the void R , in the directions X_1, X_2 and X_3 of the principle strain rates for the remote strain rate field, were shown to have the form:

$$\dot{R}_K = \left[(1+E)\dot{\epsilon}_K + \sqrt{\frac{2}{3}}\dot{\epsilon}_K D_S \right] R \quad \text{for non-hardening material} \quad (2.9)$$

$$\dot{R}_K = [(1+E)\dot{\epsilon}_K + \dot{\epsilon}_K D_S] R \quad \text{for hardening material} \quad (2.10)$$

where $K = 1, 2, 3$ and $(1+E)$ is a factor between 5/3 and 2 that describes the amplification of the void's growth rate relative to the strain rate of the matrix. The 5/3 factor is given as an appropriate value of $(1+E)$ for strain hardening and low triaxiality in non-hardening, and the 2 factor is appropriate for the higher triaxiality in the non-hardening case. D_S is given by the following equations:

$$D_S = 0.558 \sinh\left(\frac{3 \sigma_H}{2 \sigma_o}\right) + 0.008\nu \cosh\left(\frac{3 \sigma_H}{2 \sigma_o}\right) \quad \text{for non-hardening material} \quad (2.11)$$

$$D_S = \frac{\sqrt{3} \sigma_H}{2 \sigma_f} \quad \text{for hardening material} \quad (2.12)$$

where σ_H is the mean or hydrostatic stress, σ_o is the yield stress and σ_f is the equivalent flow stress. For the condition of plane strain, the state of deformation is pure shear, where $\dot{\epsilon}_1 = \dot{\epsilon}$, $\dot{\epsilon}_2 = 0$, $\dot{\epsilon}_3 = -\dot{\epsilon}$ and $\nu = 0$. In this condition, the overall void growth rate \dot{R} of a void of radius R in a ductile matrix during shear was shown to depend on the ratio of hydrostatic stress and flow (or yield) stress of the material:

$$\dot{R} = \left[\frac{5}{3} \text{to} 2 + \sqrt{\frac{2}{3}} \left(0.558 \sinh\left(\frac{3 \sigma_H}{2 \sigma_o}\right) \right) \right] \dot{\epsilon} R \quad \text{for non-hardening material} \quad (2.13)$$

$$\dot{R} = \left[\frac{5}{3} + \frac{\sqrt{3}}{2} \frac{\sigma_H}{\sigma_f} \right] \dot{\epsilon} R \quad \text{for hardening material} \quad (2.14)$$

Equations 2.13 and 2.14 suggest that the deformation transforms voids that are initially spherical into “infinitesimally neighbouring ellipsoids”. It should be noted that the interaction and unstable coalescence of neighbouring voids are not covered by this analysis. However, the variation of the damage rate beneath the contact surface of a ductile material can be evaluated with respect to the depth of deformation using Equations 2.13 and 2.14—provided that the variations in flow stress, hydrostatic pressure and strain rate can be determined with the depth. The experimental determination of the subsurface deformation state, in particular the hydrostatic stresses and strain rates generated during sliding contact, is a significant challenge. Analytical or numerical analyses are necessary to predict the subsurface damage gradients under various loading conditions. The next section reviews analytical and numerical solutions of contact stress fields.

2.2. ANALYTICAL AND NUMERICAL SOLUTIONS OF CONTACT STRESS FIELDS

Subsurface damage processes have dominant effects on the sliding wear behaviour of ductile materials. Therefore, understanding the subsurface damage processes, including the subsurface stresses and strains produced in the contacting materials, is vital. This section reviews published literature on the analytical and numerical solutions of contact problems.

2.2.1. ANALYTICAL SOLUTIONS OF CONTACT PROBLEMS

Hertz [1] presented the first analysis of the stresses at the contact of two elastic solids. His approach is frequently used in contact stress calculations. The main assumptions of this theory are continuous surfaces, small strains, elastic half-space solids and frictionless contact. According to the Hertz theory, when two cylinders or spheres are pressed against each other, or a cylinder is loaded against a half-space, the

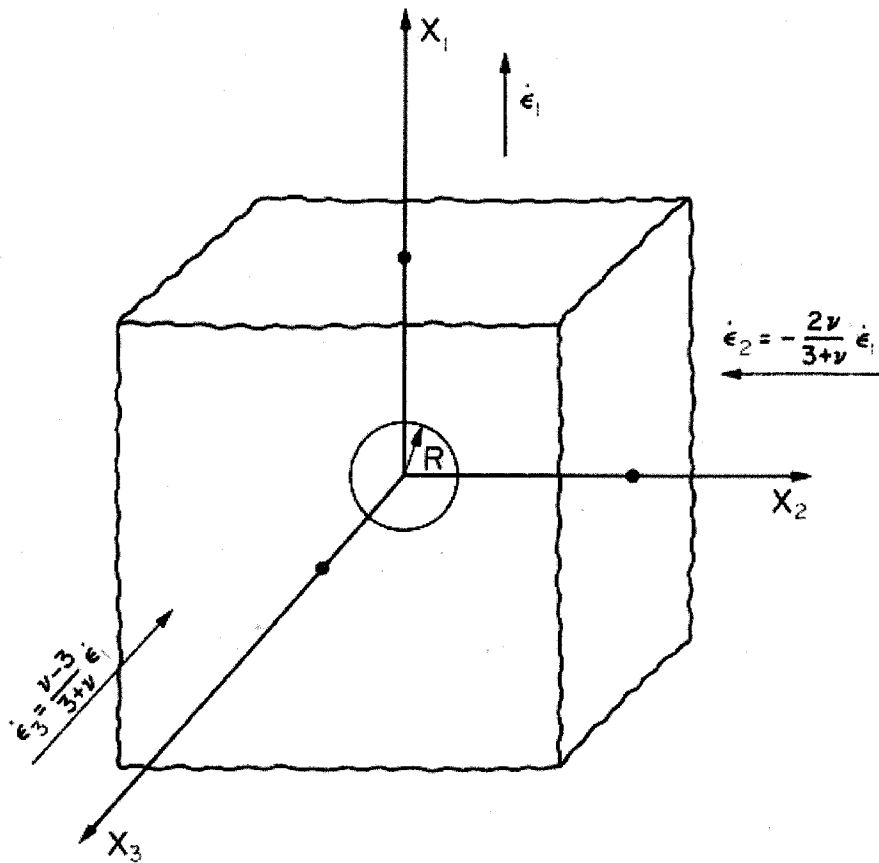


Figure 2.8: A spherical void subjected to remote stress and strain rate fields [25, 47].

area of contact is elliptical in shape (Figure 2.9). This elliptical pressure distribution is formulated, and the pressure at any position x is given by [49]:

$$P(x) = P_0 \sqrt{1 - \left(\frac{x}{a}\right)^2} \quad (2.15)$$

where $P(x)$ is pressure distribution, P_0 is the maximum contact pressure and a is semi-contact width.

The equation relating applied load (P) to the maximum contact pressure (P_0) within the solids is as follows [49]:

$$P_0 = \sqrt{\frac{PE^*}{\pi R}} \quad \text{for cylinders in contact} \quad (2.16)$$

$$P_0 = \sqrt[3]{\frac{6PE^{*2}}{\pi^3 R^2}} \quad \text{for spherical contact} \quad (2.17)$$

The semi-contact width is given by:

$$a = \sqrt{\frac{4PR}{\pi E^*}} \quad \text{for cylinders in contact} \quad (2.18)$$

$$a = \sqrt[3]{\frac{3PR}{4E^*}} \quad \text{for spherical contact} \quad (2.19)$$

where E^* is the combined modulus given by $E^* = \left(\frac{1-\nu_1^2}{E_1} + \frac{1-\nu_2^2}{E_2}\right)^{-1}$, E_1 and E_2 are the elastic modulus of the contacting solids, ν_1 and ν_2 are the Poisson's ratio of the

contacting solids, R is the combined radius given by $R = \left(\frac{1}{R_1} + \frac{1}{R_2} \right)^{-1}$,

R_1 and R_2 are the radius of the contacting solids.

Stress distributions for cylinders in contact under the surface of solids along z axis at $x=0$ are given as [49]:

$$\sigma_x = -\frac{P_0}{a} \{ (a^2 + 2z^2)(a^2 + z^2)^{-1/2} - 2z \} \quad (2.20)$$

$$\sigma_y = -P_0 a (a^2 + z^2)^{-1/2} \quad (2.21)$$

$$\sigma_z = \nu(\sigma_x + \sigma_y) \quad (2.22)$$

$$\tau = -\frac{P_0}{a} \{ z - z^2 (a^2 + z^2)^{-1/2} \} \quad (2.23)$$

These stresses are all independent of Poisson's ratio, except for the third principle stress (σ_z). The variations of σ_x , σ_y and τ with depth below the surface given by Equations 2.20, 2.21 and 2.23 are shown in Figure 2.10. Maximum shear stress (τ) occurs at $x = 0.78 a$.

The stresses and displacements produced by a concentrated point force P acting normally to the surface of an elastic half-space (Figure 2.11) are given by Boussinesq and Cerruti [49]. Stress components are given by the following equations:

$$\sigma_x = -\frac{P}{2\pi} \left[\frac{(1-2\nu)}{r^2} \left\{ \left(1 - \frac{z}{\rho} \right) \left(\frac{x^2 - y^2}{r^2} \right) + \frac{zy^2}{\rho^3} \right\} - \frac{3zx^2}{\rho^5} \right] \quad (2.24)$$

$$\sigma_y = \frac{P}{2\pi} \left[\frac{(1-2\nu)}{r^2} \left\{ \left(1 - \frac{z}{\rho} \right) \left(\frac{y^2 - x^2}{r^2} \right) + \frac{zx^2}{\rho^3} \right\} - \frac{3zy^2}{\rho^5} \right] \quad (2.25)$$

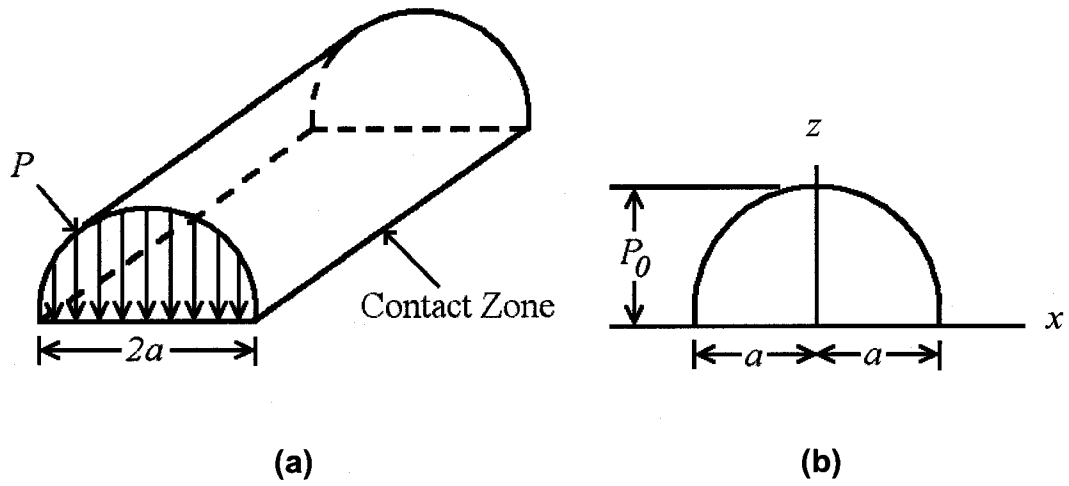


Figure 2.9: Contact between cylindrical surfaces: (a) Area of contact in Hertz theory, (b) Maximum contact pressure and axes.

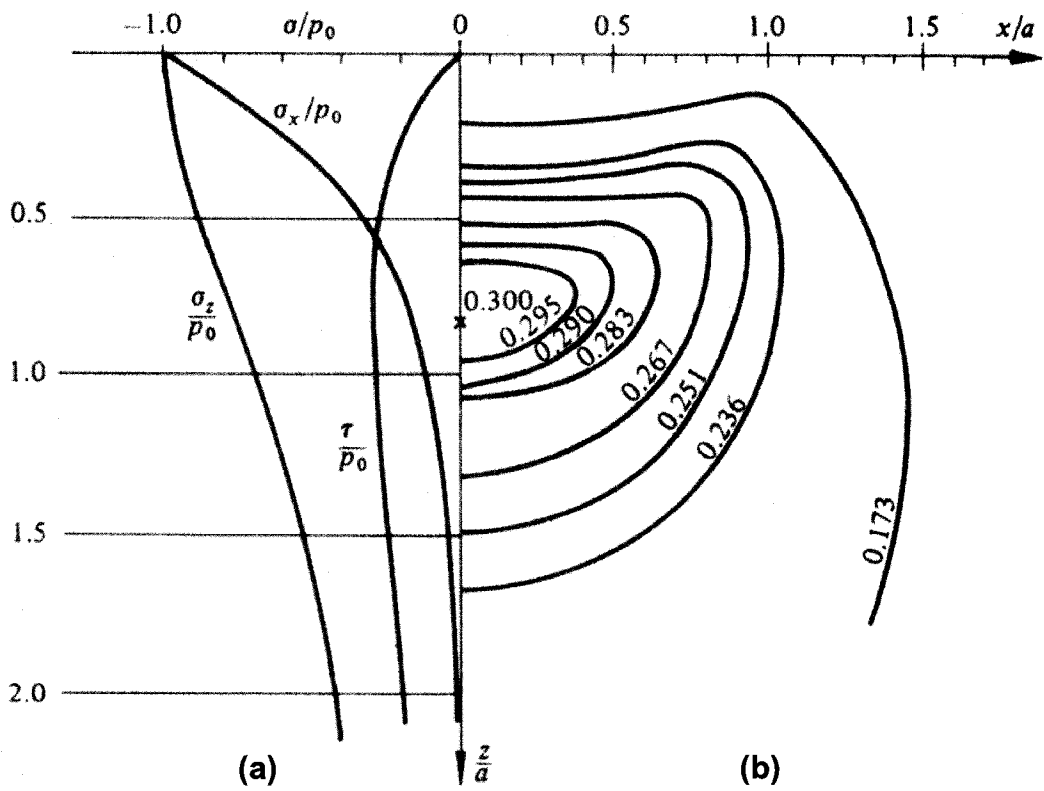


Figure 2.10: Hertz theory (a) Subsurface stresses along the axis of symmetry, (b) Contours of maximum shear stress [49].

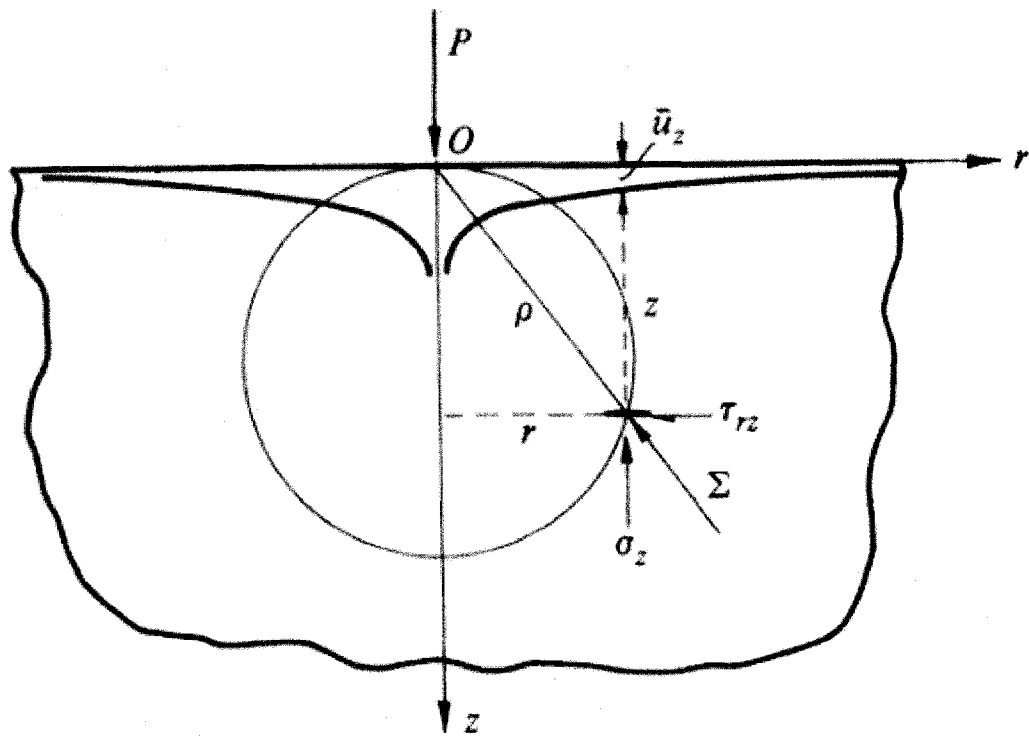


Figure 2.11: Geometry of the single point contact problem by Boussinesq and Cerruti [49].

$$\sigma_z = -\frac{3P z^3}{2\pi \rho^5} \quad (2.26)$$

$$\tau_{xy} = \frac{P}{2\pi} \left[\frac{(1-2\nu)}{r^2} \left\{ \left(1 - \frac{z}{\rho} \right) \left(\frac{xy}{r^2} \right) - \frac{xyz}{\rho^3} \right\} - \frac{3xyz}{\rho^5} \right] \quad (2.27)$$

$$\tau_{xz} = -\frac{3P xz^2}{2\pi \rho^5} \quad (2.28)$$

$$\tau_{yz} = -\frac{3P yz^2}{2\pi \rho^5} \quad (2.29)$$

where $r^2 = x^2 + y^2$, ν is the Poisson's ratio and $\rho^2 = x^2 + y^2 + z^2$. Alternatively, the stress components may be given by using symmetry in polar coordinates [49]:

$$\sigma_r = \frac{P}{2\pi} \left[(1-2\nu) \left\{ \left(\frac{1}{r^2} - \frac{z}{\rho r^2} \right) - \frac{3zr^2}{\rho^5} \right\} \right] \quad (2.30)$$

$$\sigma_\theta = -\frac{P}{2\pi} (1-2\nu) \left(\frac{1}{r^2} - \frac{z}{\rho r^2} - \frac{z}{\rho^3} \right) \quad (2.31)$$

$$\sigma_z = -\frac{3P z^3}{2\pi \rho^5} \quad (2.32)$$

$$\tau_{rz} = -\frac{3P rz^2}{2\pi \rho^5} \quad (2.33)$$

Strains can be derived from the stresses, and the integration of strain equations provides the displacements. On the surface of the solid ($z=0$), displacements are given by the following equations, and the displacement in the z direction is also shown in Figure 2.11.

$$\bar{u}_r = -\frac{(1-2\nu)P}{4\pi G} \frac{1}{r} \quad (2.34)$$

$$\bar{u}_z = \frac{(1-\nu)P}{2\pi G} \frac{1}{r} \quad (2.35)$$

Hamilton and Goodman [50] derived equations for the stress field created by a circular sliding contact. They defined a circular contact region carrying a hemispherical Hertzian normal pressure, and a proportional distributed shear traction. Shear traction or tangential traction was calculated from Hertzian normal pressure by the following equation:

$$Q(x) = \mu P(x) \quad (2.36)$$

where $P(x)$ is the normal pressure distribution, $Q(x)$ is shear traction distribution and μ is the coefficient of friction (COF). Superposition of normal and shearing distributions on the circular contact region created the sliding contact geometry as shown in Figure 2.12. The equations of stresses are given by:

On the surface inside the zone of contact;

$$\sigma_x = \left(\frac{3P}{2\pi a^3}\right) [2\nu K_0 + (1-2\nu)(G_0 r^{-2} - 2x^2 r^{-4} G_0 + x^2 r^{-2} K_0)] \quad (2.37)$$

$$\sigma_y = \left(\frac{3P}{2\pi a^3}\right) [2\nu K_0 + (1-2\nu)(G_0 r^{-2} - 2y^2 r^{-4} G_0 + y^2 r^{-2} K_0)] \quad (2.38)$$

$$\tau_{xy} = \left(\frac{3P}{2\pi a^3}\right) [(1-2\nu)(xy_0 r^{-2} K_0 - 2xyr^{-4} G_0)] \quad (2.39)$$

Outside the zone of contact;

$$\sigma_x = \left(\frac{3P}{2\pi a^3}\right) \left[\frac{1}{3} a^3 (1-2\nu)(2x^2 r^{-4} - r^{-2}) \right] \quad (2.40)$$

$$\sigma_y = \left(\frac{3P}{2\pi a^3}\right) \left[\frac{1}{3} a^3 (1-2\nu)(2y^2 r^{-4} - r^{-2}) \right] \quad (2.41)$$

$$\tau_{xy} = \left(\frac{3P}{2\pi a^3}\right) \left[\frac{2}{3} a^3 (1-2\nu)(xyr^{-4}) \right] \quad (2.42)$$

where

$$G_0 = \frac{(a^2 - r^2)^{3/2} - a^3}{3} \quad (2.43)$$

$$K_0 = -(a^2 - r^2)^{1/2} \quad (2.44)$$

$$r = (x^2 + y^2)^{1/2} \quad (2.45)$$

$$a = \left(\frac{3PR}{4E^*}\right)^{1/3} \quad (2.46)$$

R : radius of the sphere,

E^* : combined elastic modulus calculated by $E^* = \left(\frac{1-\nu_1^2}{E_1} + \frac{1-\nu_2^2}{E_2} \right)^{-1}$

Figures 2.13 to 2.15 present the distribution of von Mises stress—normalized by maximum contact pressure (P_0 is defined by Equation 2.17)—predicted by Hamilton and Goodman's stress field equations on plane $y = 0$ beneath circular contact. For frictionless conditions ($\mu = 0.0$), Figure 2.13 shows that the region of maximum yield occurs on the centerline a distance of $0.5a$ below the surface. Figures 2.14 and 2.15 show the effect of friction ($\mu = 0.25$ and 0.5). The maximum von Mises stress moves toward the surface and becomes more intense, while a second region of high von Mises stress develops simultaneously in the surface at $x = -1.0a$. The point of maximum von Mises stress changes from below the surface to a position on the surface at an approximate coefficient of friction of 0.27.

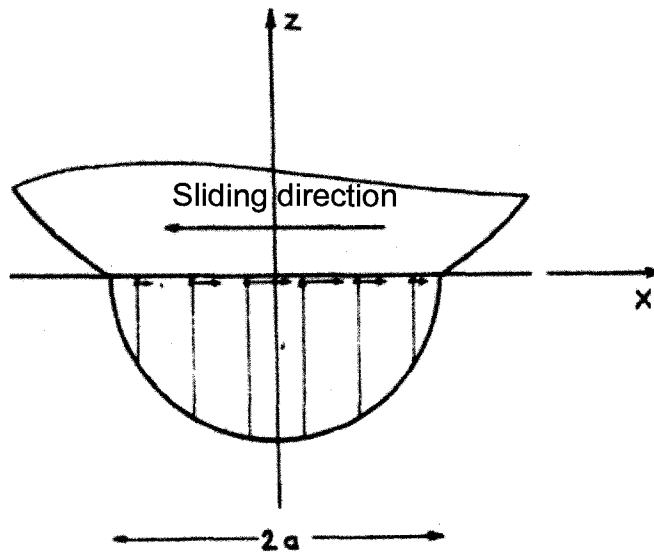


Figure 2.12: Schematic view of sliding contact from Hamilton and Goodman [50].

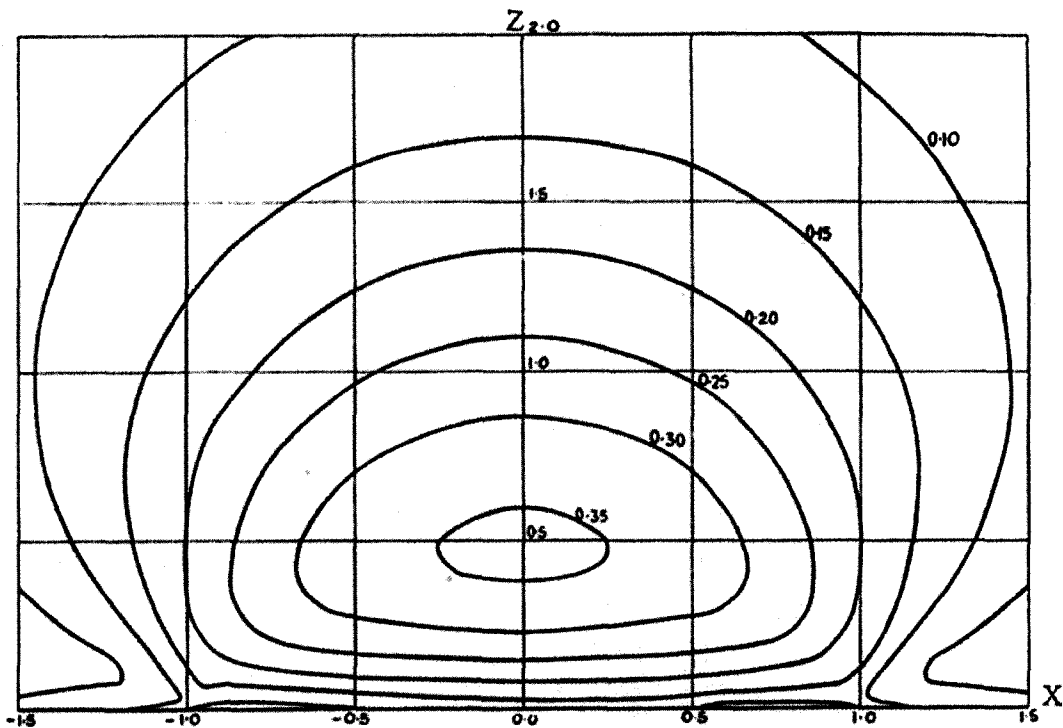


Figure 2.13: Lines of constant von Mises stress normalized by maximum contact pressure (P_0) on plane $y = 0$ beneath circular contact [50].

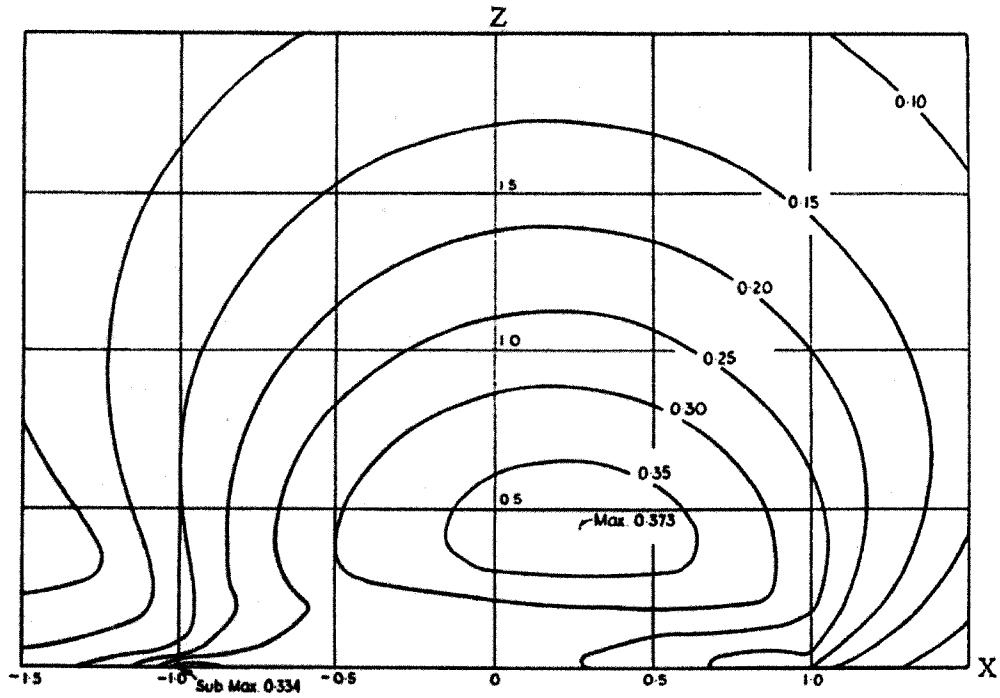


Figure 2.14: Lines of constant von Mises stress normalized by maximum contact pressure (P_0) on plane $y = 0$ beneath circular contact, $\mu = 0.25$ [50].

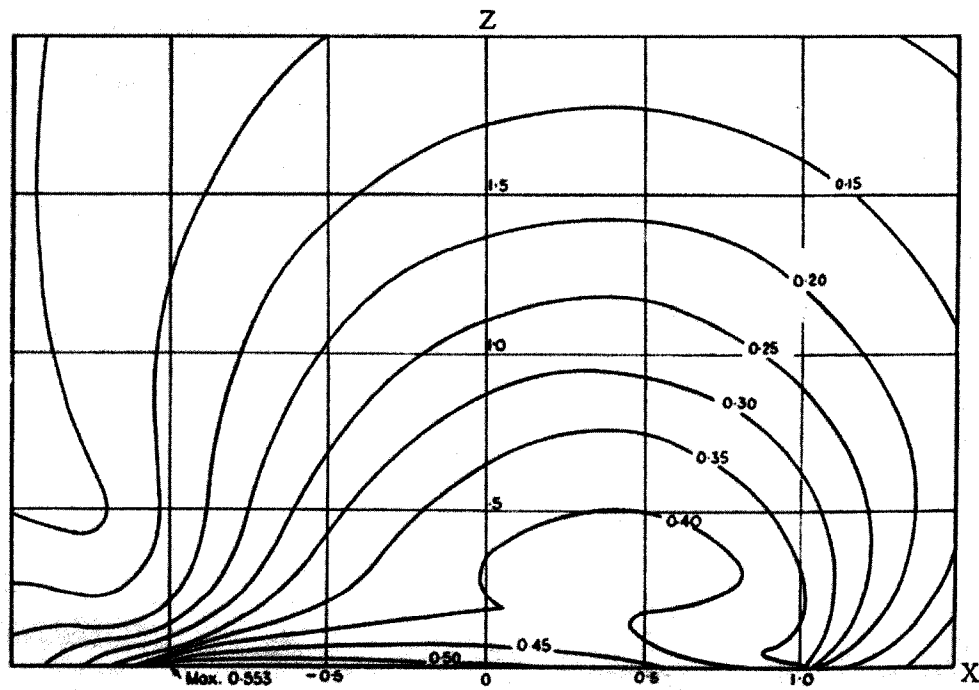


Figure 2.15: Lines of constant von Mises stress normalized by maximum contact pressure (P_0) on plane $y = 0$ beneath circular contact, $\mu = 0.50$ [50].

Figures 2.16 to 2.18 present the distribution of the von Mises stress for the cylinders in line contact, assuming a state of plane strain. The region of maximum von Mises stress moves toward the surface in both cases as the friction is increased, but less rapidly in the case of a circular contact.

Johnson [49] calculated the stresses produced by the sliding of a curved profile over a flat surface (Figure 2.19). He followed a similar approach to Hamilton and Goodman to define tangential traction at the surface. Pressure distribution of a normal load P was given by the Hertz formulation:

$$P(x) = \frac{2P}{\pi a^2} (a^2 - x^2)^{1/2} \quad (2.47)$$

Then, assuming Amonton's law of friction (Equation 2.36) the tangential traction is given as follows:

$$Q(x) = \mp \frac{2\mu P}{\pi a^2} (a^2 - x^2)^{1/2} \quad (2.48)$$

The stresses in the contact surface due to both pressure and frictional tractions are calculated as:

$$\sigma_x = -P_0 \left\{ \left(1 - \frac{x^2}{a^2}\right)^{1/2} + \frac{2\mu x}{a} \right\} \quad (2.49)$$

$$\sigma_y = -2\nu P_0 \left\{ \left(1 - \frac{x^2}{a^2}\right)^{1/2} + \frac{\mu x}{a} \right\} \quad (2.50)$$

$$\sigma_z = -P_0 \left(1 - \frac{x^2}{a^2}\right)^{1/2} \quad (2.51)$$

$$\tau_{xz} = -\mu P_0 \left(1 - \frac{x^2}{a^2}\right)^{1/2} \quad (2.52)$$

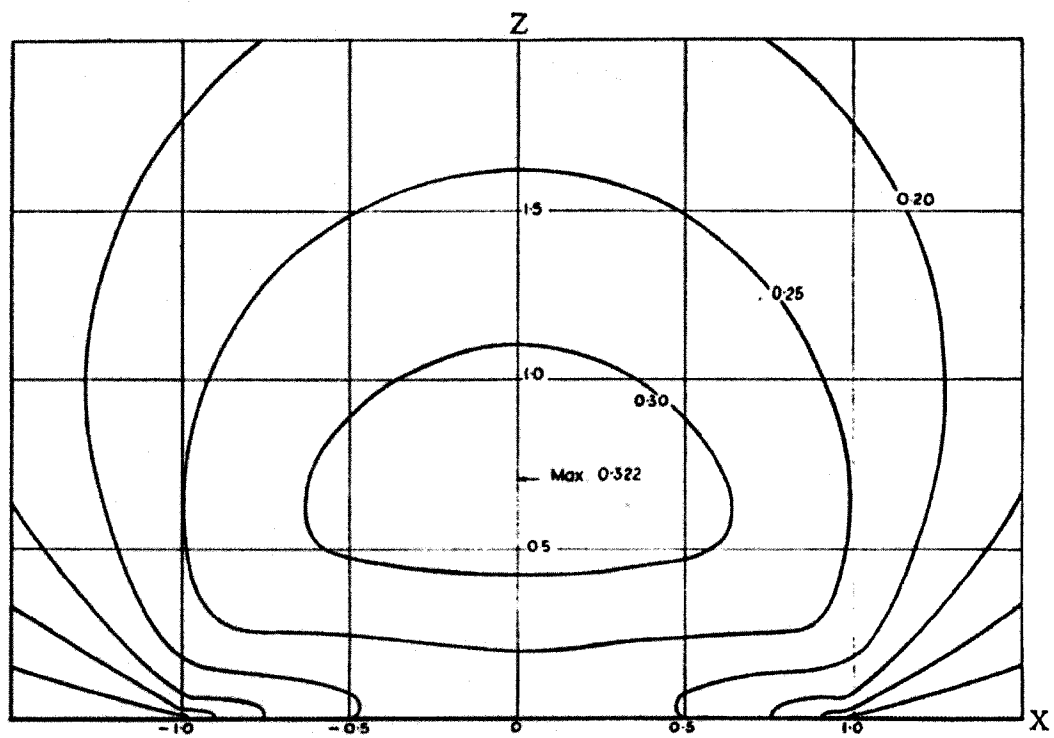


Figure 2.16: Lines of constant von Mises stress normalized by maximum contact pressure (P_0) beneath contact between normally loaded cylinders [50].

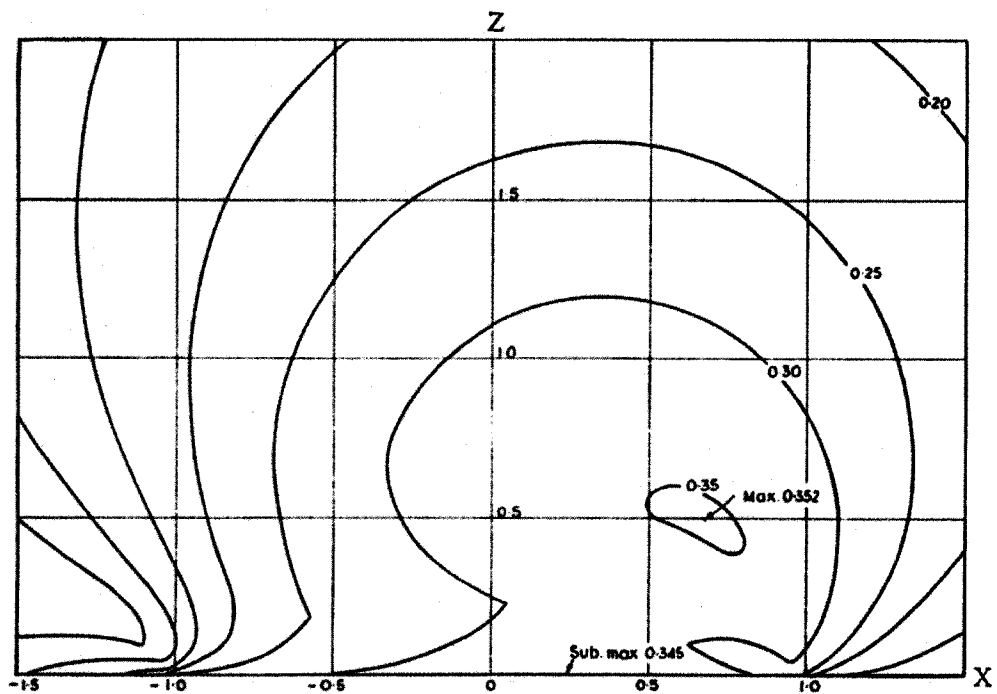


Figure 2.17: Lines of constant von Mises stress normalized by maximum contact pressure (P_0) beneath contact between cylinders, $\mu = 0.25$ [50].

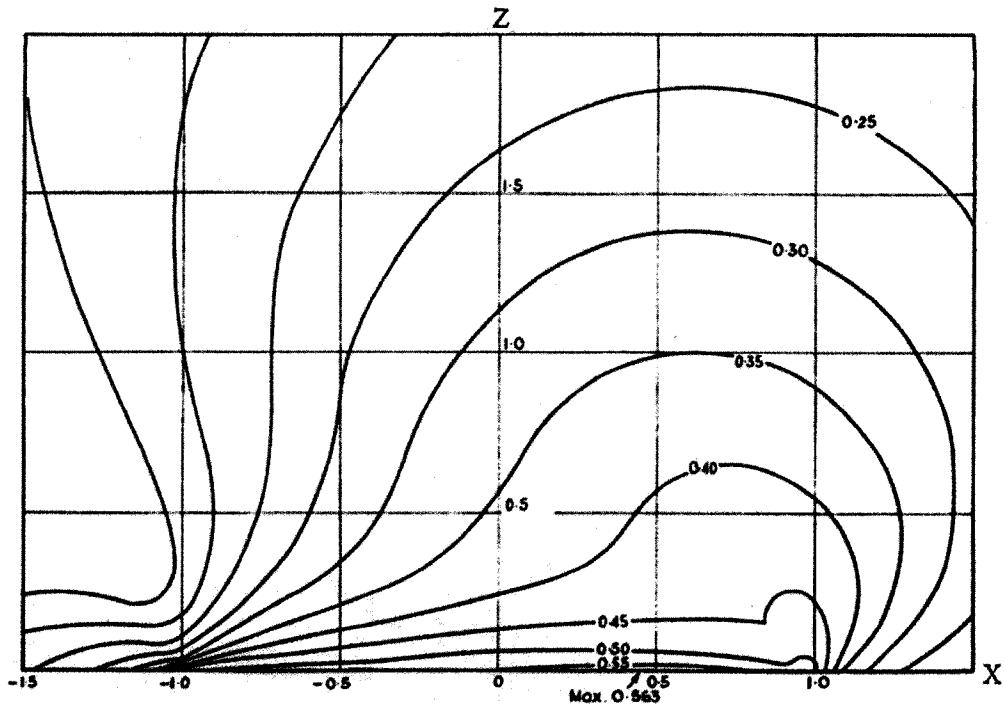


Figure 2.18: Lines of constant von Mises stress normalized by maximum contact pressure (P_0) beneath contact between cylinders, $\mu = 0.50$ [50].

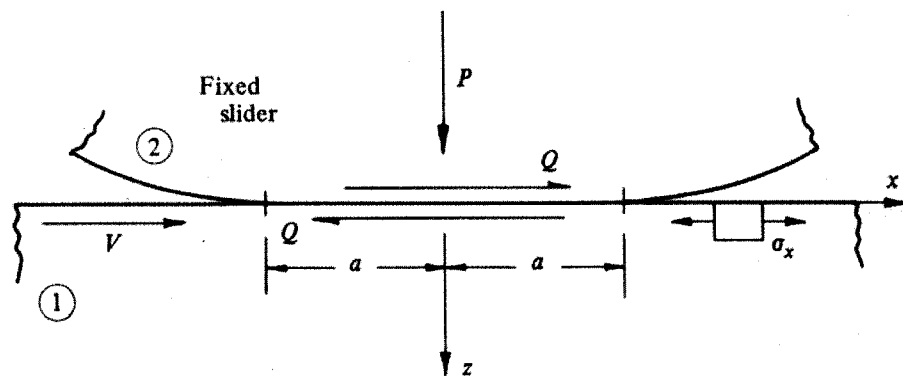


Figure 2.19: Sliding contact by Johnson [49] P is the normal load and Q is the tangential traction.

The principal shear stress in the plane of the deformation is given by:

$$\tau_1 = \frac{1}{2} \{ (\sigma_x - \sigma_z)^2 + 4\tau_{xz}^2 \}^{1/2} = \mu P_0 \quad (2.53)$$

where

$$P_0 = \frac{2P}{\pi a} \quad (2.54)$$

Contours of τ_1 due to combined normal pressure and tangential traction for $\mu = 0.2$ are illustrated in Figure 2.20.

Merwin and Johnson [51] developed an approximate analytical and numerical method to calculate the state of stress for the rolling contact of an elastic-perfectly plastic material. This method was modified for sliding contacts by Jahanmir and Suh [13]. Figure 2.21 shows the model of the contact between a stationary rigid asperity and a sliding elastic-perfectly plastic plane [32]. The stress distribution at the asperity contact was assumed to be elliptic over the contact area (p_0), and the tangential traction (q_0) was calculated by Equation 2.36. The stepwise analytical and numerical solution was obtained by using FORTRAN programming language. Details of the step-by-step solution procedure can be found in [13, 32 and 51]. The result for the applied stress $p_0 = 4k$ and different tangential stresses—ranging from $q_0 = 0$ to $q_0 = 4k$ —is given in Figure 2.22 where k is the yield strength in shear. Figure 2.22 implies that the size of the plastic region increases with an increasing coefficient of friction. For coefficients of friction smaller than a critical value (0.25), the plastic region is below the surface whereas at larger coefficients of friction, the plastic region extends to the surface.

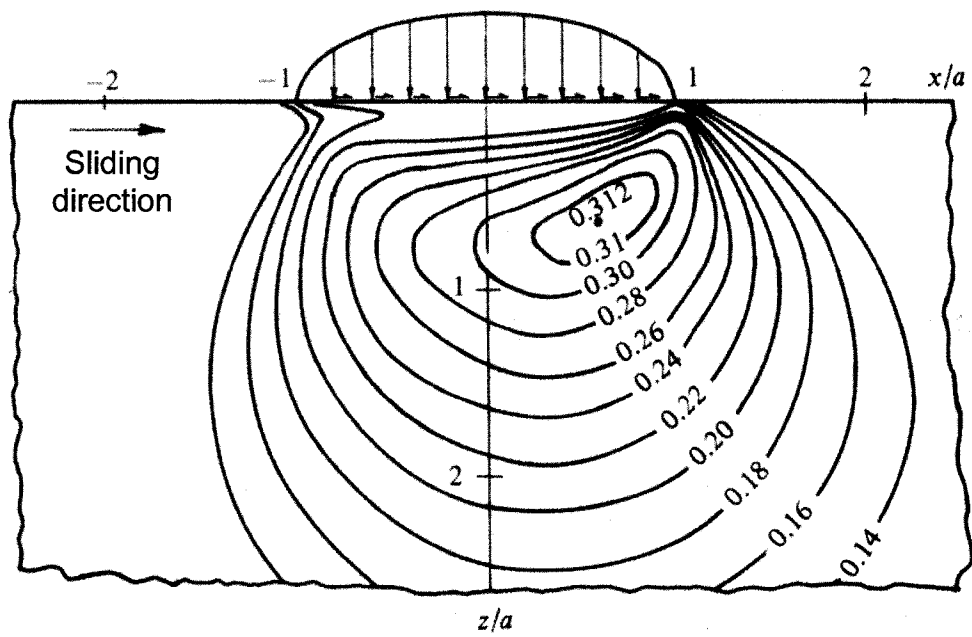


Figure 2.20: Contours of the principal shear stress beneath a sliding contact ($\mu = 0.2$) [49].

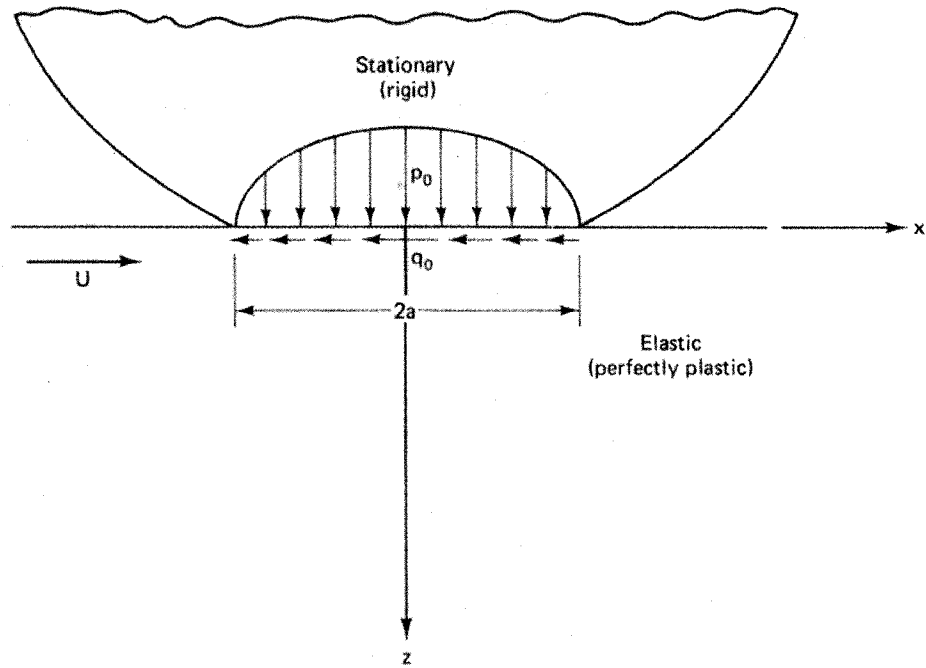


Figure 2.21: Model of a contact between a stationary rigid asperity and a sliding elastic-perfectly plastic plane (U : sliding velocity) [32].

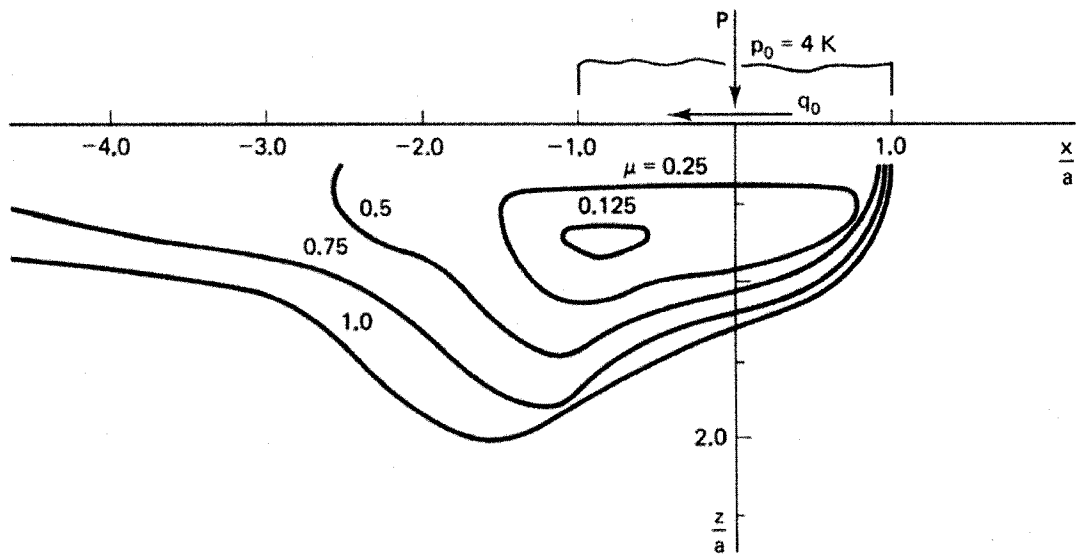


Figure 2.22: Steady state plastic deformation regions in an elastic-perfectly plastic material under a sliding contact, for a maximum applied normal stress $p_0 = 4k$ and different coefficients of friction [32].

2.2.2. FINITE ELEMENT ANALYSES APPLIED TO SLIDING CONTACT PROBLEMS

The finite element analysis method is a well-known technique for investigating the deformation behaviour of materials, as well as a versatile tool for computing stress and strain distributions. As a result, the finite element techniques are frequently applied to contact problems involving wear. The objective of this section is to review published literature on the finite element analysis of sliding contact wear.

One of the early attempts to analyze wear processes using the finite element method was conducted by Ohmae and Tsukizoe [52]. They studied the wear of a pure aluminum pin on a pure copper plate in a two-dimensional, elastic-plastic problem where a normal load of 9.8×10^{-2} N was applied to the pin. There is not enough information in the published paper about the material model, or a definition of the sliding action. They observed the origination of a failure zone at the rear portion of the sliding surface, which extends parallel to the sliding direction.

Sin and Suh [53] used the finite element method to investigate subsurface crack propagation prompted by surface traction in sliding wear. They used the ADINA finite element program. The finite element mesh used around the crack tip is shown in Figure 2.23. A Hertzian pressure distribution was applied to the top of a half-space, and surface traction was defined by a coefficient of friction (COF) of 0.25. The surface studied was defined as an elastic-perfectly plastic material. Although the computational costs and the finite element code limited their study, the numerical results indicated that the relative displacements of crack tips vary with the magnitude of the moving load, and are a function of the geometric location of cracks. Specifically, the crack closer to the surface was found to have larger displacements. It was concluded that cracks near the surface should propagate faster than those away from the surface. According to their experimental observations, cracks were present at a finite distance below the surface because of high compressive stresses developed near the surface.

Bhargava et al. [54] studied a plane strain elastic-perfectly plastic finite element model of rolling contact. The rolling contact was simulated by translating a semi-elliptical pressure distribution. They assumed the frictionless contact of a rigid cylinder with a steel half-space. The finite element software ABAQUS was used, with 0.2 mm smallest mesh dimension. The results were tested by comparing the von Mises stresses predicted by the finite element model with the predictions of the Hertz Theory (Figure

2.24). From the deformed mesh, forward flow near the contact surface and backward flow under the surface was reported. They concluded that the pressure distribution and contact width for the simulation of rolling contact were similar to Hertzian predictions. More recent studies have proved that an elliptical pressure distribution is only valid for elastic contact, and it changes with plasticity to a more uniform distribution over the contact length [55-57].

Bhargava et al. [58] also analyzed repeated contacts using the finite element model presented above. Contact width and maximum pressure were calculated for a rigid cylinder with a 50 mm radius on an elastic steel half-space, and multiple translation of the semi-elliptical pressure distribution was used to simulate rolling contacts. Up to 4 contact cycles were studied. The results indicated that with repeated rolling contact, a steady state is attained within the first two cycles—provided the flow stress did not change.

An updated Lagrangian formulation was used to solve a large plastic deformation problem in plane strain by Ohmae [59]. A 99.999 % purity Cu pin (30 mm length and 6 mm diameter) with a hemispherical tip (10.5 mm diameter) was loaded with 4.9 N and 6.37 N normal loads and slid over a 99.999 % purity Cu disk (45 mm diameter). Triangular elements with a 0.5 μm minimum size were used in the model. Information about the finite element model, material model, sliding conditions and whole geometry were addressed poorly in the manuscript. The generation of a large tensile stress at the rear portion of the slider with frictional contact was reported. The researcher concluded that large plastic deformation resulted in void nucleation and crack propagation, which might act as origins of fracture during friction processes.

One of the first credible studies of the finite element analysis of sliding contact was performed by Komvopoulos et al. [60]. They conducted lubricated and dry sliding experiments on titanium and steel surfaces, with and without TiN sputtered coatings of various thicknesses. The significance of layer thickness, interfacial friction, magnitudes of normal and tangential surface tractions and the mechanical properties of the layers (e.g. elastic modulus and hardness) were examined by experimental evidence and analytical results. After experimental studies, the finite element software ABAQUS was used to simulate the plane strain sliding contact of a rigid cylinder (28.1 μm radius) and an elastic layered half-space. Sliding was simulated by imposing 0.5 μm upward

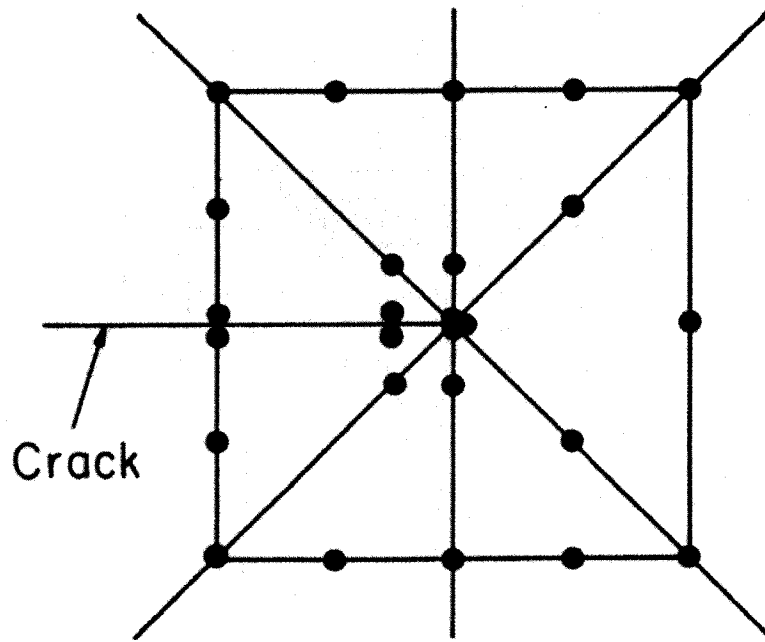


Figure 2.23: Finite element mesh around a crack tip by Sin and Suh [53].

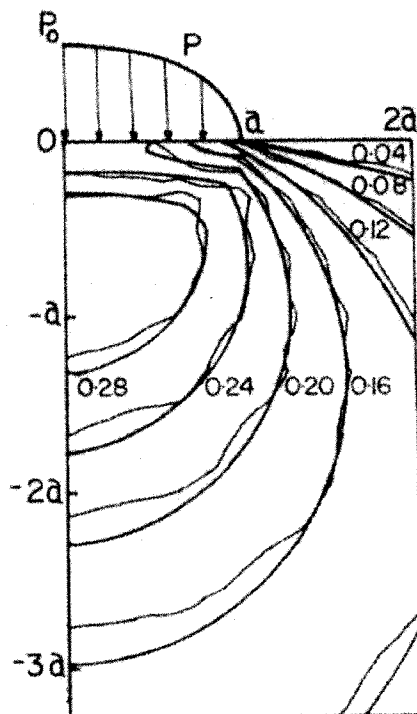


Figure 2.24: Comparison of contours of von Mises stress values normalized by P_0 ; sharp lines: finite element analysis, smooth lines: theoretical values [54].

displacements and 0.5 μm horizontal displacements of the half-space. The finite element mesh contained 326 quadrilateral, 8-node isoperimetric elements with minimal dimensions of $1 \times 0.5 \mu\text{m}^2$ and 1148 nodes. A 3x3 integration scheme was used for the elements, and three different coefficients of friction (0.0, 0.1 and 0.5) were used in the investigation. They revealed that yielding initiates below the surface with non-layered elastic half-space, and von Mises equivalent stress in the substrate is greatly reduced if a layer is used. Figure 2.25 shows the von Mises stress contours predicted by the finite element model after the penetration and sliding of a half-space surface and a layered surface for two different friction values.

King and O'Sullivan [61] investigated the sliding line contact of a single-layer elastic half-space. They developed a finite element code and established integral equations based on displacement constraints at the contact interface, and at the layer-substrate interface—which was assumed to be perfectly bonded. Normal contact simulations were assessed against the Hertz theory, while sliding contact simulations were compared to the exact solution presented by Hamilton and Goodman [50]. Changes in von Mises stress, shear stress, tensile stress (σ_{xx}) with friction and different elastic modulus ratio of layers were discussed. They showed that the size of the contact zone and the pressure under the centre of the indenter was quite different from the Hertzian case when the elastic moduli of the layers differ. Figure 2.26 presents the change of pressure profiles under the indenter for a layered medium with the elastic modulus ratio of layers.

Tian and Saka [62] conducted a two-dimensional finite element stress and strain analysis of the sliding contact of a two layer bilinear elastic-plastic work hardening (i.e. the plastic modulus E_p is calculated by multiplication of elastic modulus E by a constant α) half-space for various friction coefficients between 0.0 and 0.5. A rigid cylinder with a radius of 0.75 mm was pressed into the half-space of $200 \times 200 \mu\text{m}^2$ with normal loads of 5 N and 10 N. The finite element software ABAQUS was used, with 630 quadrilateral eight-node isoperimetric elements and 2023 nodes. The first two rows of the mesh were assigned to the gold top layer (1.25 μm), and the next two rows were assigned to the nickel interlayer (2.5 μm). The substrate was defined as a copper alloy. Figure 2.27 shows the geometry of the problem studied by the authors. It was assumed that the normal contact pressure distribution was independent of the tangential loading, and hence the pressure distribution of normal indentation was used for the tangential traction

determination. Tangential traction was calculated by multiplying normal surface loads and the friction coefficient along the contact line. Perfect bonding was assumed at the interface between layers. The results of the elastic sliding of a homogeneous half-space was compared with Hamilton and Goodman's [50] analytical solutions. The authors found that when the friction coefficient was small (less than 0.3), yielding initiated in the substrate region near the leading edge of the contact—provided that the normal load was large enough. However, when the friction coefficient was large (greater than 0.3), yielding initiated on the surface at the trailing edge of the contact. They showed that surface deformation, the location of initial yield and stresses and strains along the interface between layers strongly depended on the friction coefficient. In addition, a small bulge formation was observed at the leading edge of the contact when the friction coefficient was large.

The effects of roughness and sliding friction on contact stresses were investigated by Bailey and Sayles [63]. They developed a numerical normal contact model where the dry elastic contact of a smooth, cylindrical body was studied against digitized topographic data recorded by a stylus-measuring instrument. In this analysis, the imposition of tangential traction was assumed to have no effect on the normal pressure. To assess the accuracy of the subsurface stress model, a series of test cases using smooth body Hertzian pressure distributions were computed and compared with the Hertz Theory solutions. Figure 2.28 shows the distribution of subsurface principal shear stress for the elastic contact of surfaces. It reveals that for a range of real rough engineering surfaces, the maximum principle shear stress occurs very close to the surface, even when frictionless conditions are considered.

Tian and Saka [64] studied the growth of an interface crack during sliding contact in an elastic-bilinear plastic Au/Ni/Cu multilayer half-space structure used in electrical contacts in a plane strain finite element model. The effect of friction—both on the surface and between crack faces—was investigated. The finite element model by the same authors—previously presented in this review [62]—was used in this analysis, and a crack was added to the model by not connecting the elemental nodes along the crack (Figure 2.29). 1200 quadrilateral eight-node isoperimetric elements and 4423 nodes were used in the model. The crack length ($2c$) was specified as $6\ \mu\text{m}$ for the simulations. The analysis revealed that the size of the plastic zone around the crack tips was comparable to the crack length and coating thickness. Plastic deformation at the crack

tips expanded primarily in two directions, as predicted by a slip line field for a closed interface crack. The results indicated that the surface sliding friction tended to increase the plastic zone size and enhance the relative displacement of the crack faces in the direction of the friction force. The level of friction between the crack faces, in contrast, considerably reduced the size of the plastic zone.

Djabella and Arnell [65] investigated the stress field created by a combined normal pressure and tangential traction in a coating/substrate system consisting of a high elastic modulus thin coating on a relatively low elastic modulus substrate. A Hertzian pressure distribution was first applied, then the equivalent normal load at each node of the loaded area was multiplied by the COF to obtain the corresponding tangential traction. Three values of COF—0.15, 0.3 and 0.5—were considered. The PAFEC finite element package was used with 8 node isoperimetric elements for the numerical calculations. The results of a finite element analysis corresponding to an uncoated substrate were compared with a corresponding analytical solution by Hamilton and Goodman [50]. It has been shown that both direct and shear stresses are considerably dependent on the system elastic modulus ratio and the coefficient of friction. Moreover, this analysis revealed that both tensile and compressive stresses—which may lead, respectively, to tensile fracture and buckling—and the shear stress—which can be responsible for delamination at the interface—vary, in a rather complicated fashion, as a function of the coating thickness. The results indicated that a relatively thin layer is preferred to avoid brittle fracture at the surface of the coating, whereas a relatively thick layer reduces the risk of delamination at the interface.

Djabella and Arnell [66] used the finite element model discussed above to investigate the two-dimensional analysis of elastic stresses in double-layer systems. They showed that for double-layer coatings with a decreasing elastic modulus from the surface to the bulk, the surface maximum tensile stress at the trailing edge of the contact zone increased with friction and decreased with the total thickness of the double-layer. In addition, at the coating/substrate interface, the effect of the friction coefficient becomes negligible for thick coatings. Moreover, at the surface, the maximum shear stress—which also increases with friction—is higher than that of a homogeneous material for the same friction coefficient. Conversely, in the substrate, the maximum shear stress is lower than that of a homogeneous material for the same loading condition.

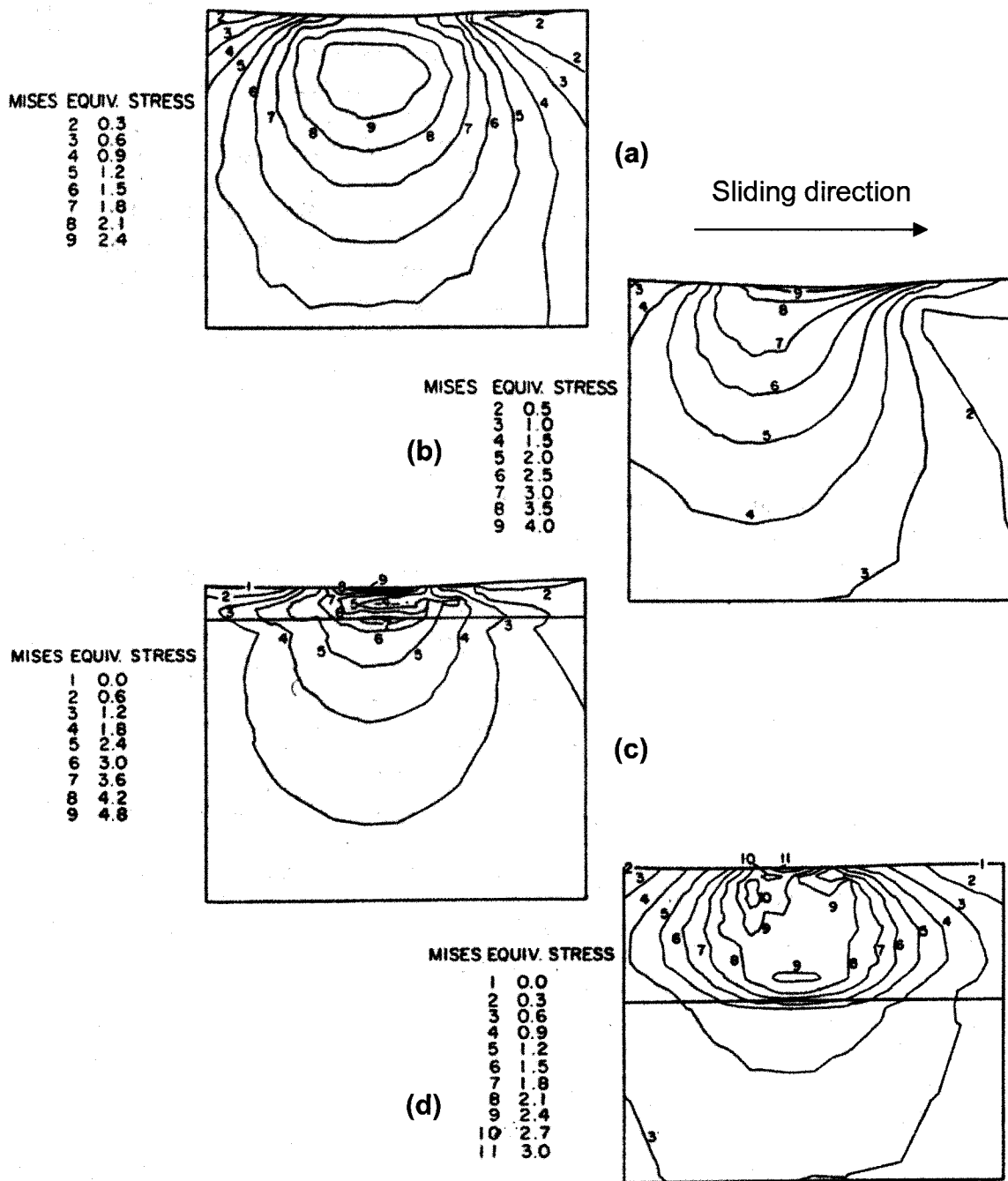


Figure 2.25: von Mises stress contours after penetration and sliding of a half-space surface: (a) $\mu=0.1$, (b) $\mu=0.5$, von Mises stress contours after penetration and sliding of a layered surface for $\mu=0.1$, $E(\text{layer})/E(\text{substrate})=4$: (c) $h/R=0.0356$ (d) $h/R=0.142$ (Stresses are in GPa, h : height of layer, R : radius of cylinder, E : elastic modulus) [60].

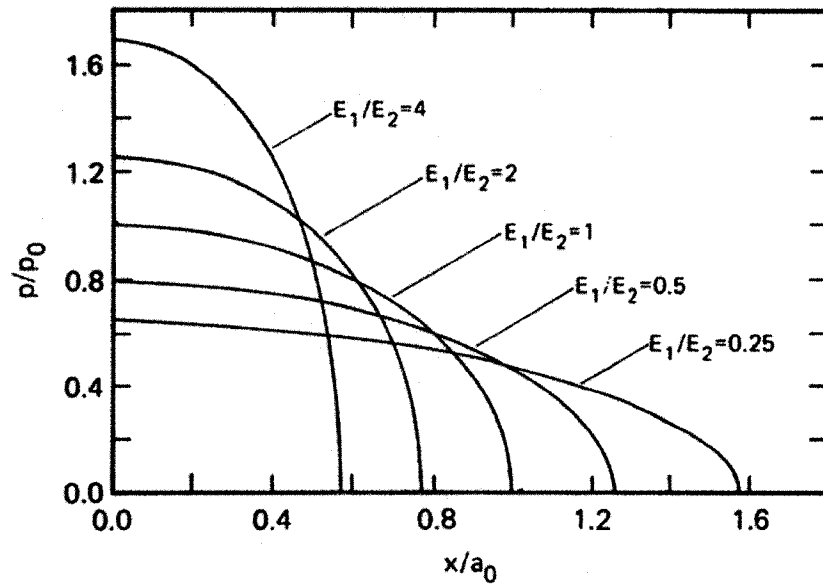


Figure 2.26: Pressure profiles under the indenter for a layered medium [61].

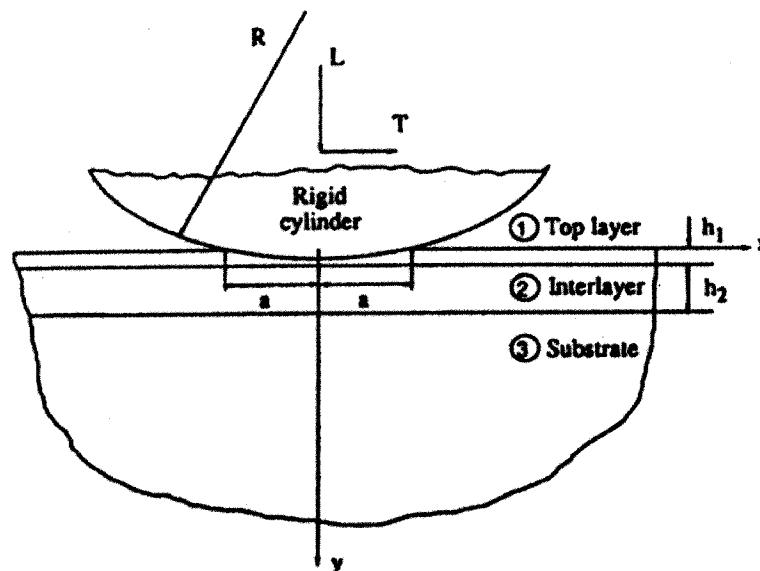


Figure 2.27: Schematic view of sliding contact of a two-layer half-space by Tian and Saka [62].

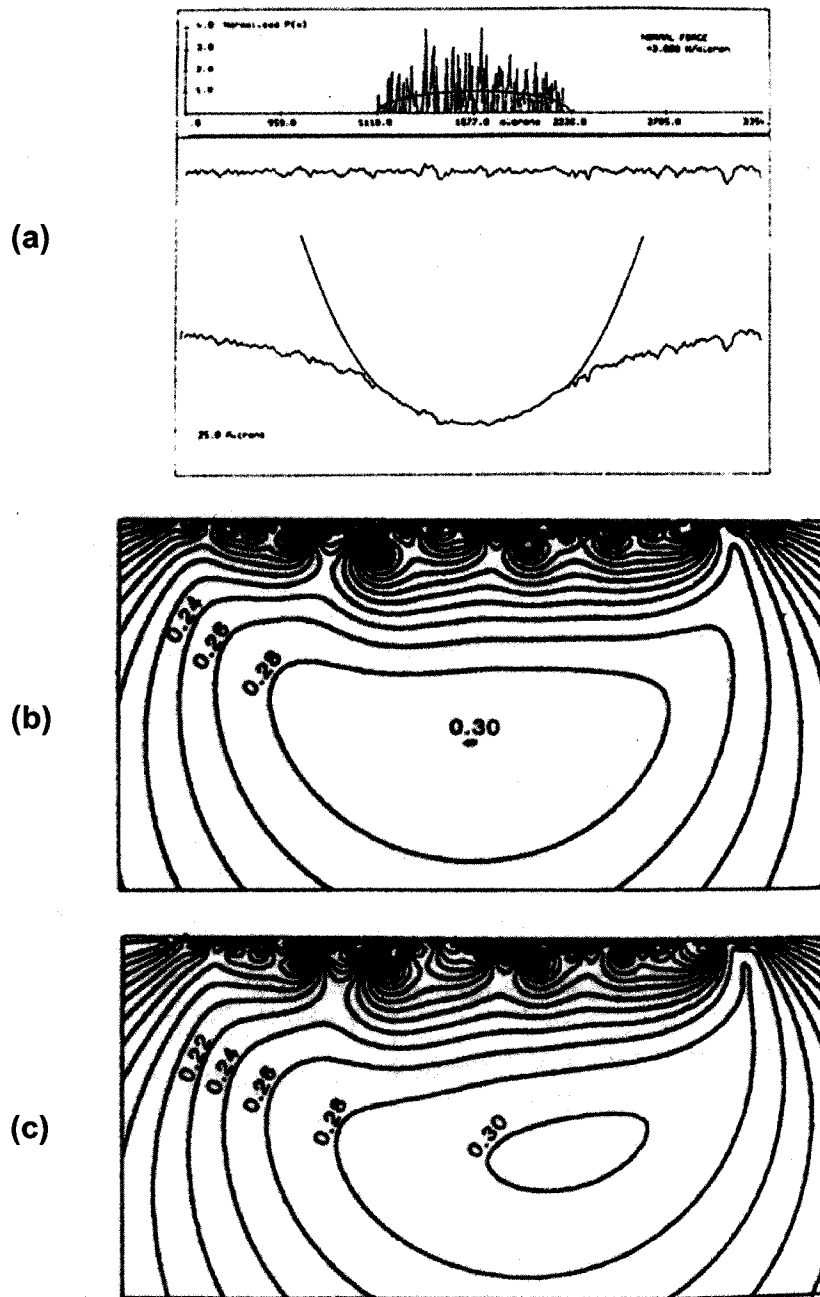


Figure 2.28: Distribution of contact pressure and subsurface principal shear stress for simulated elastic contact of surfaces: (a) Contact geometry and surface pressure distribution, (b) Contour plot of principle shear stress distribution normalized by maximum contact pressure, (c) Effect of friction, $\mu=0.1$, on stress distribution shown in (b) (Due to the effect of rough engineering surface, the maximum principle shear stress is observed very close to the surface, even when frictionless conditions are considered) [63].

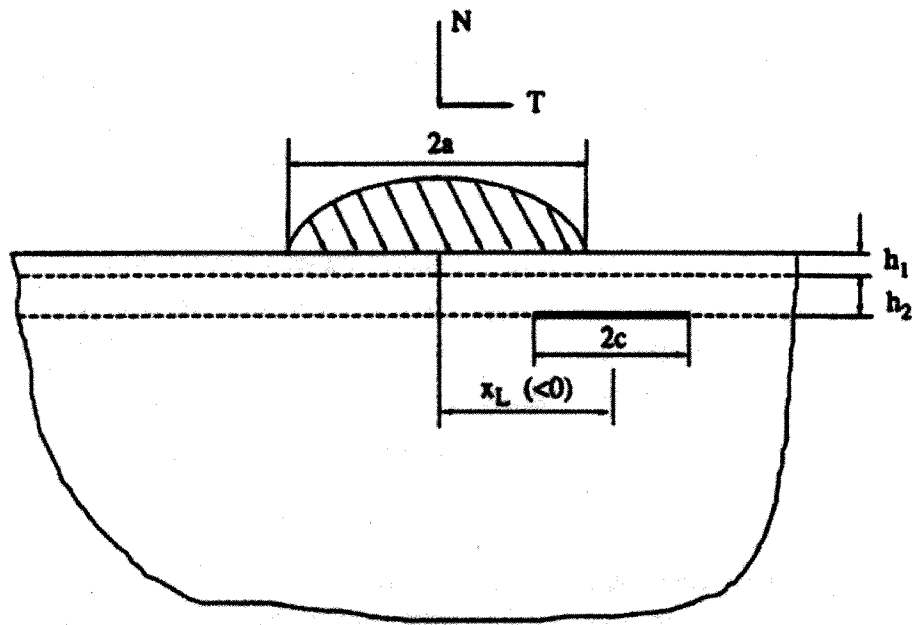


Figure 2.29: Schematic diagram of the geometry of an interface crack by Tian and Saka [64].

Komvopoulos and Cho [67] analyzed subsurface cracking in a homogeneous half-space due to a moving asperity, using linear elastic fracture mechanics and finite element simulations. A rigid cylindrical asperity of radius 25 μm was assumed to indent and slide over a cracked half-space of 164X200 μm^2 . The asperity was first displaced toward the half-space by a total distance of 0.3 μm , and was subsequently translated parallel to the surface while it was constrained against vertical displacement. A horizontal crack (length $2c = 8\mu\text{m}$, depth $d = 4$ and $8 \mu\text{m}$) was modeled by the approach used by Tian and Saka [64]. The finite element mesh consisted of 2762 isoperimetric 8 node quadrilateral plane strain elements. The minimum element size around the crack was 1 μm . The finite element software ABAQUS was used in the simulations. Figure 2.30 shows the schematic representation of the geometry investigated. The simulations indicated that in-plane crack growth occurs due to shear mechanisms, whereas there is also the possibility of out-of-plane crack growth due to tensile mechanisms. The effects of crack length-to-depth ratio and friction (at the contact region and at the crack interface) on the shear and tensile mode crack growth directions were found to be insignificant.

Pödra and Andersson [68] simulated sliding wear with the finite element software package ANSYS. They assumed that the wear rate obeyed Archard's law (Equation 2.1) and developed special subroutines to calculate linear wear by using the following equation:

$$\frac{V}{sA} = \frac{h}{s} = kP \quad (2.55)$$

where V is the volume wear (m^3), s is the sliding distance (m), A is the contact area (m^2), h is the wear depth (m), k is the dimensional wear coefficient (Pa^{-1}) and P is the normal contact pressure (Pa). The written subroutines used to calculate wear by using the following equation derived from Equation 2.55:

$$\Delta h = kP\Delta s \quad (2.56)$$

An elastic steel pin ($R = 5$ mm) was tested on an elastic steel disk with the normal loads of 21 N and 50 N. The linear wear law presented in Equation 2.56 was used to calculate wear in sphere-on-plane simulations, and the results were compared to experimental ones. The wear simulation results deviated from the experimental results within the limits of ± 40 -60%, due to the model simplifications. It was concluded that these FEA wear simulation results should be evaluated to compare different design options, rather than be used to the absolute wear life.

A tool wear prediction algorithm has been implemented into the finite element software ABAQUS in order to predict tool wear evolution during blanking/punching processes by Hambli [69].

$$V = \gamma F_N s \quad (2.57)$$

where V is the volume of the material removed, γ is the wear coefficient, F_N is the normal load applied and s is the sliding distance. Equation 2.57 was used to calculate wear and the wear coefficient was taken as 1.3×10^{-4} corresponding to a hard tool steel. A damage model was also used to describe crack initiation and propagation. The distribution of the tool wear on the tool profile was obtained by finite element simulations and compared to industrial observations. The meshing of the model was carried out by means of 1500 quadrilateral four node axisymmetric elements. The wear profiles obtained by FEM calculations and experiments are compared in Figure 2.31. Finite element simulations indicated that the punch initiates cracks at the cutting edges of the tools, and the cracks propagate in the same direction of the punch penetration.

Molinari et al. [70] modeled dry sliding wear of metals within a Lagrangian element formulation capable of accounting for large plastic deformations and history dependent material behaviour. An adaptive meshing was used to eliminate the deformation induced element distortion—minimizing the numerical error associated with distorted elements. They assumed that the wear rate obeyed Archard's law (Equation 2.1). The model was calibrated and validated against the experimental observations of Lancaster [71], where the wear of a 60-40 brass pin set against a rotating high-strength steel disk was studied. A square, cross-section brass pin was

moved at a velocity ranging from 0.2 to 20 m/s along the length of the steel plate. The applied contact pressure was 1.82×10^5 Pa and the friction coefficient was assumed to be 0.3. Pressure was calculated to be higher at the leading edge of the brass pin than the average contact pressure, which resulted in higher wear rates and mass losses.

In summary, most of the published literature regarding finite element analyses of sliding contact used plane strain conditions in the finite element model to analyze sliding contact. To test and validate finite element models, the Hertz Theory was used for the normal contact cases, and Hamilton and Goodman's analytical solutions were used for the sliding contact cases. Sliding contact is generally achieved by the imposition of a Hertzian normal pressure distribution and a tangential traction, which is calculated from the Hertzian normal pressure distributions. The imposition of tangential traction is assumed to have no effect on the normal pressure [53, 54, 58, 62-66]. This is true only when the two bodies are smooth, or have the same elastic constants [49]. In addition, the utilization of a predetermined pressure distribution is questionable and may lead to significant errors [55-57]. The material models used are generally simple in nature (elastic, elastic-perfectly plastic). Material models that incorporate plastic deformation of the contacting materials observed during sliding wear need to be implemented into the finite element models. Wear prediction equations are used in order to predict wear rates by finite element calculations; however, deviation from experimental results is extensive because of assumed linear wear laws.

2.3. CONSTITUTIVE EQUATIONS FOR ALUMINUM ALLOYS

Constitutive models are the equations that define the changes in flow stress of a material depending on the deformation conditions. In a finite element model, constitutive equations are used to simulate the material behaviour, and the success of the simulation depends on the accuracy of the chosen mathematical model used to describe the deformation of the material. Therefore, this section reviews some of the constitutive equations used for FEM analysis.

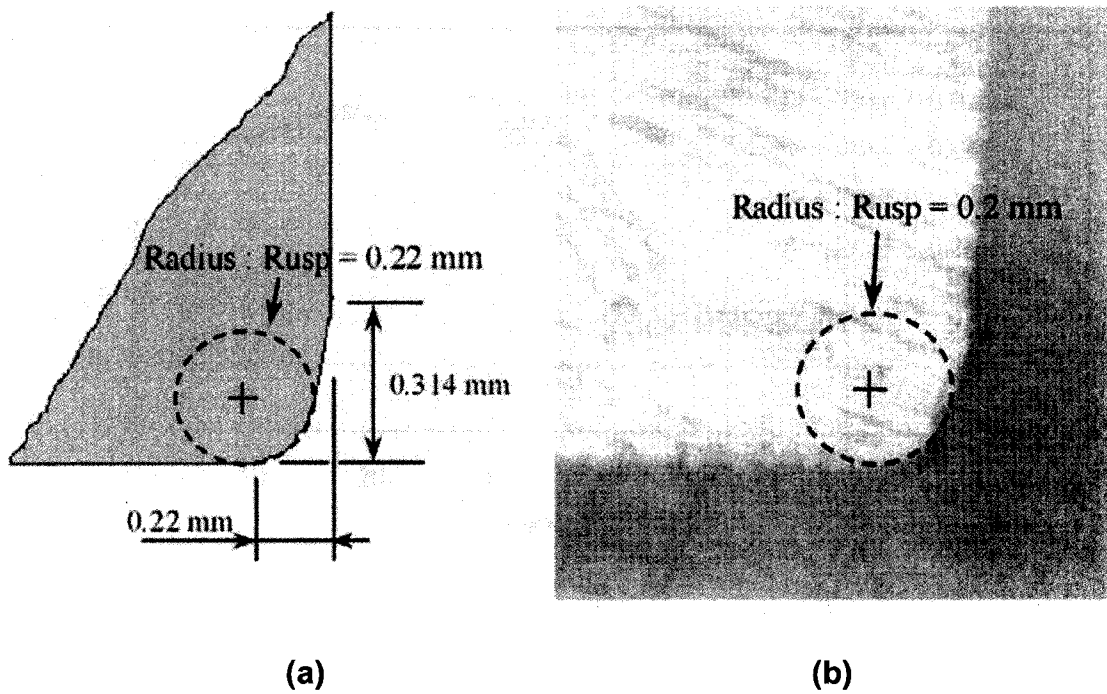


Figure 2.31: Wear profile of the punch after 20000 blanking cycles (a) FEM calculation, (b) Experiment [69].

Classical engineering description of the small strain behaviour of metals assumes dependence of the flow stress on only strain [72]:

$$\bar{\sigma}_f = f(\bar{\epsilon}) \quad (2.58)$$

where $\bar{\sigma}_f$ is the equivalent or flow stress and $\bar{\epsilon}$ is the equivalent strain. Two parabolic equations of this type are the Hollomon [73] and Ludwik [74] equations:

$$\bar{\sigma}_f = K_n \bar{\epsilon}^n \quad (2.59)$$

$$\bar{\sigma}_f = \bar{\sigma}_0 + K_n \bar{\epsilon}^n \quad (2.60)$$

where K_n is the work hardening coefficient, n is the work hardening exponent and $\bar{\sigma}_0$ is the initial yield stress. Equations 2.59 and 2.60 have been used in many technological applications giving sufficient accuracy for many materials [72]. However, infinite flow stress and work hardening are predicted for infinite strain, in contradiction with the behaviour of metals at large strain. Unlike the maximum uniform strain attainable in a tensile test, the total equivalent strain in many practical processes—including cold working and forming operations—is higher than unity. Sevillano et al. [72] reviewed the stress-strain behaviour of many metals and alloys at large strains, and presented a comprehensive study of the flow curves obtained from cold working processes, compression and torsion tests. They pointed out that the typical flow curve of a face centred cubic (fcc) metal or alloy reflects a gradually decreasing work hardening rate at large strains. For a 99.99 % pure Al sample, a saturation flow stress of 375 MPa was observed at the equivalent strain of 3.2. Similarly, ETP Cu and 99.99 % Ag samples reached saturation at the equivalent strains of 4.7 and 3.0, respectively. They reported that alloying increases the work hardening rate and delays saturation of the flow stress until larger strains are applied by comparing the flow curves of some α -brasses. A 5 % Zn brass reached saturation at the flow stress of 425 MPa and at the equivalent strain

1.5, while a 28 % Zn brass work hardened up to the stress of 800 MPa at the same level of strain without reaching saturation.

Attempts have been made to describe the whole process of stress-strain behaviour in a constitutive relationship. Voce proposed the following equation for large strain flow curves [75]:

$$\frac{\bar{\sigma}_s - \bar{\sigma}_0}{\bar{\sigma}_s - \bar{\sigma}_f} = \exp\left(-\frac{\bar{\epsilon}}{\epsilon_c}\right) \quad (2.61)$$

which can be given alternatively as:

$$\bar{\sigma}_f = \left[\bar{\sigma}_s - (\bar{\sigma}_s - \bar{\sigma}_0) \exp\left(-\frac{\bar{\epsilon}}{\epsilon_c}\right) \right] \quad (2.62)$$

where $\bar{\sigma}_s$ is the saturation stress (the stress at which the work hardening rate becomes zero) and ϵ_c is a material constant. Voce showed that Equation 2.62 is applicable for many materials at large strains. Table 2.1 lists $\bar{\sigma}_0$, $\bar{\sigma}_s$ and ϵ_c values for eight copper-based alloys obtained by compression tests. He also showed that the relationship in Equation 2.62 is valid for tension test up to necking. The values obtained from a tensile test for an annealed steel is also given in Table 2.1.

Understanding of the deformation behaviour of materials at large strains is important for tribological applications, and large plastic deformation is strain, strain rate ($\dot{\epsilon}$) and temperature (T) dependent:

$$\bar{\sigma}_f = f(\bar{\epsilon}, \dot{\epsilon}, T) \quad (2.63)$$

The next sections summarize current literature data about the effects of the hydrostatic pressure, strain rate and temperature on the mechanical behaviour of aluminum alloys.

Table 2.1: Flow stress-plastic strain curve constants for different materials represented by Equation 2.57 [75].

Material	$\bar{\sigma}_0$ (MPa)	$\bar{\sigma}_s$ (MPa)	ϵ_C
Copper (99.96 % Cu)	13.8	271.7	0.14
Gilding Metal (89.8 % Cu, 10.1 % Zn)	38.6	324.1	0.13
Cupro_Nickel (79.7 % Cu, 19.8 % Ni)	75.8	390.3	0.12
70:30 Brass (70.0 % Cu, 30.0 % Zn)	75.8	486.8	0.22
64:36 Brass (63.5 % Cu, 36.4 % Zn)	68.9	510.2	0.25
Nickel Silver (62.9 % Cu, 18.5 % Ni, 18.5 % Zn)	75.8	537.8	0.19
Aluminium Bronze (94.7 % Cu, 5.1 % Al)	55.2	579.2	0.29
Phosphor Bronze (94.4 % Cu – 5.3 % Sn)	110.3	586.1	0.29
Steel (0.95 % C)	330.9	728.1	0.09

2.3.1. THE EFFECT OF HYDROSTATIC PRESSURE ON THE MECHANICAL PROPERTIES

The effects of hydrostatic pressure on the mechanical properties of metals have been extensively studied for many years. The first extensive study was carried out by Bridgman on a wide range of materials [76, 77]. He observed an increase in the ductility of a commercial aluminum rod under pressure. The aluminum rod was fractured at atmospheric pressure, at a natural strain of 1.74. True stress at the maximum tensile load was 131 MPa. Under a hydrostatic pressure of 2827 MPa the same material was stretched to a natural strain of 2.87, without fracture. The tensile strength under pressure was 434 MPa. Pugh and Green [78] performed tension tests under hydrostatic pressure up to 827 MPa. To carry out tensile tests under pressure, a tensile testing apparatus was assembled in a high-pressure container (Figure 2.32). Figure 2.33 shows the effect of pressure on the ductility of a commercial purity aluminum alloy taken from their study. True strain at fracture was 0.4 for ambient conditions, but reached 5.0 with the application of a pressure of 552 MPa. Similarly, for the same pressure conditions, a reduction of the area was increased from 35% to almost 100%. They concluded that hydrostatic pressure inhibited the formation and spreading of voids or cracks in the neck area of the tensile test specimens.

2.3.2. STRAIN RATE SENSITIVITY OF ALUMINUM ALLOYS

Aluminum alloys have low strain rate sensitivity when compared with steel. Hauser [79] performed dynamic uniaxial compressive tests on a work hardened aluminum at various strain rates. Figure 2.34 presents the results of these tests, where low strain rate dependency can be observed for low strains. However, work hardened aluminum alloys show strain rate dependency for high strain values. Tsao and Campbell's [80] dynamic shear test results are presented in Figure 2.35. Their experimental results showed some strain rate sensitivity for commercially pure aluminum. Ng et al. [81] examined the dynamic behaviour of thin-walled, tubular specimens of aluminum 6061-T6 and found important strain rate effects. Figure 2.36 presents static and dynamic yield stresses for biaxial stress states in a cylindrical tube where the dynamic curve was evaluated for a strain rate of 40 s^{-1} . Sevillano et al. [72] reported that at increasing strain rates, work hardening rate of 99.99 % Al increased and

the saturation stress was delayed to larger strains at constant temperature plane strain compression tests.

Cowper and Symonds [82] suggested the following constitutive equation for strain rate sensitivity of materials:

$$\sigma = \sigma_0 \left[1 + \left(\frac{\dot{\epsilon}}{D} \right)^{1/q} \right] \quad (2.64)$$

where σ is the dynamic flow stress at a plastic strain rate of $\dot{\epsilon}$, σ_0 is the static flow stress, D and q are constants for a particular material (determined as 6500 s^{-1} and 4 respectively for aluminum alloys [83, 84]).

Johnson and Cook [85] used torsion tests over a wide range of strain rates (quasi static to 400 s^{-1}) and dynamic Hopkinson bar tensile tests over a range of temperatures to define a constitutive relationship for several materials. They defined the following relationship for the strain rate sensitivity:

$$\sigma = \sigma_0 (1 + C \ln \dot{\epsilon}^*) \quad (2.65)$$

where σ is the dynamic flow stress at a dimensionless plastic strain rate of $\dot{\epsilon}^*$ defined as $\dot{\epsilon}^* = (\dot{\epsilon} / \dot{\epsilon}_0)$, C is a material constant and $\dot{\epsilon}_0$ is the reference strain rate set to 1.0 s^{-1} . Figure 2.37 shows the stress-strain curves for 2024-T351 and 7039 aluminum alloys obtained by torsion tests and dynamic Hopkinson bar tensile tests [85, 86].

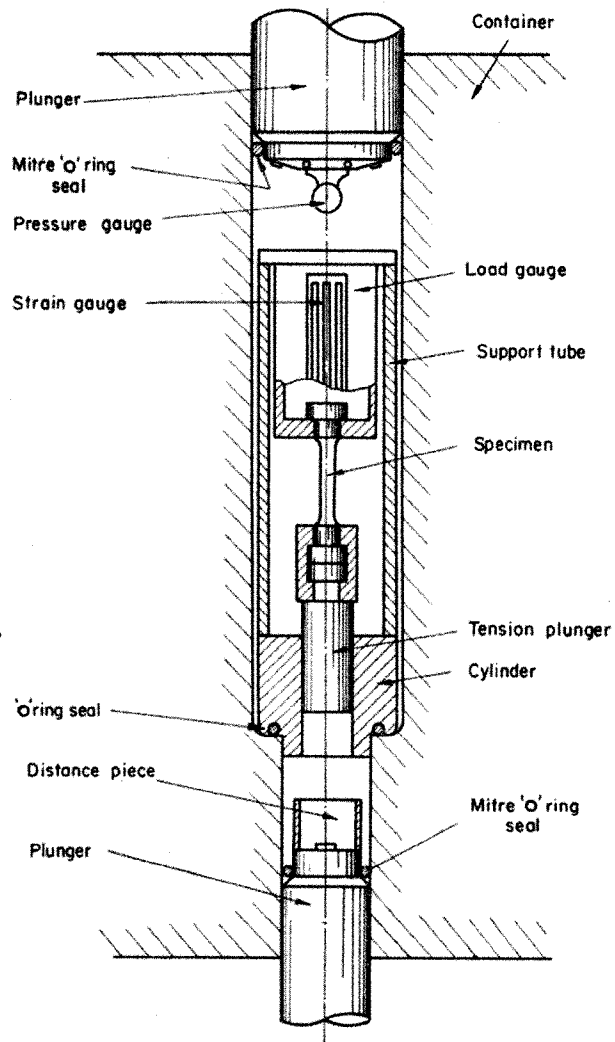


Figure 2.32: Tension testing apparatus under hydrostatic pressure [78].

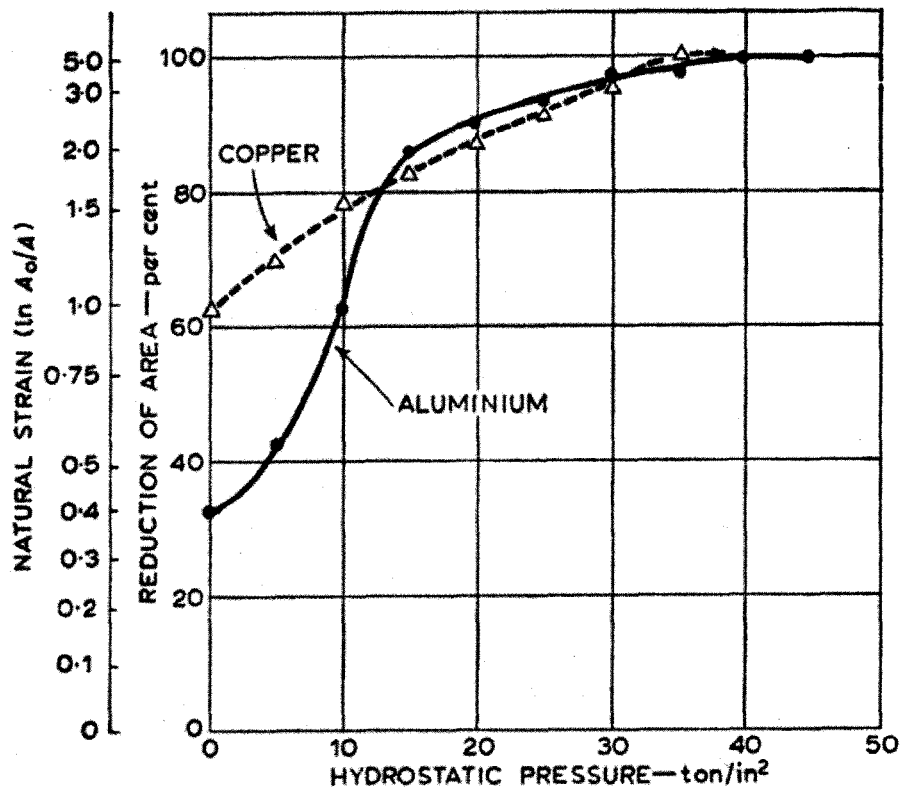


Figure 2.33: The effect of pressure on the ductility of aluminum subjected to tensile test [78].

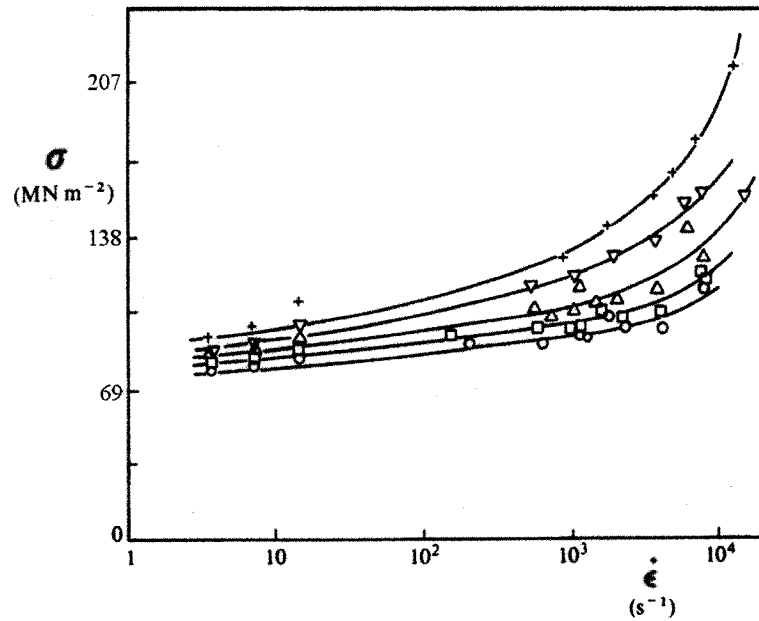


Figure 2.34: Dynamic uniaxial compressive tests on work hardened aluminum at various constant strains (o: $\epsilon=0.01$, \square : $\epsilon=0.02$, Δ : $\epsilon=0.04$, ∇ : $\epsilon=0.08$, $+$: $\epsilon=0.16$) [79].

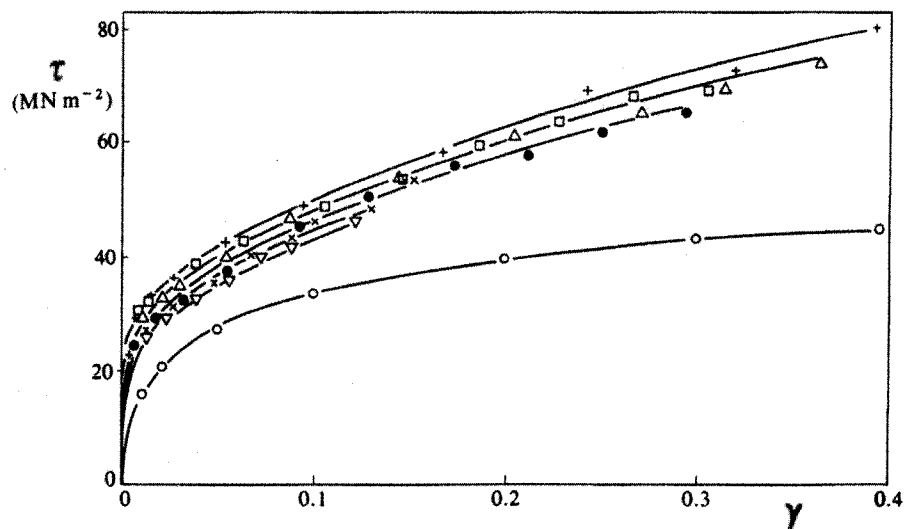


Figure 2.35: Dynamic shear stress-shear strain curves for commercially pure aluminum at various strain rates (the nominal shear strain rates are given by the following symbols: $+$: $\dot{\gamma}=2800 \text{ s}^{-1}$; Δ : $\dot{\gamma}=2200 \text{ s}^{-1}$; \square : $\dot{\gamma}=1600 \text{ s}^{-1}$; \bullet : $\dot{\gamma}=1450 \text{ s}^{-1}$; \times : $\dot{\gamma}=800 \text{ s}^{-1}$; ∇ : $\dot{\gamma}=600 \text{ s}^{-1}$; \circ : $\dot{\gamma}=0.002 \text{ s}^{-1}$,) [80].

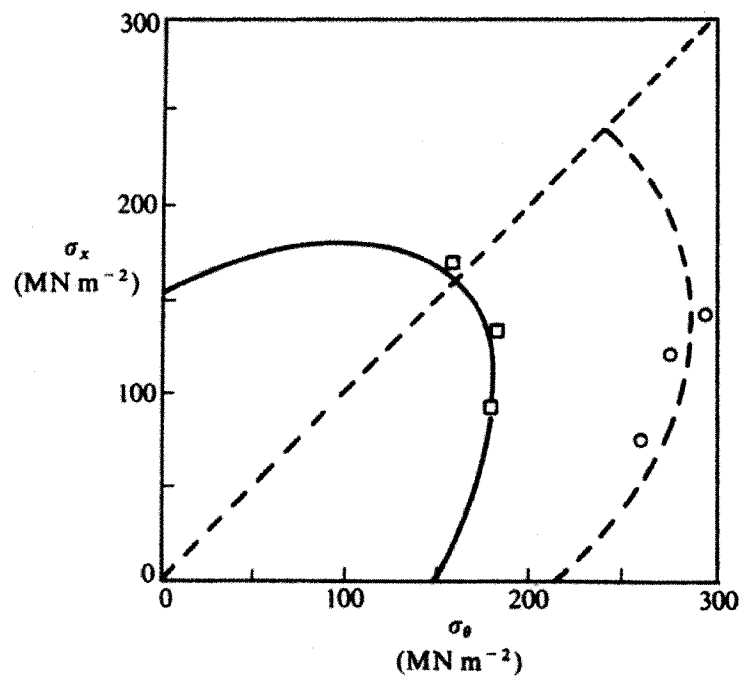
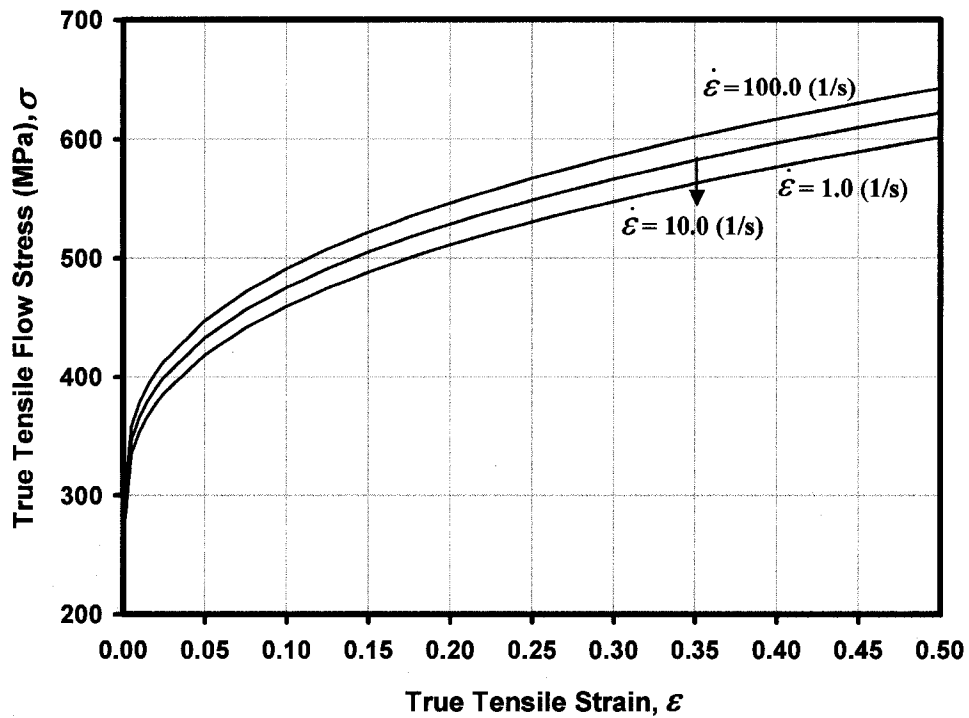
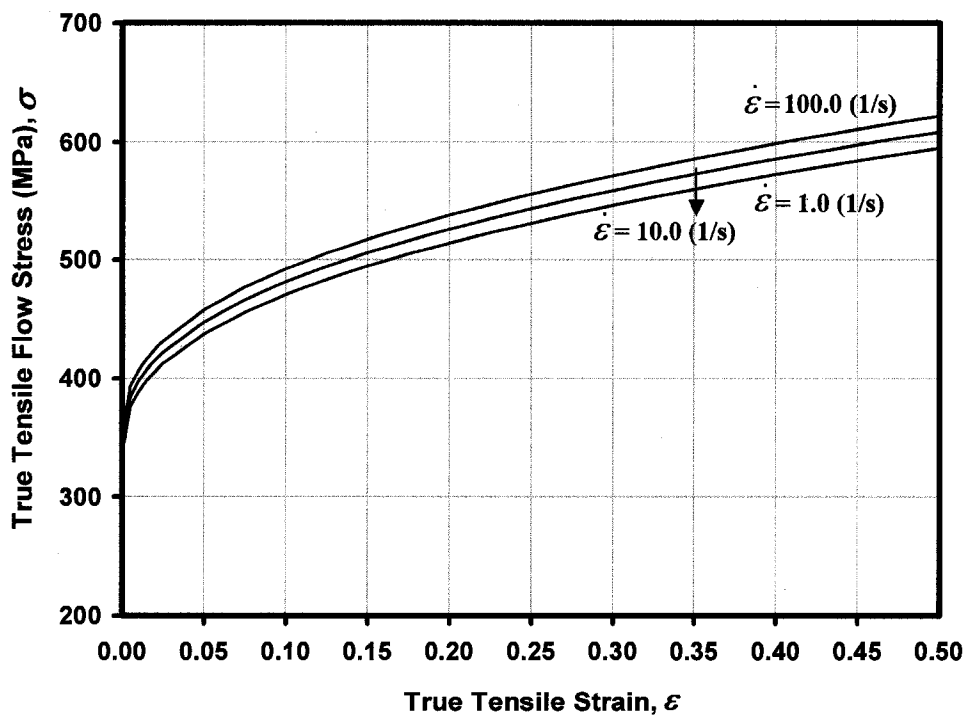


Figure 2.36: Comparison of static and dynamic yield stresses for 6061-T6 aluminum obtained by biaxial tensile test (o: dynamic yield point (40 s^{-1} strain rate), \square : static yield point) [81].



(a)



(b)

Figure 2.37: Stress-strain relationships obtained by torsion tests and dynamic Hopkinson bar tensile tests for (a) 2024-T351 Aluminum, (b) 7039 Aluminum [85, 86].

Many ductile metals display an enormous increase in yield stress for strain rates in excess of 10^3 s^{-1} [87, 88]. Strain rates of this magnitude are generally considered to be beyond the capability of the split-Hopkinson pressure bar tests. Flyer plate testing and Taylor impact testing are the alternatives. Rule and Jones [88] performed Taylor impact tests with four different materials, including a 7075-T6 aluminum alloy. They proposed a revised Johnson-Cook strength model where 1.6×10^3 to 1.9×10^3 MPa flow stress was reported for the 7075-T6 aluminum alloy for strain rates between $5 \times 10^4 \text{ s}^{-1}$ and $1 \times 10^6 \text{ s}^{-1}$. Laser-driven shock waves were also used to measure the spall strength of aluminum alloys at strain rates up to $2 \times 10^7 \text{ s}^{-1}$ [89, 90]. Figure 2.38 shows the spall strengths of 6061-T6 Al alloy and 99.0 % pure aluminum. A spall strength of 3.0 ± 0.2 GPa for pure aluminum is observed at a strain rate of $(1.8 \pm 0.9) \times 10^7 \text{ s}^{-1}$.

2.3.3. THERMAL SOFTENING OF ALUMINUM ALLOYS

Johnson and Cook [85] also defined a relationship for the thermal softening of materials by using dynamic Hopkinson bar tensile tests over a range of temperatures.

$$\sigma_T = \sigma_{room} \left[1 - \left(\frac{T - T_{room}}{T_{melt} - T_{room}} \right)^m \right] \quad (2.66)$$

where σ_T is the flow stress at temperature T (K), σ_{room} is the flow stress at room temperature, T_{room} is the room temperature (K), T_{melt} is the melting temperature (K) and m is the Johnson-Cook thermal material parameter (determined as 1.0 for 2024-T351 and 7039 aluminum alloys [85]).

Change of the flow stress for some aluminum alloys with temperature is presented in Figure 2.39 [91, 92]. The thermal material parameter (m) in Equation 2.66 can be calculated for different temperatures by using the flow stress data at room temperature as a base in Figure 2.39. The thermal material parameter (m) can be calculated by using the following mathematical operations:

$$(\sigma_T - \sigma_{room}) = 1 - \left(\frac{T - T_{room}}{T_{melt} - T_{room}} \right)^m \quad (2.67)$$

$$\left(\frac{T - T_{room}}{T_{melt} - T_{room}} \right)^m = 1 - (\sigma_T - \sigma_{room}) \quad (2.68)$$

$$m \log \left(\frac{T - T_{room}}{T_{melt} - T_{room}} \right) = \log[1 - (\sigma_T - \sigma_{room})] \quad (2.69)$$

$$m = \frac{\log[1 - (\sigma_T - \sigma_{room})]}{\log \left(\frac{T - T_{room}}{T_{melt} - T_{room}} \right)} \quad (2.70)$$

Equation 2.70 was used to calculate the thermal material parameter m for the alloys whose flow stress is given as a function of temperature in Figure 2.39, and Figure 2.40 was obtained. Figure 2.40 indicates that the thermal material parameter is not constant, but changes with temperature. However, an extrapolation of the curve for the A356 Al alloy shows that m is between 0.85-1.00 up to 150 °C.

When Johnson and Cook defined the constitutive relationships for the strain rate dependency and thermal softening effects, they assumed that the strain rate and thermal effects were not coupled. However, strain rate sensitivity is also dependent on the temperature. Blaz and Evangelista [93] studied the strain rate sensitivity of pure aluminum (99.99 % Al) and Al-Mg-Si alloy (Si 0.56 %, Mg 0.53 %, rest is Al) by performing hot compression tests. They found that the strain rate sensitivity depends on the temperature and the strain for the materials used in the experiments. Figure 2.41 shows the strain and temperature dependency of the strain rate sensitivity presented in their study, where the strain rate sensitivity (n_R) was calculated as follows:

$$n_R = \frac{d \log \sigma}{d \log \epsilon} \quad (2.71)$$

where σ is the flow stress and $\dot{\epsilon}$ is the plastic strain rate. Similarly, Stuwe and Les [94] showed that the strain rate sensitivity of 99.99 % purity aluminum is strain dependent, and strain rate sensitivity measurements depend quite strongly on the interval of strain rates chosen.

Zerilli and Armstrong [95] took the experimental data of Johnson and Cook and derived a new constitutive relation based on the dislocation mechanics. They obtained two different constitutive equations for face centred cubic (fcc) and body centred cubic (bcc) metals. The plastic flow stress (σ) for fcc materials is given by:

$$\sigma = \Delta\sigma'_G + c_2\dot{\epsilon}^{1/2} \exp(-c_3T + c_4T \ln \dot{\epsilon}) + kl^{-1/2} \quad (2.72)$$

For the bcc case;

$$\sigma = \Delta\sigma'_G + c_1 \exp(-c_3T + c_4T \ln \dot{\epsilon}) + c_5\dot{\epsilon}^n + kl^{-1/2} \quad (2.73)$$

where $\Delta\sigma'_G$ is a stress constant, ϵ is the plastic strain, $\dot{\epsilon}$ is the strain rate, l is the average grain diameter, k is the microstructural stress intensity, n is the strain hardening exponent and c_1, c_2, c_3, c_4, c_5 are material constants.

In this chapter, published literature on the sliding wear of ductile materials and the experimentally observed wear mechanisms is summarized. Specifically, the deformation and damage accumulation processes observed during the sliding wear of aluminum alloys is discussed and the missing elements in the current scientific and engineering knowledge are pointed. The numerical models developed in this study were built on guidance obtained from this critical literature review. In the next chapter, the objectives of this study are presented in the view of this literature summary.

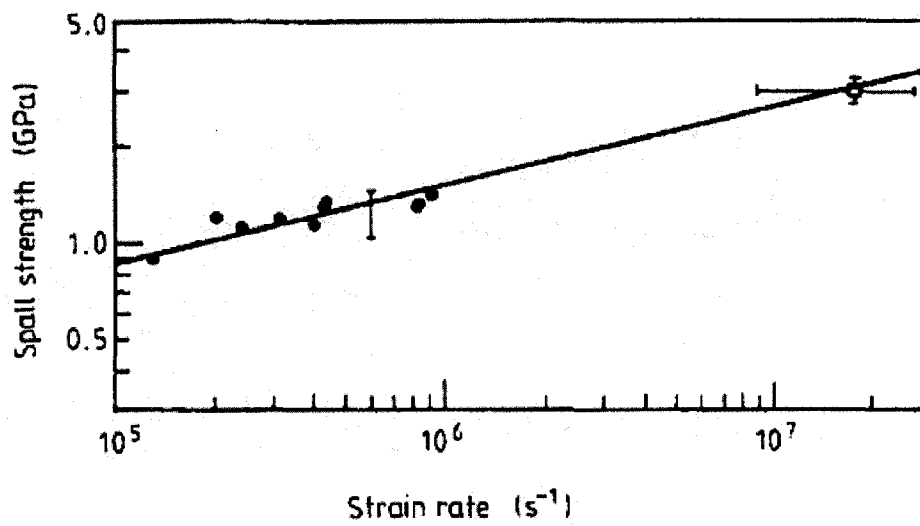


Figure 2.38: Spall strength versus strain rate for 6061-T6 Al alloy (●) and 99.0 % pure aluminum (□) [89, 90].

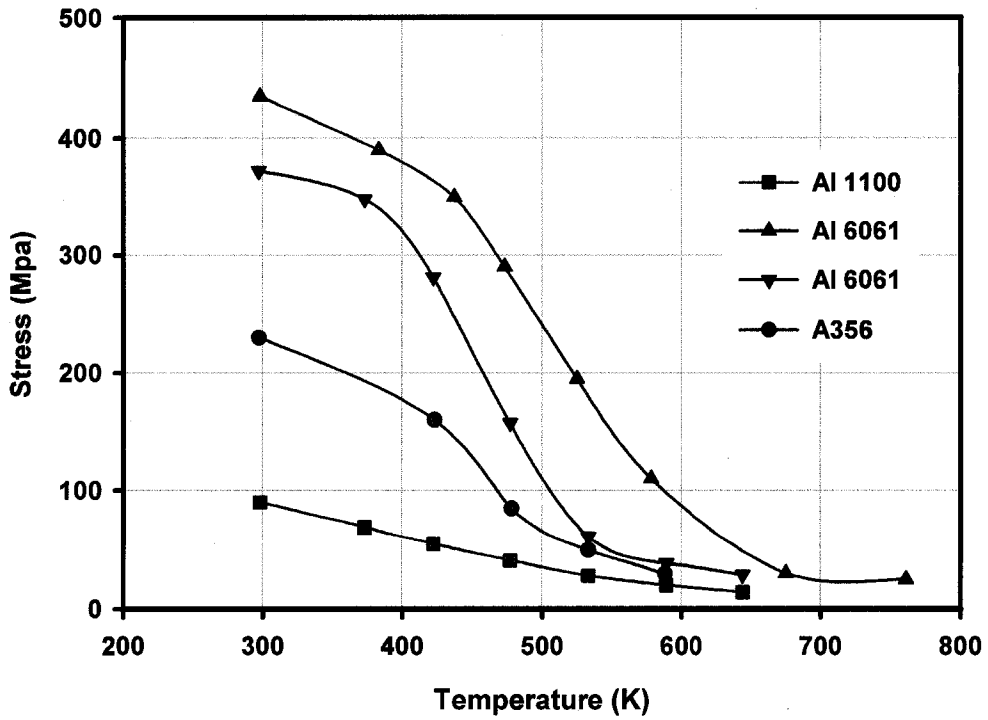


Figure 2.39: Change of flow stress for some aluminum alloys with temperature [91, 92] (True stresses are given at 0.2 true plastic strain).

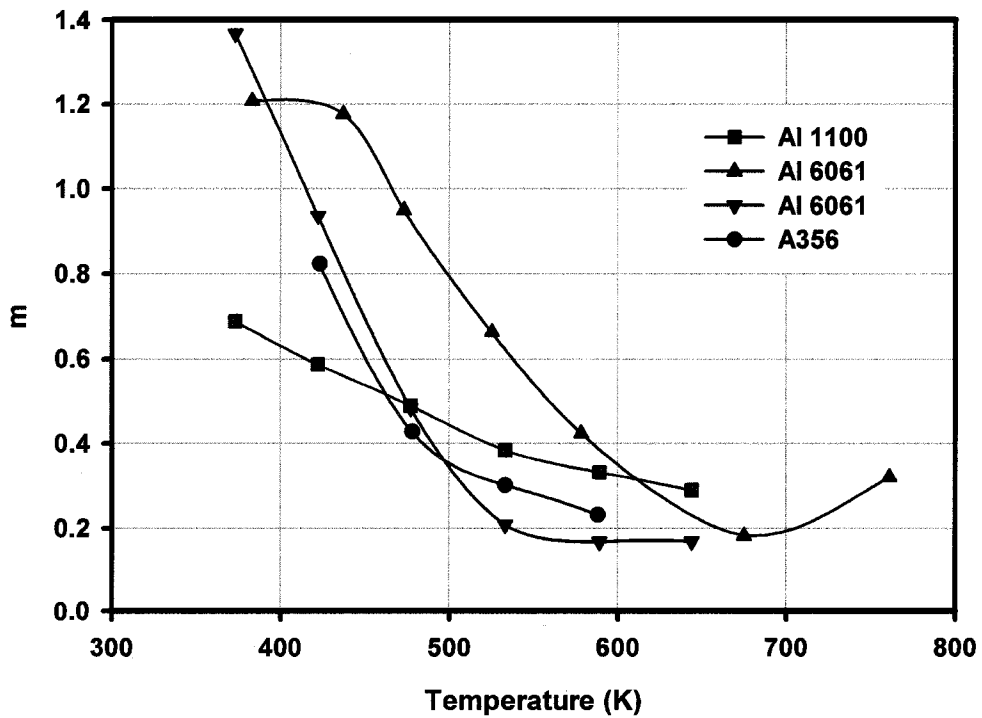
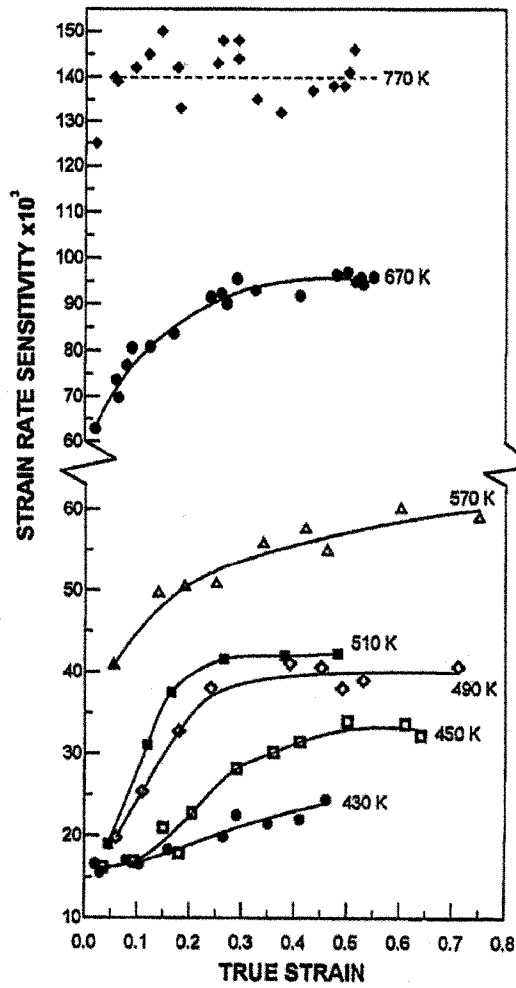
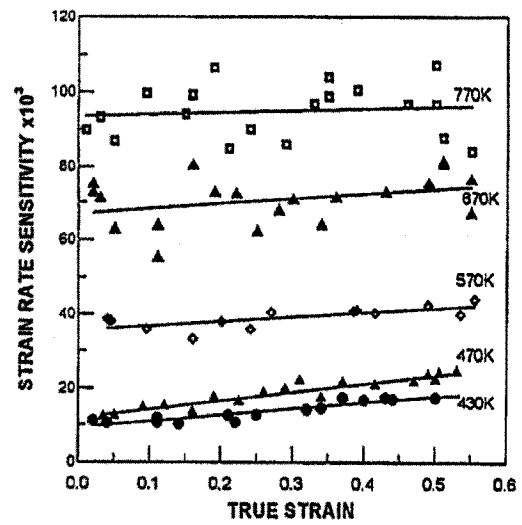


Figure 2.40: Change of the Johnson-Cook thermal material parameter (m) with temperature for some aluminum alloys calculated using stress-strain curves from Figure 2.39.



(a)



(b)

Figure 2.41: Strain and temperature dependence of the strain rate sensitivity for (a) Al-Mg-Si alloy, (b) pure aluminum [93].

CHAPTER 3

SCOPE OF THE PRESENT RESEARCH

Subsurface deformation mechanics must be understood in order to achieve both wear control and prevention. While there is data available on the sliding wear behaviour of Al-Si alloys, further investigation is necessary to fully understand subsurface deformation and damage accumulation events, and their relationship to subsurface void growth. The delamination of subsurface layers--a process that produces plate-like wear debris--is initiated when the subsurface plastic deformation that occurs during sliding causes the nucleation of voids and cracks. The basic need in modeling the subsurface delamination processes is to define the depth at which cracks initiate and propagate to form plate-like wear debris. Ductile void growth theories may be used to study how a void grows under an imposed stress and strain field.

Ductile void growth theories provide insight into the damage processes observed in ductile materials during sliding wear. One element to consider is the competition between the hydrostatic pressure, which suppresses void growth, and the flow stress, which enhances it. In order to quantify the delamination processes, distributions of the subsurface stresses and strains must be determined. The subsurface deformation state, however, is difficult to determine experimentally. Analytical and theoretical solutions for the contact stress fields have limited applications in this area, due to the assumptions made to reach a solution. Numerical methods, on the other hand--like the finite element method--are capable of surmounting the shortcomings of the theoretical solutions. The literature available on the topic of finite element analyses of sliding contact has revealed that most of the published studies suffer from a number of problems, including the questionable determination of normal and tangential load distributions during sliding. Realistic elastic-plastic material models, which reflect the deformation processes observed during sliding wear, are another issue that must be addressed in the numerical investigations. Factors such as strain rate and deformation induced heating have to be considered in a model that aims to study sliding wear, because those factors can change the mechanical properties of the sliding surfaces. An analysis that couples thermal and structural approaches, including strain rate and thermal effects on the subsurface deformation, has not yet been provided.

Therefore, the present study was carried out to investigate the subsurface deformation and damage accumulation events observed in the dry sliding wear of aluminum alloys. Although a particular aluminum alloy was chosen for this work, the general approach used for damage accumulation processes are applicable to the sliding wear of similar ductile materials. The explicit finite element program LS-DYNA was utilized in this numerically based investigation to model the deformation of an aluminum alloy (used in automotive applications). The analysis was carried out in several steps, beginning with the normal contact investigations. To investigate the multiple sliding contacts, cylindrical asperities were loaded and prescribed a constant sliding velocity over a three dimensional 356 Al structure. The finite element models were validated by comparing the numerical results with those of the normal and sliding contact experiments. The main objectives of this study were:

- To investigate the accumulation of the subsurface stresses and strains during the sliding contacts of aluminum alloys,
- To estimate the damage gradient below the contacting surfaces,
- To determine the distribution of the hydrostatic pressure, the strain rate and their effects on the formation of a damage gradient,
- To calculate temperature increase in sliding surfaces and its effects on the subsurface damage,
- To study the factors influencing the damage gradient (sliding velocity, normal load, friction and second phase particles).

CHAPTER 4

FINITE ELEMENT PROCEDURES

This chapter provides the details of the numerical models used to study the contact between a 356 Al alloy surface and an asperity. Finite element analysis basics are reviewed in Appendix A using a point of view that covers all the numerical approaches used in this study. Appendix A presents information about time integration methods, element formulations, contact algorithms and energy analysis.

4.1. ANALYSIS OF NORMAL CONTACT BETWEEN SOLIDS

This section presents the finite element models developed for normal contact analysis between a cylindrical asperity and an aluminum half-space surface. A sample finite element input file is summarized in Appendix B. Explicit dynamic and implicit static time integration schemes of the finite element (FE) software—LS-DYNA version 970 release 3858 from Livermore Software Technology Corporation (LSTC) [96]—were used in the normal contact simulations.

4.1.1. FE MODEL GEOMETRY

A half-space of 30 μm width and 100 μm length was defined and subjected to normal contact by a semi-cylindrical asperity with a radius of 10 μm . The third dimension of the half-space and the asperity was assumed to be infinitely long, and therefore a plane strain condition exists. The geometries of the considered finite element models are shown in Figure 4.1 (Models A and B) and Figure 4.2 (Models C to F).

4.1.2. ELEMENT FORMULATION AND PROPERTIES

The numerical models utilized 3D Lagrangian solid elements of plane strain formulation with single-point Gaussian quadrature were used for the models utilizing the explicit integration scheme. The simulations employing the implicit solution algorithm

used four-point Gaussian quadrature. The largest element aspect ratio for all the models was 2.7; however, the aspect ratio of elements in the vicinity of the critical contact region was approximately one. The minimum element size utilized at the vicinity of the contact region was 0.1 μm for the finest discretized model, and 0.8 μm for the coarsest discretized model.

Mesh convergence was investigated for both explicit and implicit time integration schemes, then assessed by comparing the results of different mesh density models with each other and with the predictions of Hertz theory—the comparison details are presented in Chapter 6. Table 4.1 provides the characteristics for the finite element mesh, and geometry for all six models examined (Models A to F). The most highly discretizing model contained 8022 elements and 8245 nodes. To decrease processing time, the smallest sized elements were placed at a critical region of the half-space, while larger sized elements were placed further from the contact region (Figures 4.1 and 4.2).

In trial simulations, the high-stressed region of the subsurface was localized near the contact zone, and a reduction in the subsurface width to half the original dimension of 100 μm did not alter the numerical simulation findings (Model F). A comparison of the maximum shear stress, maximum hydrostatic pressure and principal stresses illustrated only a minor variation of less than 0.5 % for a reduction in the subsurface width. The decrease in subsurface width reduced computational time by approximately 50 %.

4.1.3. MATERIAL MODEL

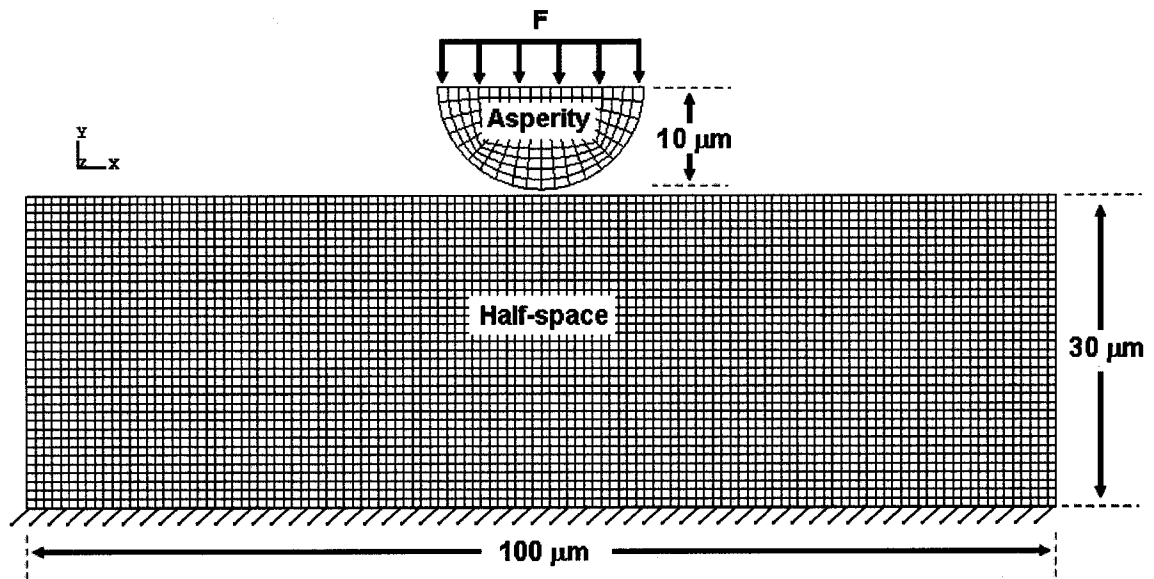
The asperity was defined as an elastic deformable material, and an elastic material model of LS-DYNA [96] was used to characterize the material behaviour of the asperity. The Young's modulus, Poisson's ratio and mass density values assigned to the asperity were 400 GPa, 0.3 and 7800 kg/m^3 , respectively. The same material model was utilized for the 356 Al half-space under assumed elastic conditions. The Young's Modulus, Poisson's ratio and mass density of the 356 Al half-space were specified as 72.4 GPa, 0.33 and 2669 kg/m^3 .

4.1.4. LOADING AND BOUNDARY CONDITIONS

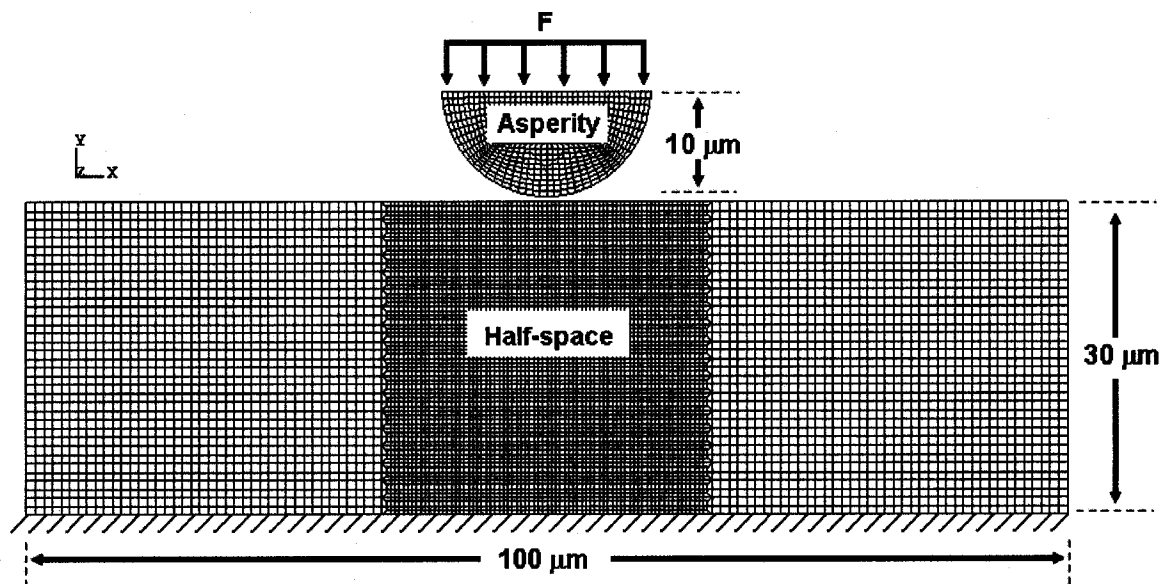
For the elastic indentation simulations, the asperity was loaded with a total force of 3.3 N per unit thickness in mm. The load was distributed equally on each node located at the top layer of the asperity. All nodes at the bottom of the half-space were constrained from motion (Figures 4.1 and 4.2). The load application curves for the explicit and the implicit time integration schemes are presented in Figure 4.3. For the simulations using the explicit dynamic approach, the load was linearly increased from zero to a maximum value of 3.3 N/mm in 3×10^{-4} s and then held constant for the remaining time (i.e. up to 1×10^{-3} s). The ramping to maximum load at times 2×10^{-4} s and 5×10^{-4} s were investigated, and no difference in deformation response was observed. Thus, 3×10^{-4} s was selected as the duration for the load ramping time. For the simulations employing the implicit static time integration scheme, a step size of 0.01 was utilized and the total size of the analysis was 1.0. The applied load was ramped to its maximum prescribed value of 3.3 N/mm at the 0.3 step, then held constant for the rest of the simulation. Displacement convergence tolerance and energy convergence tolerance were set at 0.01 and 0.5, respectively. These tolerance values are unitless quantities since displacement and energy of the system is checked at each step as percentage for convergence.

4.1.5. CONTACT ALGORITHM

A penalty type, two-dimensional, two-way contact algorithm was used to simulate contact between the asperity and the 356 Al half-space where the penetration of slave nodes into the master segment is checked and prohibited [96]. Static and dynamic coefficients of friction were set to zero to study frictionless conditions. Due to the excessive nodal penetrations observed in initial trial simulations, the default value of the penalty scale factor was increased—by a factor of eight—for numerical models employing the explicit solution scheme, and by four orders of magnitude for models utilizing the implicit solution scheme.

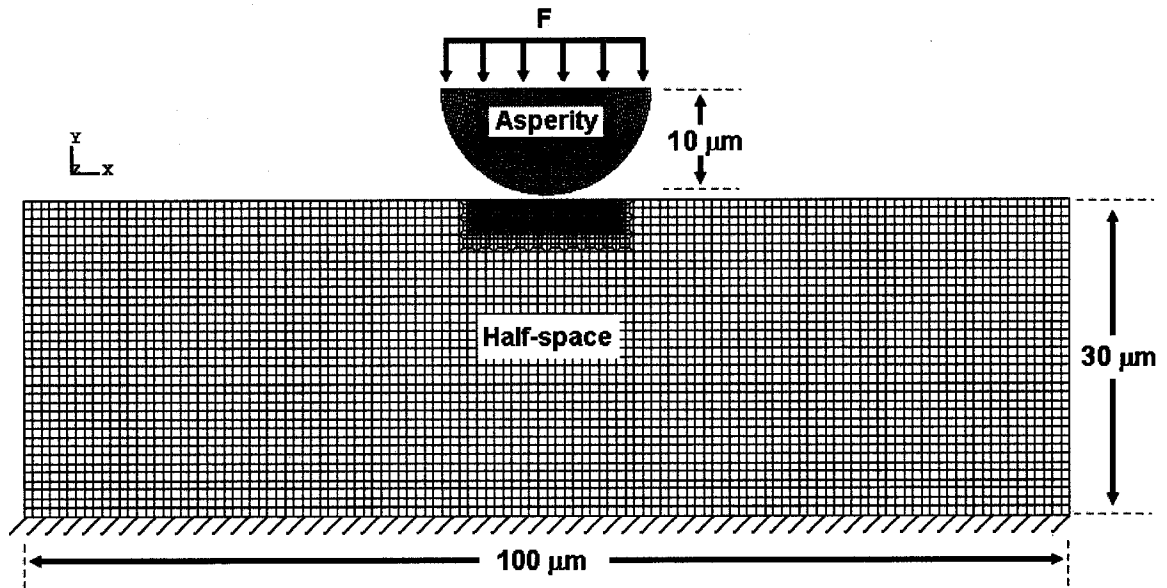


(a)

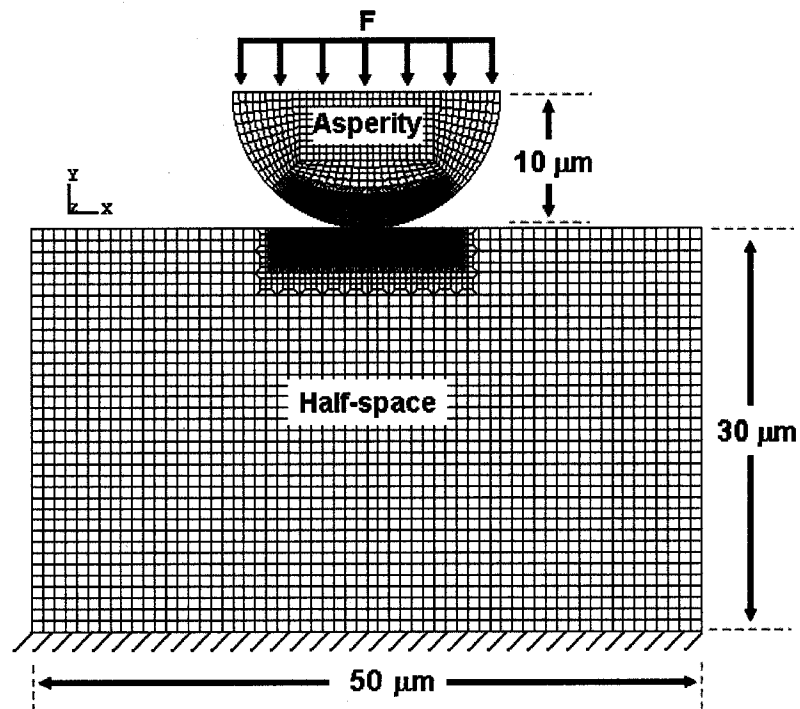


(b)

Figure 4.1: General view of the normal contact finite element models, loading (F : distributed normal load) and boundary conditions (restriction of the bottom nodes from the motion): (a) Model A and (b) Model B.



(a)



(b)

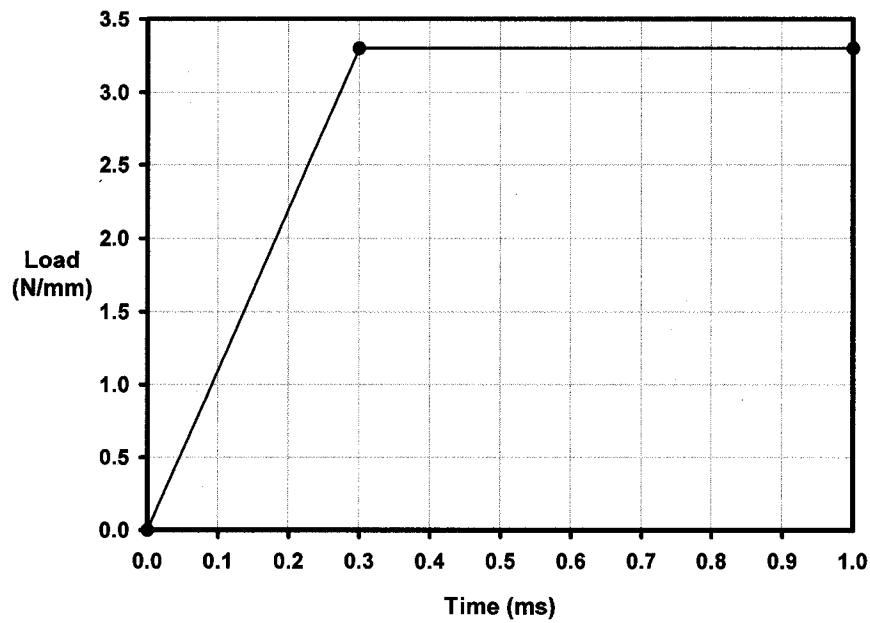
Figure 4.2: General view of the normal contact finite element models, loading (F : distributed normal load) and boundary conditions (restriction of the bottom nodes from the motion): (a) Models C, D, E and (b) Model F.

Table 4.1: Comparison of the different meshed elastic normal contact models.

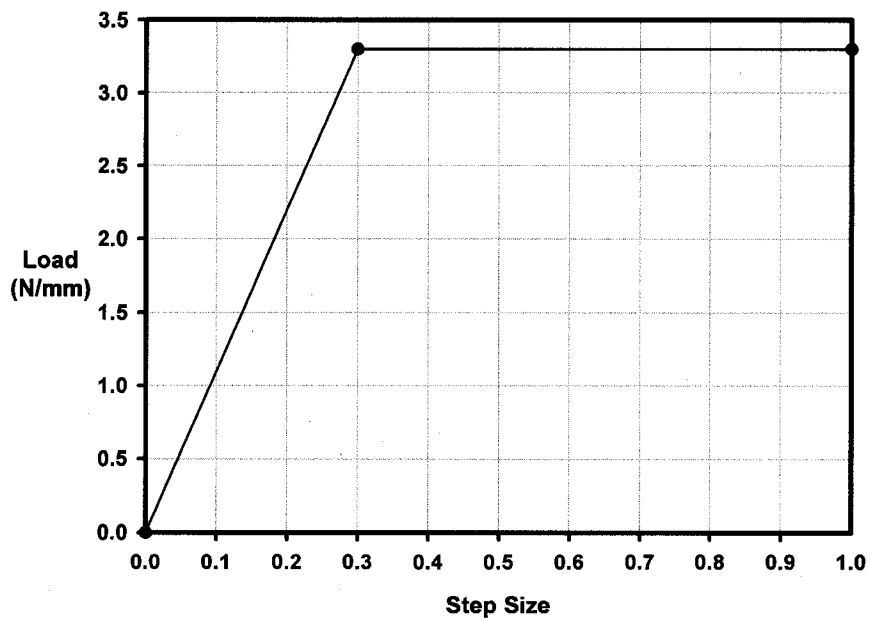
Model*	Min. Element Size (μm)	Total Number of Elements	Total Number of Nodes	Mass Scaling (Times)
Explicit Time Integration Scheme				
Model A	0.83	4470	4648	40.60
Model B	0.42	8952	9186	18.10
Model C	0.21	7864	8128	6.04
Model D	0.21	7864	8128	3.60
Implicit Time Integration Scheme				
Model E	0.21	7864	8128	-
Model F	0.10	8022	8245	-

* Models A, B, C, D, and E: half-space dimensions $30\mu\text{m} \times 100\mu\text{m}$

Model F: half-space dimensions $30\mu\text{m} \times 50\mu\text{m}$



(a)



(b)

Figure 4.3: Normal load application curve for the simulations using: (a) the explicit solution scheme and (b) the implicit solution scheme.

4.1.6. HOURGLASS MODES

Hourglass mode deformation is resisted automatically in LS-DYNA by a viscous control, which is a very CPU efficient method. However, it may not be very well effective to minimize the hourglassing modes. In preliminary simulations, hourglass modes were observed in solutions utilizing the explicit time integration scheme. Flanagan-Belytschko stiffness form hourglass mode control [96] was applied to the half-space and the asperity. Since this hourglass control added further processing overhead, it was applied only to a critical upper portion of the half-space where the hourglass modes were observed. For the rest of the half-space, only the viscous form hourglass mode control was applied. This approach was successful to minimize the hourglass modes and details of the energy balance discussion for the normal contact simulations are given in Section 6.1.1. Four-point Gaussian quadrature was used for the simulations employing the implicit method, and thus no hourglass modes were present.

4.1.7. MASS SCALING

The use of a highly discretized mesh resulted in excessively long processing times for the simulations employing explicit time integration. A number of ways to simulate a quasi-static situation exist using the explicit finite element method. One of the techniques, called mass scaling, increases the time step by adding mass to an element. Effectively, the mass density of the model is increased and, as a result, the total computational time is decreased. Mass scaling was applied to the models that were simulated using the explicit approach, in an effort to decrease CPU time. Test simulations proved that mass scaling did not significantly affect the results, because the variations in asperity penetration depths and subsurface stresses were only 1 % and 4 %, respectively for up to 20 times mass scaling when compared with the simulations conducted without mass scaling.

4.2. ANALYSIS OF SLIDING CONTACT BETWEEN SOLIDS

This section presents the details of sliding contact investigations between a 356 Al alloy surface and a steel asperity. A sample finite element input file is presented in

Appendix C. Due to some element distortion problems observed in trial simulations, the Lagrangian elements that were utilized in the elastic normal contact problem (see Section 4.1) could not be used to model the large plastic strains observed during the sliding wear of the aluminum alloys. Hence, an Eulerian FE model was used to account for the high deformation of the aluminum alloy, and the finite element geometry was modified accordingly. The details of the Eulerian explicit dynamic sliding contact models are presented in the following sections.

4.2.1. FE MODEL GEOMETRY

An asperity contact model was considered in the finite element model because contact between two solid surfaces occurs at asperities, and these asperities are responsible for supporting the normal loads and tractions between the surfaces. The finite element model used in the sliding contact simulations consisted of three main parts: the 356 Al, the asperities and the airmesh. Since the airmesh did not initially contain any material, its material was defined as void. The sliding contact was modeled by pressing a cylindrically shaped steel asperity with a 2.0mm diameter and 0.5mm thickness onto a 356 Al surface (2.9mm x 13.3mm x 0.5mm), then sliding the steel asperity over the Al surface with a constant sliding velocity. Several asperities were passed, one after the other, to investigate the cumulative effect of multiple asperity sliding contacts. When a steel asperity completed its sliding motion, the subsequent one was designed to begin moving on the surface. A schematic view of the numerical set-up is shown in Figure 4.4. In an effort to minimize CPU time requirements, a dimensional analysis was applied and the defined geometry of both the asperity, and the 356 Al surface was chosen carefully. Appendix G records the details of the dimensional analysis for sliding contact models. The dimensional analysis proved that the results of the presented finite element model are applicable to asperity contacts of different sizes (i.e. asperity diameter), provided that the applied force is scaled by the square of the geometric scaling factor.

The 356 Al alloys, the airmesh and the asperities were all modeled as hexagonal elements. In order to obtain stress and strain data below the surface, the results from some elements in the 356 Al alloy were specifically recorded in the numerical output. The row of elements at the centre of the 356 Al mesh were chosen for this purpose.

4.2.2. ELEMENT FORMULATION AND PROPERTIES

The numerical model only utilized solid elements, and Lagrangian solid elements were used for the asperities. An Eulerian solid element formulation with a 1-point integration with single material and void was chosen for the aluminum alloy. Because material is not constrained to the original mesh in the Eulerian formulation, a void air mesh was constructed to allow the 356 Al material to flow out of the mesh and deform throughout the simulation. The air mesh was modeled large enough to provide space around the 356 Al alloy for any possible material flow. The mesh was carefully discretized in the vicinity of the critical contact region with aspect ratios of approximately one. The minimum element size utilized at the vicinity of the contact region was 0.1mm, and the mesh generated is shown in Figure 4.5.

Each steel asperity was discretized with 1440 Lagrangian elements and 1908 nodes. 11280 Eulerian elements and 14082 nodes were used in the discretization of the 356 Al surface, and 11995 elements and 14546 nodes were used for the void air mesh. The Eulerian calculation control parameters were designed to perform an advection after every time cycle, using the second order Van Leer method.

4.2.3. MATERIAL MODEL

Tensile and compression test data are not well suited to represent the large plastic deformation characteristics experienced during sliding wear. Bulge tests simulate high stress-strain behaviour better than tensile tests for the metal forming processes, during which high strains occur [97-100]. Similarly, Raczy et al. [101] developed a finite element model for the orthogonal cutting of copper, where material data was obtained directly from cutting experiments. The material model used in the current finite element analysis of the sliding wear is based on the experimentally determined stress-strain curve of a 356 Al alloy. The stress-strain behaviour was obtained directly from an analysis of the deformation state of material layers located below the contact surface that was subjected to sliding wear [17].

Zhang and Alpas [17] performed dry sliding wear tests using a block-on-ring type wear machine, and tested a 356 Al alloy against a bearing steel. The plastic strains in the subsurface regions were determined by measuring the displacement of a metallographic marker that had been placed perpendicular to the contact surface before

the sliding test. In order to estimate the flow strength of the deformed layers, microhardness measurements were taken at various sliding distances and loads. Low sliding speeds (0.2 m/s) and small normal loads (10 N and 45 N) were chosen so that any frictional temperature increase during sliding remained negligible. Experimental data indicated that the subsurface layers strain hardened steeply, but at equivalent plastic strains larger than 5, the stresses reached a plateau and remained constant. A regression analysis revealed that the flow stress (σ_f) and the equivalent plastic strains (ε) in the deformed zones obeyed an exponential work hardening law—expressed in the form of a Voce type equation [17]:

$$\sigma_f = \left[\sigma_s - (\sigma_s - \sigma_0) \exp\left(-\frac{\varepsilon}{\varepsilon_c}\right) \right] \quad (4.1)$$

where σ_f is the flow stress (effective stress), ε is the equivalent plastic strain, σ_0 (= 240 MPa) is the bulk flow strength and σ_s (= 400 MPa) is the saturation stress (the stress at which the work hardening rate becomes zero). ε_c is a material constant, and was observed to be equal to 4.79 for the 356 Al material. Figure 4.6 presents the curve representing Equation 4.1 and the sixteen data points—obtained from the experimentally determined stress/strain behaviour and entered into LS-DYNA employing an elastic-plastic material type [102]—that were used to discretize the stress/strain relationship. The data points representing the stress/strain relationship of the 356 Al alloy are also listed in Table 4.2. The shear modulus and mass density of the 356 Al material were specified as 27.2 GPa and 2.669 Mg/m³, respectively [17, 91]. The asperities were assumed to be of a rigid material, made of steel with 207 GPa Young’s modulus, 0.3 Poisson’s ratio and 7.8 Mg/m³ density.

When the amplitude of stress waves in a material exceeds the dynamic flow strength, the hydrostatic component of stress dominates [102]. Therefore, when a material model is used to model hydro materials or fluids, it must be accompanied by an equation of state to account for any resistance to hydrostatic stresses. Gruneisen equation of state (EOS) was employed to define the pressure-volume relationship of the 356 Al material. In addition, a linear polynomial EOS was also used in initial trial

simulations. A detailed analysis of the results indicated that the difference between two models using two different EOS was always less than 10% for the loading conditions studied and both EOS could be used in the simulations. The Gruneisen EOS was chosen to complete the simulations, since the constants for the full equation were available from literature (for a comprehensive discussion of the EOS and comparison of the results please refer to Appendix D). The Gruneisen EOS with cubic shock velocity-particle velocity defines pressure for compressed materials as [102]:

$$P = \frac{\rho_0 C_0^2 \psi \left[1 + \left(1 - \frac{\gamma_0}{2}\right) \psi - \frac{b}{2} \psi^2 \right]}{\left[1 - (S_1 - 1) \psi - S_2 \frac{\psi^2}{\psi + 1} - S_3 \frac{\psi^3}{(\psi + 1)^2} \right]^2} + (\gamma_0 + b \psi) E \quad (4.2)$$

and for expanded materials as:

$$P = \rho_0 C_0^2 \psi + (\gamma_0 + b \psi) E \quad (4.3)$$

where E is the energy per unit volume, ρ_0 is the initial density, C_0 is the bulk sound speed, γ_0 is the initial value of Gruneisen's gamma, b is the coefficient of the volume dependence of gamma and S_1 , S_2 and S_3 are the linear, quadratic and cubic coefficients, respectively. ψ is the compression defined as:

$$\psi = \frac{\rho}{\rho_0} - 1 \quad (4.4)$$

where ρ is the density of the material. In order to implement the Gruneisen EOS into the finite element model, the required parameters of C_0 , S_1 , S_2 , S_3 , γ_0 and b were

Reproduced with permission of the copyright owner. Further reproduction prohibited without permission.

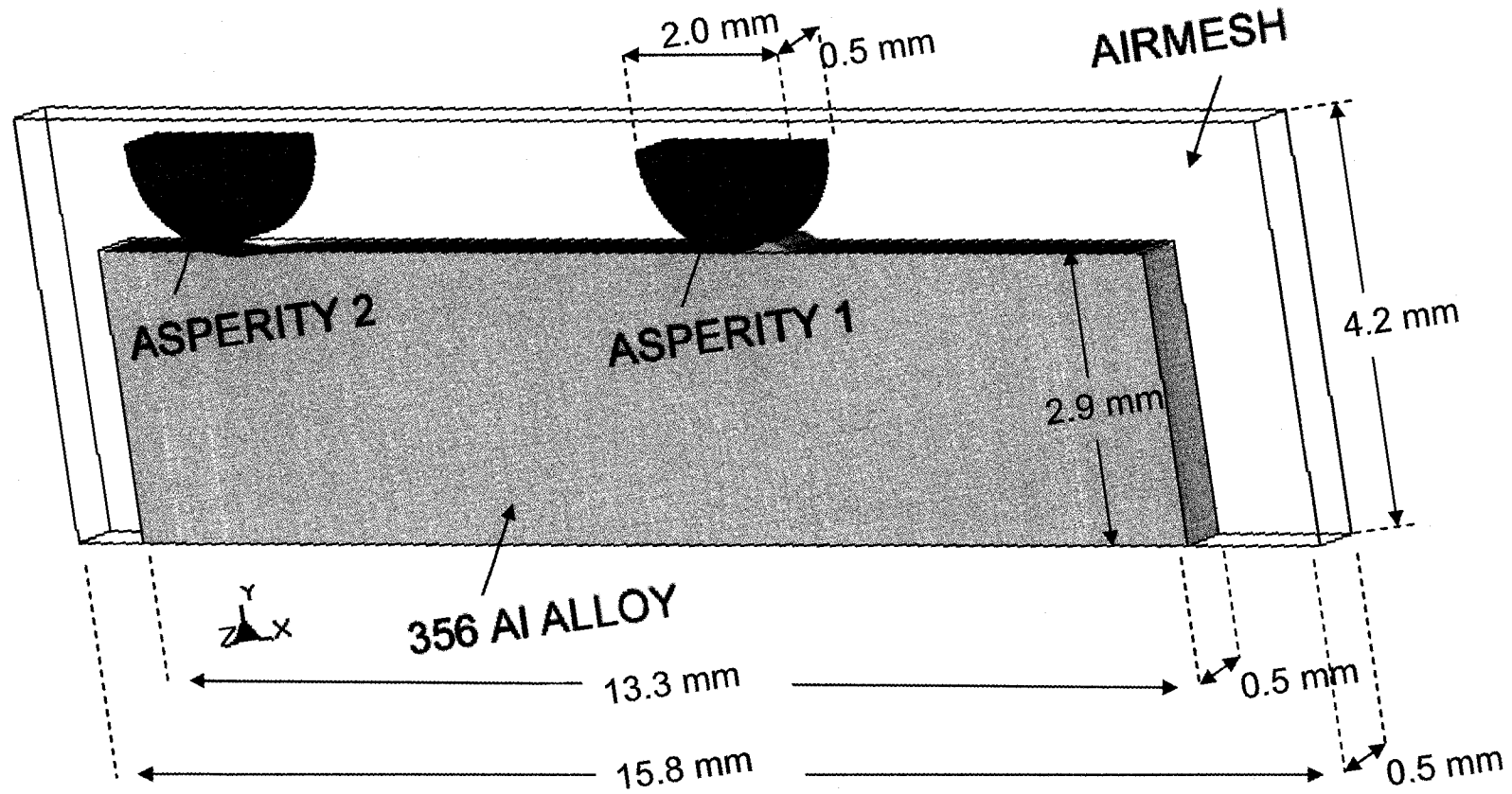


Figure 4.4: General view of the multiple asperity contacts model (The first asperity is shown during sliding while the following asperity is at rest).

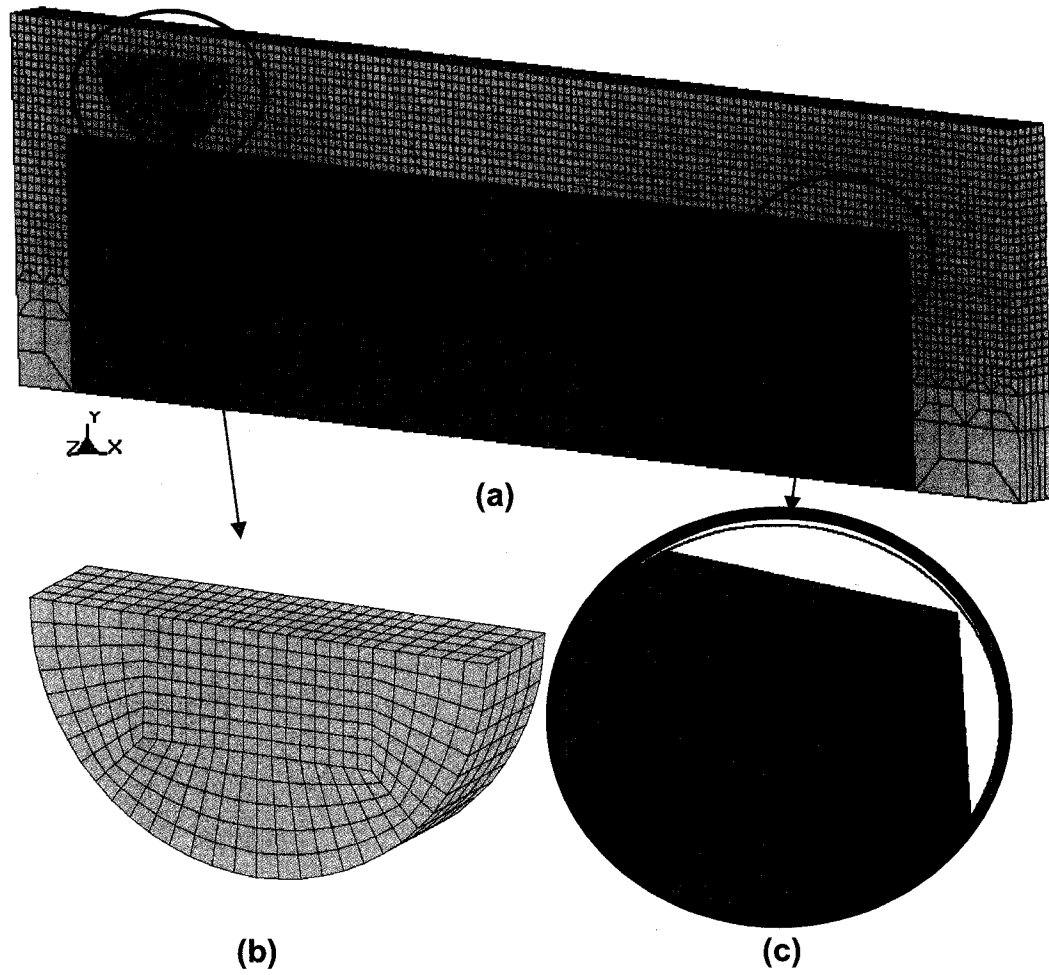


Figure 4.5: Mesh generated for the finite element model: (a) the complete mesh, (b) the asperity and (c) part of the 356 Al structure closer to the contact surface.

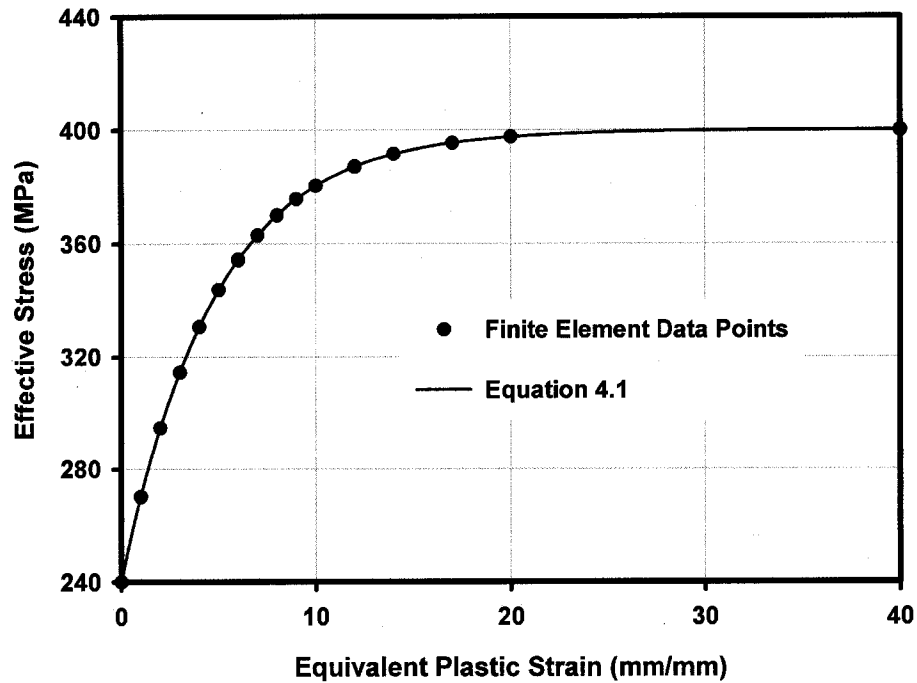


Figure 4.6: Experimentally determined stress/strain behaviour of the 356 Al alloy and the data points used to discretize it in the finite element material model.

Table 4.2: Data points used to discretize the experimentally determined stress/strain relationship of the 356 Al alloy.

Equivalent Plastic Strain (mm/mm)	Effective Stress (MPa)
0.0	240.0
1.0	270.1
2.0	294.6
3.0	314.5
4.0	330.6
5.0	343.7
6.0	354.3
7.0	362.9
8.0	369.8
9.0	375.5
10.0	380.2
12.0	386.9
14.0	391.4
17.0	395.4
20.0	397.5
40.0	399.9

obtained from Steinberg [103] for the 356 Al alloy. Table 4.3 lists the EOS parameters used in the numerical model.

4.2.4. LOADING AND BOUNDARY CONDITIONS

The steel asperity was indented on the 356 Al surface by applying a constant normal load in the Y direction. The applied normal load was distributed equally on each node located at the top layer of the asperity—as illustrated in Figure 4.7. In order to keep the 356 Al alloy stationary, all nodes at the bottom of the 356 Al structure were constrained in all degrees of freedom (DOF) (X translation, Y translation, Z translation, X rotation, Y rotation and Z rotation). A plane of X-Y symmetry (restricting Z translation, X rotation and Y rotation) was assigned to the nodes on the 356 Al surfaces parallel to the X-Y plane in order to provide a thicker modeling of the 356 Al structure. Figure 4.8 shows the boundary conditions and the symmetry axes assigned in the numerical model.

Sliding velocities ranging from 0.5 m/s to 40 m/s were assigned to the asperities in the X direction. Loading was specified in such a way that the asperities were first loaded with a constant normal load, then translated with a constant sliding velocity over the 356 Al surface.

4.2.5. CONTACT ALGORITHM

Contact between the asperities, and the aluminum entity was numerically implemented using a penalty-type contact algorithm in LS-DYNA [102]. The asperities were designated as slave entities, while the 356 Al surface and the airmesh were defined as master entities for the numerical contact. Contact coupling was determined in the normal direction by using 4 x 4 x 4 coupling points distributed over each Lagrangian slave entity [102]. Coupling points represent the nodes located at the Gauss points of the asperities, which were checked for penetration into the 356 Al structure. Due to the excessive nodal penetrations observed in initial trial simulations, the default value of the penalty scale factor was increased from 0.1, to 3.0 for the numerical models.

The coefficient of friction for contact between the asperities and the aluminum entity was initially specified as zero in the contact algorithm, assuming that the frictional effects were already included within the experimentally determined local stresses and

strains used in the numerical material model. To investigate the effect of additional friction on the subsurface stresses and strains during multiple sliding contacts, several coefficients of friction (μ) ranging from 0.0, to 0.8 were considered in the contact algorithm.

4.3. EFFECTS OF TEMPERATURE AND STRAIN RATE ON THE SUBSURFACE DAMAGE

Strain rate and thermal effects were considered in an analysis that coupled thermal and structural finite element analyses, and the temperature increase in sliding materials was investigated. This section presents a Lagrangian explicit dynamic numerical model that accounts for the strain hardening, thermal softening and the strain rate hardening of the aluminum alloy. The Eulerian finite element model provided in the previous section could not be used in the modeling of thermal and strain rate effects on the subsurface damage, since the thermal and structural solvers are not coupled in LS-DYNA for the Eulerian element formulation. Coupling the thermal and structural solutions for the Eulerian elements is a significant numerical challenge that had yet to be addressed in any of the commercial finite element analysis programs. Therefore, the developed finite element model was modified to use a Lagrangian element formulation for the 356 Al alloy. Appendix E contains a sample finite element input file for the coupled thermal and structural sliding contact analysis.

Table 4.3: EOS parameters for the 356 Al alloy obtained from Steinberg [103].

Parameter	Value
C_0	0.535 cm/ μ s
S_1	1.338
S_2	0.0
S_3	0.0
γ_0	1.97
b	0.48

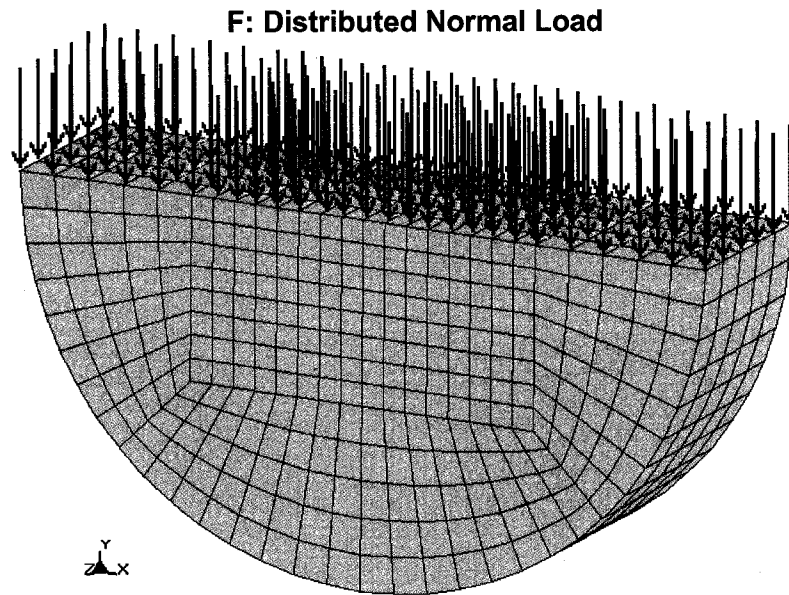


Figure 4.7: Distribution of the normal load equally on each node located at the top layer of the asperity.

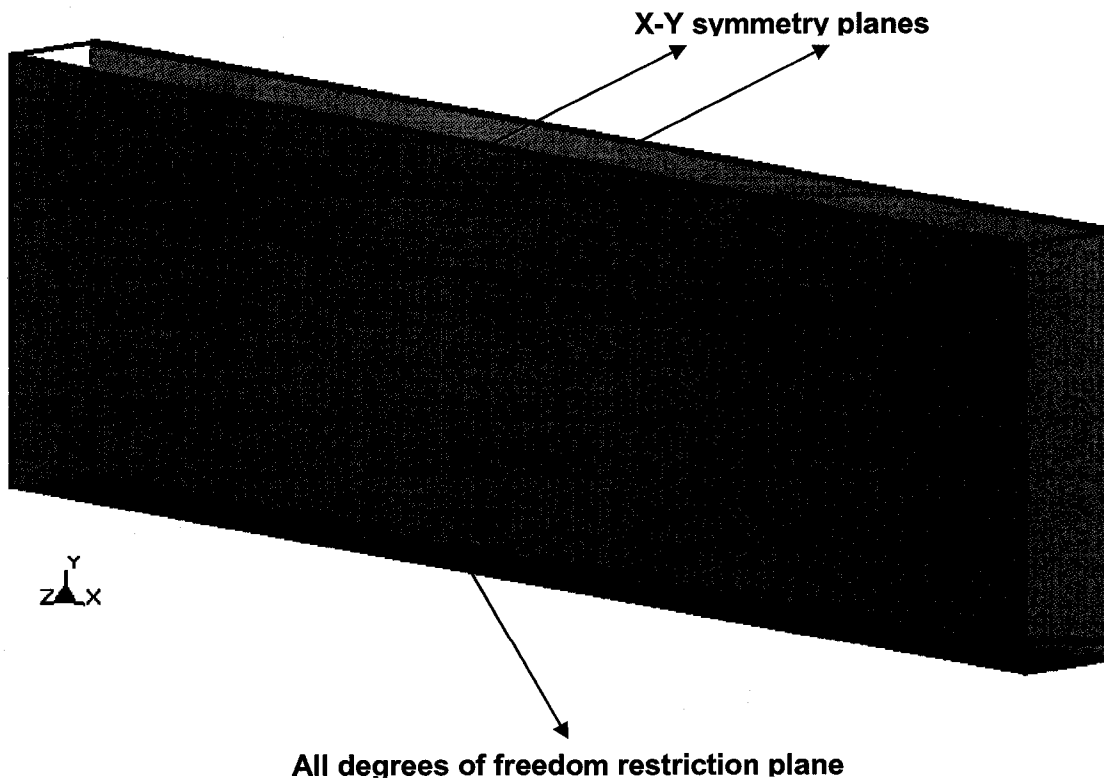


Figure 4.8: Boundary conditions and symmetry axes.

4.3.1. FE MODEL GEOMETRY

The finite element model used in the coupled thermo-mechanical analysis of the sliding contact consisted of two main parts: the Al-Si half-space, and the steel asperities. The geometry and the mesh of the model were similar to that used in the Eulerian model (Section 4.2). The sliding contact was modeled by pressing a rigid, cylindrically shaped steel surface—2.0mm diameter—against a 356 Al surface of 2.9 x 13.3 mm² and then sliding the asperity over the half-space surface repeatedly at a constant sliding velocity. The third dimension of the model was assumed to be infinite (plane strain condition). A schematic view of the set-up is shown in Figure 4.9.

4.3.2. ELEMENT FORMULATION AND PROPERTIES

3D Lagrangian solid elements of the plane strain element formulation were used with four Gaussian integration points [102]. Eight Gaussian points per element were specified for the thermal analysis calculations. Meshes at the contact region were carefully discretized with aspect ratios of unity. The minimum element size utilized in the vicinity of the contact region was 0.02mm. Each steel counterface was discretized with 1530 elements and 1618 nodes. In the discretization of the 356 Al half-space, 10,825 elements and 11,076 nodes were used.

4.3.3. MATERIAL MODEL

Strain rate and thermal effects were taken into account in the numerical material model using a special material type in LS-DYNA that allows the user to define an elastic-plastic stress-strain relationship that incorporates thermal and strain rate effects. Consequently, the stress-strain behaviour of the material below the contact surfaces can be modeled for conditions where the temperature and rate at which the layers deform (strain rate) are important. A constitutive equation—consisting of the experimentally defined Voce-type stress-strain relationship (Equation 4.1)—combined with a Cowper and Symond-type [82] strain rate equation and a Johnson-Cook-type [85] temperature equation, was proposed:

$$\sigma_f = \left[\sigma_s - (\sigma_s - \sigma_0) \exp\left(-\frac{\epsilon}{\epsilon_C}\right) \right] \left[1 + \left(\frac{\dot{\epsilon}^p}{D}\right)^{1/q} \right] \left[1 - \left(\frac{T - T_{room}}{T_{melt} - T_{room}}\right)^m \right] \quad (4.5)$$

where $\dot{\epsilon}^p$ is the plastic strain rate in s^{-1} units, D (s^{-1}) and q are the Cowper and Symond material parameters. T (K) is the temperature of the contacting material, T_{room} is the room temperature (K), T_{melt} is the melting temperature (K) and m is the dimensionless Johnson-Cook thermal material parameter. In Equation 4.5, the expression in the first set of brackets represents the strain hardening behaviour under athermal conditions. The expressions in the second and third sets of brackets represent the strain rate hardening and the thermal softening effects on the flow stress (σ_f). Different constitutive equations were proposed in the literature for the strain rate sensitivity of materials. The Cowper and Symond constitutive equation is one of the most commonly used equations for large deformation type problems, especially when dealing with automotive applications [84]. The material parameters in Equation 4.5—taken from the literature—were $D = 500 s^{-1}$ and $q = 4$ for the 356 Al alloy [84]. The temperature coefficients were taken from the work of Johnson and Cook [85] who used torsion and dynamic tensile Hopkinson bar tests to determine the dependence of the flow stress of materials to temperature. The thermal material parameter (m) was determined as 1 for different aluminum alloys. In addition, investigations in Section 2.3.3 indicated that the thermal material parameter is not constant, and changes with the temperature. However, it was also shown that m is between 0.85-1.00 up to 150 °C for the A356 Al alloy. Therefore, m was defined as 1.00 for the A356 Al alloy in this study's numerical simulations. The initial room temperature and the melting temperature of the 356 Al were 300 K and 828 K, respectively.

Figure 4.10 illustrates the relationships among stress, strain and temperature at various strain rates. A zero strain rate implies that during sliding, the material layers below the worn surfaces were not subjected to a strain rate that exceeded the experimentally applied strain rate. Thus, in Figure 4.10 the stress-strain curve at 300 K and $\dot{\epsilon} = 0 s^{-1}$ is identical to the experimental stress-strain curve of the 356 Al alloy's worn surfaces in Figure 4.6.

Young's modulus (E), Poisson's ratio (ν) and mass density (ρ) of the 356 Al half-space were 72.4 GPa, 0.33 and 2.669 Mg/m³ [17, 91]. The steel asperities were modelled as rigid materials, and the properties of the asperities were E = 207 GPa, $\nu = 0.3$ and $\rho = 7.8$ Mg/m³.

During sliding contact of the solids, most of the plastic work done is converted into heat [104]. The fraction of plastic work converted into heat can be estimated using calorimetric methods [105]. Mason et al. [106] used a Hopkinson pressure bar coupled with infrared detectors to examine the conversion rate of plastic work to heat. The work rate to heat rate conversion fraction values for steel and aluminum alloy samples were between 0.85 and 0.95. Here 0.95 of the mechanical work was assumed to be converted into heat. The thermal material properties of the 356 Al alloy were determined from the literature and defined in an isotropic thermal material model as follows; heat capacity: 963 J/kg·K, thermal conductivity: 151 W/m·K and coefficient of thermal expansion: 23.5 $\mu\text{m/m}\cdot\text{K}$ [91].

The temperature rise during sliding is calculated using the following equation [102, 104]:

$$\Delta T = \frac{\beta}{\rho C_P} \int_0^{\varepsilon_f} \sigma_f d\varepsilon \quad (4.6)$$

where $T (= T(x_i, t))$ is temperature, $x_i (= x_i(t))$ are coordinates as a function of time, β is the work rate to heat rate conversion factor (defined as 0.95 in this study), $\rho (= \rho(x_i))$ is the density and $C_P (= C_P(x_i, T))$ is the specific heat.

The flow stress in Equation 4.6 is calculated from Equation 4.5. In order to test the effects of the material model on the prediction of deformation, the following constitutive equations were also used:

$$\sigma_f = \left[\sigma_s - (\sigma_s - \sigma_0) \exp\left(-\frac{\varepsilon}{\varepsilon_C}\right) \right] \quad (4.7)$$

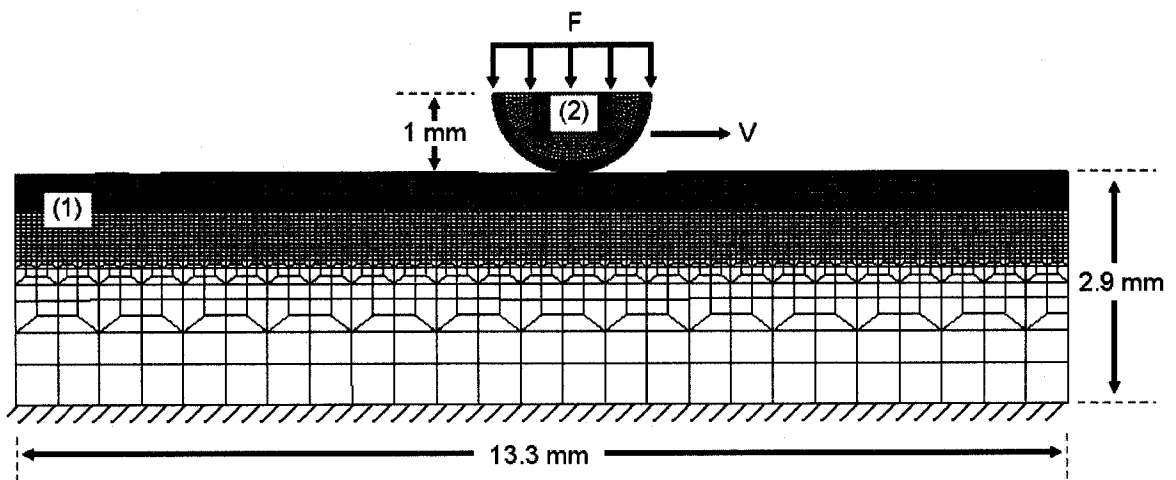


Figure 4.9: Geometry of the finite element model ((1) is the 356 Al half-space and (2) is the steel counterface), loading (F: Distributed normal load, V: Sliding velocity) and boundary conditions (restriction of the bottom nodes from the motion).

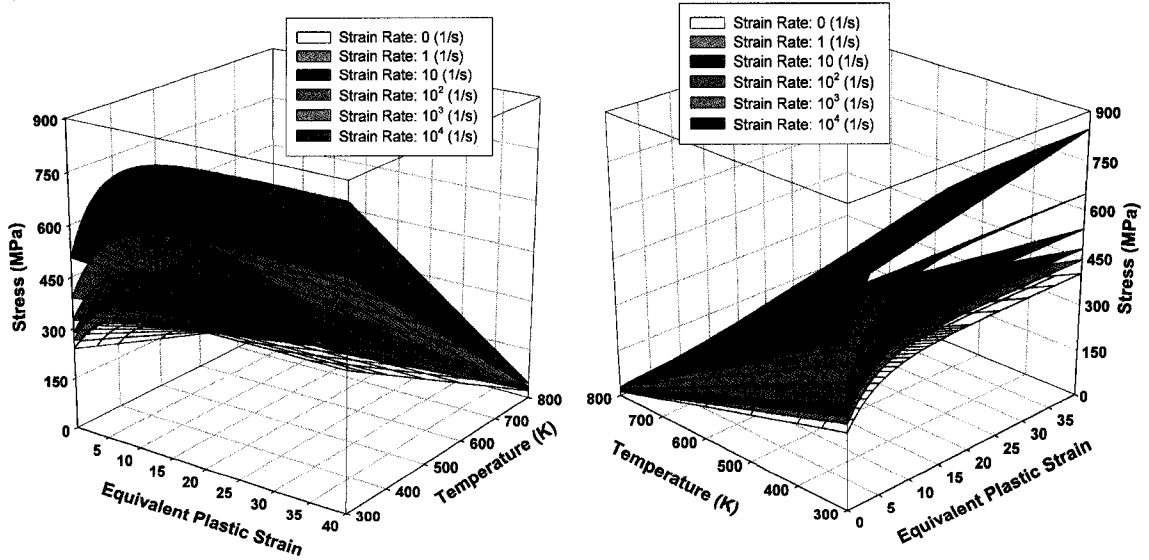
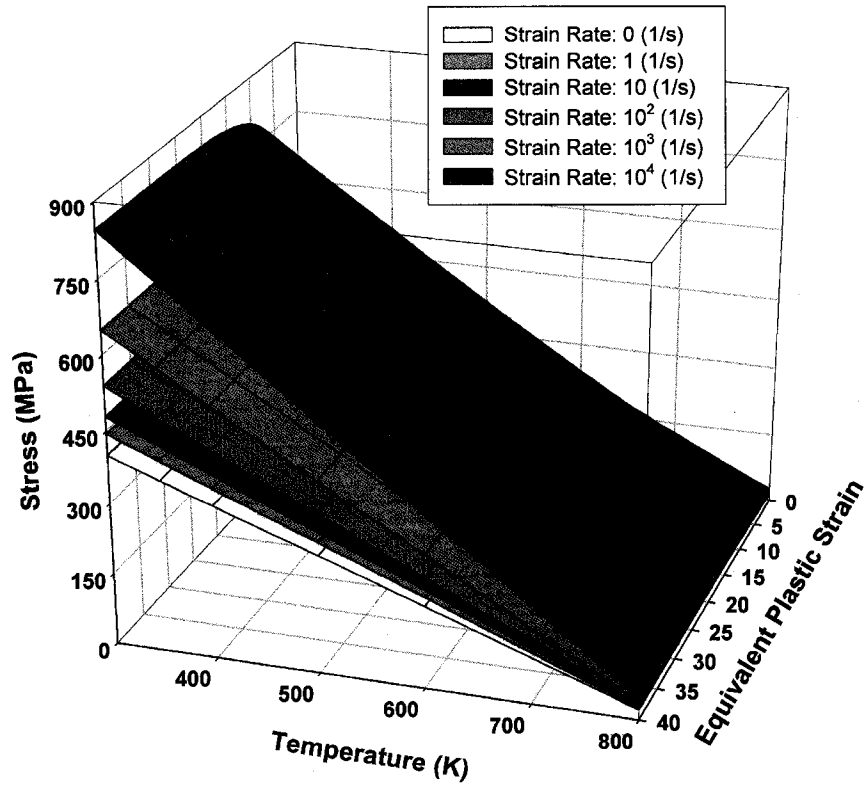


Figure 4.10: The relationship among stress, strain, strain rate and temperature according to Equation 4.5.

$$\sigma_f = \left[\sigma_s - (\sigma_s - \sigma_0) \exp\left(-\frac{\varepsilon}{\varepsilon_C}\right) \right] \left[1 + \left(\frac{\dot{\varepsilon}^p}{D}\right)^{1/q} \right] \quad (4.8)$$

$$\sigma_f = \left[\sigma_s - (\sigma_s - \sigma_0) \exp\left(-\frac{\varepsilon}{\varepsilon_C}\right) \right] \left[1 - \left(\frac{T - T_{room}}{T_{melt} - T_{room}}\right)^m \right] \quad (4.9)$$

Deformation induced temperature calculated by equation 4.6 is conducted inside the aluminum alloy by the following heat conduction equation [102, 104]:

$$\rho C_p \frac{\partial T}{\partial t} = (k_{ij} T_{,j})_{,i} + Q \quad (4.10)$$

where k_{ij} ($= k_{ij}(x_i, T)$) is the thermal conductivity and Q ($= Q(x_i, T)$) is internal heat generation rate per unit volume.

4.3.4. LOADING AND BOUNDARY CONDITIONS

The steel, semi-cylindrical asperity was pressed against the aluminum half-space with a constant normal load in the Y direction (Figure 4.9). Analyses were done for two normal load levels of 150 and 250 N per mm thickness. The applied normal load was distributed equally on each node located at the top layer of the asperity (Figure 4.9). All nodes at the bottom of the 356 Al half-space were constrained in all degrees of freedom (Figure 4.9).

Two sliding velocities of 5 m/s and 10 m/s in the X direction were assigned to the steel asperity motion. Loading was prescribed in such a way that during each contact cycle, the asperity was first loaded with a constant normal load, then translated with a constant sliding velocity over the half-space surface.

In initial trial simulations, heat convection and radiation to surroundings were considered. However, the results indicated that effect of those terms on the solution were negligible. Therefore, in order to decrease solution times, heat convection and radiation to the surroundings are neglected and adiabatic thermal boundary conditions

were applied to the half-space. Both thermal and structural calculations were completed by doing a transient time dependent analysis [102]. An explicit dynamic time integration approach was used for the structural analysis, and a fully implicit time integration scheme was utilized for the thermal analysis calculations [102]. For every ten explicit structural time steps completed, a thermal implicit time step calculation was performed.

4.3.5. CONTACT ALGORITHM

Contact between the steel and the aluminum entities was modeled using a two-dimensional automatic type contact algorithm, with the thermal option [102]. The 356 Al half-space was designated as the slave entity, while the steel counterfaces were defined as the master entities for the numerical contact. Due to the excessive nodal penetrations observed in initial trial simulations, the default value of the penalty scale factor was increased from 1.0 to 5.0 for the numerical models. In order to achieve a stable simulation, the time step was lowered by changing the time step scale factor from the default value of 0.9, to one of 0.8.

Initially, the coefficient of friction between the steel and aluminum entities was defined as zero in the contact algorithm. To investigate the effect of friction on the subsurface stresses and strains during multiple sliding contacts, 0.3 coefficient of friction (μ) was also considered in the contact algorithm. Friction was modeled as a constant during the simulations by making the static and dynamic coefficients of friction identical.

4.4. EFFECTS OF SECONDARY HARD PARTICLES ON THE SUBSURFACE DAMAGE

Si particles of various sizes embedded below the 356 Al surface were studied in a Lagrangian finite element analysis that coupled structural and thermal elements in an attempt to investigate the influence of the hard particles on the distribution of subsurface stresses and strains in the aluminum matrix. This section presents the numerical setup details exploring the effects of secondary hard particles on subsurface damage. A detailed discussion of the developed model was presented in Section 4.3. The computation procedures were the same as the ones used in the previous section, with

the exception of new features designed to consider Si particles—such as the addition of a new material model for the Si particles. Another important change was the reduction of the time step scale factor from 0.9, down to 0.5 with the purpose of obtaining a good energy distribution and stable simulations. In the following sections, only these added features will be presented. A sample finite element input file is summarized in Appendix F.

4.4.1. FE MODEL GEOMETRY

The numerical model consisted of three parts with the implementation of hard particles; the 356 Al half-space, the asperities and the Si particle. The dimensions of the 356 Al half-space and asperities were the same as Section 4.3 presented. A typical microstructure of the 356 Al alloy after the heat treatment is shown in Figure 4.11 where the Al and Si phases can be observed. Two distinct Si particle morphologies are illustrated in Figure 4.11—one that is spherical equiaxed shaped, and one that is long and needle shaped. The aspect ratio of the needle-like particles could be approximately as large as five or six. In order to consider various Si particle morphologies, three different cross-sectional geometries were created in the finite element model: one square shaped with an aspect ratio of 0.75, one rectangular shaped with an aspect ratio of 2.25 and one circular equiaxed shaped with an aspect ratio of 1.0. All the Si particles in this study, despite different geometries, were placed at a constant depth below the surface. Schematic views of the numerical set-up for the hard particles are shown in Figures 4.12 and 4.13. The third dimension of the model was assumed to be infinite, and thus plane strain conditions were investigated.

4.4.2. ELEMENT FORMULATION AND PROPERTIES

The numerical model only utilized 2D solid elements. The Lagrangian plane strain element formulation was used, with four integration points, and eight Gaussian points were used for the thermal analysis calculations. The minimum element size was 0.02mm for the models with rectangular and square shaped Si particles. The circular Si particle was discretized very finely to represent curved boundaries with a 0.004 mm

minimum element size. The discretization properties of the models are listed in Table 4.4.

4.4.3. MATERIAL MODEL

The material model developed and discussed in Section 4.3 that accounts for strain hardening, strain rate hardening and thermal softening of the 356 Al Alloy was also used in this numerical analysis. The details of the material model's characteristics for the 356 Al alloy and rigid asperities were presented in Section 4.3. The Si particles were modeled as elastic materials, and the elastic modulus, Poisson's ratio and mass density of the Si particles were specified as 112.7 GPa, 0.28 and 2.33 Mg/m³, respectively [91, 107-109].

4.4.4. LOADING AND BOUNDARY CONDITIONS

A sliding velocity of 10 m/s and a normal load of 250 N/mm were applied to the asperities. The loading and boundary conditions—discussed in detail in Section 4.3—were adopted for the hard particle investigation models. Multiple investigations determined that the interface strengths of different matrix-particle systems range from 1000 MPa to 3000 MPa [39-43]. In addition, Gall et al. [110] studied the tensile debonding of an aluminum-silicon interface using modified embedded atom method atomistic simulations and identified the Al-Si interface strength to be 20 GPa. This high interface strength value was caused by their model's assumptions—including defect and impurity-free interfaces—and by the limitations of the current atomistic modeling efforts. However, in the initial simulations of this study with Si particles, the stresses at the Al-Si interface and at the Si particles did not reach the strength levels given in the literature. Therefore, the interface between the Al matrix and the Si particle was assumed to be infinitely strong, and the nodes were merged at the interface of the two materials. By this way, evolution of local stress and strain distributions were aimed to be studied without implementation of any predetermined failure constraint on the model.

Table 4.4: Total number of elements and nodes used in the discretization of the finite element models.

Model	Part	# of Elements	# of Nodes	Minimum Element Size (mm)
A, B, C	Asperities	1,530	1,618	0.020
A	356 Al surface	10,816	11,072	0.025
A	Square Si particle	9	16	0.025
B	356 Al surface	10,783	11,050	0.025
B	Rectangular Si particle	42	60	0.025
C	356 Al surface	10,919	1,185	0.025
C	Circular Si particle	260	281	0.004

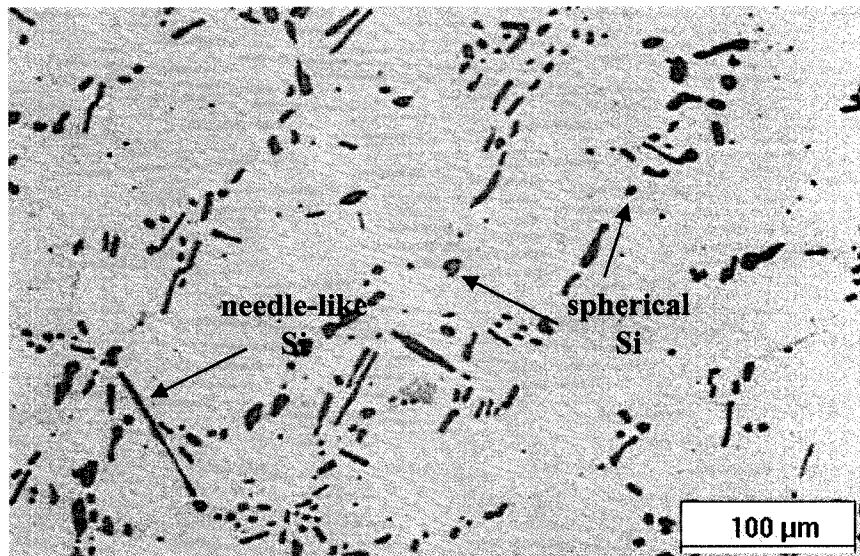


Figure 4.11: A typical microstructure observed in a 356 Al alloy after T6 heat treatment.

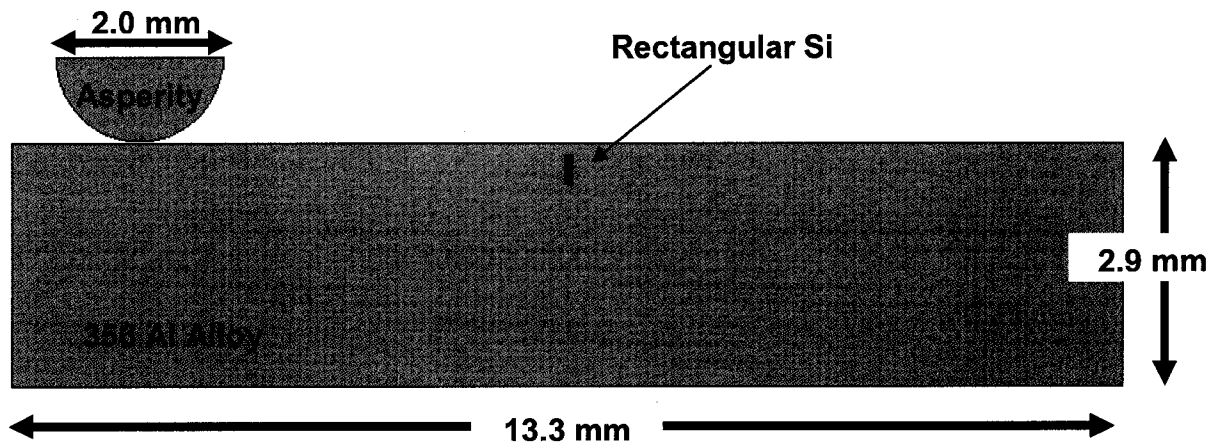


Figure 4.12: General view of the finite element model developed for the investigation of influence of the hard particles.

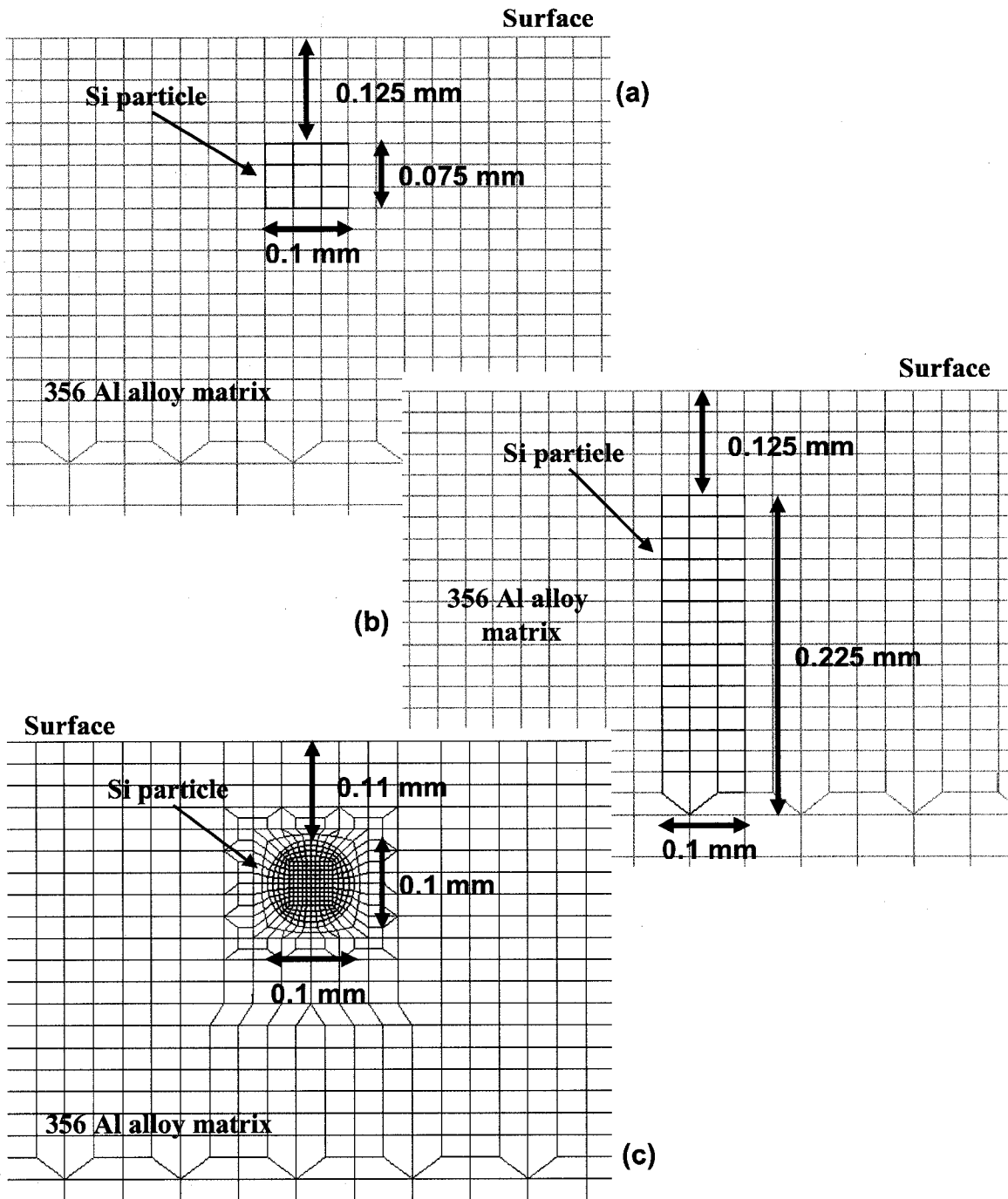


Figure 4.13. Geometric details of the finite element model for the hard particles: (a) square shaped Si particle, (b) rectangular shaped Si particle and (c) circular shaped Si particle.

CHAPTER 5

EXPERIMENTAL PROCEDURES

Despite the fact that the numerical models used in this study were built on an aluminum alloy's stress-strain relationship—obtained from sliding wear tests—the accuracy of the finite element results were not assured. In order to test the accuracy of the numerical models, normal contact and sliding contact experiments were performed using similar geometry, and the experimental observations were compared with the predictions of the numerical models. This section presents the details of the experimental tests, performed for this purpose.

5.1. NORMAL AND SLIDING CONTACT EXPERIMENTS

5.1.1. SAMPLE MATERIALS

A 356 aluminum alloy with a composition 7.00 % Si, 0.35 % Mg, 0.11 % Fe, 0.20 % Ti, 0.05 % Mn, 0.05 % Zn and the balance Al [91] was used in the experiments. The material was received in as-cast condition, solution treated at 813 K for 36 hours and aged to T6 condition at 428 K for 5 hours. Figure 5.1 provides optical microscopy images of 356 Al sample microstructures after several steps of the heat treatment. The long, planar-shaped secondary particles transformed, taking on a more equiaxed shape when subjected to increasing solution treatment time. The hardness of the heat-treated 356 Al samples was measured as 50.6 ± 2.0 by Rockwell hardness (HRB, 15kg, 1/16", superficial) and 84.1 ± 1.5 by Vickers hardness (50 g). Cylindrical M2 tool steel samples with a diameter of 2 mm were utilized as counterface material against the 356 Al alloy. M2 tool steel samples were received in heat-treated condition with 60 to 63 HRC hardness.

5.1.2. EXPERIMENTAL SET UP

M2 tool steels were pressed against the 356 Al samples at different loads that ranged from 306 to 390 N/mm, at which point the impressions left on the 356 Al were investigated. Figure 5.2 shows photographs of the samples that were subjected to normal contact. The 356 Al samples were polished before the indentation testing, and the deformation patterns created at the edge of the samples as a result of the tests were determined as an estimation of the plastic deformation. Figure 5.3 (a) illustrates the deformation zone on the edge of the 356 Al that was tested using a normal load of 335.82 N/mm. The plastic deformation zone depth and width—determined in this way—were compared to the values predicted by numerical models of appropriate loading (Figure 5.3 (b)). A WYKO HD 3300 optical surface profilometer was used to inspect indentation impressions on the 356 Al surface. Figure 5.4 shows a sample surface profile with the contact length and depth clearly indicated. The measured contact length and depth were later compared to the numerical contact predictions. 8 to 10 measurements were performed for each length and width measurement, with the average values presented in Chapter 6.

A reciprocating sliding wear machine was used to conduct the sliding experiments. Figure 5.5 displays a photograph of the reciprocating sliding machine in which specimen holders, load application and sliding direction is clearly indicated. To measure the subsurface sliding displacements of the 356 Al samples, a metallographic reference marker method was used [3, 4 and 17]. A marker machined from the same material as the test sample was introduced in a slit cut perpendicular to the contact surface [Figure 5.6 (a)]. M2 tool steels were subjected to uniaxial sliding contact up to seven times over the 356 Al samples of 70 mm length with a constant load of 250 N/mm and a sliding velocity of 0.15 m/s. After each sliding contact test, the forward displacements of the marker boundaries were measured and used to estimate the shear strain gradients, which were compared with the plastic strain predictions of the finite element model in Chapter 6. Figure 5.6 (b) is a micrograph of a 356 Al sample after four consecutive sliding tests at a sliding velocity of 0.15 m/s and a normal load of 250 N/mm.

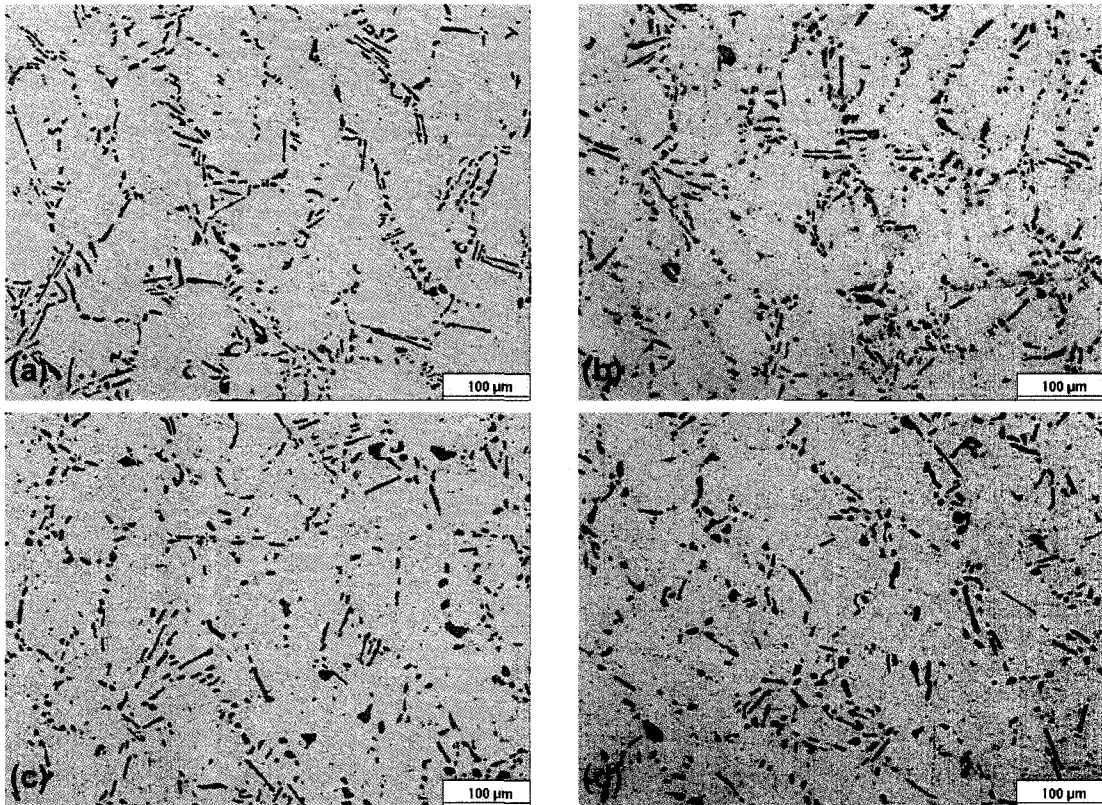


Figure 5.1: Microstructure of the 356 Al samples: (a) after a solution treatment of 12 hours at 813 K, (b) after a solution treatment of 24 hours at 813 K, (c) after a solution treatment of 36 hours at 813 K (35.0 ± 2.5 HRB, 74.5 ± 6.0 Vickers hardness) and (d) after a solution treatment of 36 hours at 813 K and an aging heat treatment of 5 hours at 428 K (50.6 ± 2.0 HRB, 84.1 ± 1.5 Vickers hardness).

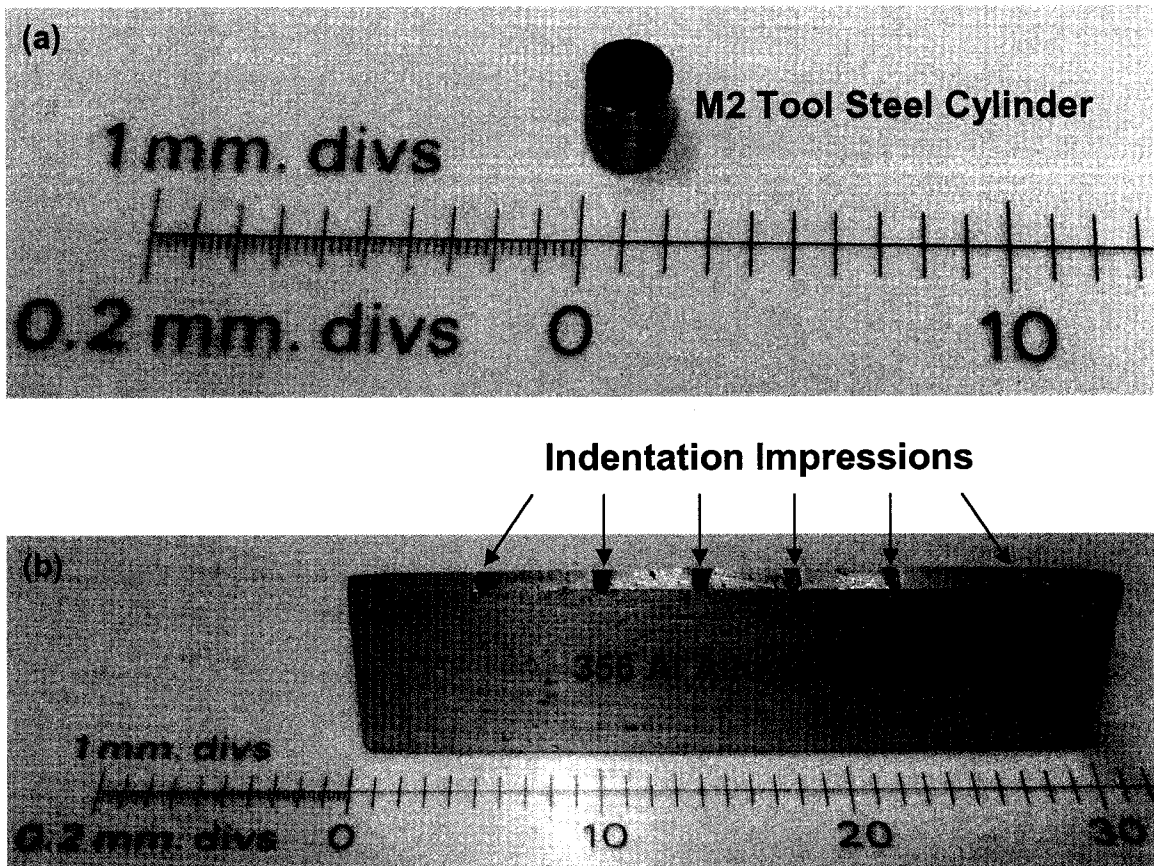


Figure 5.2: Views of the normal contact samples: (a) 2mm diameter M2 tool steel cylinder and (b) the 356 Al sample after several normal contacts (indentations).

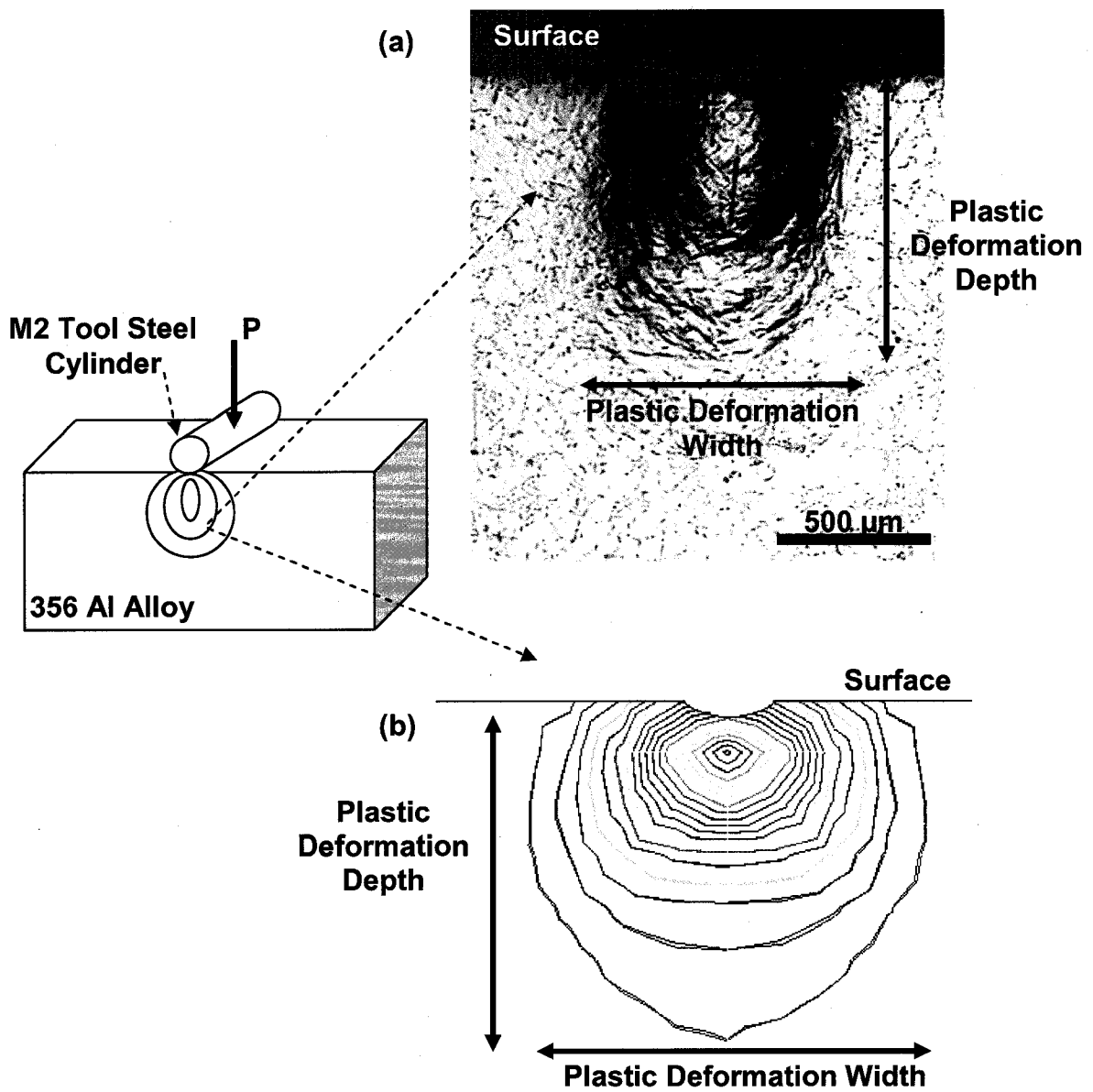


Figure 5.3: (a) Surface profile obtained by optical surface profilometer: Determination of the plastic deformation characteristics (plastic deformation width and depth) from the experimental studies (Load: 335.8 N/mm),
 (b) Determination of the plastic deformation characteristics (plastic deformation width and depth) from the numerical studies (Load: 335.82 N/mm).

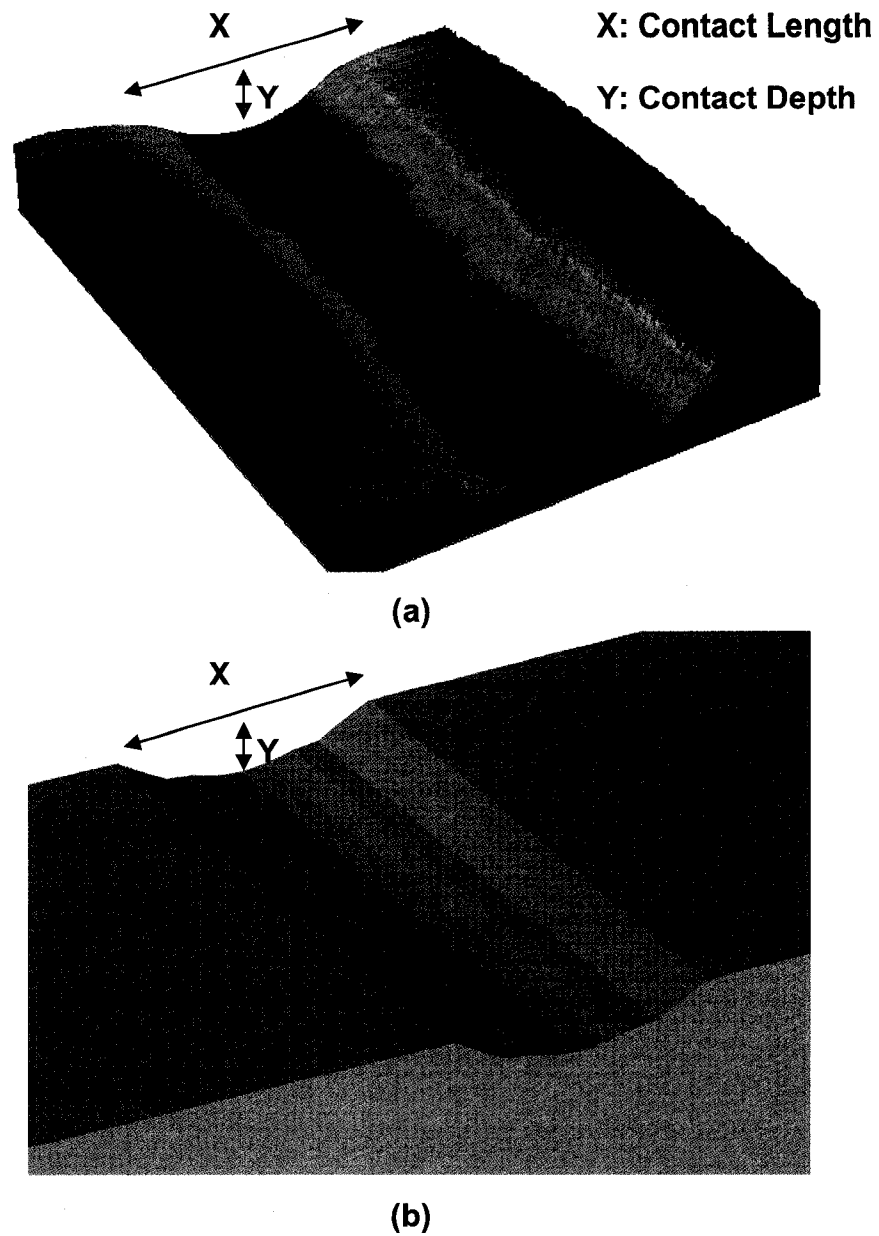


Figure 5.4: (a) Surface profile obtained by optical surface profilometer: Determination of the contact characteristics (contact length and depth) from the experimental studies (Load: 335.82 N/mm),
 (b) Determination of the plastic deformation characteristics (contact length and depth) from the numerical studies (Load: 335.82 N/mm).

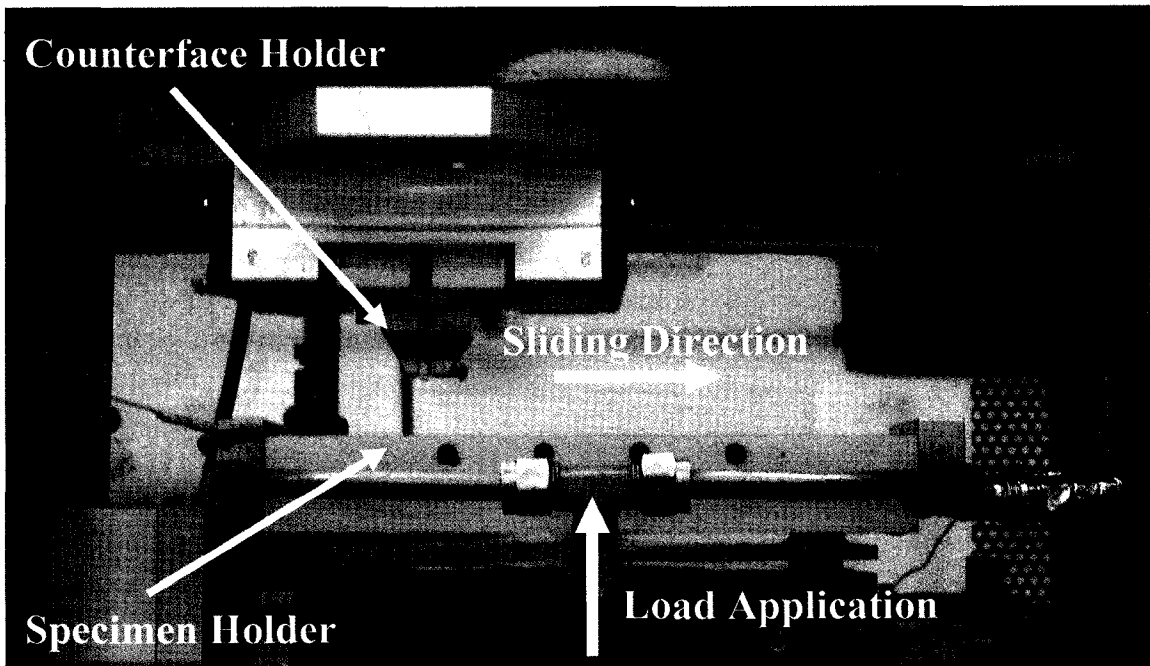


Figure 5.5: Photograph of the reciprocating wear machine with its specimen holders used in sliding contact experiments.

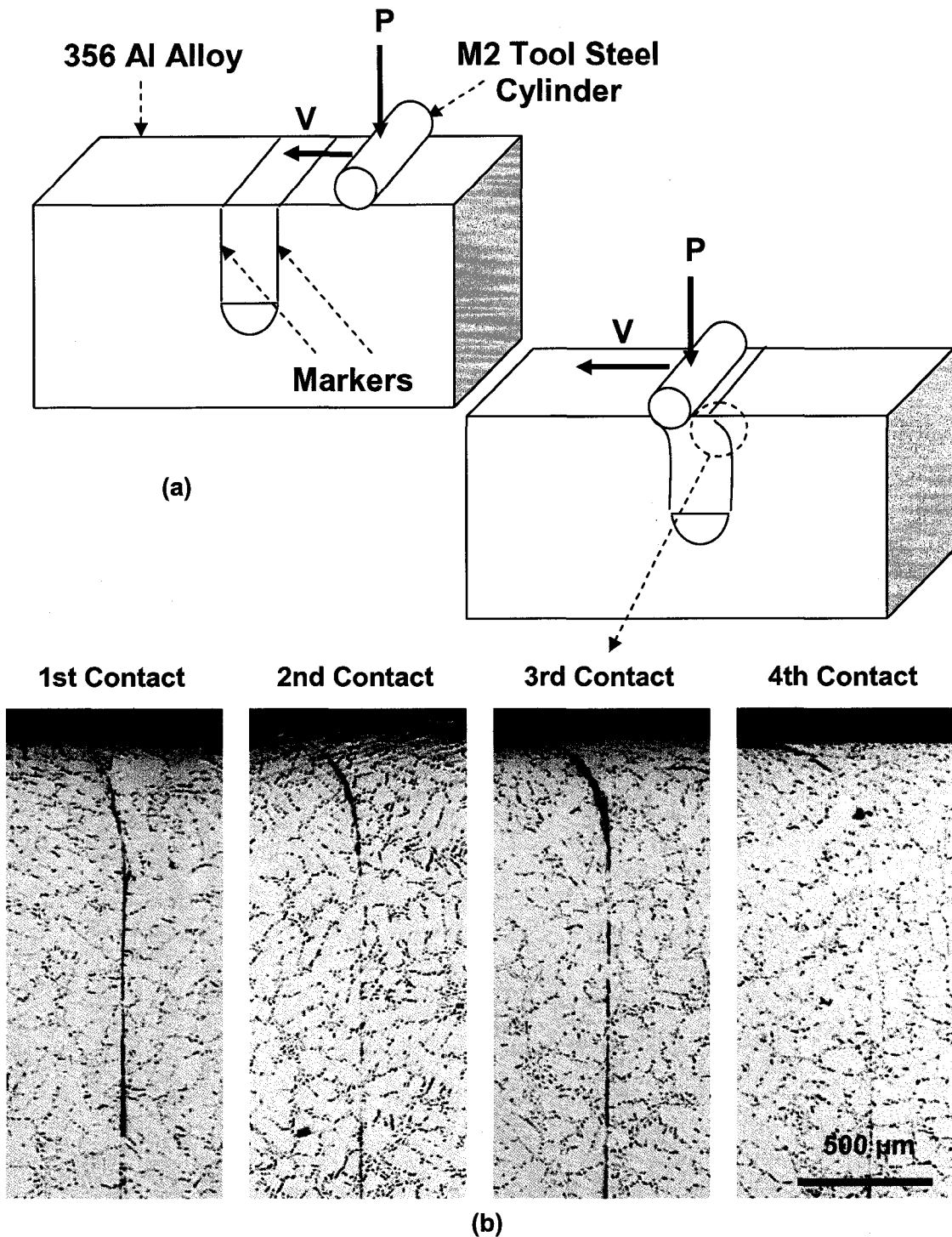


Figure 5.6: (a) Schematic view of the sliding contact samples: the 356 Al, M2 tool steel cylinders and markers.

(b) Subsurface micrograph showing displacement of the marker after multiple sliding contacts (sliding velocity: 0.15 m/s, normal load: 300 N/mm).

5.2. TEMPERATURE MEASUREMENT DURING SLIDING

Sliding contact experiments that included temperature measurements were completed in order to explore thermal softening constitutive equation, which was proposed in the numerical modeling of this work (Section 4.3), applicability to wear test conditions. The resulting experimental observations were compared with predictions of the thermal softening model. This section presents the experimental setup used for this purpose.

5.2.1. SAMPLE MATERIALS

Commercial purity 1100 Al samples were used in the wear experiments. Dry sliding wear tests were performed to test 1100 Al samples against SAE 52100 bearing steel rings (outer diameter = 38 mm, width = 12 mm). 1100 Al test samples were machined into 5 mm x 10 mm x 10 mm rectangular blocks and the samples and the rings were polished to 0.5 μm alumina, then cleaned ultrasonically with methanol before the wear tests.

5.2.2. EXPERIMENTAL SET UP

Dry wear tests were performed using a block-on-ring type wear machine. A schematic view of the block-on-ring wear test setup is shown in Figure 5.7. The specimens were tested in a controlled air atmosphere (20.5 % relative humidity) at a sliding speed of 1 m/s. 10 N and 30 N normal loads were applied, and the temperature of the contact surfaces was continuously measured during the tests using a thermocouple, then recorded with a data acquisition system.

A metallographic reference marker method was used to measure the 1100 Al samples' subsurface sliding displacements [3, 4 and 17]. A marker machined from the same material as the test sample was introduced into a slit cut perpendicular to the contact surface. After wear tests, the forward displacements of the marker boundaries were measured and used to estimate the shear strain gradients. Figure 5.8 shows a micrograph of an 1100 Al sample after the wear test with a sliding velocity of 1 m/s and normal load of 30 N.

The hardness distributions under the worn surfaces were measured using a Vickers microhardness tester with a load of 10 g. Worn samples were sectioned at an angle of approximately 5.7° to the sliding direction, and microhardness measurements were taken from these tapered sections. The tapered sections were used to provide a 10 times magnification of the sectioned subsurface zones compared to the normal cross sections.

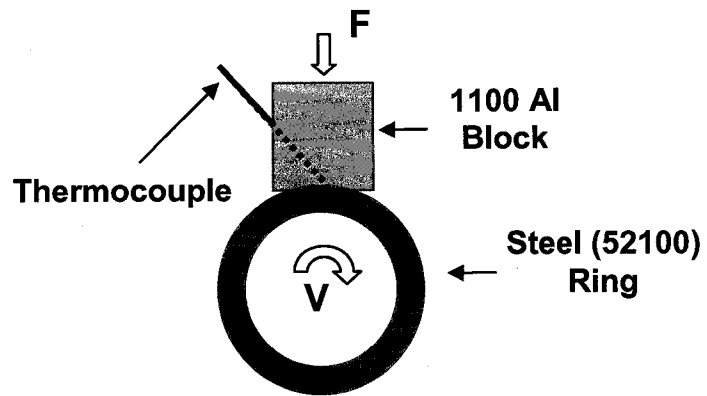


Figure 5.7: Schematic view of the block-on-ring wear test setup.

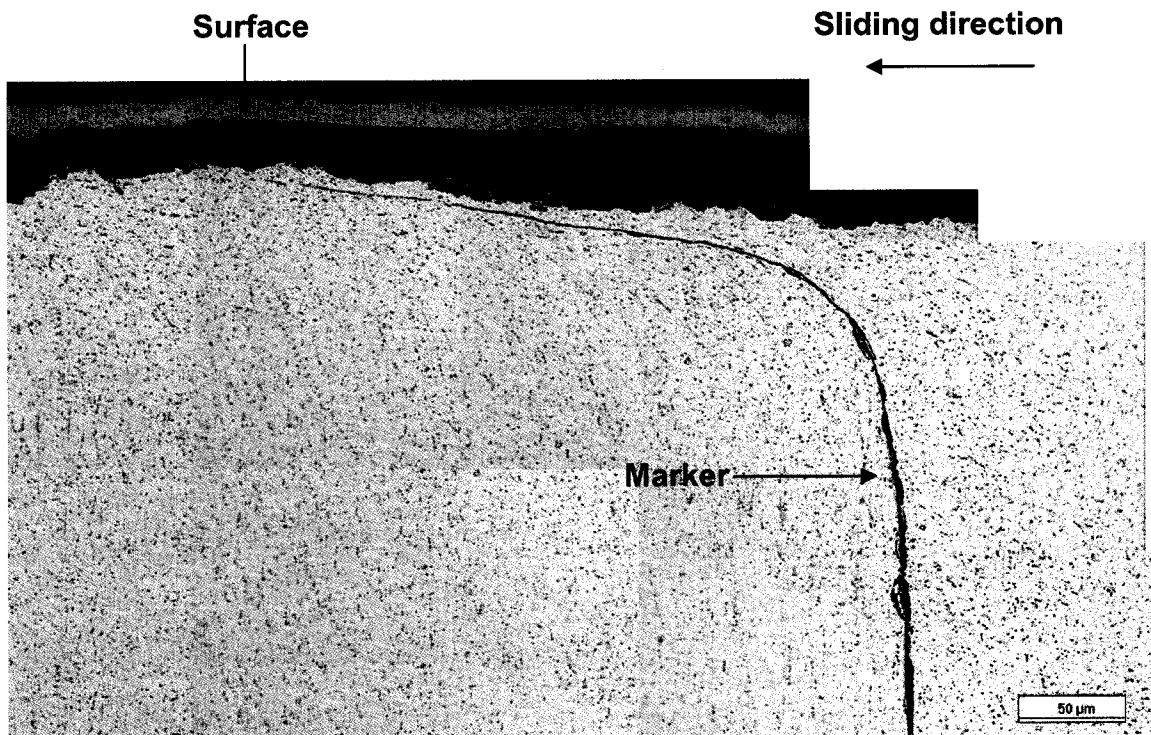


Figure 5.8: Subsurface micrograph showing the deformation of the reference marker along the direction of sliding (Test result with 1 m/s sliding velocity and 30 N normal load).

CHAPTER 6

VALIDATION OF NUMERICAL MODELS

This chapter summarizes the completed investigations to confirm the validity of the numerical simulations. First, the energy balance is discussed, and sample energy balance curves for the numerical models are presented. Second, time-history data samples are illustrated to discuss the force balance of simulations and interface forces during contacts. Next, the normal contact simulation results are compared with the Hertz theory predictions. Later, the experimental and numerical results are compared. Finally, applicability of the thermal softening constitutive equation, which was proposed in this work, was confirmed by the experimental findings.

6.1. ENERGY AND EXTERNAL WORK ANALYSIS FOR THE FINITE ELEMENT MODELS

In order to confirm the validity of a numerical simulation, a researcher must initially address the energy and external work analysis. If there is no energy formation process modeled in a finite element model, the total energy should be always equal the initial energy of the system. Detailed information about the energy and external work analysis is given in Appendix A.

6.1.1. ANALYSIS OF NORMAL CONTACT BETWEEN SOLIDS

Figure 6.1 illustrates the energies and external work associated with the normal contact models. The maximum energy values obtained from a typical normal contact simulation are also listed in Table 6.1. The external work was equal to the total energy, and the total energy was mainly composed of internal energy—stored in the deformed material (90 % of the total energy)—and kinetic energy (7 % of the total energy). This indicates that kinetic energy was insignificant when compared to the internal energy of the system and the quasi-static condition existed in the normal contact models. Sliding interface energy and hourglass energy contributed less than 3 % of the total energy, and

applied hourglass control was successful in keeping hourglass energy at an acceptable level (see Appendix A for a discussion on the hourglass energy levels).

6.1.2. ANALYSIS OF SLIDING CONTACT BETWEEN SOLIDS

Figure 6.2 illustrates a typical energy and external work distribution as observed in the sliding simulations and Table 6.2 presents the maximum energies calculated. The analyses of energies and external work for the models indicate that the total energy of the system was composed mainly of internal energy stored during the deformation. Hourglass energy was less than 4 % of the total energy, and was therefore deemed acceptable (Appendix A). Sliding energy was negligible, indicating an insignificant amount of penetration. Kinetic energy appears as zero in Figure 6.2, since it only comprises 0.1 % of the total energy. Hence, near quasi-static conditions existed in these simulations. Ideally, the external work done should be completely converted into energy, and the amounts of external work and total energy should be equal. However, a difference between total energy and external work towards the end of the simulation was detected. Contact coupling was determined by using 4 x 4 x 4 coupling points distributed over each Lagrangian slave entity, and the penalty scale factor was increased from 0.1 to 3.0 in the contact algorithm in order to obtain a good energy distribution and keep the difference between total energy and external work below 6 to 7 %—accepted as a tolerable level. Kinetic energy comprised less than 2 % of the internal energy and total energy (Figures 6.2, 6.3 and 6.4, pages 116 to 118).

6.1.3. EFFECTS OF TEMPERATURE AND STRAIN RATE ON THE SUBSURFACE DAMAGE

Figure 6.3 shows energies and external work observed in a coupled thermo-mechanical simulation. In addition, Table 6.3 lists the calculated maximum energies. 99.6 % of the total energy was converted into internal energy stored during the deformation. Hourglass energy was zero, because under integration was not used. Sliding energy was negligible, indicating a good simulation (Appendix A). Kinetic energy only comprised 0.4 % of the total energy. Therefore, near quasi-static conditions also existed in these simulations. The difference between total energy and external work was

lower than 2 to 3 % as a result of an increased scale factor for the penalty force stiffness—increased five times. In order to decrease time step size and obtain a stable simulation, the scale factor for the time step calculation was decreased from 0.9 to 0.8 (see Appendix A for energy and external work analysis discussion and time step size calculations).

6.1.4. EFFECTS OF SECONDARY HARD PARTICLES ON THE SUBSURFACE DAMAGE

The energies and external work obtained in a typical simulation modeling the influence of hard particles, and the maximum energies observed are presented in Figure 6.4 and Table 6.4, respectively. Energy comparisons indicate that the finite element simulations were acceptable in terms of an energy and external work analysis. The internal energy stored during the deformation comprised 99 % of the total energy. Hourglass energy did not contribute to the total energy, and sliding energy was negligible. Kinetic energy comprised only 1 % of the total energy, and the difference between total energy and external work was less than 2%.

6.2. TIME-HISTORY DATA

This section presents time-history data where the contact interface forces—specifically the frictional force and the normal contact force at the Al alloy/asperity interface—are given as a function of time. In addition, the variations in stress and strain for elements located at the center line of the Al alloy are illustrated as a function of time, and the transient and steady-state natures of the results are discussed.

6.2.1. ANALYSIS OF NORMAL CONTACT BETWEEN SOLIDS

Figure 6.5 shows the interface forces that were applied to the asperity in the normal contact simulations. Since these forces are contact interface forces, an equal amount of force was applied to the aluminum alloy in the opposite direction. Figure 6.5 indicates that the force in the X direction was negligible during normal contact when

compared to the force in the Y direction, which was the total force applied to push the asperity into the aluminum alloy. During normal contact simulations, the normal load applied in the Y direction was linearly increased from zero to a maximum value of 3.3 N/mm in 3×10^{-4} s, then held constant for the remaining time. Figure 6.6 shows the variation of the von Mises stress at 0.2 μm depth. Damping was not considered to minimize the inertial effects and fluctuations in the von Mises stress are prompted by the dynamic nature of the simulations (inertial forces).

6.2.2. ANALYSIS OF SLIDING CONTACT BETWEEN SOLIDS

Figure 6.7 illustrates the interface forces that were applied to the asperity in the Eulerian sliding contact simulations. The interface forces indicate that in order to move the asperities from their initial stationary conditions, a relatively higher load was required. The force in the X direction obtained a steady state value once the asperity had reached the predetermined constant sliding velocity, and dropped to zero after the completion of the sliding motion (Figure 6.7 (a)). It was observed that the inertia effects found in the Y direction were negligible (Figure 6.7 (b)), while the interface force in the Y direction was equal in magnitude to the total force applied to push the asperity into the aluminum alloy (300 N/mm). In addition, Figure 6.7 proves that the forces generated during the sliding contact do not drop to zero —implying that during sliding the sliding motion was continuous, with no asperity contact loss or lift-off. Figure 6.8 illustrates the accumulation of von Mises stress and plastic strain at a specific depth (200 μm) in the aluminum alloy. Changes in the stresses and strains can be observed after each asperity contact in the figure. The results indicated that the von Mises stress for a given element in the Al alloy was at a maximum when the vertical center line of the element coincided with the vertical center line of the asperity (peaks observed at each asperity contact, Figure 6.8 (a)). The maximum value of the von Mises stress increased after each asperity contacts due to strain hardening of the material. The plastic strain for a given element was at a maximum value when the corresponding element experienced the maximum von Mises stress (Figure 9.8 (b)). For a given element, a continuous increase in the plastic strains was observed for additional asperity contacts.

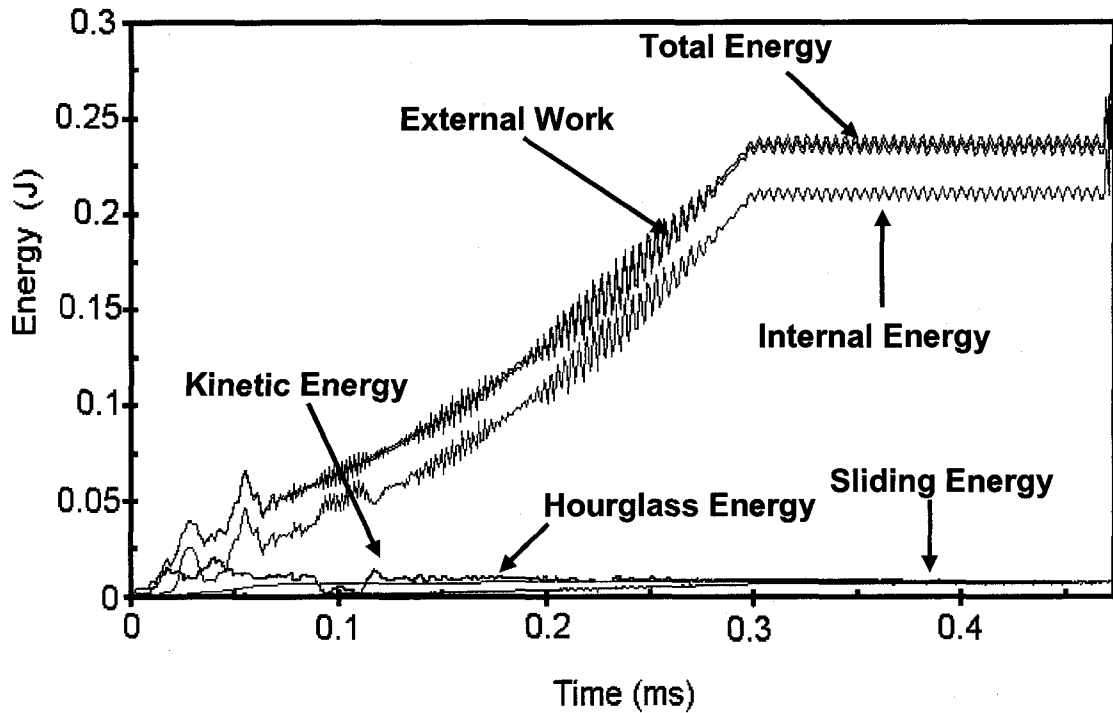


Figure 6.1: Typical energies and external work observed in the normal contact simulations.

Table 6.1: Maximum values of energies obtained from a typical normal contact simulation.

Energy Type	Energy Values (J)	(En. Type / Total En.) x 100
Hourglass Energy	8.425×10^{-3}	2.95
Sliding Energy	8.600×10^{-3}	3.01
Kinetic Energy	1.999×10^{-2}	7.00
Internal Energy	2.585×10^{-1}	90.56
Total Energy	2.855×10^{-1}	100.00
External Work	2.889×10^{-1}	101.20

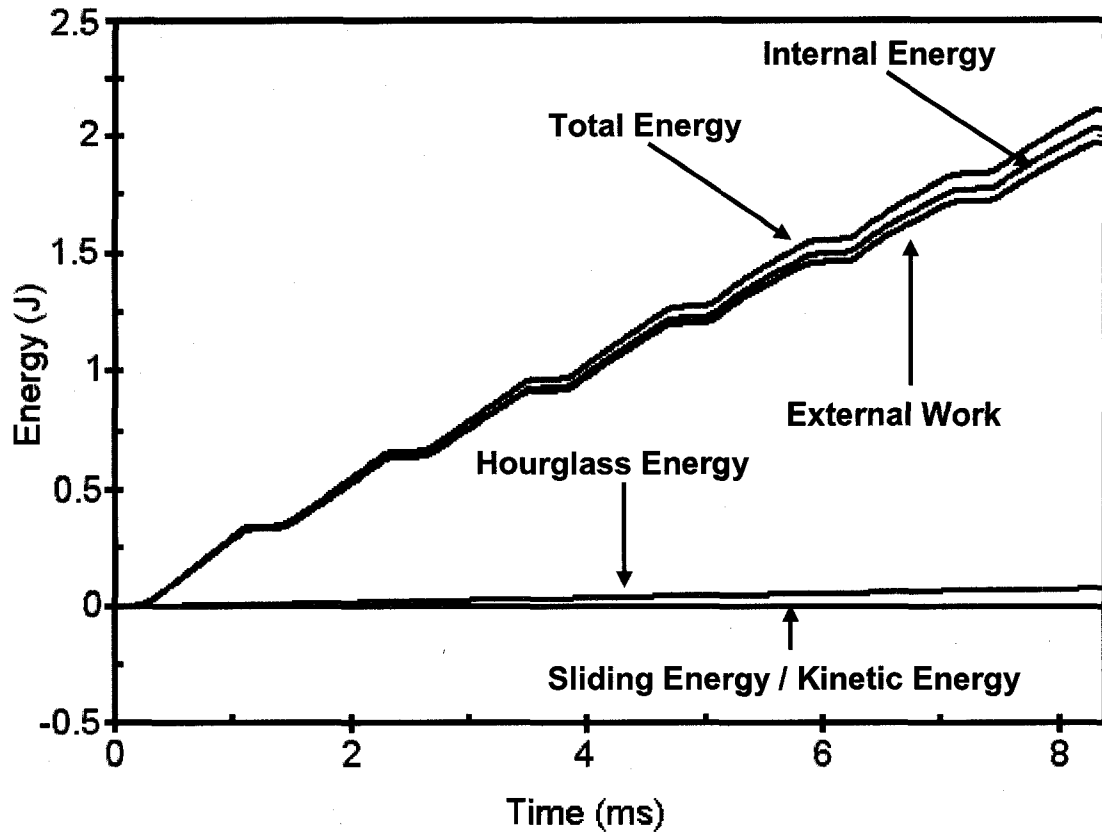


Figure 6.2: Energies and external work typical of the sliding contact modeling simulations (Eulerian model).

Table 6.2: Maximum values of energies obtained from a typical sliding contact simulation (Eulerian model).

Energy Type	Energy Values (J)	(En. Type / Total En.) x 100
Hourglass Energy	7.746×10^{-2}	3.6
Sliding Energy	6.924×10^{-5}	0.003
Kinetic Energy	1.860×10^{-3}	0.088
Internal Energy	2.044	96.3
Total Energy	2.121	100.0
External Work	1.979	93.3

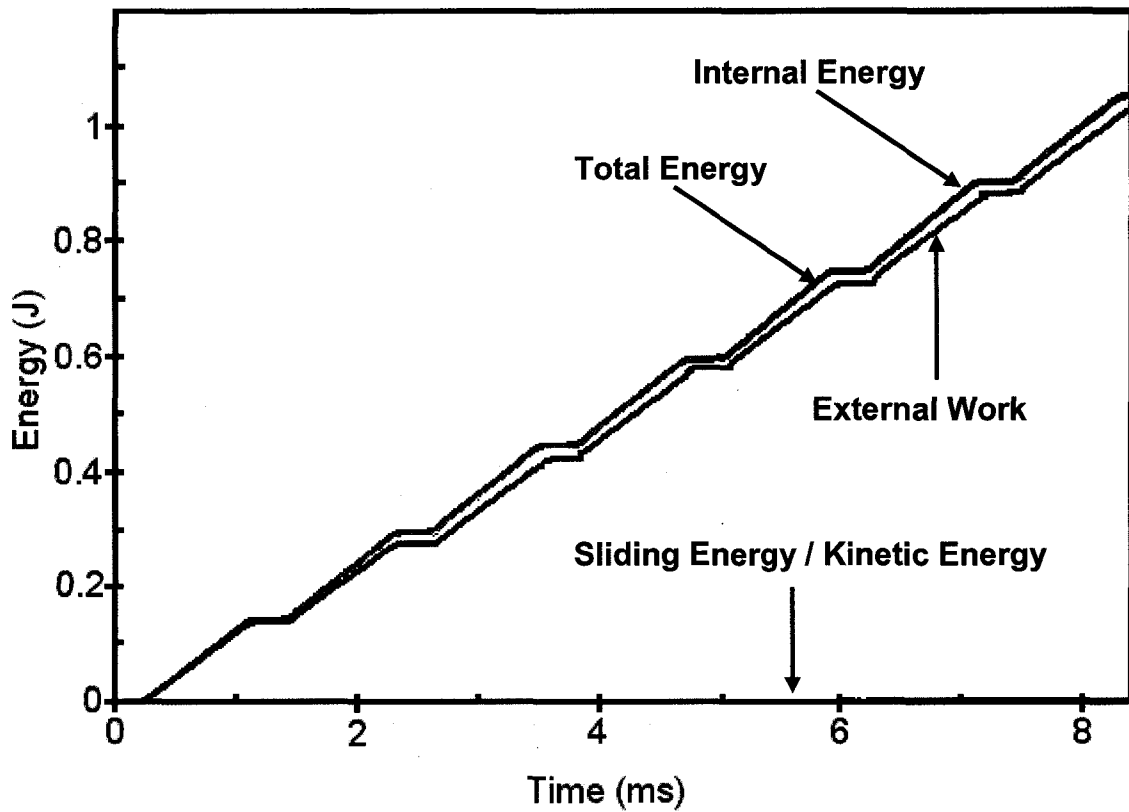


Figure 6.3: Typical energies and external work observed in the sliding contact simulations with Lagrangian thermo-mechanical model.

Table 6.3: Maximum values of energies obtained from a typical sliding contact simulation using Lagrangian thermo-mechanical model.

Energy Type	Energy Values (J)	(En. Type / Total En.) x 100
Hourglass Energy	0.000	0.000
Sliding Energy	3.666×10^{-5}	0.003
Kinetic Energy	4.378×10^{-3}	0.414
Internal Energy	1.054	99.59
Total Energy	1.058	100.00
External Work	1.034	97.79

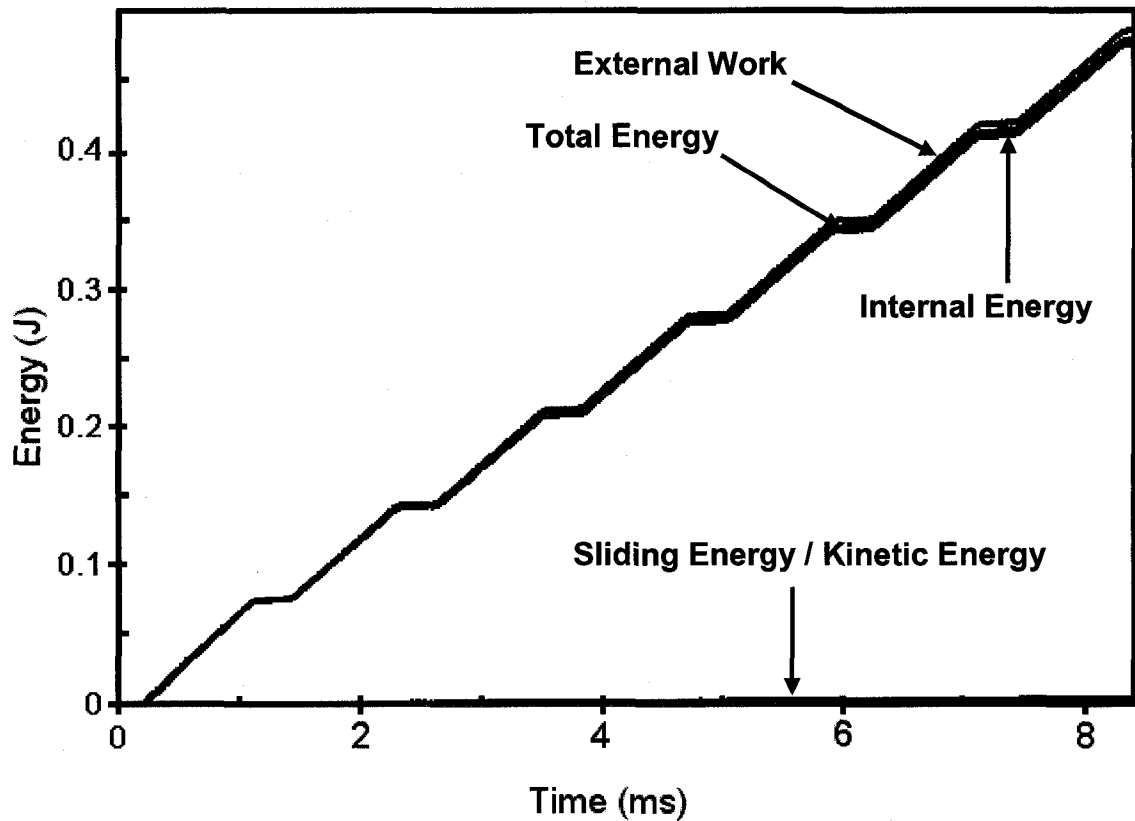


Figure 6.4: Energies and external work typical of the sliding contact modeling simulations with hard particles.

Table 6.4: Maximum values of energies obtained from a typical sliding contact simulation with hard particles.

Energy Type	Energy Values (J)	(En. Type / Total En.) x 100
Hourglass Energy	0.000	0.00
Sliding Energy	4.830×10^{-5}	0.01
Kinetic Energy	4.3736×10^{-3}	0.91
Internal Energy	4.742×10^{-1}	99.09
Total Energy	4.785×10^{-1}	100.00
External Work	4.866×10^{-1}	101.67

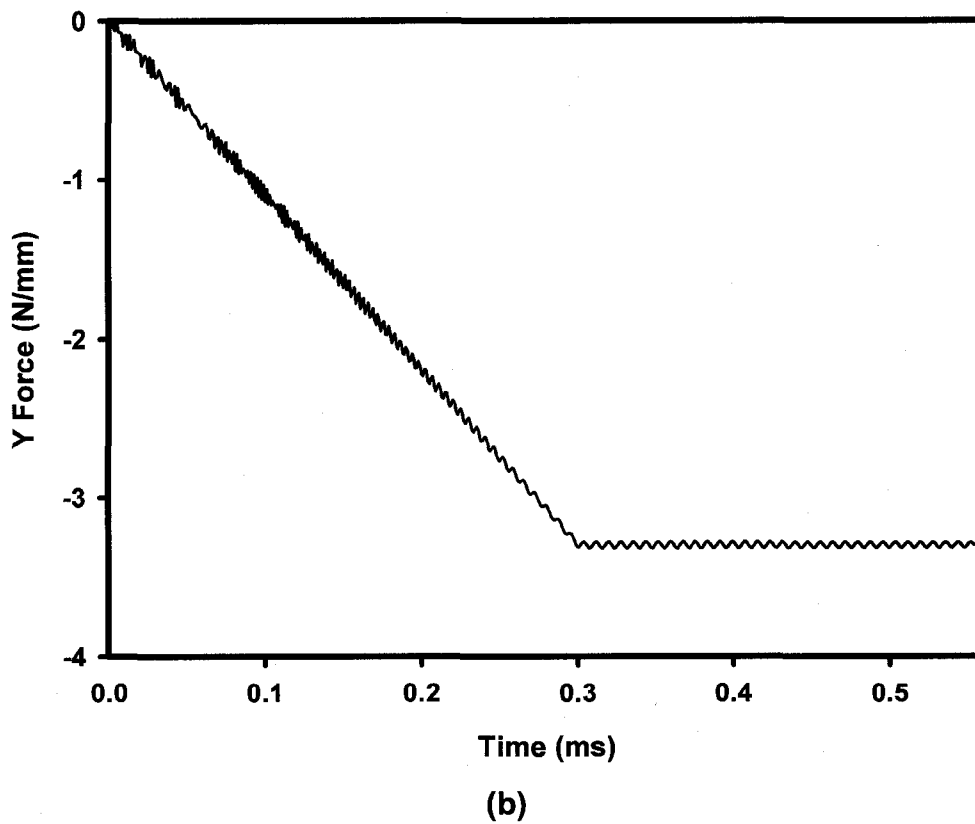
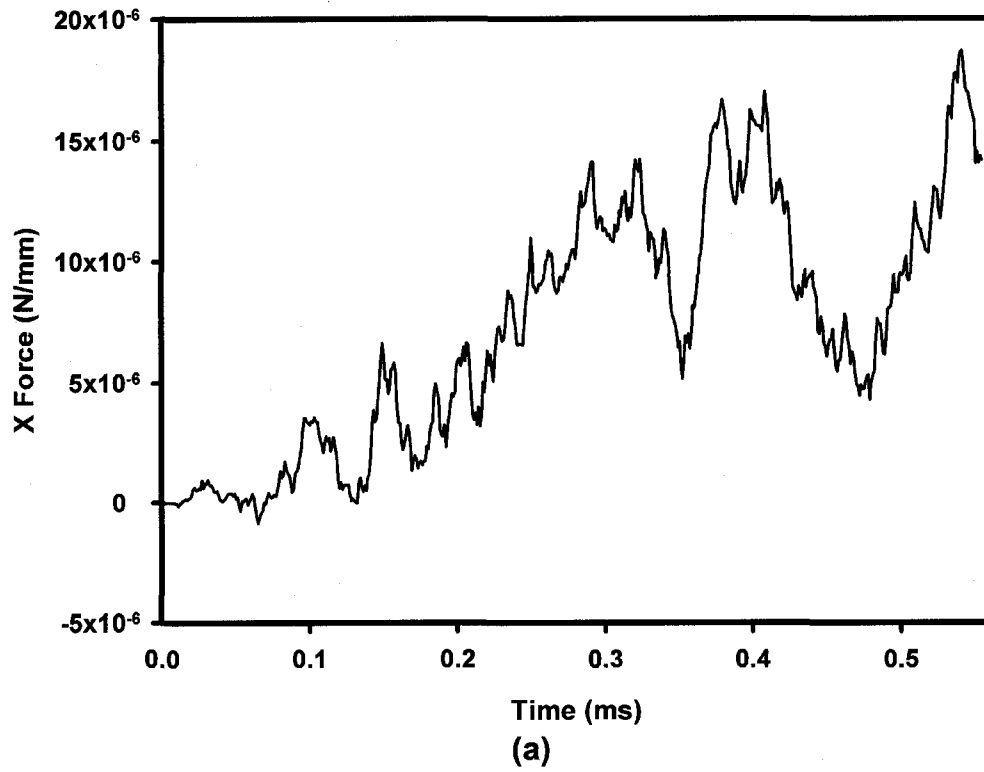


Figure 6.5: Interface forces applied to the asperity in the normal contact modeling simulations: (a) Force in the X direction, (b) Force in the Y direction.

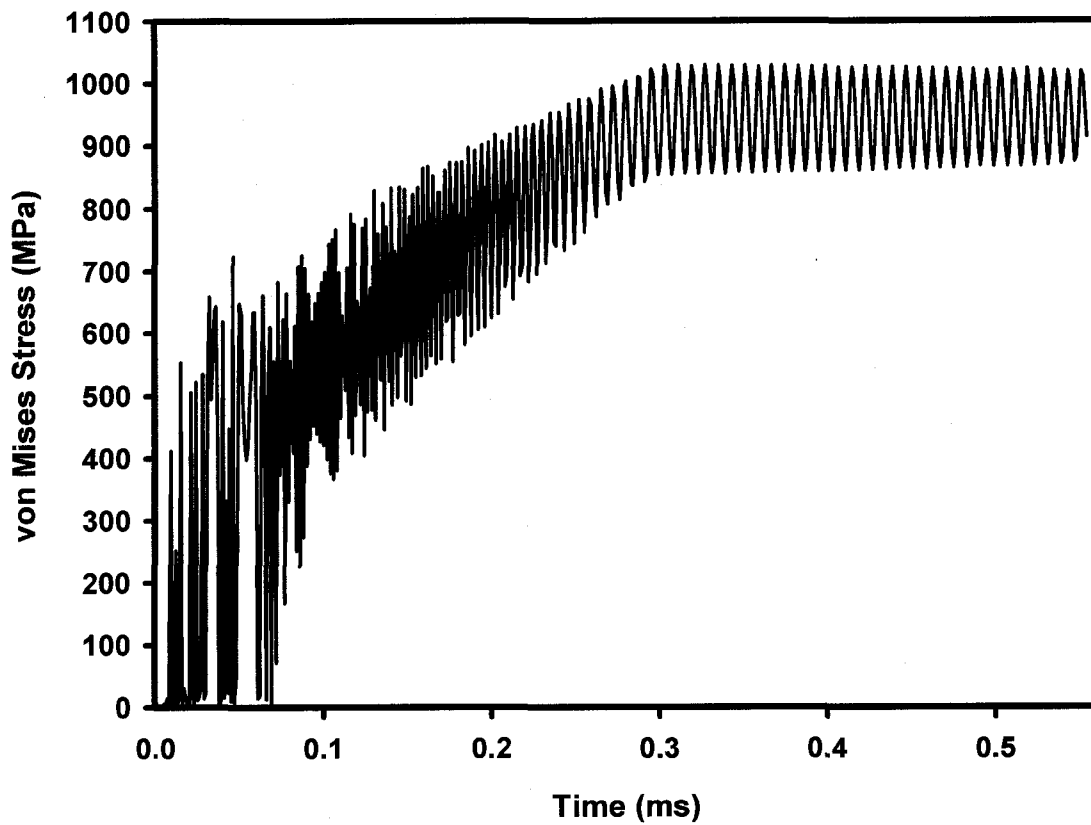


Figure 6.6: Variation of the von Mises stress at 0.2 μm depth (Normal load: 3.3 N, Normal contact model).

6.2.3. EFFECTS OF TEMPERATURE AND STRAIN RATE ON THE SUBSURFACE DAMAGE

The interface forces applied to the asperities in the Lagrangian thermo-mechanical models are illustrated in Figure 6.9 for each asperity contact. Similar to the observations made with Eulerian sliding contact models, the asperities needed relatively high forces to start their motion. However, after the motion was initiated, forces reached a steady state value. The force distribution indicates that there was no loss of contact during the sliding motion. Figure 6.10 shows the change of the X direction forces with the normal load, while Figure 6.11 shows the variation of the same forces with the sliding velocity. Figure 6.10 indicates that the force in the X direction (needed to move the asperities with constant sliding velocity) increased in tandem with an increasing normal load. However, an opposite situation was observed with the increase of the sliding velocity. When the sliding velocity increased from 10 m/s to 40 m/s, the force in the X direction initially increased. However, after the asperity achieved steady state motion a reduction in the force in the X direction was observed, which is a dynamic effect.

Figure 6.12 shows the variation of the von Mises stress and the equivalent plastic strain in an element at a 25 μm depth. Oscillations in the von Mises stress are prompted by dynamic effects (Figure 6.12 (a)). A continuous increase in the plastic strain can be observed with seven asperity contacts in Figure 6.12 (b).

6.2.4. EFFECTS OF SECONDARY HARD PARTICLES ON THE SUBSURFACE DAMAGE

The force balance observed in a simulation that models the influence of hard particles was the same as that observed in Lagrangian thermo-mechanical models. Therefore, force balance figures are not given separately.

6.3. HERTZ THEORY COMPARISONS

In this section, the finite element analysis results for normal contact between a cylindrical asperity and an aluminum half-space surface are compared with the predictions of the Hertz theory in an effort to test and validate the accuracy of the

developed finite element models. Details of the normal contact models are given in Section 4.1.

The elastic numerical simulation results are summarized in Table 6.5, along with the Hertz theory predictions. The maximum shear stress—according to the Hertz theory—is 805.2 MPa at a depth of 0.61 μm for an applied load of 3.3 N/mm. All the numerical models provided acceptable predictions—comparing with the Hertz theory—for the semi-contact width. However, Model F—which utilizes the implicit time integration method and requires approximately 4 minutes of computation time—provided an excellent prediction of the maximum shear stress. Asperity penetration depths varied between 0.11 μm and 0.15 μm (Table 6.6). The large number of element edges on the contact line (18) for Model F indicated an acceptable level of discretization.

The pressure distribution predictions for the models—with a 3.3 N/mm load—are presented in Figure 6.13, and compared with the elliptical shape pressure distribution prediction of the Hertz theory. Due to symmetry, only half of the pressure distribution is plotted at zero depth (i.e., $y=0$). Numerical models showed that the area of contact was approximately elliptical in shape when a cylindrical asperity was loaded against a half-space.

Figure 6.14 illustrates the variation of stresses σ_x , σ_y and τ at the centerline of the half-space as a function of the normalized depth below the surface, as predicted by the Hertz theory and numerical models. A good agreement between theoretical and numerical observations is clearly evident.

6.4. COMPARISON OF THE EXPERIMENTAL AND NUMERICAL RESULTS

This section compares the finite element model results and the experimental observations—for validation purposes. The details of the finite element models and the experimental procedures are given in Section 4.2 and Section 5.1, respectively.

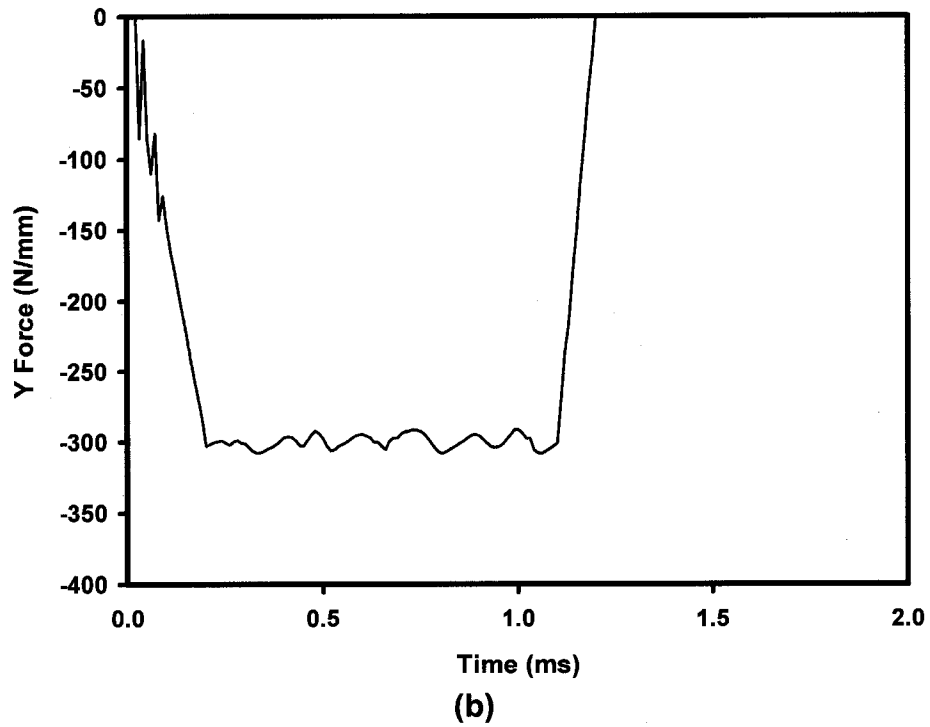
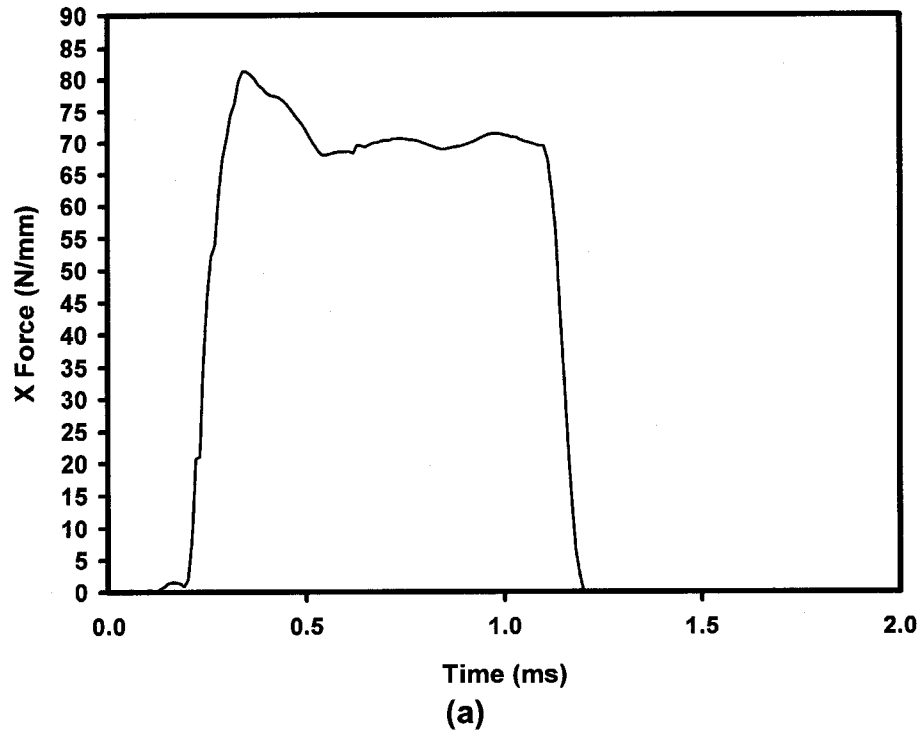


Figure 6.7: Interface forces applied to the asperity in the sliding contact modeling simulations using the Eulerian model: (a) Force in the X direction, (b) Force in the Y direction.

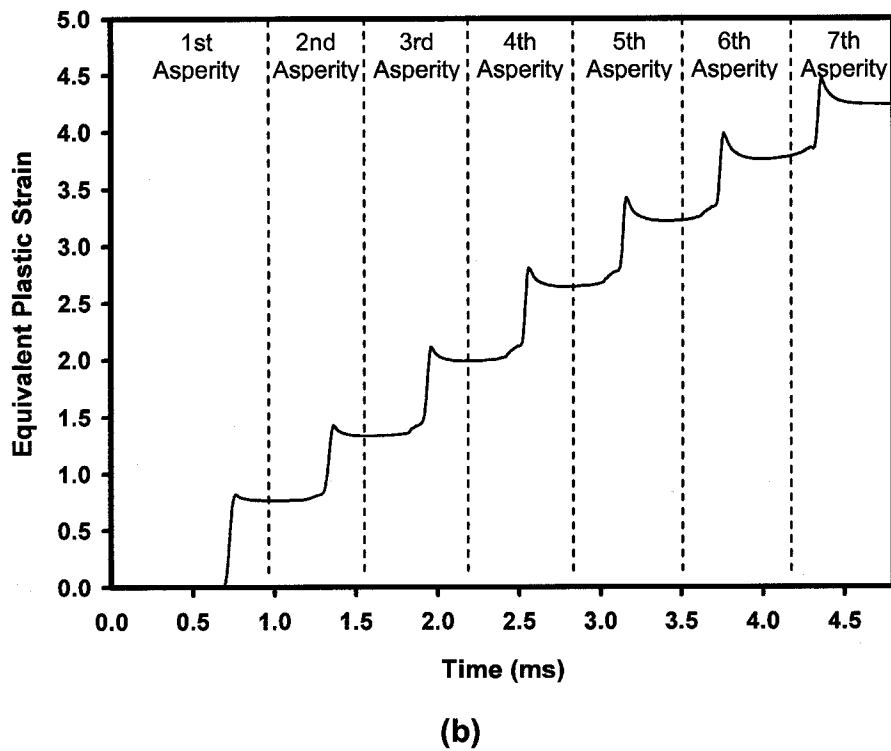
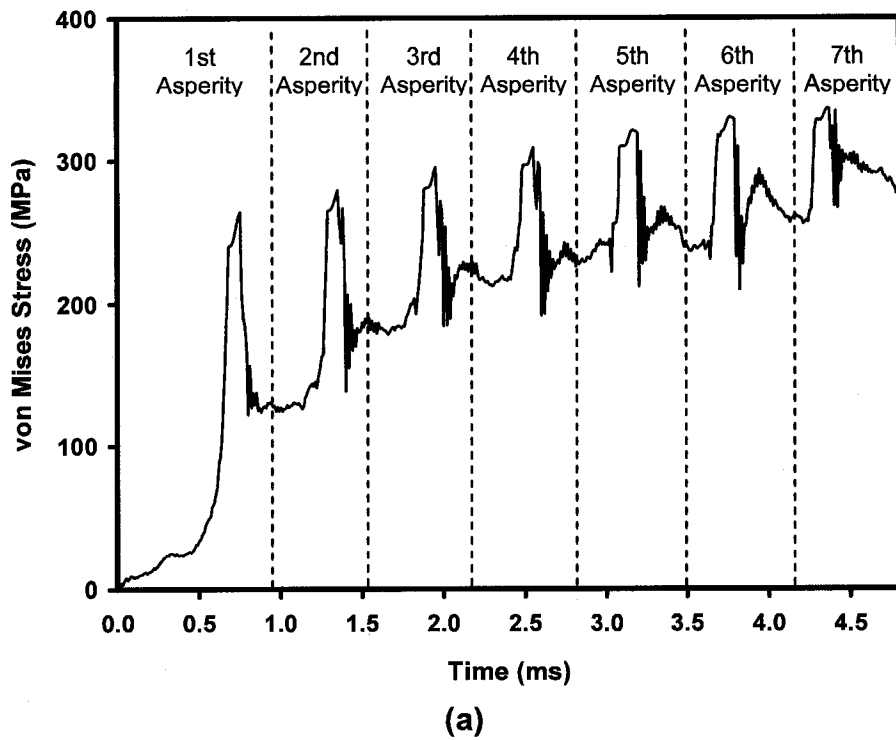


Figure 6.8: (a) Variation of the von Mises stress at 200 μm depth, (b) Accumulation of the plastic strain at 200 μm depth (Sliding velocity: 10 m/s, Normal load: 300 N/mm, Eulerian model).

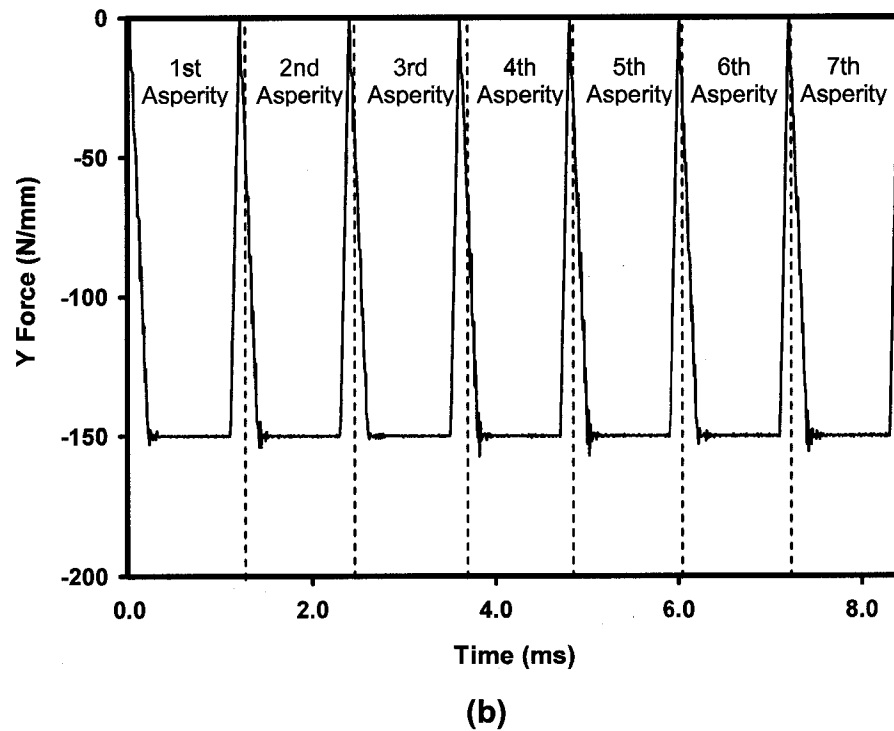
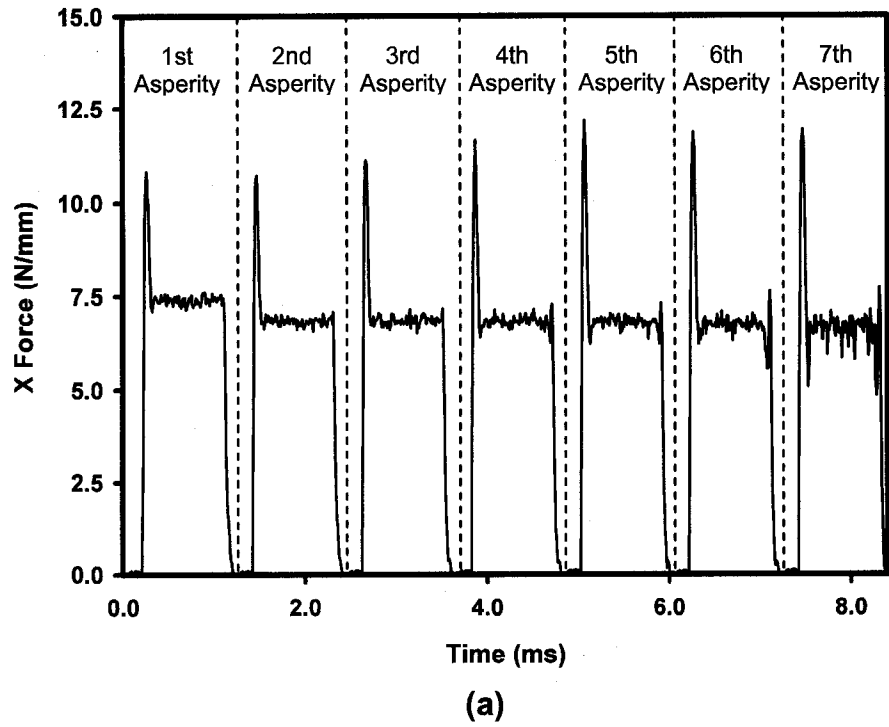


Figure 6.9: Interface forces applied to the asperities in the sliding contact simulations with Lagrangian thermo-mechanical model: (a) Force in the X direction, (b) Force in the Y direction.

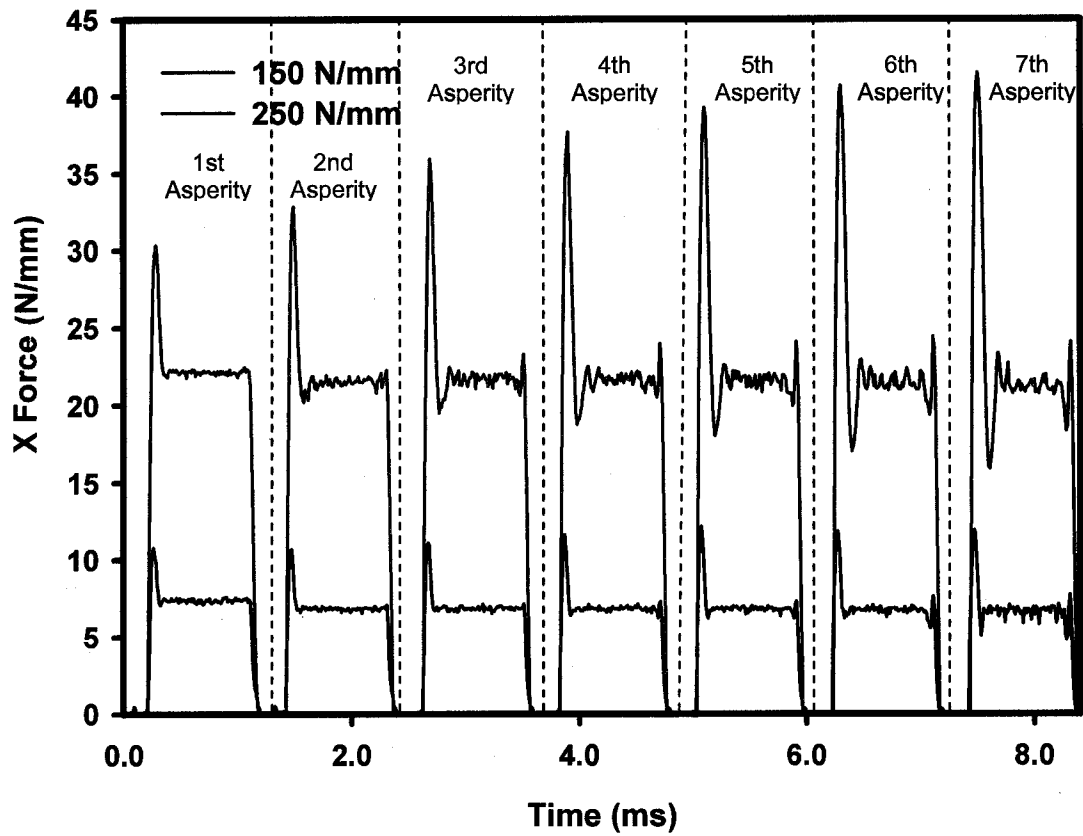


Figure 6.10: Variation of interface forces in the X direction with normal load (Sliding velocity: 10 m/s, Lagrangian thermo-mechanical model).

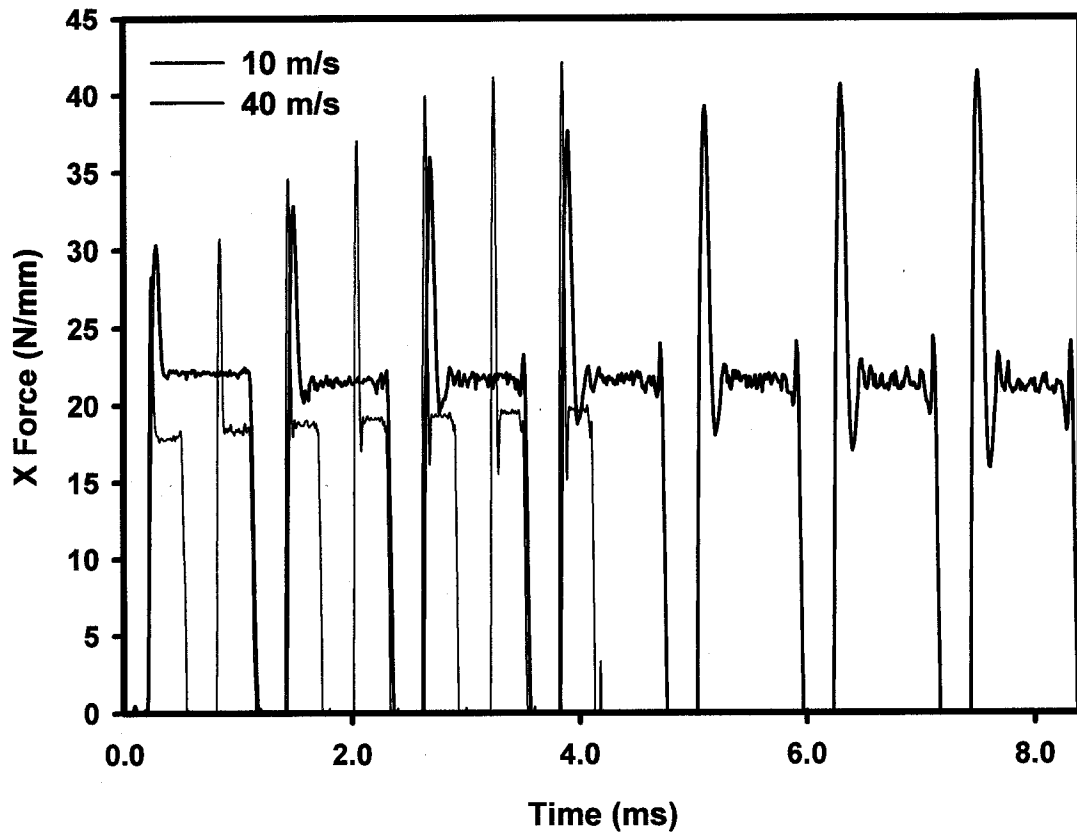


Figure 6.11: Variation of interface forces in the X direction with sliding velocity (Normal load: 250 N/mm, Lagrangian thermo-mechanical model).

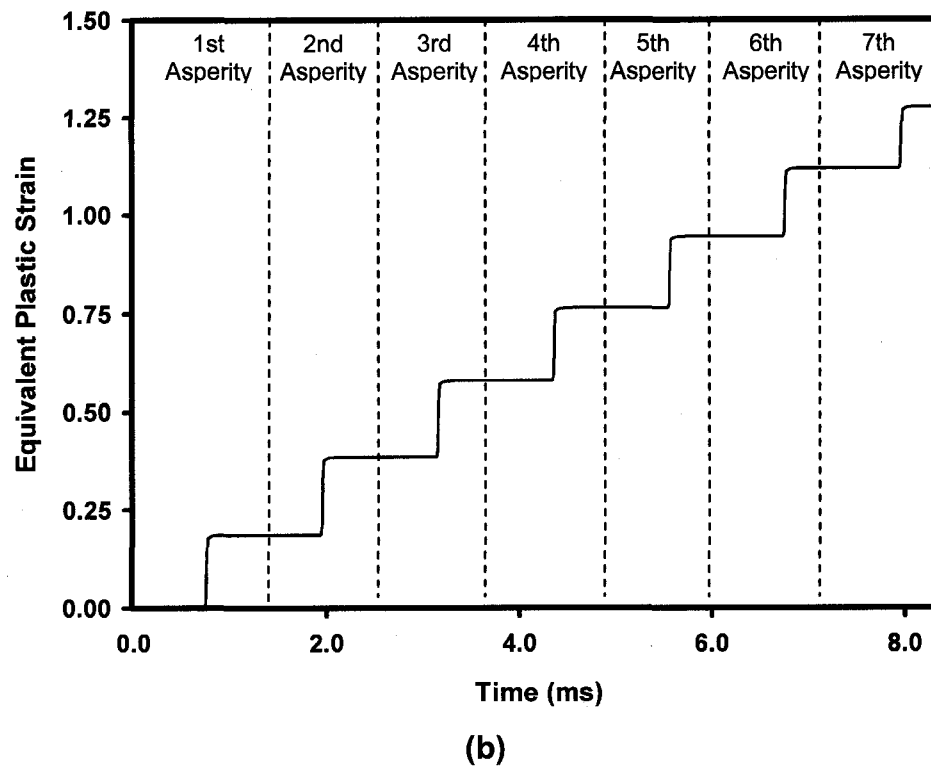
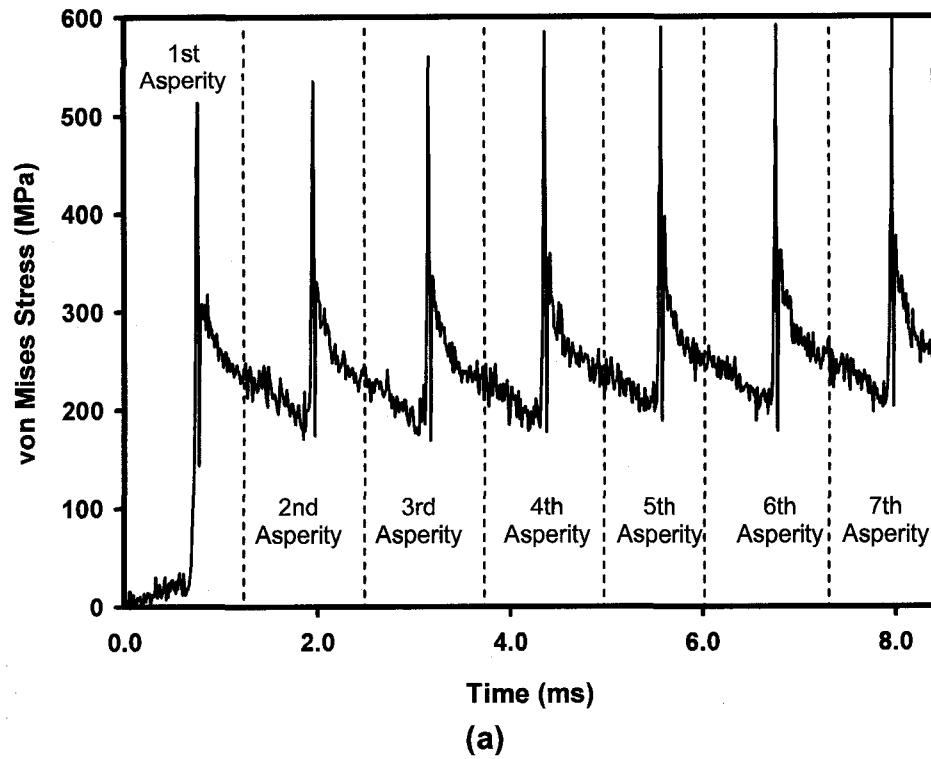


Figure 6.12: (a) Variation of the von Mises stress at 25 μm depth, (b) Accumulation of the plastic strain at 25 μm depth (Sliding velocity: 10 m/s, Normal load: 150 N/mm, Lagrangian thermo-mechanical model).

Table 6.5: Comparison of the elastic normal contact model results and the Hertz theory calculations for normal load of 3.3N/mm.

MODEL	τ_{max} (MPa)	y (at τ_{max}) (μm)	a (μm)	$y(\text{at } \tau_{max})/a$
Model A	631.781	0.83 - 1.67	0.83 - 1.67	0.50-1.00
Model B	936.718	0.42 - 0.83	0.83 - 1.25	0.33-1.00
Model C	936.390	0.62 - 0.83	0.83 - 1.04	0.60-1.00
Model D	900.263	0.62 - 0.83	0.83 - 1.04	0.60-1.00
Model E	849.414	0.42 - 0.62	0.83 - 1.04	0.40-0.75
Model F	803.246	0.62 - 0.73	0.83 - 0.94	0.67-0.87
Hertz Theory	805.155	0.61	0.78	0.78

Table 6.6: Comparison of penetration depths and element numbers in the contact line for elastic numerical models for normal load of 3.3N/mm.

MODEL	Penetration Depth, h (μm)	Number of Elements in Contact Line
Model A	0.135	3-4
Model B	0.152	5-6
Model C	0.131	9-10
Model D	0.132	9-10
Model E	0.114	9-10
Model F	0.117	17-18

6.4.1. NORMAL CONTACT

Table 6.7 compares experimentally observed and numerically calculated indentation impression depths for different loading conditions during normal loading. Both the experimental and the numerical indentation contact depths varied between 30 and 60 μm for 306 to 390 N/mm loading. Table 6.7 shows that the numerical simulations could predict the experimental contact depths with a less than 10% difference.

In addition to the contact depth, the approximate experimental indentation contact lengths were also measured by surface profilometer, and the results were compared with the predictions of the finite element simulations (see Figure 5.4 for the definition of contact depth and length). Table 6.8 presents the results obtained for contact length in various loading setups. The results indicated that the contact length was between 0.4 and 0.6 mm for 306 to 390 N/mm loads. The highest deviation observed between the experimental and the numerical results was 11.09% for a 330.88 N/mm load.

Tables 6.9 and 6.10 list the experimentally and numerically determined plastic zone depths and widths (see Figure 5.3 for the definition of plastic zone depth and width). The numerical predictions revealed a deviation of approximately 20% from the experimental observations of the plastic zone depth—perhaps due to the errors and assumptions made in the definition of the experimental values. Unlike the experimental observations, the numerical simulations predicted a slight decrease in the plastic region depth, with an increase in the normal load or contact length (Table 6.9). However, both the numerical and the experimental observations agreed with the trend of an increasing plastic zone width with an increasing normal load (Table 6.10). The difference between the experimental and the numerical plastic zone widths was less than 10%.

In summary, normal contact investigations showed that the developed finite element model could be used in the prediction of the deformation of a 356 Al alloy during normal loading.

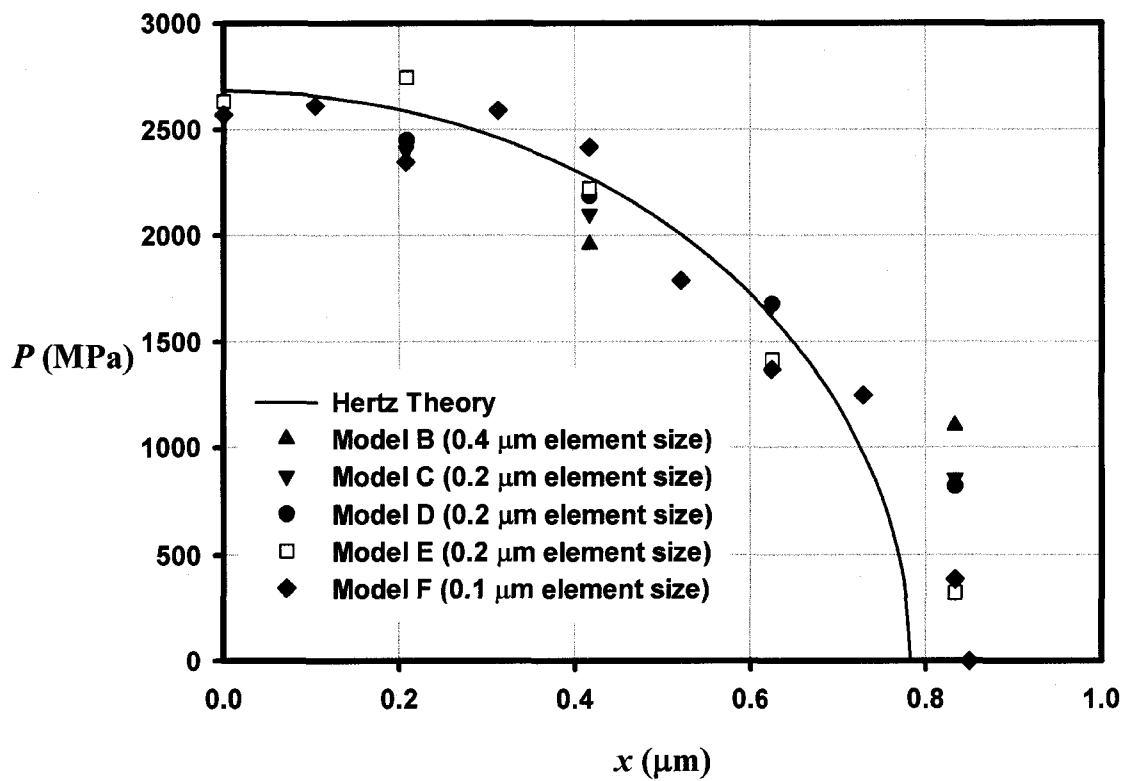


Figure 6.13: Comparison of the pressure distribution (P) in the contact zone obtained by the elastic finite element models and the analytical solution (x is the distance along the surface).

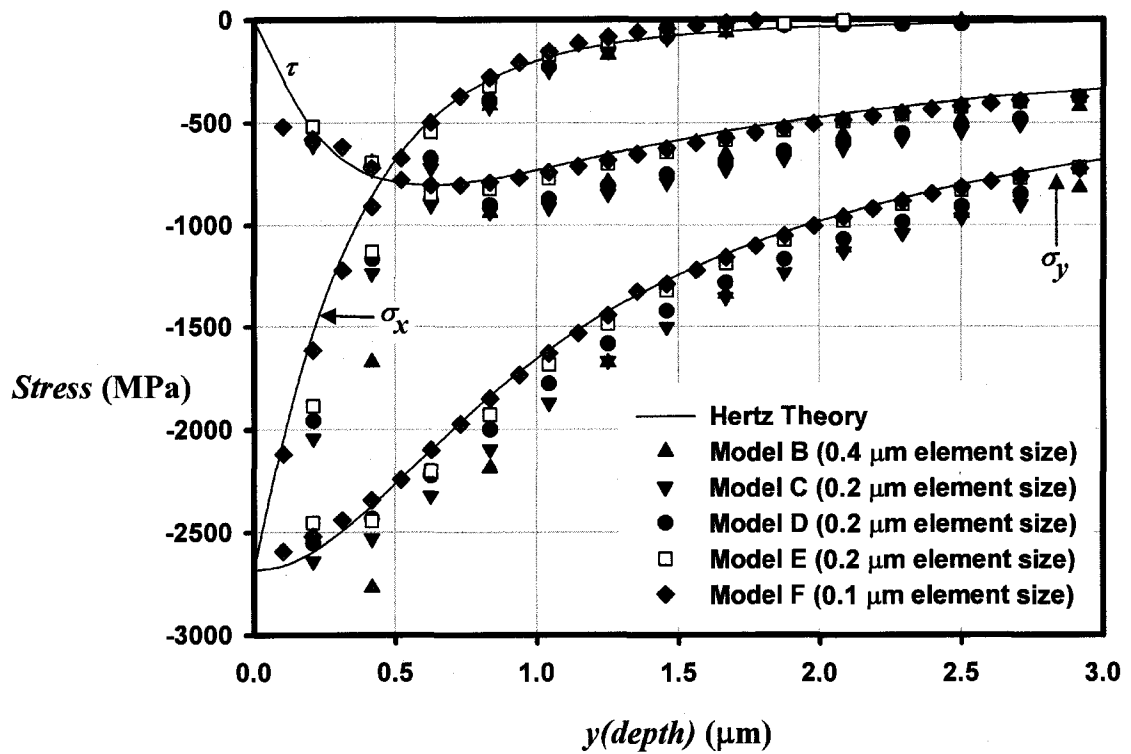


Figure 6.14: Comparison of the subsurface stresses in the aluminum half-space material along the axis of symmetry obtained by the elastic finite element models and the analytical solution.

Table 6.7: Comparison of the experimentally and numerically determined indentation contact depth on the 356 Al material.

Load/Thickness (N/mm)	Experimental Contact Depth (μm)	Numerical Contact Depth (μm)	% difference ^a
306.12	30.77	34.38	-11.74
308.22	32.70	34.62	-5.87
326.09	37.20	36.94	0.71
330.88	38.33	39.62	-3.34
335.82	39.37	40.31	-2.38
343.51	45.77	43.68	4.57
346.15	47.43	44.98	5.16
362.90	48.07	47.09	2.04
387.93	58.87	55.17	6.28

^a % difference = $\{(\text{Experimental Value} - \text{Numerical Value}) / \text{Experimental Value}\} * 100$

Table 6.8: Comparison of the experimentally and numerically determined indentation contact length on the 356 Al material.

Load/Thickness (N/mm)	Experimental Contact Length (mm)	Numerical Contact Length (mm)	% difference
306.12	0.41	0.42	-2.51
308.22	0.41	0.42	-1.14
326.09	0.45	0.41	7.99
330.88	0.49	0.43	11.09
335.82	0.49	0.46	6.74
343.51	0.49	0.48	2.66
346.15	0.51	0.50	3.28
362.90	0.54	0.52	4.44
387.93	0.58	0.60	-3.34

6.4.2. SLIDING CONTACT

Figure 6.15 illustrates the position of the marker boundaries obtained after experimental sliding tests at a sliding velocity of 0.15 m/s and a normal load of 300 N/mm. A regression analysis revealed that the position of the marker boundaries could be represented by the following exponential relation:

$$D = A + B \exp(-CZ) \quad (6.1)$$

where D is the position of the marker at a given depth Z (in μm) below the sliding surface, and A , B and C are constants. A represents the distance of the marker to the origin, and $(D-A)$ is the displacement of the marker along the sliding direction at a given depth. The values of A , B and C —obtained for the loading conditions considered—are given in Table 6.11.

The equivalent plastic strain (ε) below the contact surface was determined from the deformation angle θ , which is the angle between the line drawn tangent to the marker boundary and the axis perpendicular to the contact surface (Figure 6.16) [3, 4, 17]:

$$\varepsilon = \frac{\sqrt{3}}{3} \tan \theta \quad (6.2)$$

The slope of the tangent line was calculated from Equation 6.1:

$$\tan \theta = -\left(\frac{dD}{dZ}\right) = (BC) \exp(-CZ) \quad (6.3)$$

Figure 6.17 shows the experimental subsurface plastic strain distributions obtained after four consecutive sliding contacts at a sliding velocity of 0.15 m/s and a

normal load of 300 N/mm—along with the corresponding numerical predictions. Only two sliding contacts could be completed with finite element simulations, due to high processing times with this low sliding velocity (approximately 5 months). Therefore, the numerical results after two sliding contacts are presented in Figure 6.17. The results indicated a good agreement between the experimental and numerical observations. After the first sliding contact, the extrapolated plastic strain at the surface was observed to be 2.1 for the experimental tests, and reached 3.7 after the second sliding contact. The numerical model predicted plastic strains within 5.0 to 20.0% deviation from the experimental observations for a given depth.

6.5. COMPARISON OF THE EXPERIMENTAL OBSERVATIONS AND THERMAL SOFTENING MODEL

In order to test the applicability of the thermal softening constitutive equation for the wear tests, sliding contact experiments were performed and the experimental observations were compared with the predictions of the considered thermal softening model. This section presents the investigations performed for this purpose.

Figure 6.18 illustrates the position of the marker boundaries obtained after experimental sliding wear tests with two different loads of 10 N and 30 N. A regression analysis revealed that the position of the marker boundaries could be represented by an exponential-type equation (Equation 6.1). The values of coefficients in Equation 6.1 (A , B and C) are given in Table 6.12 for the 1100 Al. The equivalent plastic strain (ϵ) below the contact surface was determined from the deformation angle θ , whose detailed determination is given in Section 6.4. The subsurface plastic strain distribution curves obtained at 10 N and 30 N are shown in Figure 6.19. Both magnitude of the subsurface strains and depth of the plastic zone increased with the applied load.

The flow strength of the subsurface layers in Figure 6.20 was estimated from the microhardness values, using the following expression given by Bowden and Tabor [111]:

$$\sigma_f = \frac{H}{C_H} \quad (6.4)$$

Table 6.9: Comparison of the experimentally and numerically determined plastic zone depth

Load/Thickness (N/mm)	Exp. Plastic Region Depth (μm)	Num. Plastic Region Depth (μm)	% difference
335.82	801.00	909.70	-13.57
343.51	1019.00	906.32	11.06
362.90	1090.00	902.59	17.19
387.93	1108.00	894.93	19.23

Table 6.10: Comparison of the experimentally and numerically determined plastic zone width

Load/Thickness (N/mm)	Exp. Plastic Region Width (μm)	Num. Plastic Region Width (μm)	% difference
335.82	835.00	928.13	-11.15
343.51	914.00	928.13	-1.55
362.90	1093.00	1030.21	5.75
387.93	1144.50	1030.21	9.99

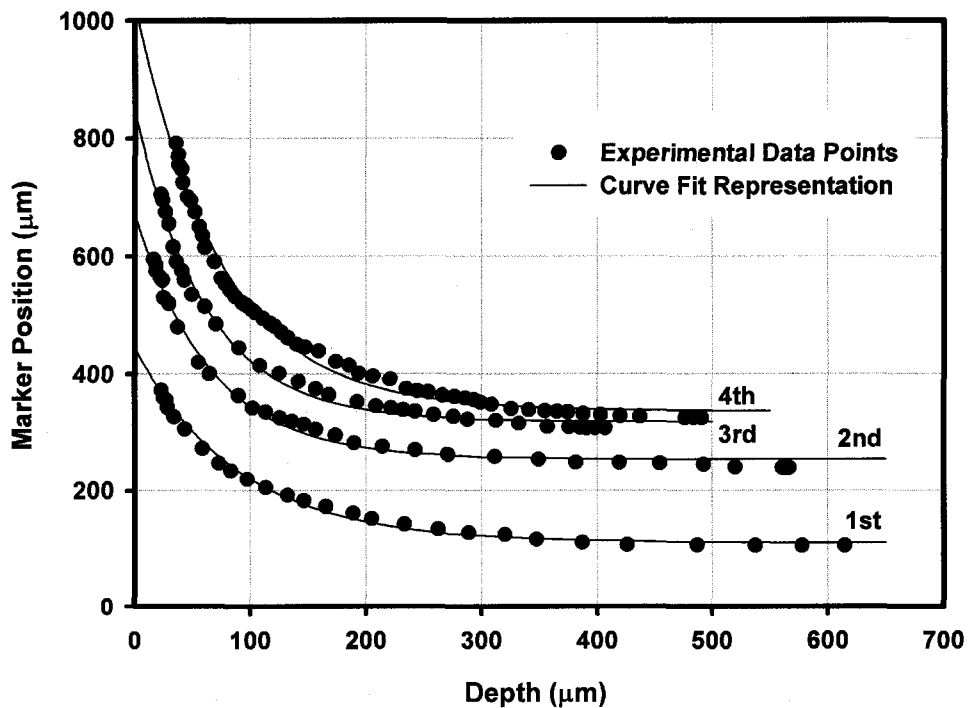


Figure 6.15: Marker position in the 356 Al alloy after four sliding tests with a sliding velocity of 0.15 m/s and normal load of 300 N/mm.

Table 6.11: Coefficients A , B and C in the Equation 6.1 for the 356 Al alloy (sliding velocity: 0.15 m/s, normal load: 300 N/mm).

Sliding Number	A (μm)	B (μm)	C ($1/\mu\text{m}$)
1	110.3	333.3	0.01108
2	253.9	417.5	0.01527
3	317.9	526.2	0.01617
4	336.1	691.4	0.01352

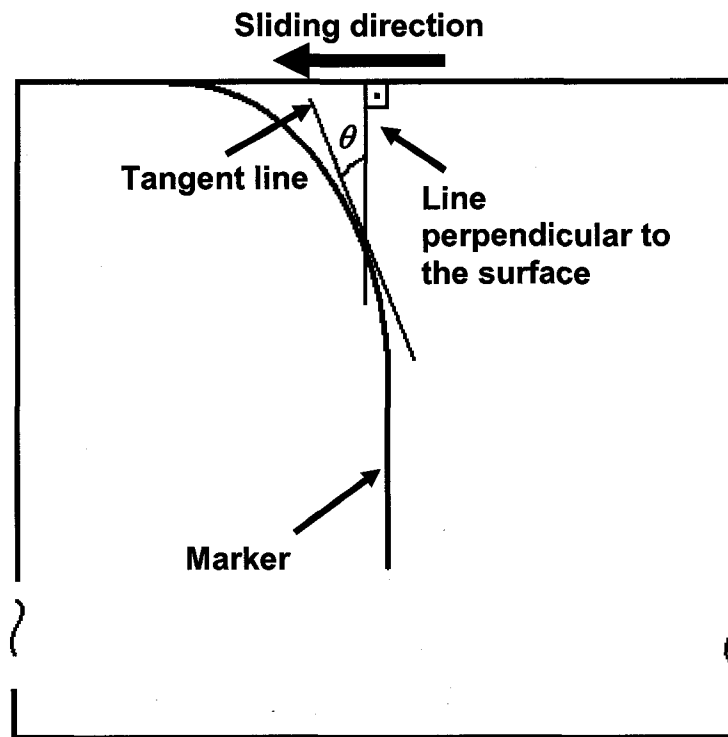


Figure 6.16: Determination of the deformation angle (θ) to calculate the equivalent plastic strain below the contact surface.

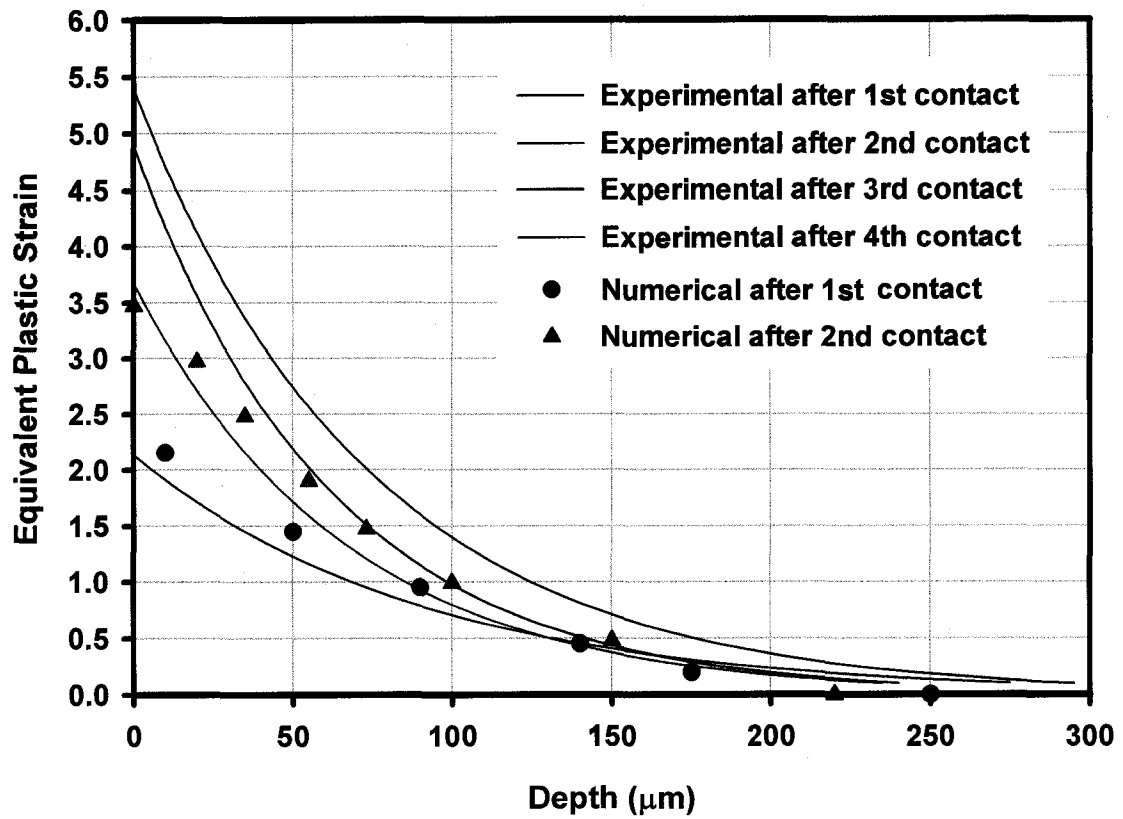


Figure 6.17: Subsurface equivalent plastic strain distribution in the 356 Al alloy after sliding contacts (sliding velocity: 0.15 m/s and normal load: 300 N/mm).

where σ_f is the flow stress, H is the microhardness and C_H is a constant with the value of 3.0.

A relationship between the flow stress and plastic strains was established by plotting the corresponding stress and strain values—determined at the same depth below the surface. The resulting relationships are shown in Figure 6.21 for two different loads. The 1100 Al material shows a rapid strain hardening up to strain values of 5. However, at higher strains, the material loses its ability to strain harden and a saturation stress is reached. For two different loading conditions, stress-strain behaviour follows two different paths with two different saturation stresses. A regression analysis showed that these curves could be represented in the form of a Voce-type exponential relationship, presented in Equation 4.1. Table 6.13 lists the constants in the Voce equations calculated for 10 N and 30 N loads.

Figure 6.22 shows the measured temperature increase during the tests. For the testing condition with the applied load of 10 N, the contact temperature was increased to 315° K at the beginning of the test, and remained constant at the same value. For the load of 30 N, the temperature was increased up to 345° K. If the effect of strain rate hardening is assumed to be the same for two different load tests (since the sliding velocity and sliding distance are the same), the change of the stress-strain behaviour in Figure 6.21 with the normal load would be explained by the thermal softening of the material—caused by the temperature difference of 30° K between the two different loadings.

Variations of the Johnson-Cook thermal material parameters (m) dependant on the temperature are presented in Figure 2.40 for some aluminum alloys. Figure 2.40 indicates that for the 1100 Al, m is equal to 0.75 for the temperature range observed in the wear tests. If the flow stress-strain relationship obtained for 10 N is accepted as a base relationship, the change in the stress-strain behaviour of the 1100 Al material for 30 N can be predicted by using the thermal softening constitutive equation. Figure 6.23 shows the results of such a calculation, where thermal softening of the 1100 Al material was predicted by using Equation 4.9 ($m = 0.75$), then compared with the experimental results. This comparison indicated that the calculated and measured flow stress-strain relationships for 30 N represent a good match for the prediction of the saturation stress. However, for the initial part of the curve, a deviation between the experimental and

calculated curves can be observed—perhaps due to the fact that the temperatures observed in the wear experiments increased slowly, and were not constant at the beginning of the test for the application of a 30 N normal load (Figure 6.22). Therefore, the thermal softening constitutive equation considered in this study was deemed an acceptable tool for representing the influence of the thermal softening processes on the mechanical behaviour of the aluminum alloys observed during sliding wear.

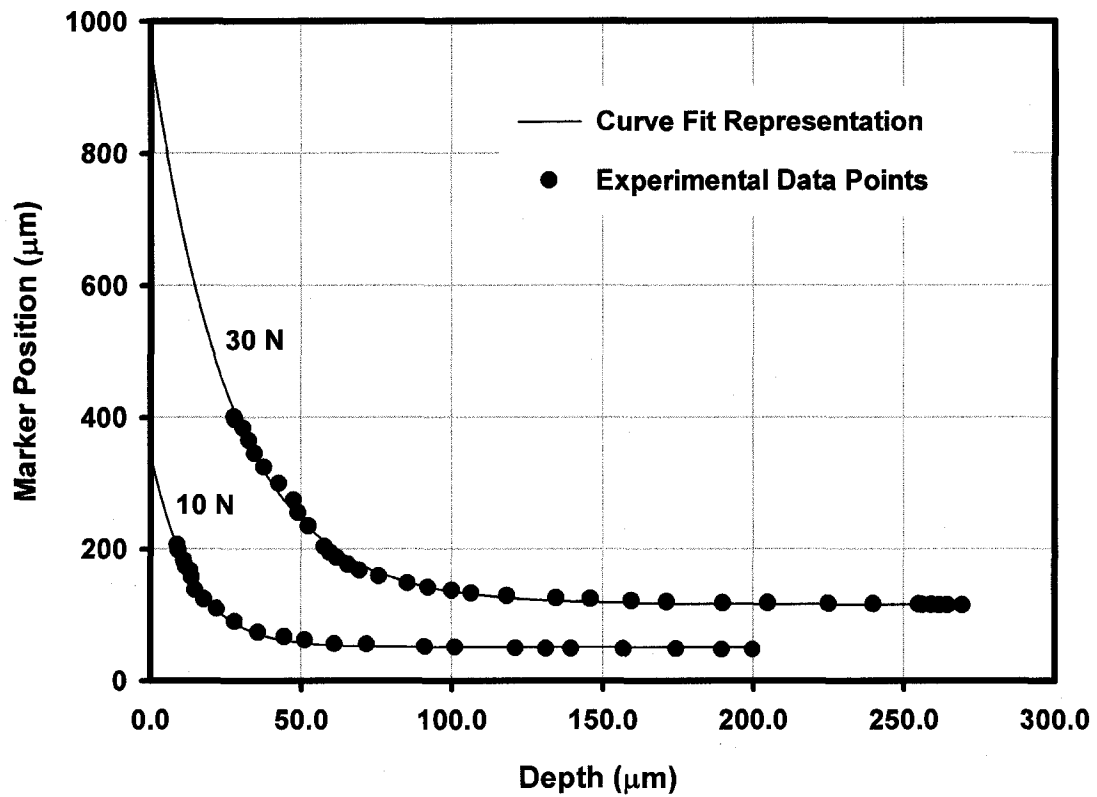


Figure 6.18: Marker position in the 1100 Al samples after wear tests with 10 N and 30 N normal loads and 1 m/s sliding velocity.

Table 6.12: Coefficients A , B and C in the Equation 6.1 for the 1100 Al.

Load (N)	Sliding Distance (m)	Sliding Velocity (m/s)	A (μm)	B (μm)	C ($1/\mu\text{m}$)
10	1000	1.0	50.7	293.8	0.07423
30	1000	1.0	116.6	838.9	0.03789

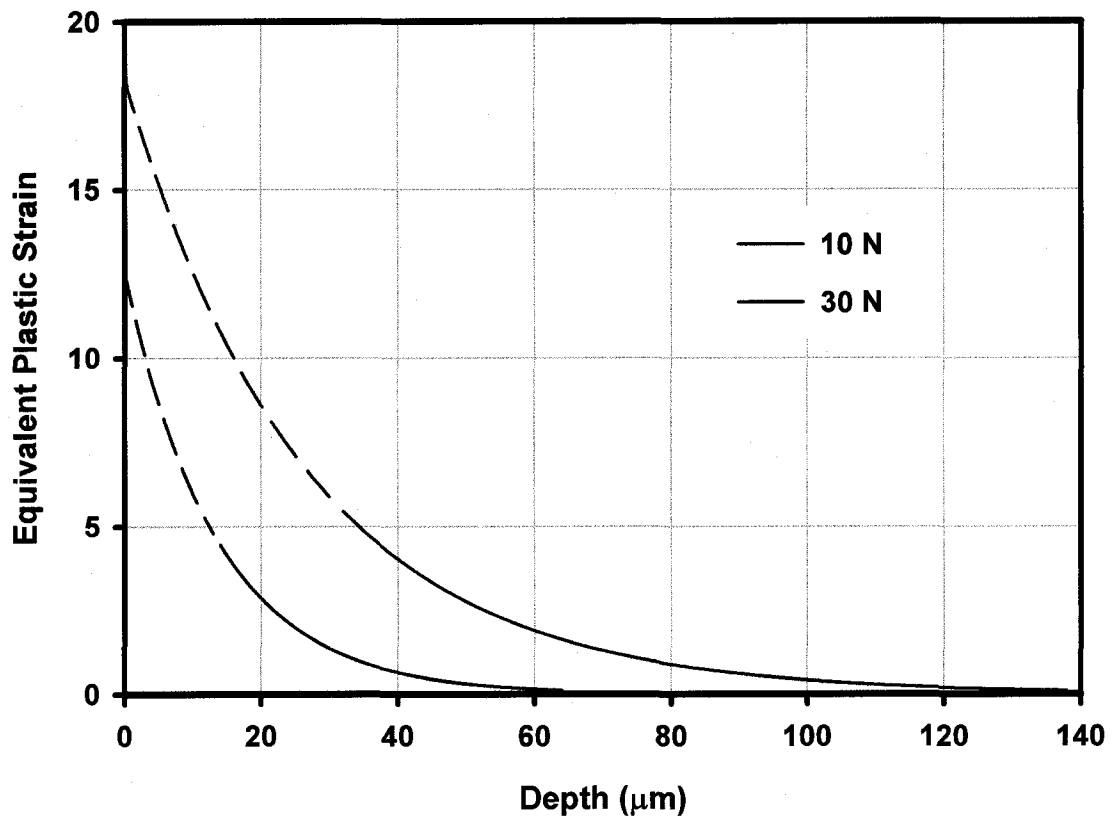


Figure 6.19: Equivalent plastic strain vs. depth below the worn surfaces at different loads (sliding distance = 1000m, sliding velocity = 1 m/s).

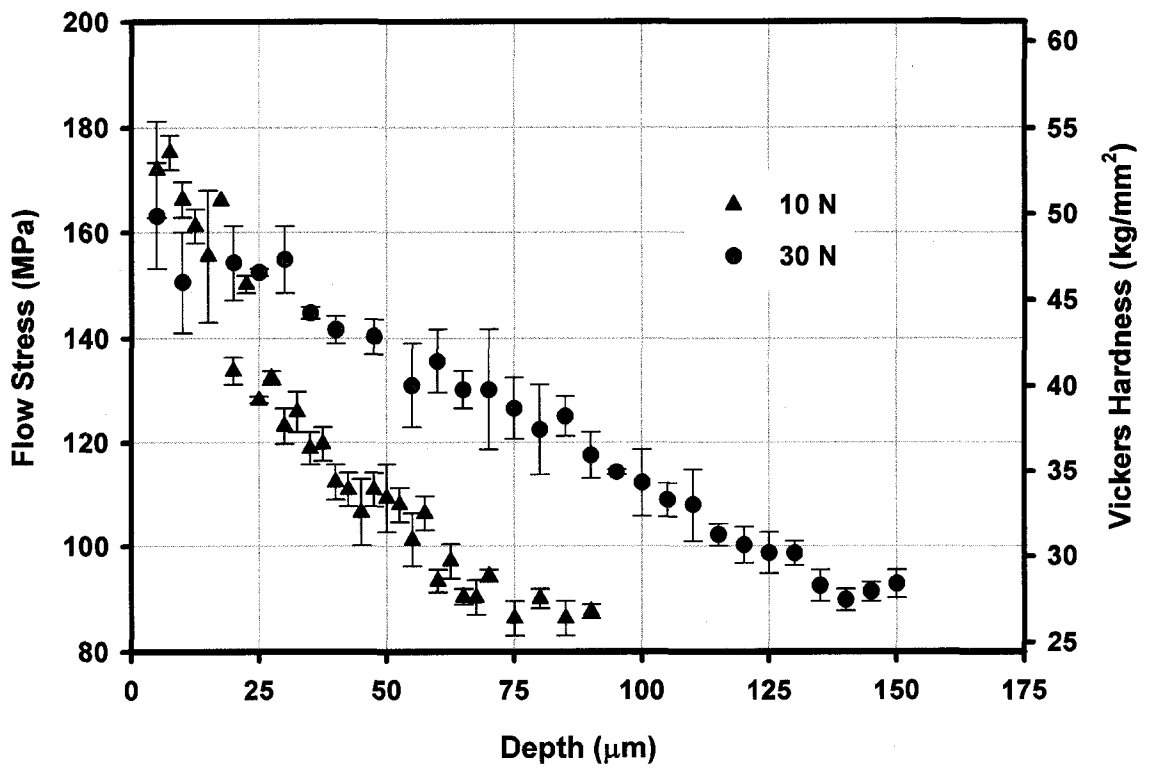


Figure 6.20: Flow stress (Vickers hardness) vs. depth below the worn surface at different loads (sliding distance = 1000m, sliding velocity = 1 m/s).

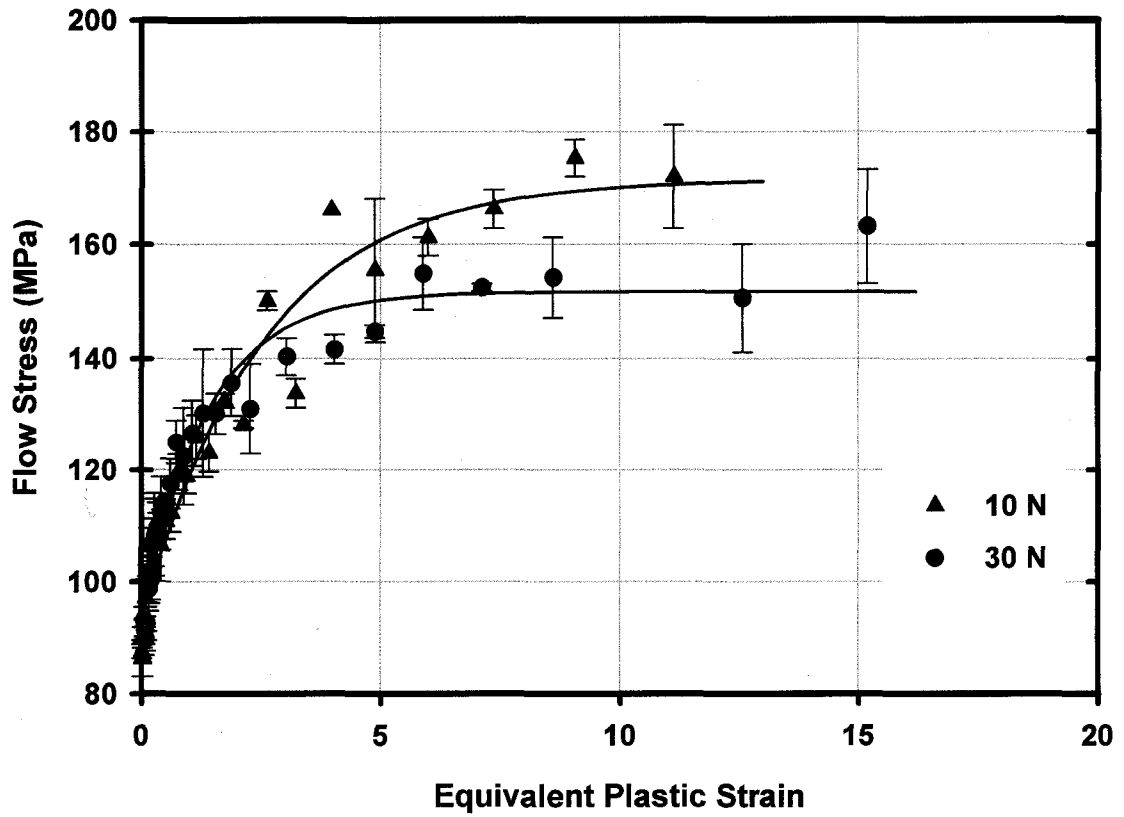


Figure 6.21: Cumulative flow stress-strain curve of the 1100 Al material for two different loads.

Table 6.13: Flow stress-plastic strain curve constants of the 1100 Al material for two different loads.

Load (N)	σ_s (MPa)	σ_0 (MPa)	ϵ_c
10	171.6	93.2	2.52
30	151.6	92.4	1.35

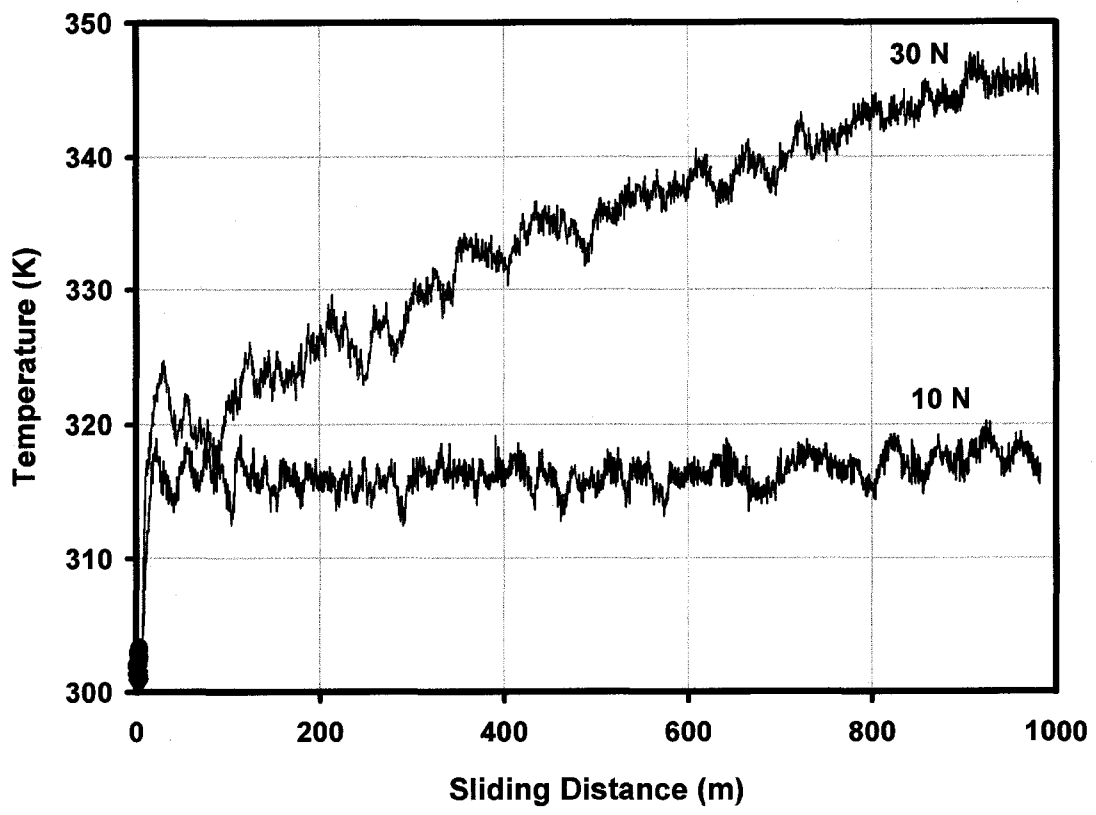


Figure 6.22: Temperature distribution at the contact surface for two different loads.

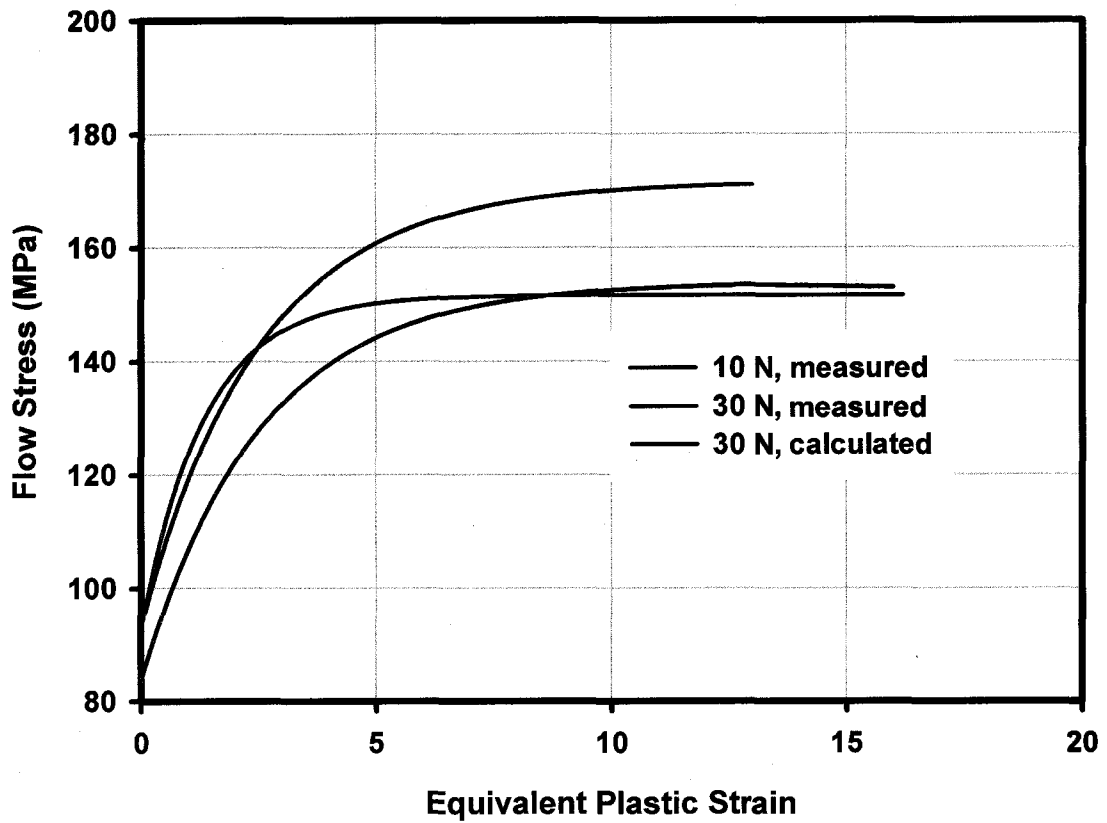


Figure 6.23: Experimental cumulative flow stress-strain behaviour of the 1100 Al material (measured) and calculated stress-strain relationship by using thermal softening equation (Equation 4.12).

CHAPTER 7

RESULTS AND DISCUSSION

7.1. SLIDING CONTACT BETWEEN SOLIDS

This section presents the Eulerian FE model's results on the accumulation of subsurface stresses and strains in the 356 Al alloy during sliding contacts. Details of the Eulerian finite element model can be found in Section 4.2, and all results are based on the moment when the asperity was at the mid-point of its sliding motion over the 356 Al alloy.

7.1.1. VARIATIONS OF STRESSES AND STRAINS WITH NUMBER OF SLIDING CONTACTS

The von Mises stress distribution in the 356 Al surface for a sliding velocity of 10 m/s and a normal load of 300 N/mm is presented in Figure 7.1 as fringe plots for the results after the initial (first), the last (seventh) and an intermediate (fourth) sliding contacts. The position of the maximum von Mises stress was located on the surface for all sliding contacts—reading between 276 MPa and 331 MPa after the first contact, and between 331 MPa and 386 MPa after the seventh contact. In addition, the position of the maximum von Mises stress was not centred under the asperity, but rather observed at the leading edge and in front of the asperity. Equivalent plastic strain distributions in the 356 Al surface after the initial, the last and the fourth sliding contacts are illustrated in Figure 7.2 as fringe plots. The maximum plastic strain was also observed at the contact surface, and calculated as 2.3, 5.7 and 8.0 after the first, fourth and seventh asperity contacts.

The fringe plots effectively display the overall results of a finite element analysis. However, they only provide a general understanding of the subsurface stress and strain distributions by averaging the results obtained from many elements. In order to gain more accurate stress and strain data along the depth of the mesh, the results from some elements in the 356 Al alloy were recorded in the numerical simulation—specifically the

row of elements at the mid-point of the 356 Al mesh. Figures 7.3 and 7.4 illustrate the accumulation of subsurface stresses and strains at the mid-point of the 356 Al alloy after multiple sliding contact cycles for a sliding velocity of 10 m/s and a normal load of 300 N/mm. In these figures, the steel asperity is at the mid-point of the 356 Al half-space. In addition, in Figures 7.3 and 7.4, the depth below the 356 Al alloy surface was presented as a dimensionless parameter (z/a)—where z is the depth beneath the contact surface and a is the asperity diameter ($=2$ mm). The highest von Mises stress calculated after a sliding contact of the first asperity was 290 MPa at a normalized depth of 0.05, with a von Mises stress of 375 MPa at the same depth after the passage of the seventh asperity. The results indicated that subsurface stresses reached a steady state value, with a finite number of contacts. The accumulation of the stress between the first and the last asperities was approximately 29 %, while it was only 1.7 % between the sixth and the seventh asperities. Unlike the von Mises stress, the plastic strains continued to increase as the number of the sliding contacts increased. The maximum equivalent plastic strain was approximately 2 at a normalized depth of 0.05 after the passage of the first asperity, and reached a value of 7.6 after the passage of the last asperity. The numerical results indicated that there was no significant plastic strain below a normalized depth of 0.5 ($z/a > 0.5$) for the loading condition investigated.

7.1.2. VARIATIONS OF HYDROSTATIC PRESSURE WITH NUMBER OF SLIDING CONTACTS

The hydrostatic pressure distribution in the 356 Al alloy is presented in Figure 7.5 as fringe plots. Figure 7.6 illustrates the variation of the subsurface hydrostatic pressure in the depth of material below the contact surface after each contact cycle. The resulting observations indicated that the hydrostatic pressure was much higher than the von Mises stress in the close vicinity of the contact region. The maximum hydrostatic pressure was 504 MPa, 637 MPa and 700 MPa after the first, fourth and seventh asperity contacts—approximately 75 to 90 % higher than the maximum von Mises stresses observed at the contact surface. Similar to the position of the maximum von Mises stress, the maximum hydrostatic pressure was also not distributed symmetrically under the asperity; but rather positioned at the leading edge.

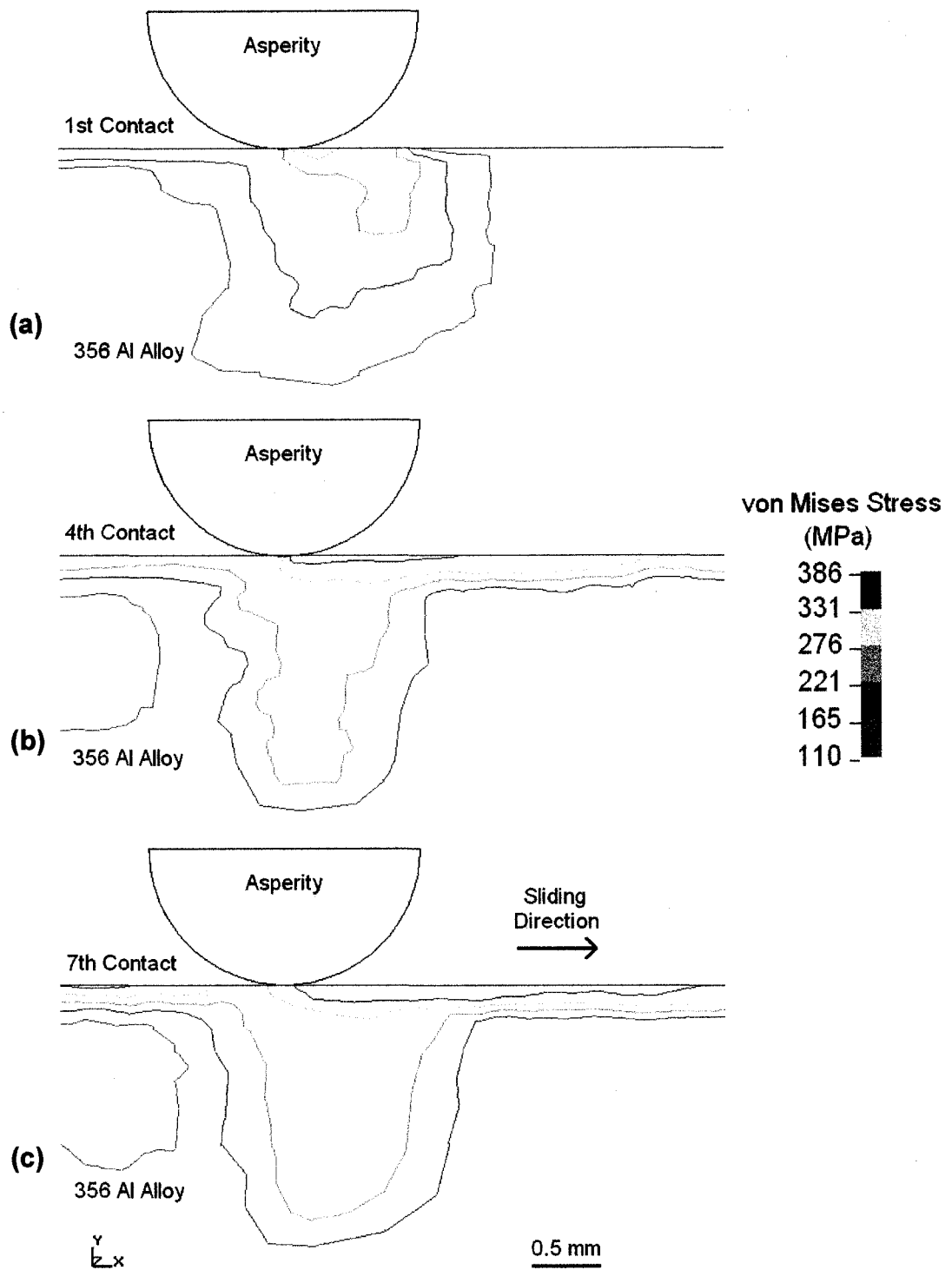


Figure 7.1: von Mises stress (in MPa units) distribution in the 356 Al alloy after multiple sliding contacts: (a) after the first contact, (b) after the fourth contact and (c) after the seventh contact (Sliding velocity: 10 m/s, Normal load: 300 N/mm, Equation 4.1, Eulerian model).

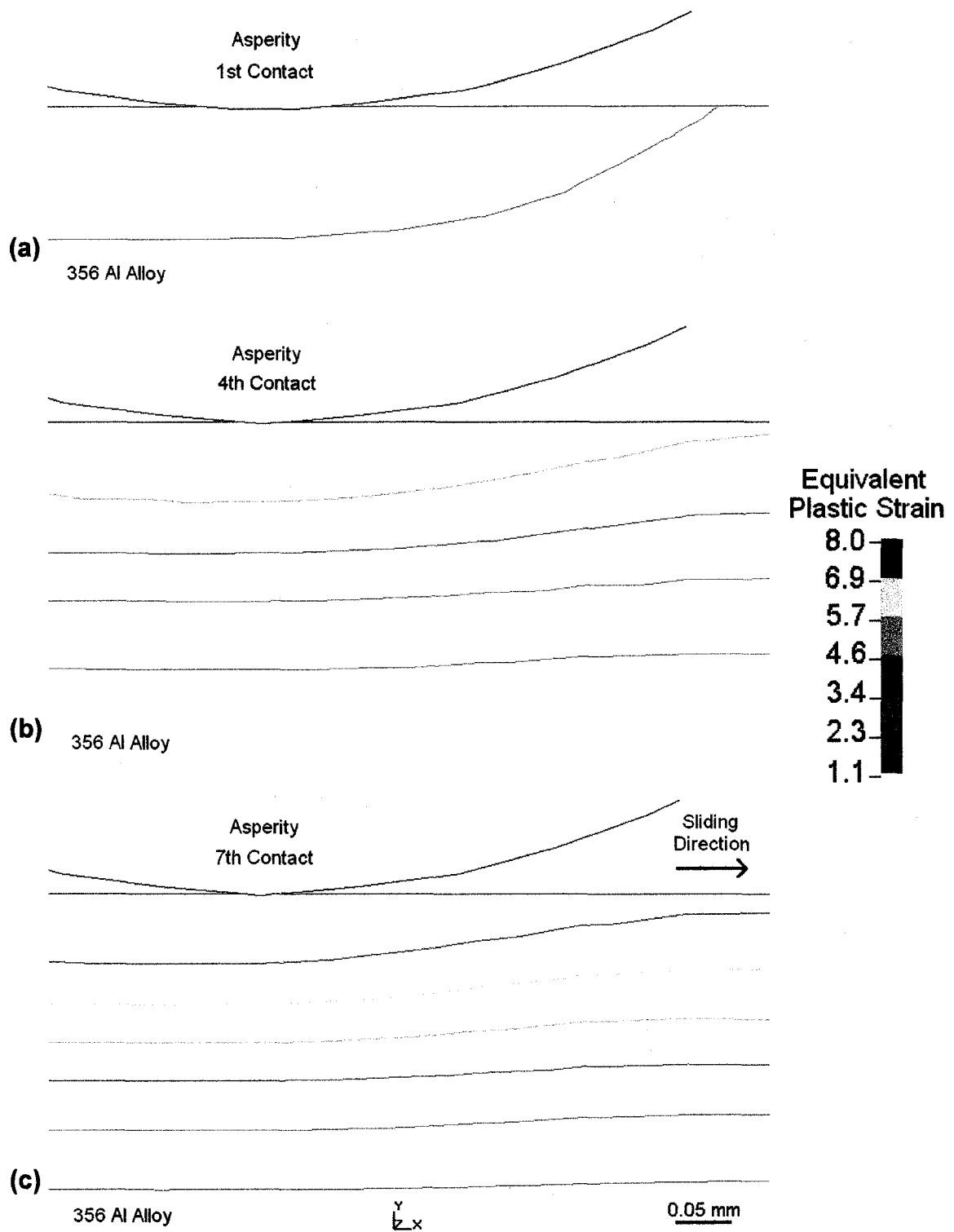


Figure 7.2: Equivalent plastic strain distribution in the 356 Al alloy after multiple sliding contacts: (a) after the first contact, (b) after the fourth contact and (c) after the seventh contact (Sliding velocity: 10 m/s, Normal load: 300 N/mm, Equation 4.1, Eulerian model).

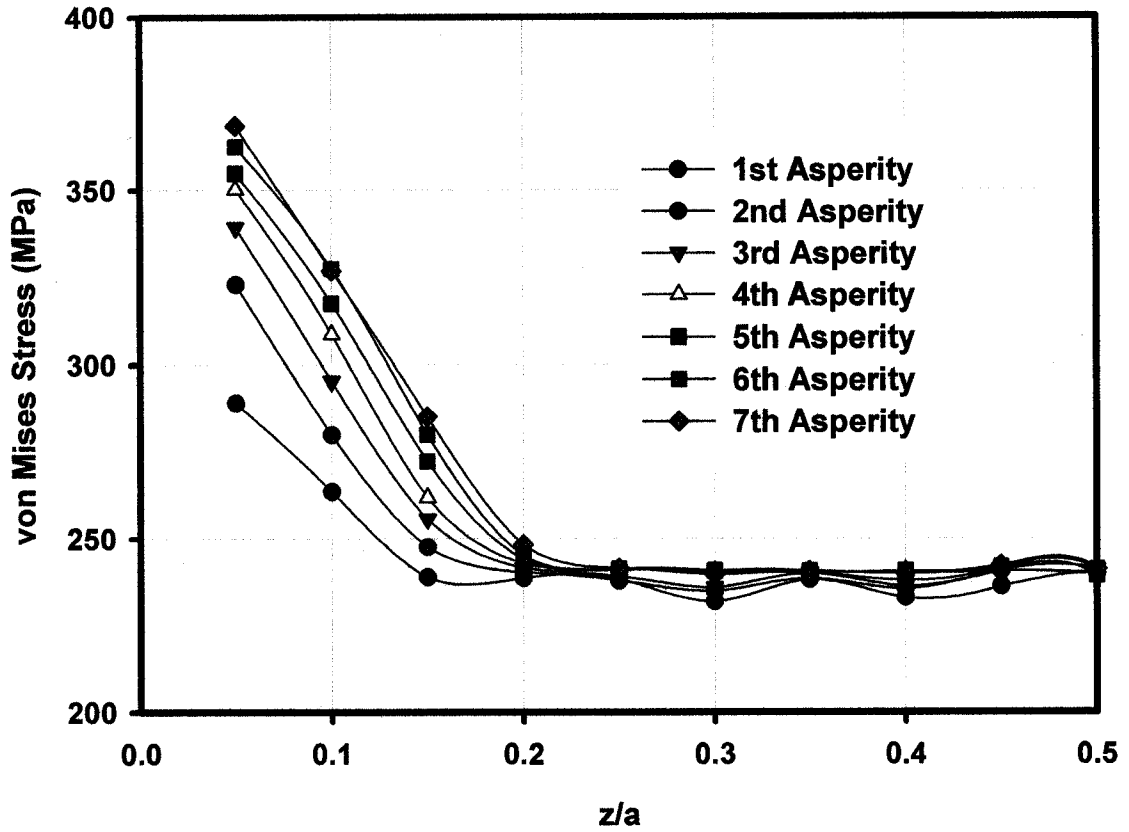


Figure 7.3: Increase in subsurface stresses with increasing number of the asperity contacts at the mid-point of the 356 Al alloy (Sliding velocity: 10 m/s, Normal load: 300 N/mm, Equation 4.1, Eulerian model). (z is the depth beneath the contact surface and a is the asperity diameter).

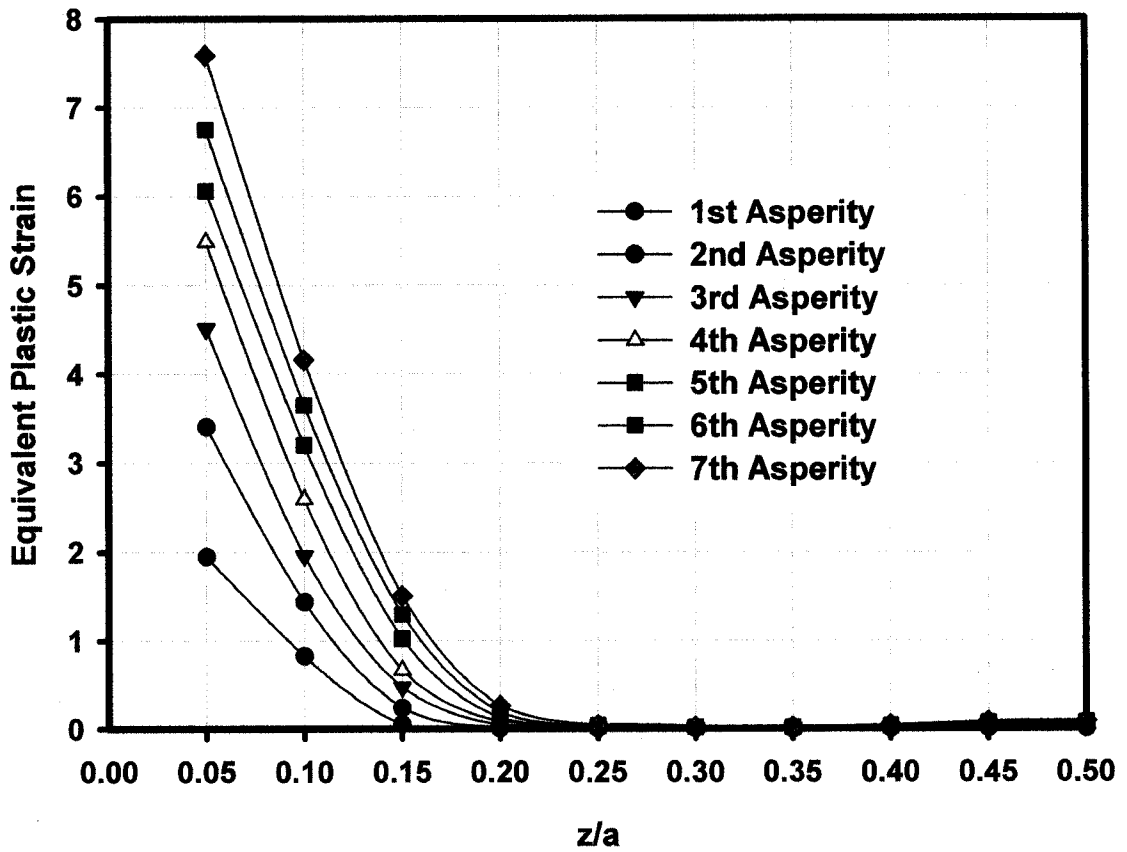


Figure 7.4: Increase in subsurface equivalent plastic strains with increasing number of the asperity contacts at the mid-point of the 356 Al alloy (Sliding velocity: 10 m/s, Normal load: 300 N/mm, Equation 4.1, Eulerian model). (z is the depth beneath the contact surface and a is the asperity diameter).

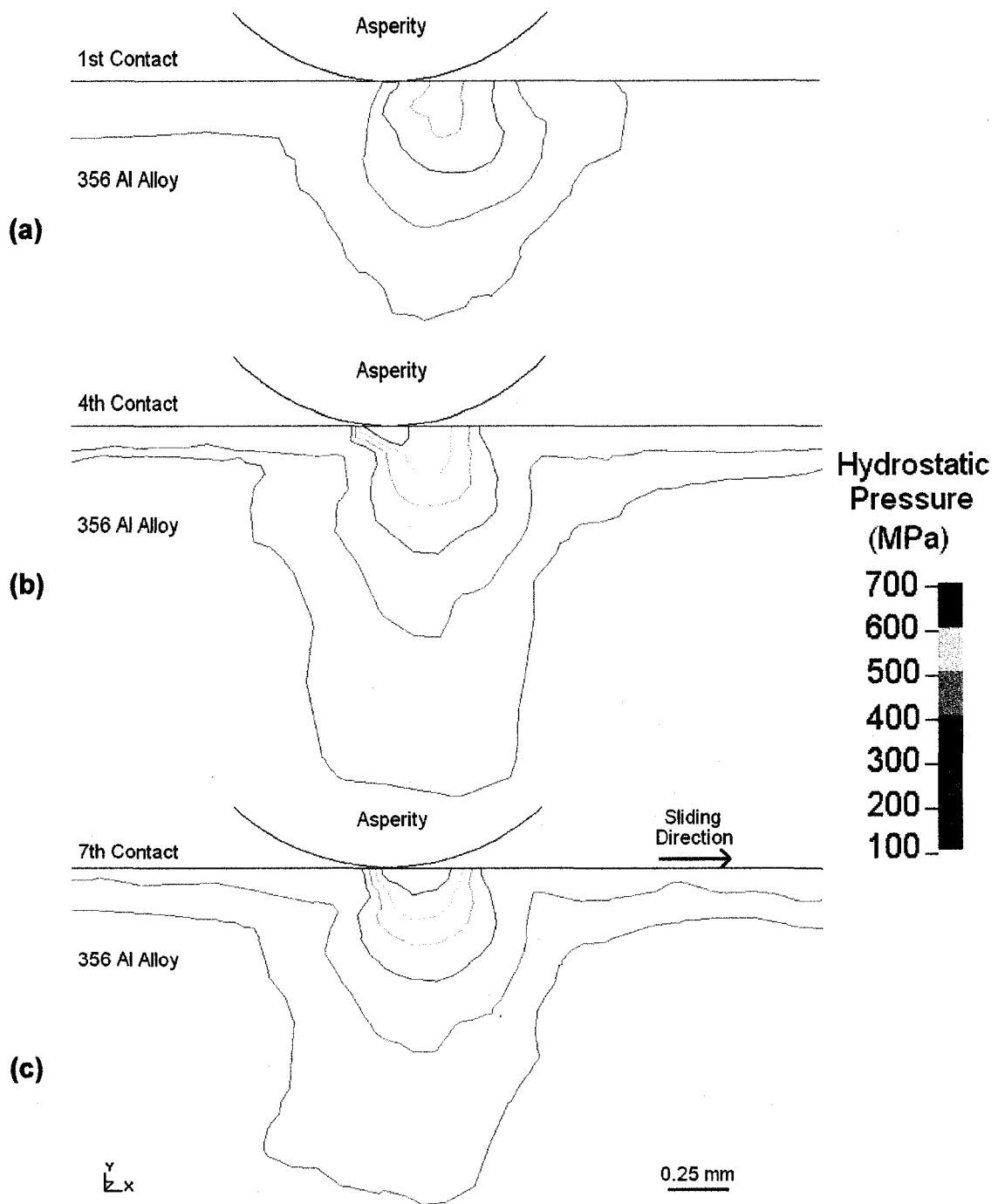


Figure 7.5: Hydrostatic pressure (in MPa units) distribution in the 356 Al alloy after multiple sliding contacts: (a) after the first contact, (b) after the fourth contact and (c) after the seventh contact (Sliding velocity: 10 m/s, Normal load: 300 N/mm, Equation 4.1, Eulerian model).

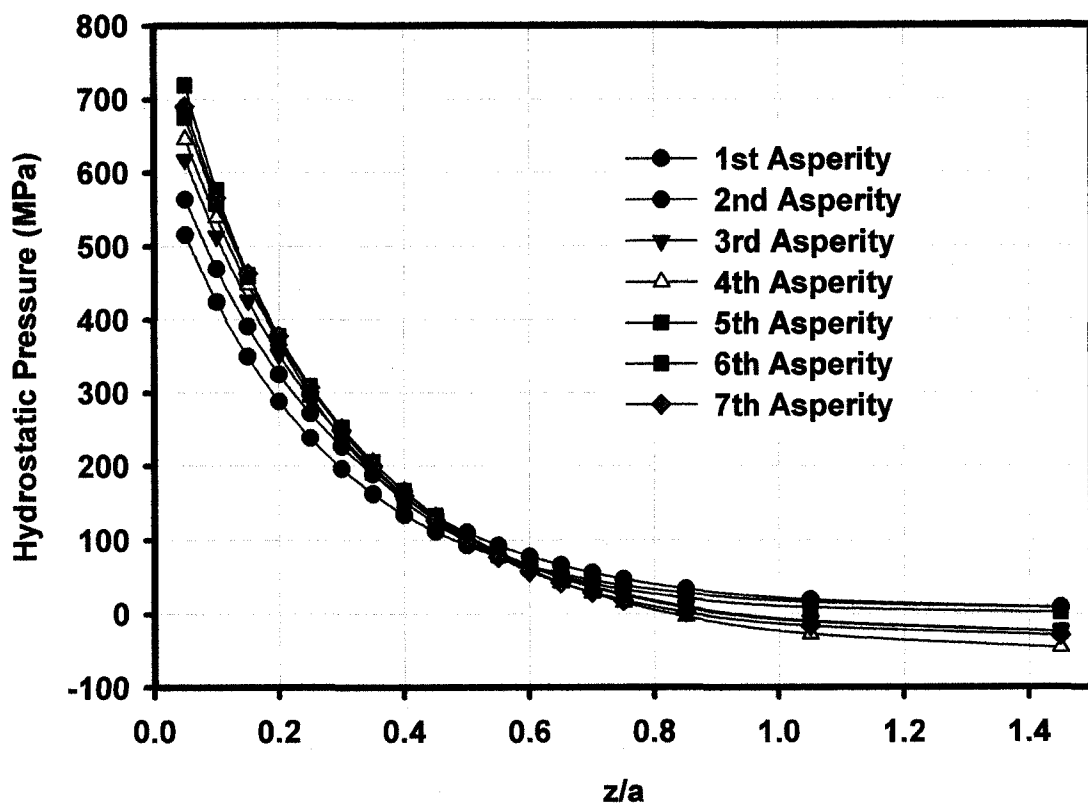


Figure 7.6: Accumulation of the hydrostatic pressure with increasing number of the asperity contacts at the mid-point of the 356 Al alloy (Sliding velocity: 10 m/s, Normal load: 300 N/mm, Equation 4.1, Eulerian model). (z is the depth beneath the contact surface and a is the asperity diameter).

7.1.3. SUBSURFACE STRAIN RATE DISTRIBUTION

Figure 7.7 shows the subsurface strain rate distribution at the mid-point of the 356 Al alloy after multiple asperity contacts (sliding velocity: 10 m/s and normal load: 150 N/mm). At a normalized depth of 0.05, the strain rate ranged from $3.35 \times 10^4 \text{ s}^{-1}$ to $5.27 \times 10^4 \text{ s}^{-1}$ between the first and last asperity contacts. However, the strain rate decreased quickly to zero at the normalized depth of 0.5.

7.1.4. EFFECT OF NORMAL LOAD

Loads of 200 N/mm and 300 N/mm were applied to the asperities to study the effect of the applied normal load on the distributions of subsurface stresses and strains. Up to 14 asperities were considered for 200 N/mm loading. Figures 7.8 and 7.9 show how the stresses and strains were affected by the change of the normal load. A decrease in the normal load from 300 N/mm to 200 N/mm caused a decrease in the von Mises stresses of approximately 10 %, and in the plastic strains by 50 % near the contact surface. In addition, the normalized depth of the plastically yielded region decreased from 0.5 to 0.3.

7.1.5. EFFECT OF FRICTION

Several coefficients of friction (μ) ranging from 0.0 to 0.8 were considered in the contact algorithm to investigate the effect of friction on the subsurface stresses and strains. Figure 7.10 illustrates the subsurface maximum von Mises stress and equivalent plastic strain values observed after each contact cycle for different values of μ . In comparison, the experimentally defined, stress/strain relationship is also included (solid line in Figure 7.10). The employment of the Eulerian finite element formulation for the 356 Al alloy revealed significantly high strains ($\epsilon_p \geq 20$) in the 356 Al alloy. With the implementation of friction, the subsurface stresses reached a saturation value of 400 MPa.

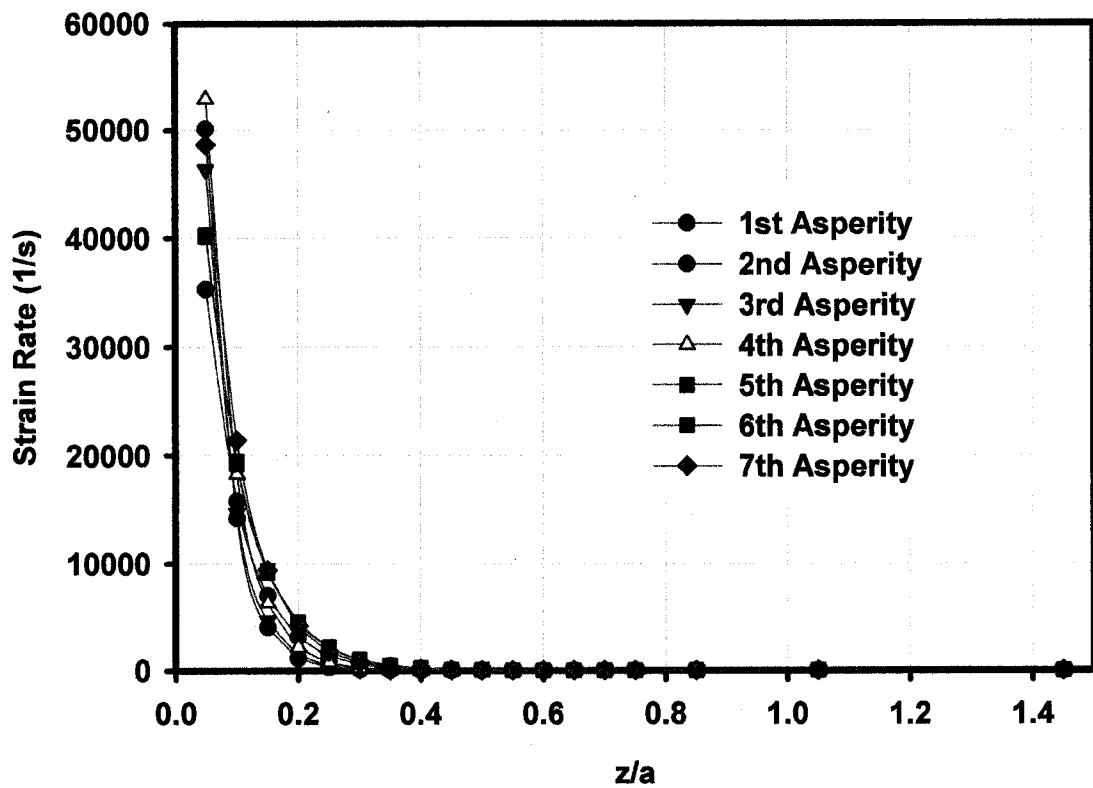


Figure 7.7: Change of the strain rate with multiple sliding contacts at the mid-point of the 356 Al alloy (Sliding velocity: 10 m/s, Normal load: 300 N/mm, Equation 4.1, Eulerian model).

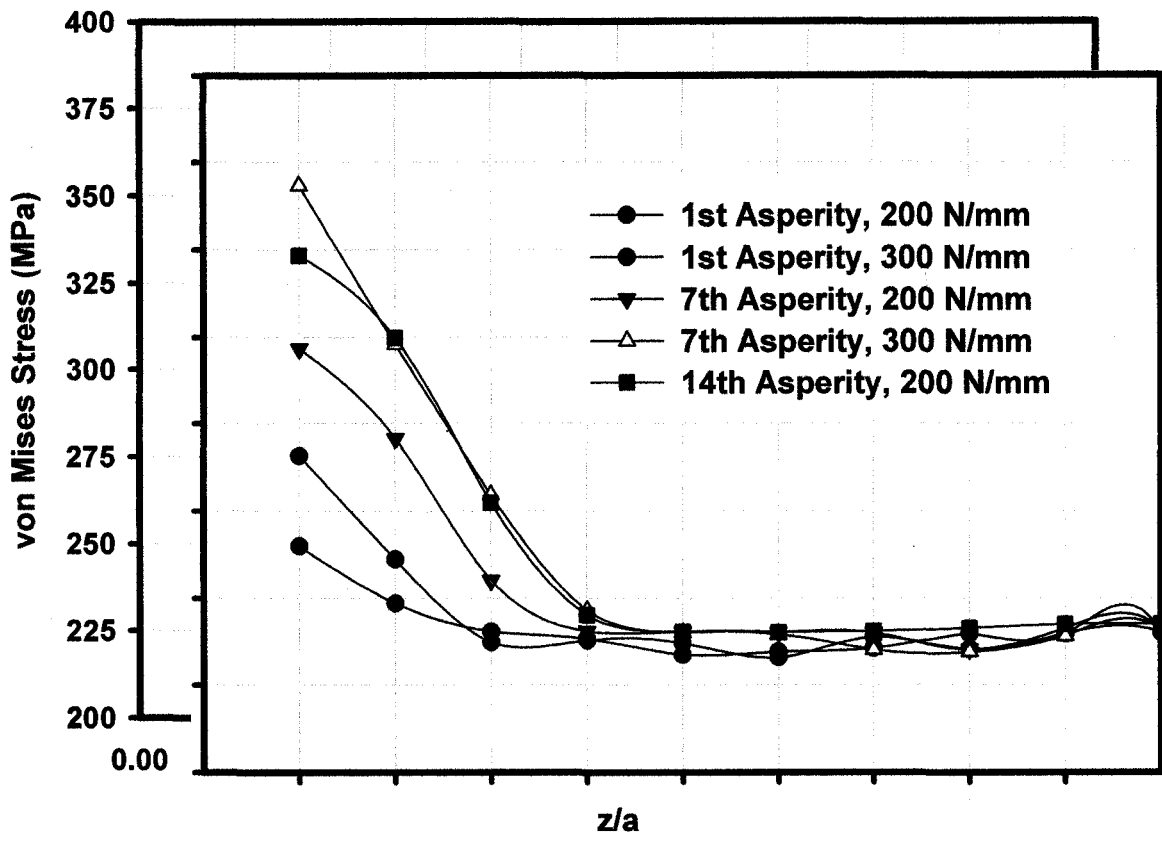


Figure 7.8. Effect of the normal load on the distribution of von Mises stress (Sliding velocity: 10 m/s, Equation 4.1, Eulerian model).

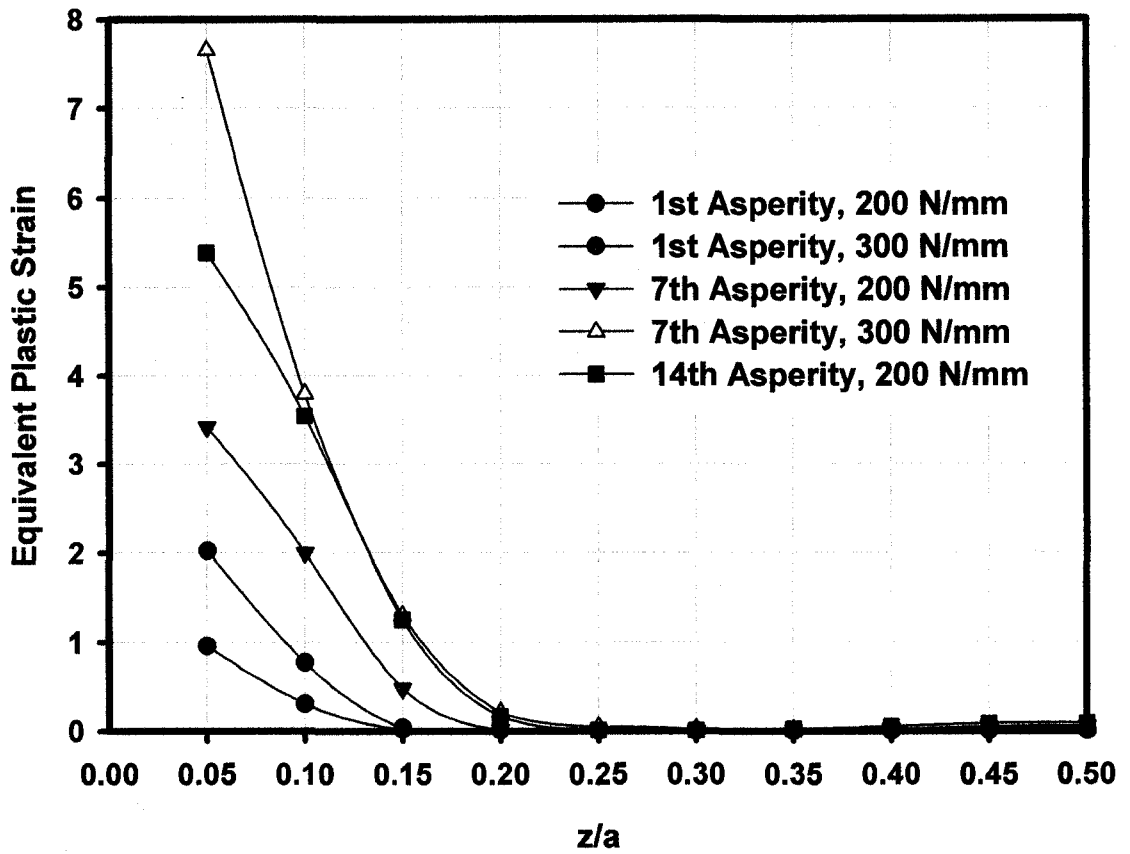


Figure 7.9. Effect of the normal load on the distribution of subsurface strains (Sliding velocity: 10 m/s, Equation 4.1, Eulerian model).

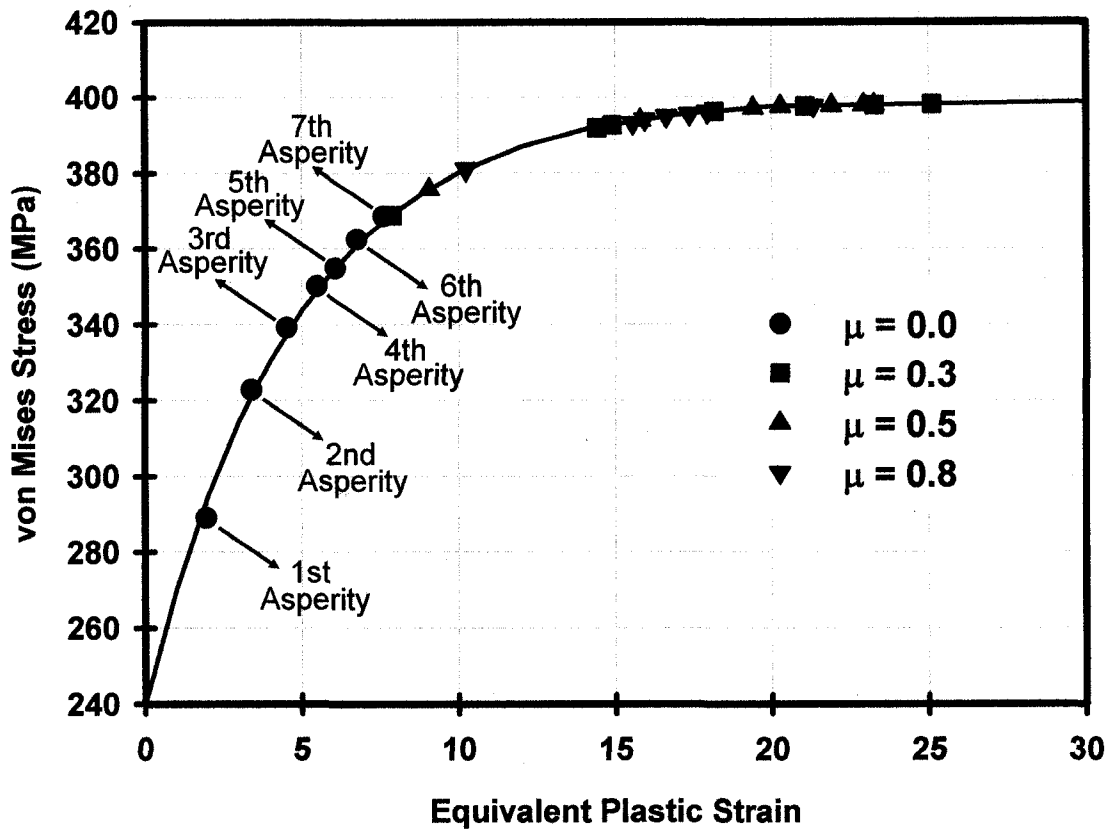


Figure 7.10: The effect of coefficient of friction ($\mu=0.0$ to 0.8) on the maximum stress and strain values. (The order of the asperities, and the resulting stresses and strains are indicated for $\mu=0.0$. The continuous curve is the experimentally defined stress/strain relationship).

Figure 7.11 presents the von Mises stress and the hydrostatic pressure distributions below the contact surface for coefficients of friction of 0.0 and 0.3, when the seventh asperity was at the mid-point of the 356 Al alloy. The magnitude of the hydrostatic pressure was approximately 700 MPa near the contact surface, compared to 375 MPa for the von Mises stress at the same location for $\mu=0.0$. The hydrostatic pressure was much larger than the effective stress at the surface to suppress the damage. However, the magnitude of the hydrostatic pressure decreased significantly faster than the von Mises stress—the two curves intersecting at a normalized depth of approximately 0.35 below the contact surface. The state of stress at this depth is such that the effective stress may be large enough to initiate void growth, while the hydrostatic pressure may not be significant enough to suppress it. The combination of an increase in the von Mises stress and a reduction in the hydrostatic pressure with $\mu=0.3$ (Figure 7.11) resulted in the movement of the maximum damage accumulation depth towards the surface ($z/a=0.25$).

7.1.6. EFFECT OF SLIDING VELOCITY

Figure 7.12 shows the effect of the sliding velocity on the distribution of equivalent plastic strain in the layers adjacent to the surface of the 356 Al alloy after sliding contact with only one asperity. When the sliding velocity was decreased from 40 m/s to 0.5 m/s, the maximum plastic strain at the surface increased approximately 40 %. In addition, a decrease in the sliding velocity increased the normalized depth of the plastically yielded region from approximately 0.4 to 1.0, which is a dynamic effect. When the sliding velocity is decreased, the force applied to the asperities in the X direction also decreases during the steady state motion (see Section 6.2.3), prompting a decrease in the penetration of the asperities into the aluminum alloy, as well as a decrease in the overall deformation.

7.1.7. EFFECT OF DISTANCE BETWEEN ASPERITIES

In order to analyze the interactions between the stress and strain fields of consecutive asperities, the distance between the asperities was altered. In initial simulations, the distance between the asperities was 9 mm. Distances of 6 mm, 3 mm

and 2 mm were also investigated. Figure 7.13 presents the accumulation of plastic strain at a specific depth (100 μm) with asperity contacts at different asperity distances. A dimensionless parameter was defined—namely d/ϕ , where d represents the distance between the asperities and ϕ is the asperity diameter. Figure 7.13 indicates that there was not a significant difference in the stress strain distribution for asperity distances of 9 and 6 mm ($d/\phi=4.5$ and $d/\phi=3$, respectively). For lower values of d/ϕ , plastic strain increased slightly.

In this section, the results of the accumulation of subsurface stresses and strains—including von Mises stress, equivalent plastic strain, strain rate and hydrostatic pressure—in the 356 Al alloy have been presented during sliding contacts. The Eulerian element formulation proved successful for modeling the extensive deformation of the 356 Al material observed during sliding wear applications. Experimental findings show that the temperature increase in contacting solids might have an effect during high plastic deformation applications, possibly changing the deformation characteristics. In addition, this investigation's numerical findings indicate that strain rates might also be high during sliding contacts—and therefore capable of changing the mechanical characteristics of the 356 Al alloy. The following section presents investigation results that explore the influences of thermal softening and strain rate hardening on the distribution of subsurface stresses and strains in the 356 Al alloy.

7.2. EFFECTS OF TEMPERATURE AND STRAIN RATE ON THE SUBSURFACE DAMAGE

This section presents the results of the Lagrangian coupled thermal and structural finite element model. Details of the finite element model can be found in Section 4.3.

7.2.1. VARIATIONS OF SUBSURFACE STRESSES AND STRAINS WITH NUMBER OF SLIDING CONTACTS

This section presents subsurface stress and strain predictions from a numerical model that considers strain hardening, strain rate and thermal effects for a sliding velocity of 10 m/s and a normal load of 150 N/mm.

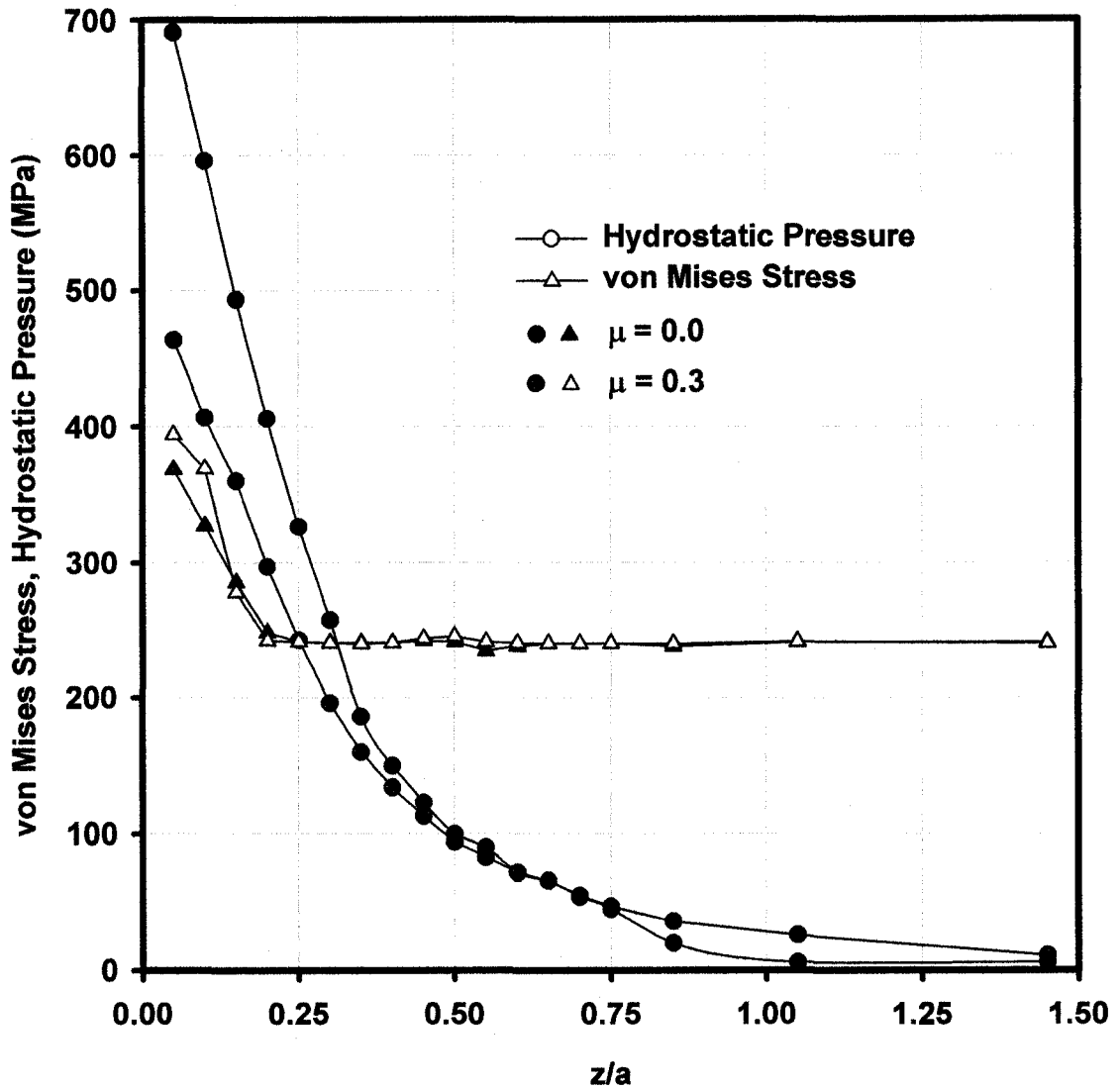


Figure 7.11: The hydrostatic pressure and the von Mises stress distributions below the surface of the 356 Al after passage of the seventh asperity for $\mu=0.0$ and $\mu=0.3$ (Sliding velocity: 10 m/s, Normal load: 300 N/mm, Equation 4.1, Eulerian model).

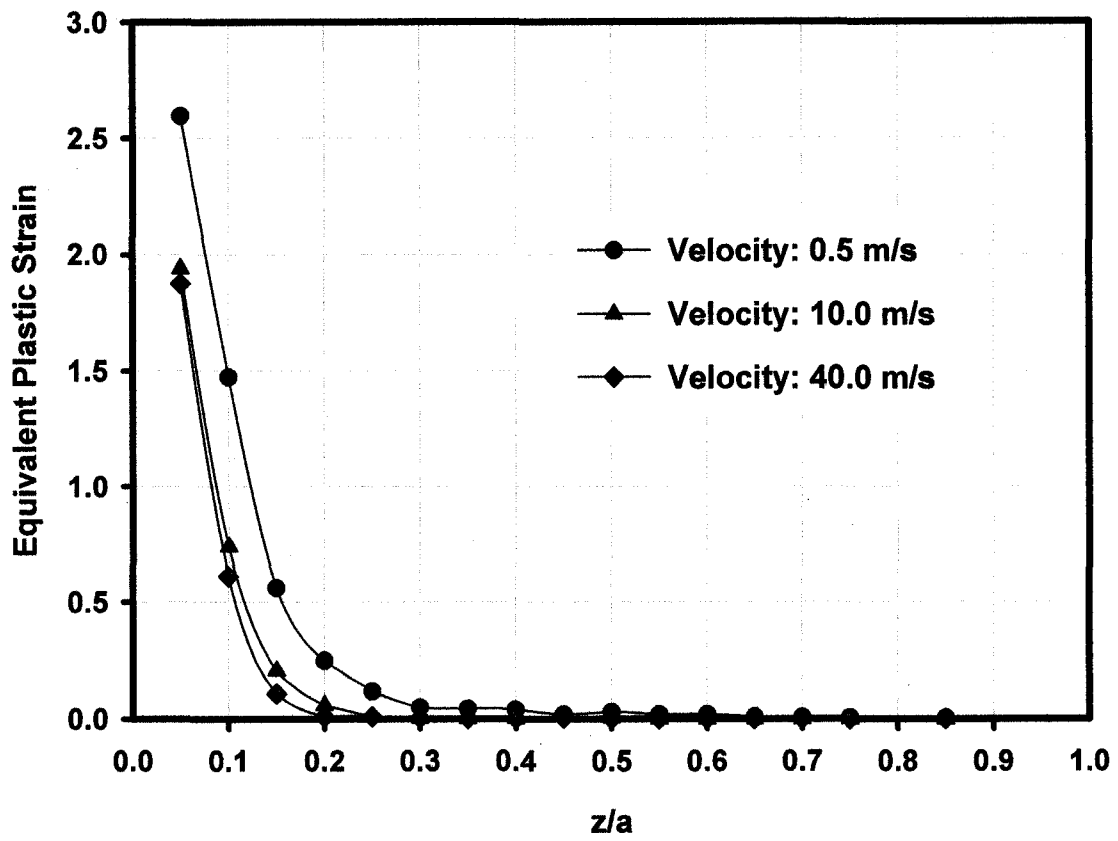


Figure 7.12: Effect of the sliding velocity on the distribution of equivalent plastic strain under the surface of 356 Al alloy (Normal load: 300 N/mm, Equation 4.1, Eulerian model, values after one asperity contact).

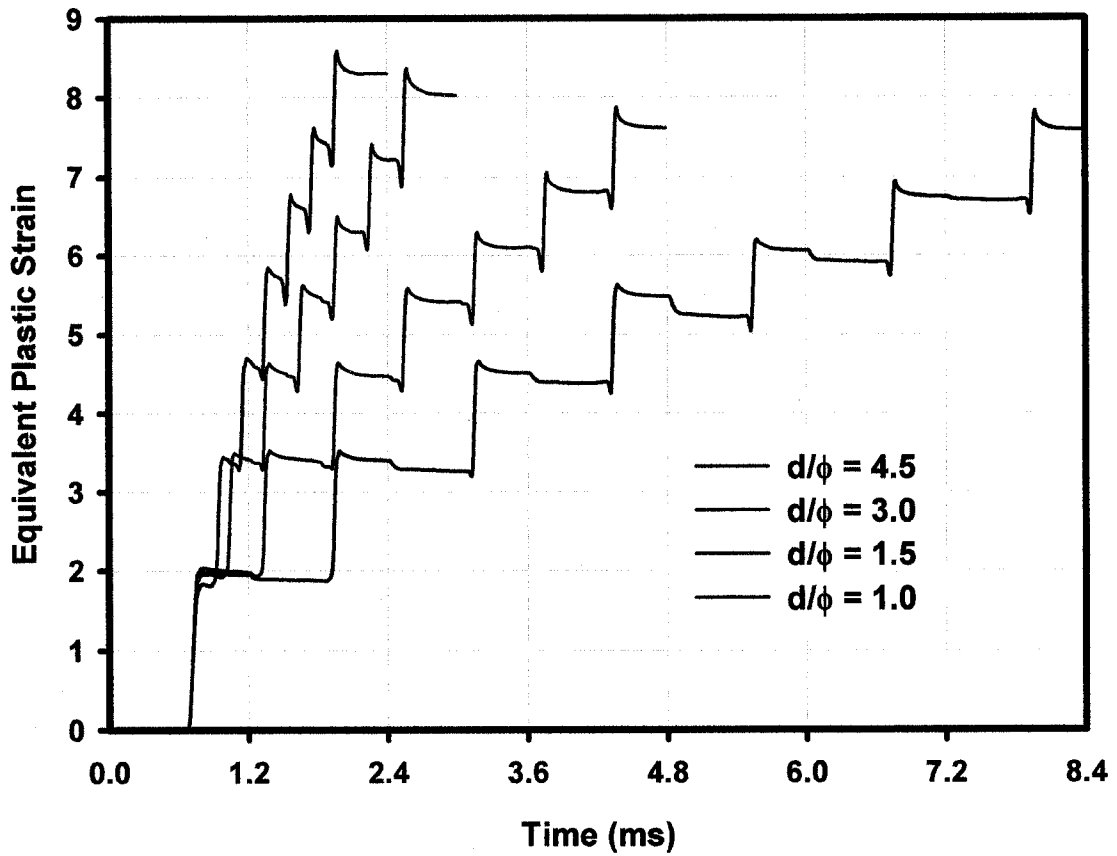


Figure 7.13: Effect of the asperity distance on the distribution of equivalent plastic strain at 100 μm depth (d represents the distance between the asperities and ϕ is the asperity diameter) (Sliding velocity: 10 m/s, Normal load: 300 N/mm, Equation 4.1, Eulerian model).

Figure 7.14 illustrates the distribution of the von Mises stress in the 356 Al half-space after the initial (first), last (seventh) and an intermediate (fourth) sliding contacts as fringe plots. Variations in the subsurface von Mises stress with the depth of material below the contact surface after each contact cycle is shown in Figure 7.15, where the steel asperity is at the mid-point of the 356 Al half-space. The X-axis in Figure 7.15 is a dimensionless normalized depth (z/a), where z is the depth beneath the contact surface and a is the counterface diameter ($= 2$ mm). The von Mises stress at the contact surface was 513.6 MPa after the first contact, 585.5 MPa after the fourth and 596.9 MPa after the seventh. The von Mises stresses observed at the surface reached a steady state after the fourth contact, with a 14 % increase between the first and the fourth contacts, but only a 2 % increase after the fourth. The maximum von Mises stress was positioned just under the asperity, close to the leading edge. A plateau was observed in the distribution of the von Mises stress approximately at $z/a = 0.15$. This plateau was caused by dynamic effects resulting from the inertia of the system. A decrease in the plateau was observed with increasing asperity contacts, which is caused by the decrease in the strain rates (Figure 7.22) and increase in the temperature (Figure 7.21) with continues asperity contacts.

Figure 7.16 shows the equivalent plastic strains in the 356 Al half-space as fringe plots. Figure 7.17 displays the variation of plastic strains as a function of z/a at different contact cycles. The maximum value of plastic strain was found at the surface—specifically 0.19, 0.78 and 1.30 for the first, fourth and seventh contacts. The plastic strains were less than 0.01 in the subsurface material layers at $z/a > 0.2$.

7.2.2. VARIATION OF HYDROSTATIC PRESSURE WITH NUMBER OF SLIDING CONTACTS

Figure 7.18 presents the fringe plots of the hydrostatic pressure distribution, obtained after multiple asperity contacts at a sliding velocity of 10 m/s and a normal load of 150 N/mm. Figure 7.19 reveals the hydrostatic pressure distribution at the mid-point of the 356 Al alloy at different contact cycles. The value of the hydrostatic pressure at the contact surface did not change with increasing asperity contact numbers. It was 1150 ± 100 MPa between the first and seventh contacts. The value of the hydrostatic pressure did however, decrease quickly with the z/a . At $z/a > 0.1$, it was less than the values of

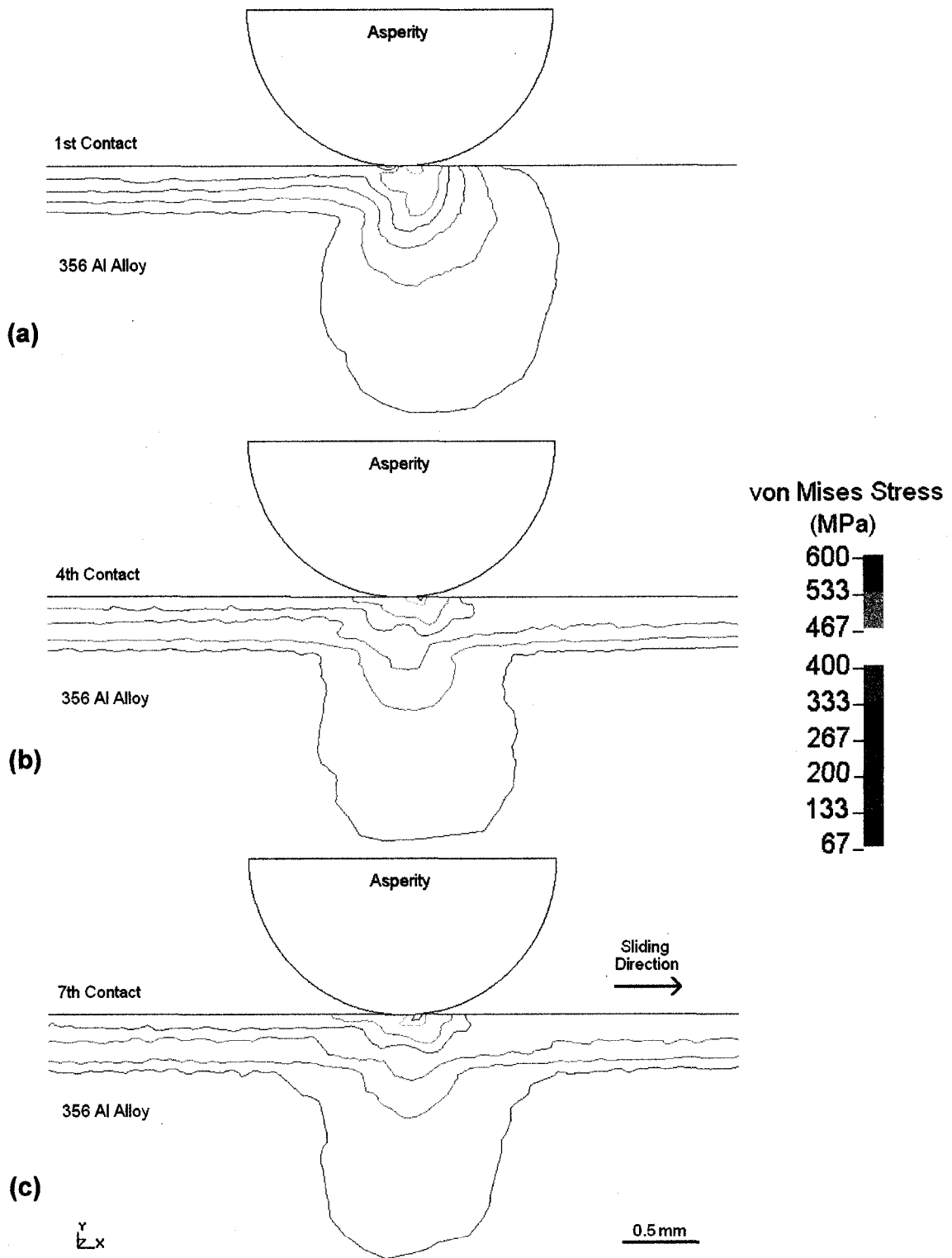


Figure 7.14: von Mises stress (MPa) distribution in the 356 Al half-space after multiple sliding contacts: (a) after the first contact, (b) after the fourth contact and (c) after the seventh contact (Sliding velocity: 10 m/s, Normal load: 150 N/mm, Equation 4.5, Lagrangian model).

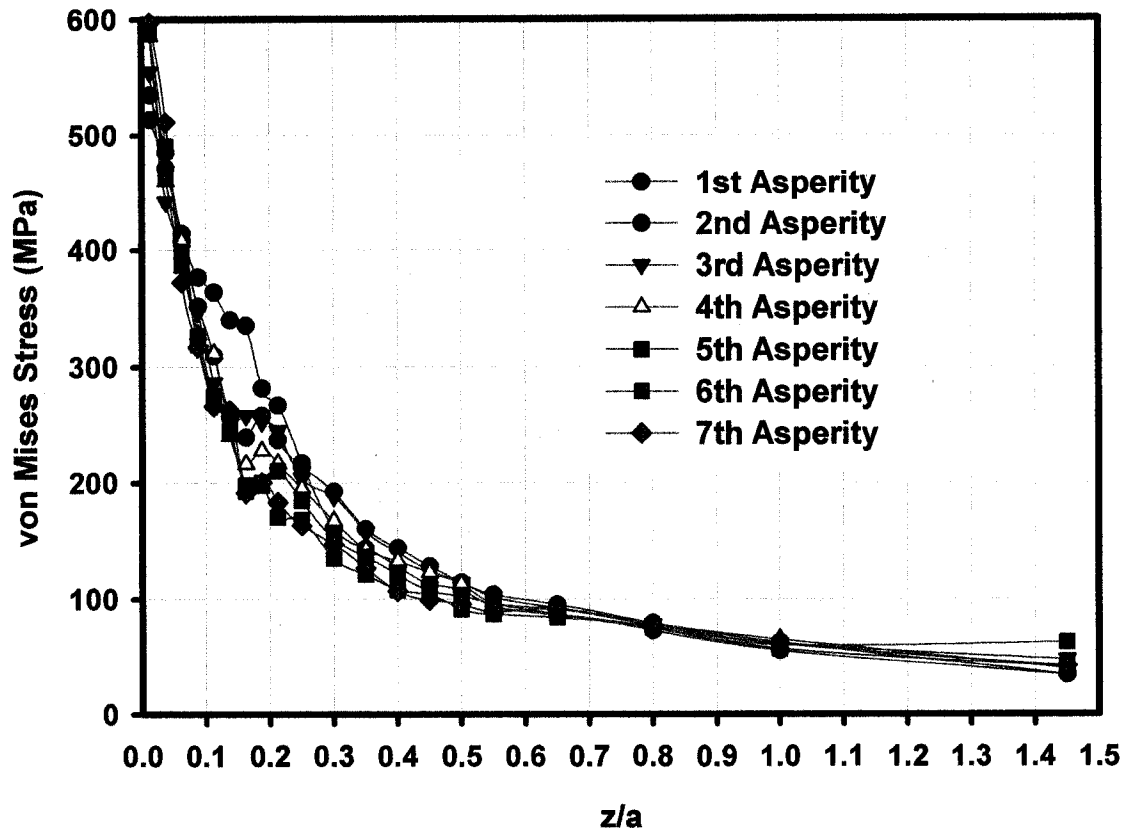


Figure 7.15: Variation of the subsurface stresses with increasing number of sliding contacts at the mid-point of the 356 Al half-space (Sliding velocity: 10 m/s, Normal load: 150 N/mm, Equation 4.5, Lagrangian model). (z is the depth beneath the contact surface and a is the counterface diameter).

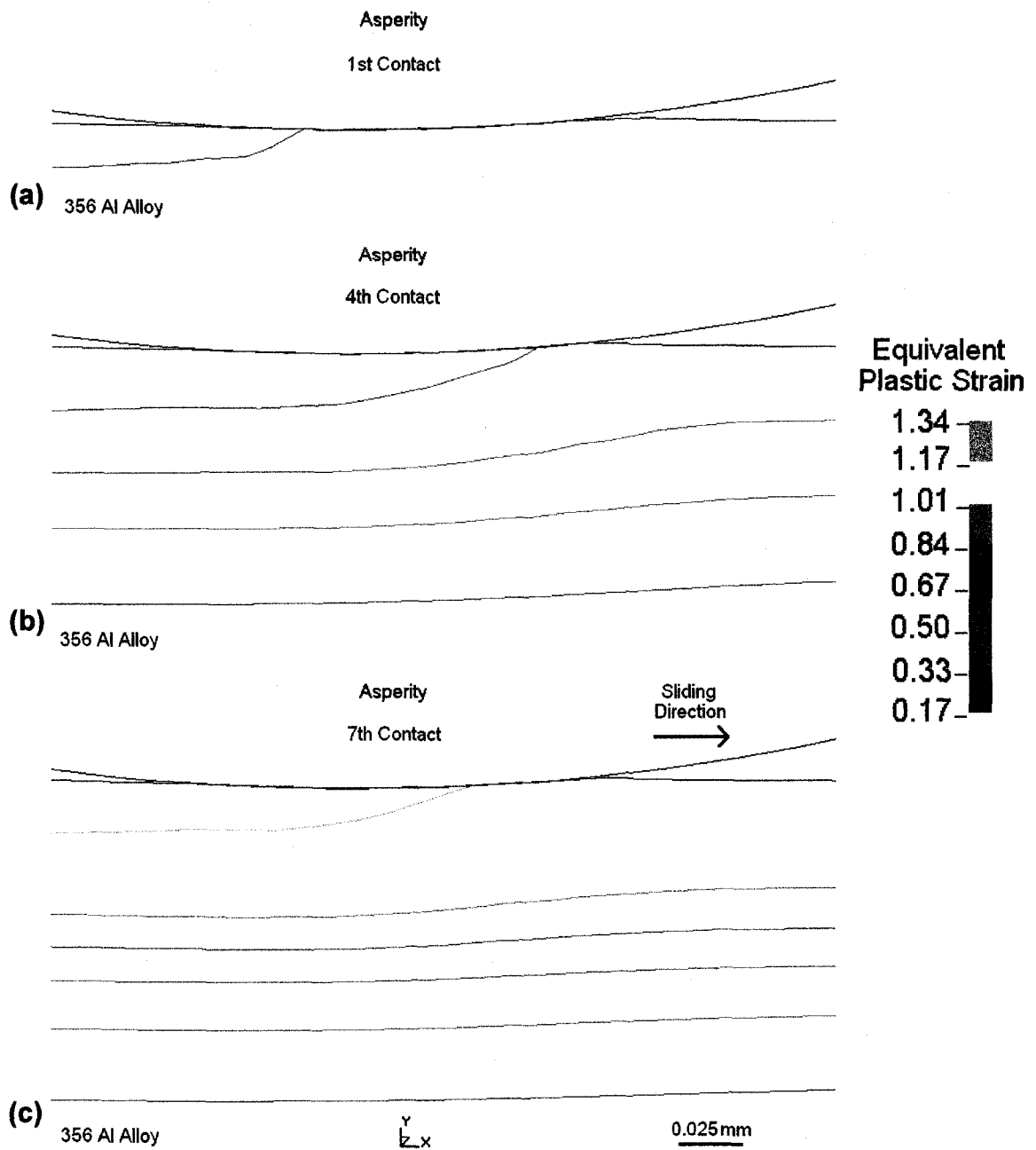


Figure 7.16: Equivalent plastic strain distribution in the 356 Al half-space after multiple sliding contacts: (a) after the first contact, (b) after the fourth contact and (c) after the seventh contact (Sliding velocity: 10 m/s, Normal load: 150 N/mm, Equation 4.5, Lagrangian model).

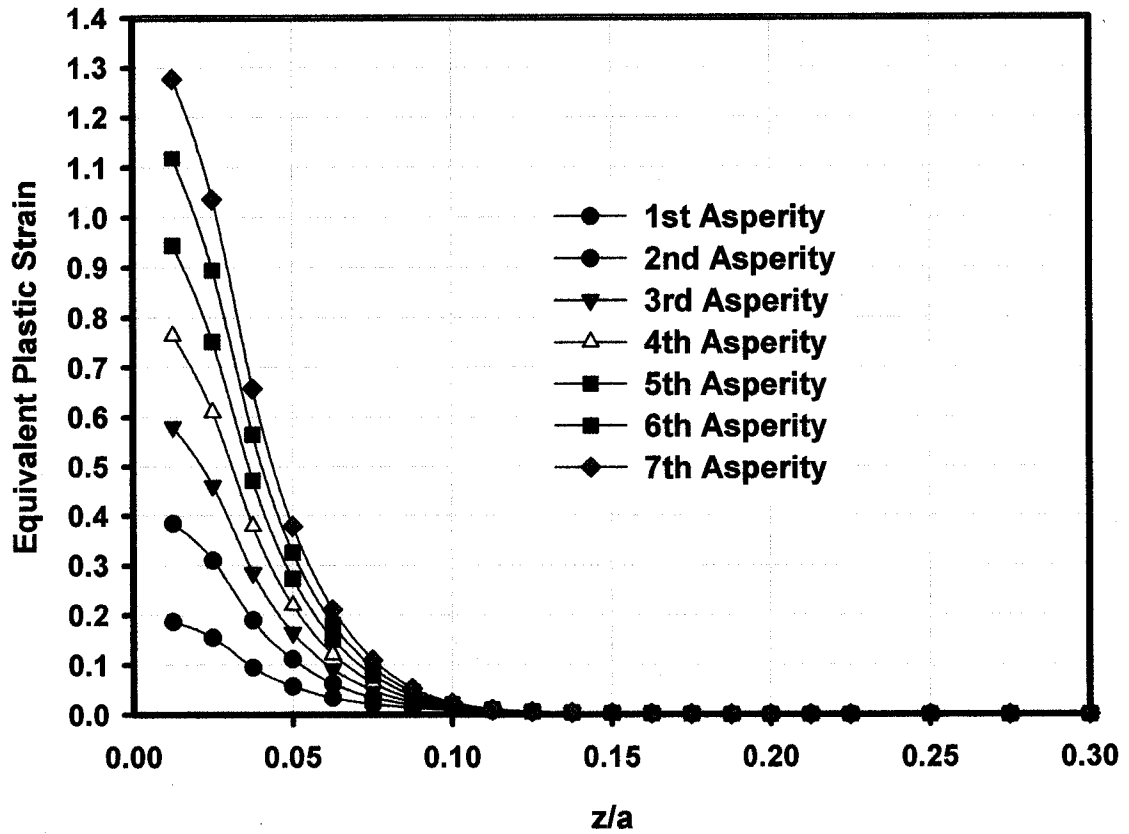


Figure 7.17: Accumulation of the subsurface equivalent plastic strains with increasing number of the sliding contacts at the mid-point of the 356 Al half-space (Sliding velocity: 10 m/s, Normal load: 150 N/mm, Equation 4.5, Lagrangian model). (z is the depth beneath the contact surface and a is the asperity diameter).

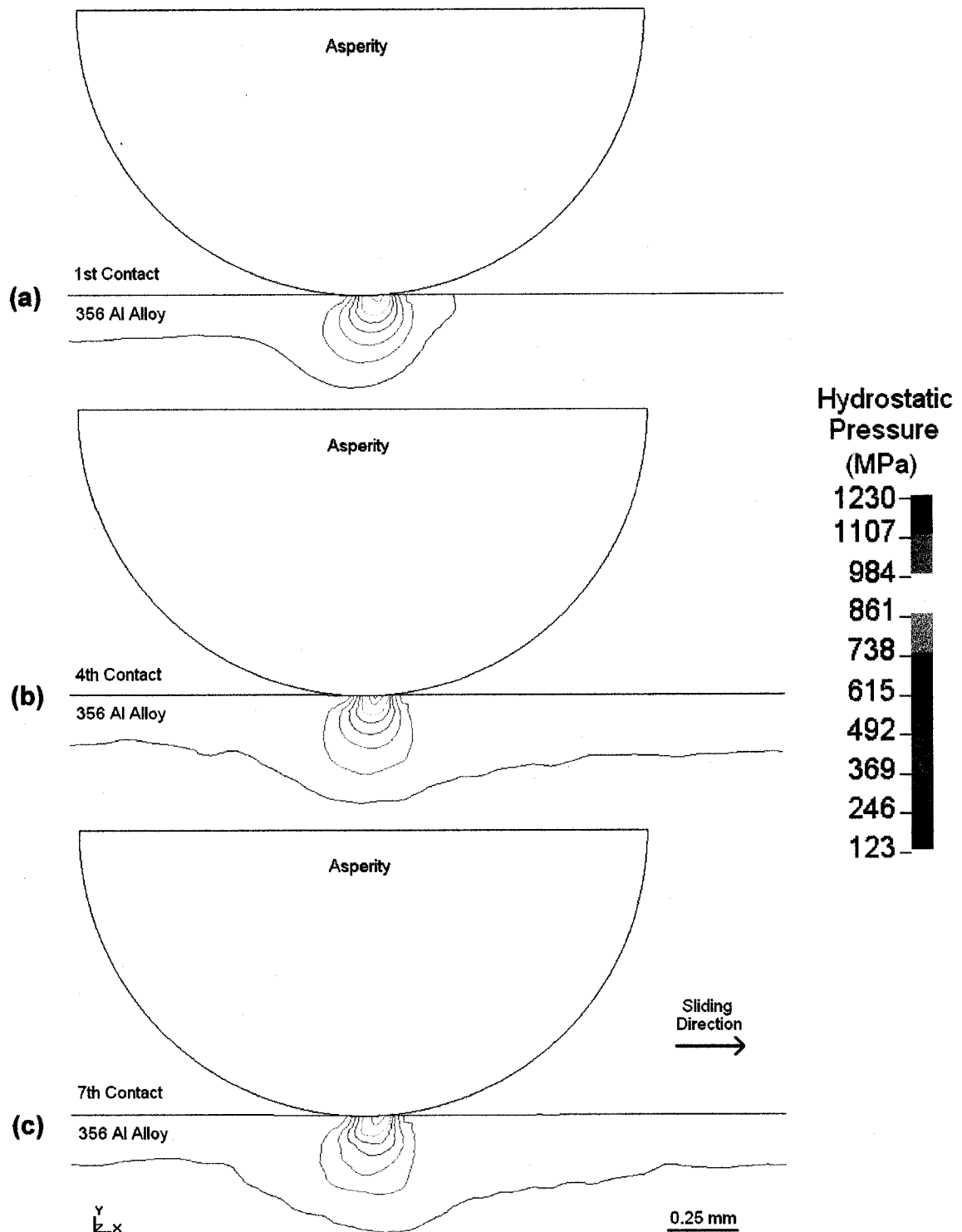


Figure 7.18: Hydrostatic Pressure (in MPa units) distribution in the 356 Al half-space after multiple sliding contacts: (a) after the first contact, (b) after the fourth contact and (c) after the seventh contact (Sliding velocity: 10 m/s, Normal load: 150 N/mm, Equation 4.5, Lagrangian model).

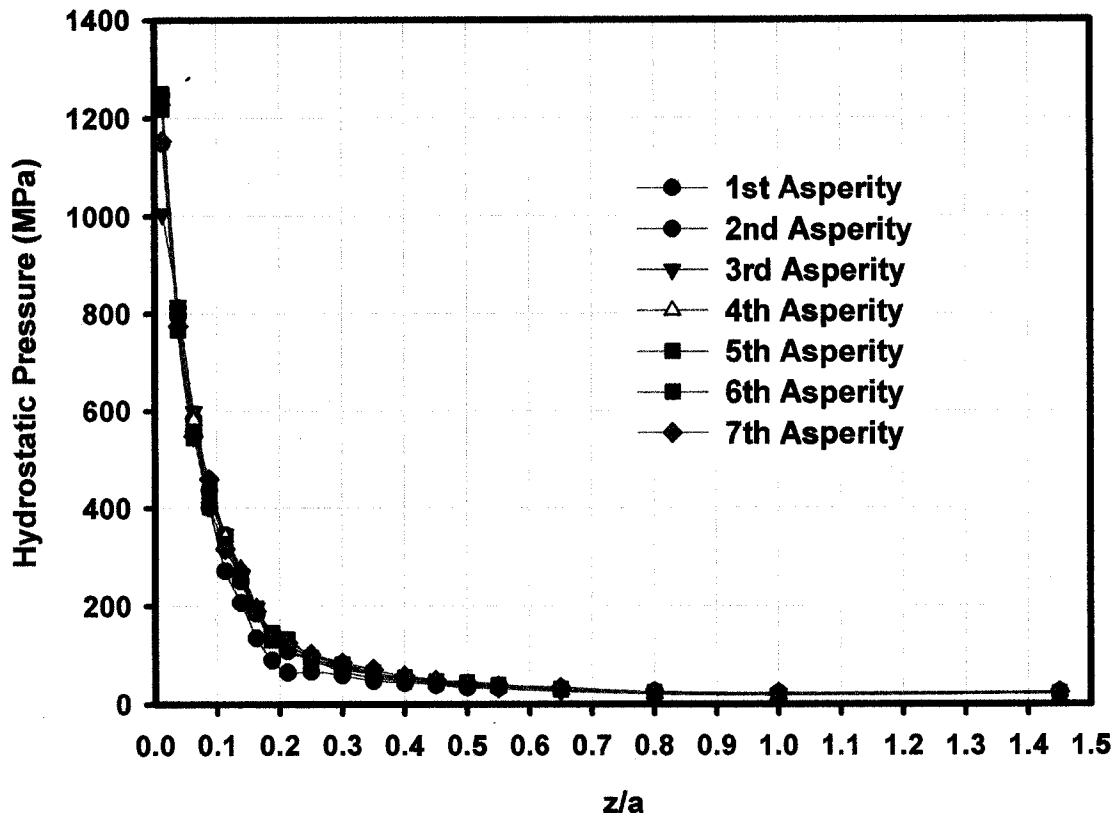


Figure 7.19: Distribution of the hydrostatic pressure with increasing number of sliding contacts at the mid-point of the 356 Al half-space (Sliding velocity: 10 m/s, Normal load: 150 N/mm, Equation 4.5, Lagrangian model).

the von Mises stress. This distribution difference creates a damage gradient that will be discussed in later sections.

7.2.3. VARIATION OF THE DEFORMATION INDUCED SUBSURFACE TEMPERATURES WITH NUMBER OF SLIDING CONTACTS

Figure 7.20 illustrates the sliding-induced temperature variation under the 356 Al half-space surface with increasing number of sliding contacts. The maximum temperature, at the end of the first asperity contact cycle, was 323 K at $z/a=0$. The temperature at $z/a=0$ increased to 341 K after the fourth contact, and 346 K after the last contact. Figure 7.21 presents the subsurface temperature distribution with the contact cycles at the mid-point of the 356 Al half-space. There was a total temperature increase of 45 K at the surface after seven sliding contacts. The temperature dropped to 300 K at $z/a=0.135$, 0.425 and 0.595 after the first, fourth and seventh contacts. The surface temperature reached a steady state after the 5th sliding contact, with only 0.3% increase in the temperature afterwards.

7.2.4. SUBSURFACE STRAIN RATE DISTRIBUTION WITH THE INCREASE IN THE NUMBER OF SLIDING CONTACTS

Figure 7.22 presents the strain rates that the material at the mid-point of the 356 Al half-space were subjected to. The strain rate ranged from $7.8 \times 10^3 \text{ s}^{-1}$ to $9.8 \times 10^3 \text{ s}^{-1}$ at $z/a=0.0125$. However, a rapid decrease was observed in the material layers at deeper locations—with the strain rate reading $1.8 \times 10^3 \text{ s}^{-1}$ at $z/a=0.05$ and $1.0 \times 10^2 \text{ s}^{-1}$ at $z/a=0.10$, after the last contact. The predicted high values of strain rate in the close vicinity of the contact surface result in an unrealistically high hardening of the aluminum alloy, due to limitations of the equations used [82]. Therefore, the results for the close vicinity of the surface are not included in the discussion of the subsurface damage rate presented in Section 7.5. In addition, the results indicated that the distribution of strain rate was independent of the number of sliding contacts after the second contact—when the positions deeper than a normalized depth of 0.05 ($z/a>0.05$) were examined.

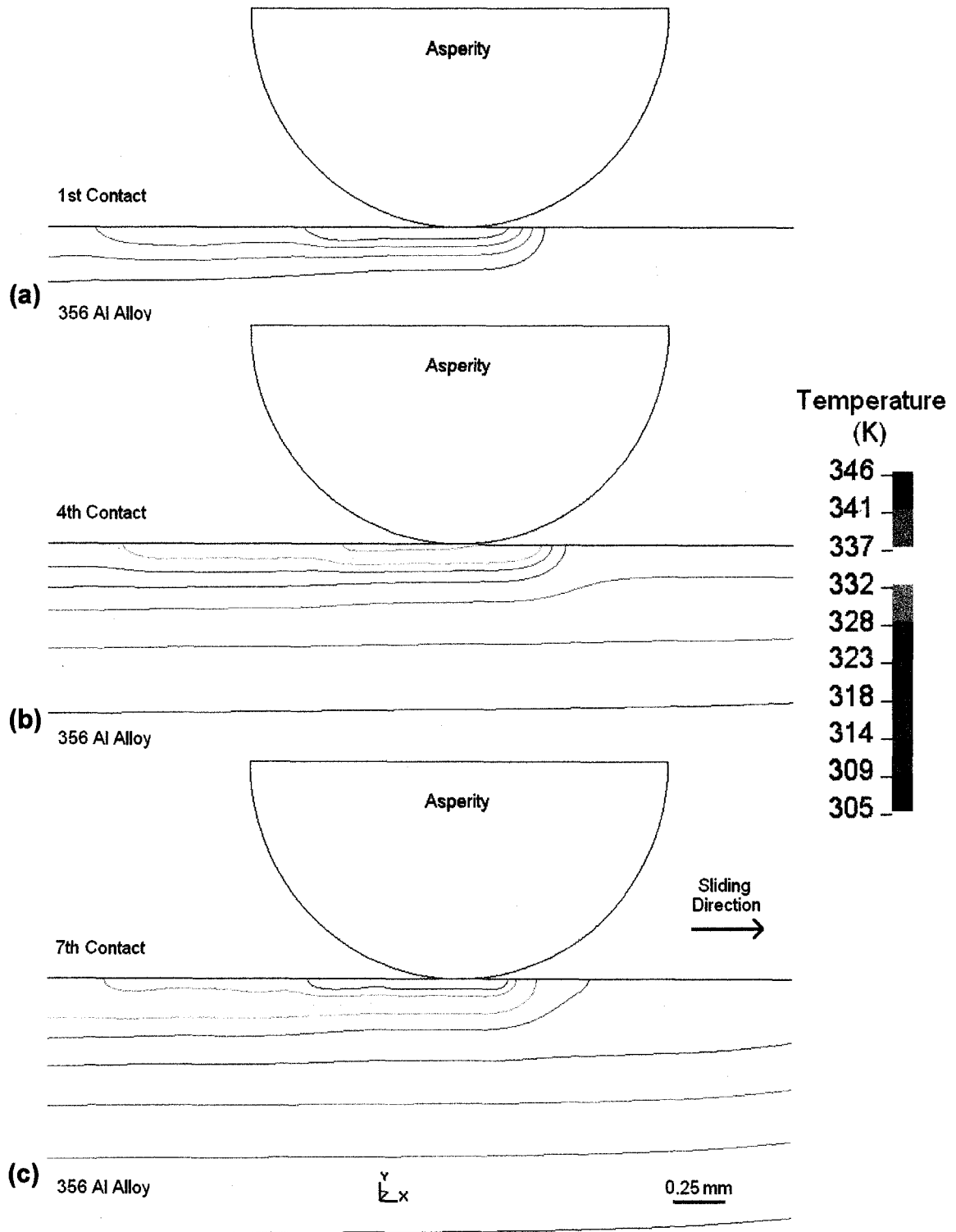


Figure 7.20: Temperature (in Kelvin) distribution in the 356 Al half-space after multiple sliding contacts: (a) after the first contact, (b) after the fourth contact and (c) after the seventh contact (Sliding velocity: 10 m/s, Normal load: 150 N/mm, Equation 4.5, Lagrangian model).

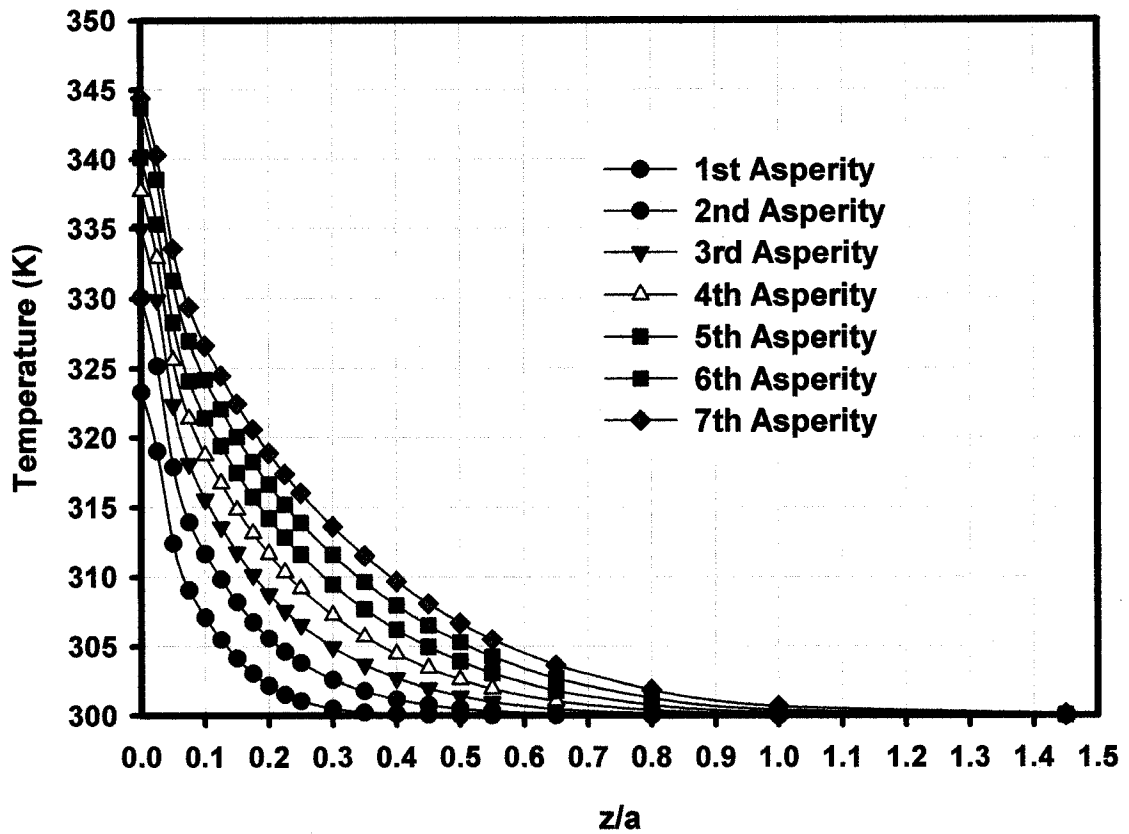


Figure 7.21: Increase of the subsurface temperature with multiple sliding contacts at the mid-point of the 356 Al half-space (Sliding velocity: 10 m/s, Normal load: 150 N/mm, Equation 4.5, Lagrangian model).

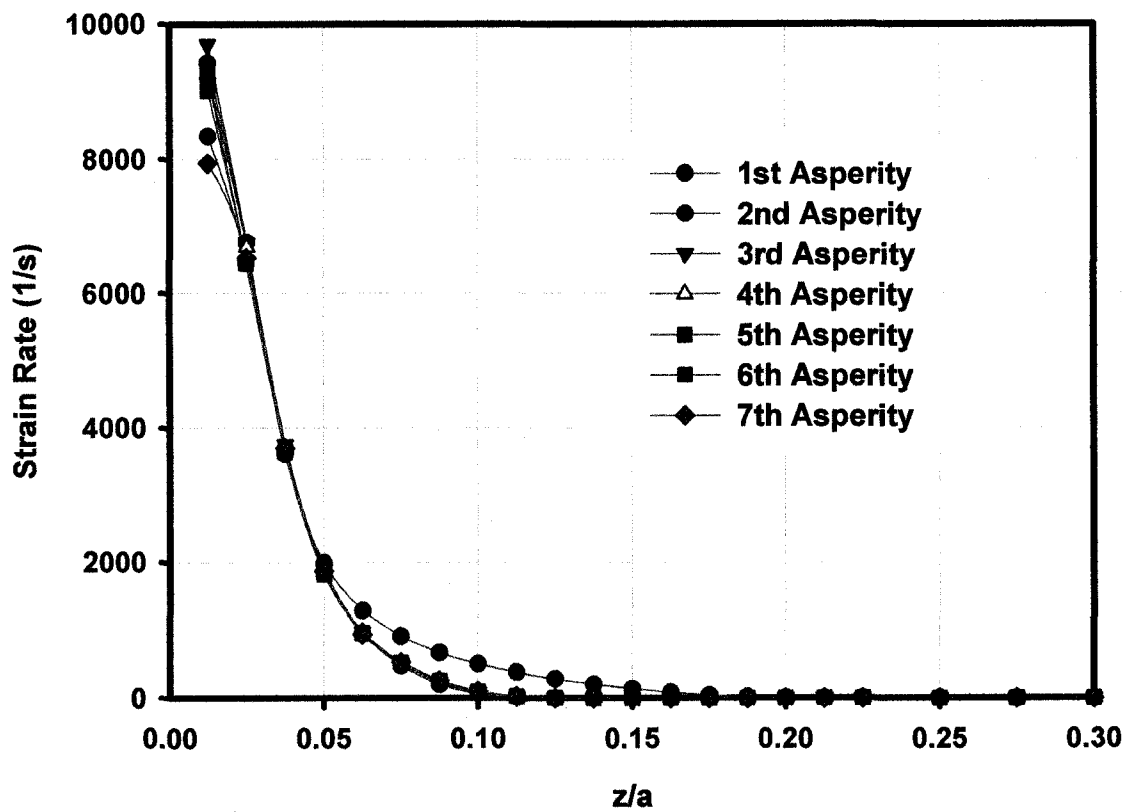


Figure 7.22: Change of the strain rate with multiple sliding contacts at the mid-point of the 356 Al half-space (Sliding velocity: 10 m/s, Normal load: 150 N/mm, Equation 4.5, Lagrangian model).

7.2.5. EFFECT OF MATERIAL MODEL ON THE PREDICTION OF SUBSURFACE DEFORMATION

Simulations using different material models were performed in an effort to explore the influence of the material model on the subsurface deformation prediction. The following material models were used, and the results were compared:

- 1- A strain hardening material model only (Equation 4.7),
- 2- A strain hardening material model with strain rate effects (Equation 4.8),
- 3- A strain hardening material model with thermal effects (Equation 4.9),
- 4- A strain hardening material model with thermal and strain rate effects (Equation 4.5).

Figure 7.23 presents a comparison of the material models' effects on the prediction of subsurface plastic strains. Similarly, Figure 7.24 shows the effects of the material model on the prediction of subsurface temperature distribution in the 356 Al half-space after the seventh sliding contact. An equivalent plastic strain of 4.7 at a normalized depth of 0.0125 was observed when using the strain hardening material model (Equation 4.7). The predicted temperature increase at the normalized depth of 0.0125 was 80 K with the strain hardening material model. When this temperature increase was considered in the constitutive equation, the thermal softening of the 356 Al material caused a 3 % increase in the predicted plastic strain. The numerical model with strain hardening and strain rate effects (Equation 4.8) predicted an equivalent plastic strain of 1.2 at the same depth—which corresponds to a 75 % decrease when compared with the strain hardening model's prediction. This difference was due to the high strain rate (7950 s^{-1}) observed at the surface. Considering strain rate in the material model caused a decrease in the plastic deformation, prompted by the strain rate hardening of the 356 Al alloy. When both strain rate and thermal effects were considered in the strain hardening material model (Equation 4.5), the plastic strain at the normalized depth of 0.0125 was approximately 1.3—a 72 % decrease when compared to the prediction of the model using Equation 4.7. This difference in the plastic strain prediction reaches 76 % at the normalized depths of 0.050 and 0.075 when the results obtained with Equations 4.5 and 4.7 are compared. In summary, Figure 7.23 indicates that strain rate effects were more dominant than thermal effects on the subsurface deformation of the 356 Al half-space for the loading conditions investigated.

A 45 % difference in the deformation-induced temperature was observed at the surface between the strain hardening model and the material model that accounts for strain hardening, strain rate hardening and thermal softening. The model considering only strain hardening predicted a temperature rise of 80 K at the surface, while the numerical model with strain hardening, thermal and strain rate effects indicated a 45 K increase (Figure 7.24).

7.2.6. EFFECT OF NORMAL LOAD

Figure 7.25 illustrates how the plastic strains were influenced by a change in the normal load. An increase of the load from 150 N/mm to 250 N/mm caused plastic strains to increase 100 %, according to Equation 4.5. In addition, the normalized depth of the plastically yielded region increased from 0.2, to 0.3. However, according to the strain-hardening model (Equation 4.7), this increase was only 50 %.

Figure 7.26 illustrates the influence of the normal load on the accumulation of the stresses, strains and temperature when the number of contacts is increased. A higher normal load caused higher plastic deformation in the 356 Al half-space, as expected, but the von Mises stress calculated after the seventh contact at a normal load of 250 N/mm was lower than that for a 150 N/mm load. This is attributed to the softening of the material prompted by the temperature increase at the contact surfaces. The temperature increase at the surface was approximately 45 K with a 150 N/mm load, and increased to 130 K at 250 N/mm.

7.2.7. EFFECT OF FRICTION

Figure 7.27 presents the effects of friction on the accumulation of the subsurface stresses, strain and temperatures in the 356 Al half-space after the third contact. The changes in the subsurface values against depth and position of the surface are also indicated in Figure 7.27. With $\mu=0.0$, the von Mises stress, plastic strain and temperature at the surface were observed to be 550 MPa, 0.55 and 330 K, respectively. With the application of friction ($\mu=0.3$), those values reached 700 MPa, 3.3 and 370 K at the surface. In addition, Figure 7.27 indicates that the deformation was similar—regardless of the friction condition—when the locations distant from the surface were examined.

7.2.8. EFFECT OF SLIDING VELOCITY

Figure 7.28 shows the effects of the sliding velocity on the accumulation of subsurface stresses, strains and temperature in the 356 Al half-space after the last contact cycle. When the sliding velocity was decreased, the equivalent plastic strain at the surface increased 15 % while the von Mises stress and the temperature stayed approximately constant at 595 MPa and 345 K. Therefore, the increase in the plastic deformation can be attributed to the decrease in the strain rate. The strain rate at the surface was $7.9 \times 10^3 \text{ s}^{-1}$ for a sliding velocity of 10 m/s, and $6.4 \times 10^3 \text{ s}^{-1}$ for 5 m/s. A decrease in the sliding velocity causes a decrease in the strain rate—resulting in a lower strain rate hardening that permits more plastic deformation. In addition, the von Mises stress, plastic strain and temperature observations were similar—regardless of the sliding velocity when locations that were distant from the surface were examined. This suggests that the results were not affected by the chosen geometry of the 356 Al half-space, and that the depth of the material considered in the finite element model was large enough to minimize the unrealistic response of the material at the ends of the mesh.

In summary, this section presents the results of the sliding contact investigation using a Lagrangian coupled thermo-mechanical model. The influence of thermal softening and strain rate on subsurface stress and strain accumulation was also explored. In the next section, the results of the Eulerian and Lagrangian sliding contact models will be compared.

7.3. COMPARISON OF EULERIAN AND LAGRANGIAN SLIDING MODELS

The results of the two sliding contact models presented in Sections 7.1 and 7.2 cannot be compared directly, because the models had both similar and dissimilar features. The main difference between the proposed models was the element formulation. The Eulerian element formulation successfully modeled the high deformation observed in the aluminum alloys under the application of high normal loads when a solution couldn't be obtained with a Lagrangian element formulation—because of the excessive element distortion. However, the Eulerian model was not successful when applied to a coupled thermal and mechanical analysis. The FE model utilizing

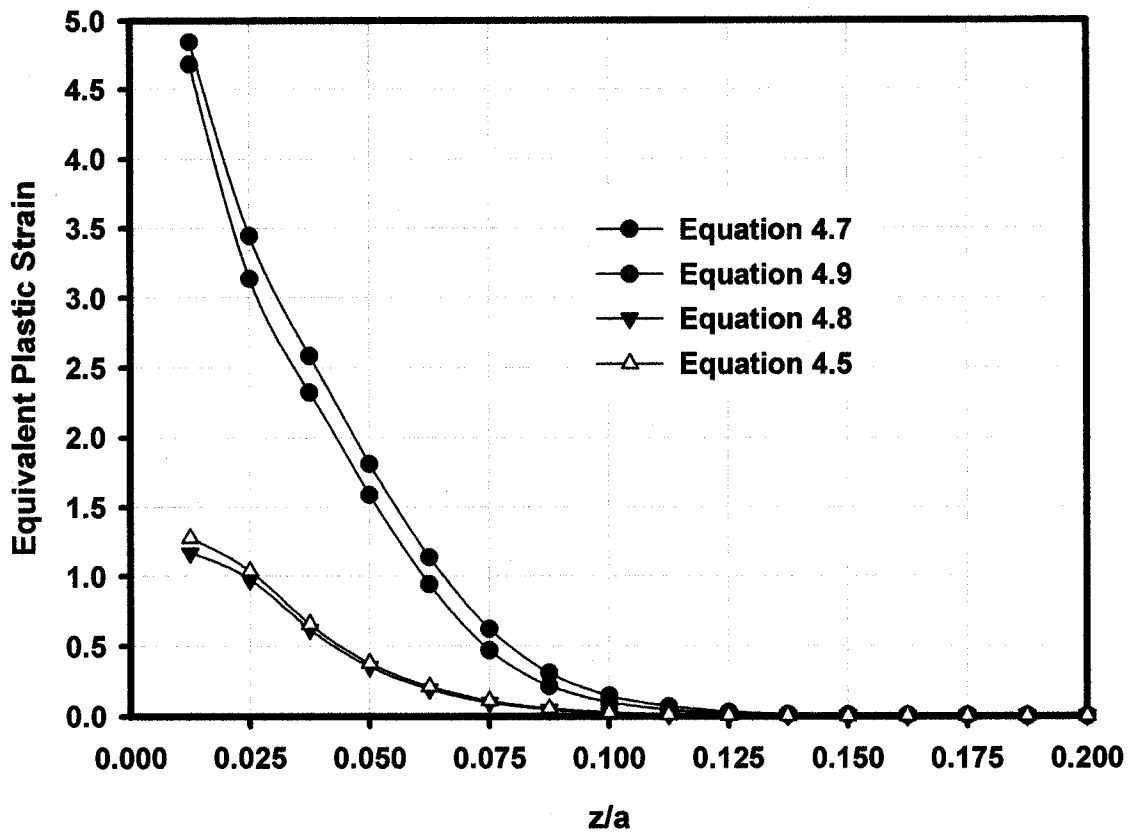


Figure 7.23: Comparison of the effect of the material model on the subsurface plastic strain distribution in the 356 Al half-space (Results after seventh sliding contact) (Sliding velocity: 10 m/s, Normal load: 150 N/mm, Lagrangian model).

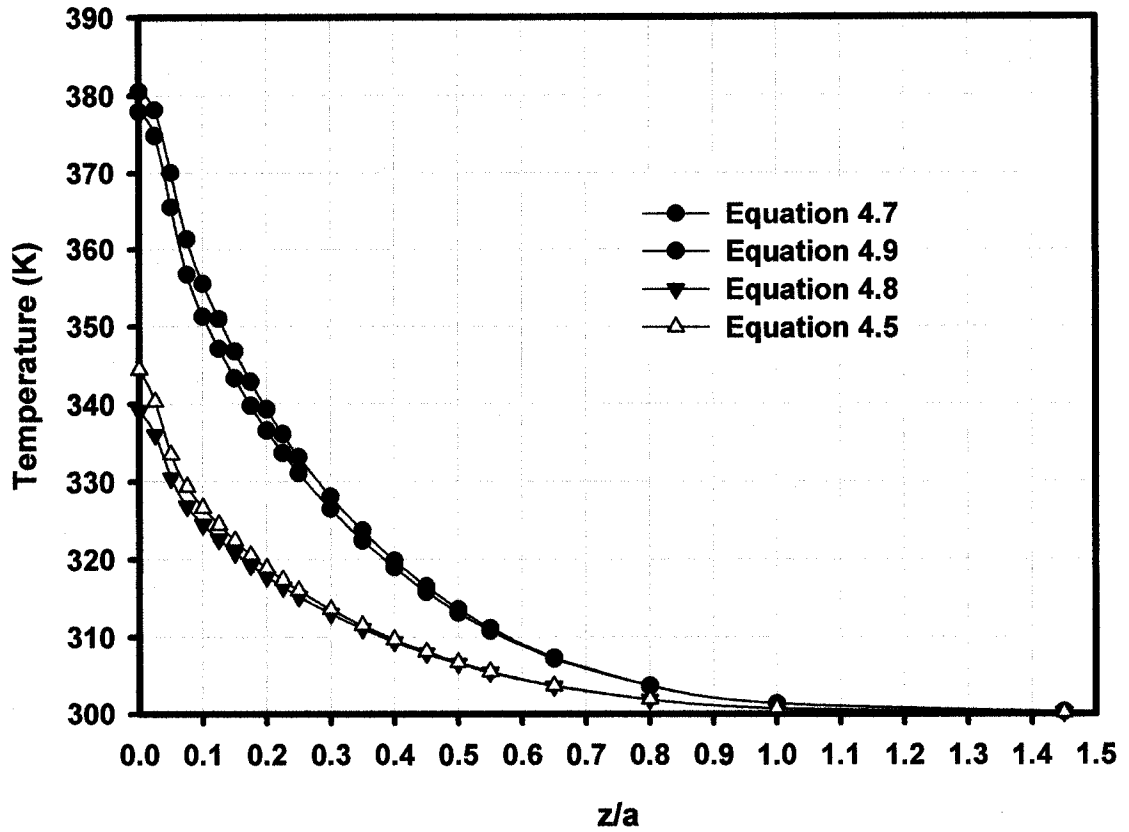


Figure 7.24: Comparison of the effect of the material model on the subsurface temperature distribution in the 356 Al half-space (Results after seventh sliding contact) (Sliding velocity: 10 m/s, Normal load: 150 N/mm, Lagrangian model).

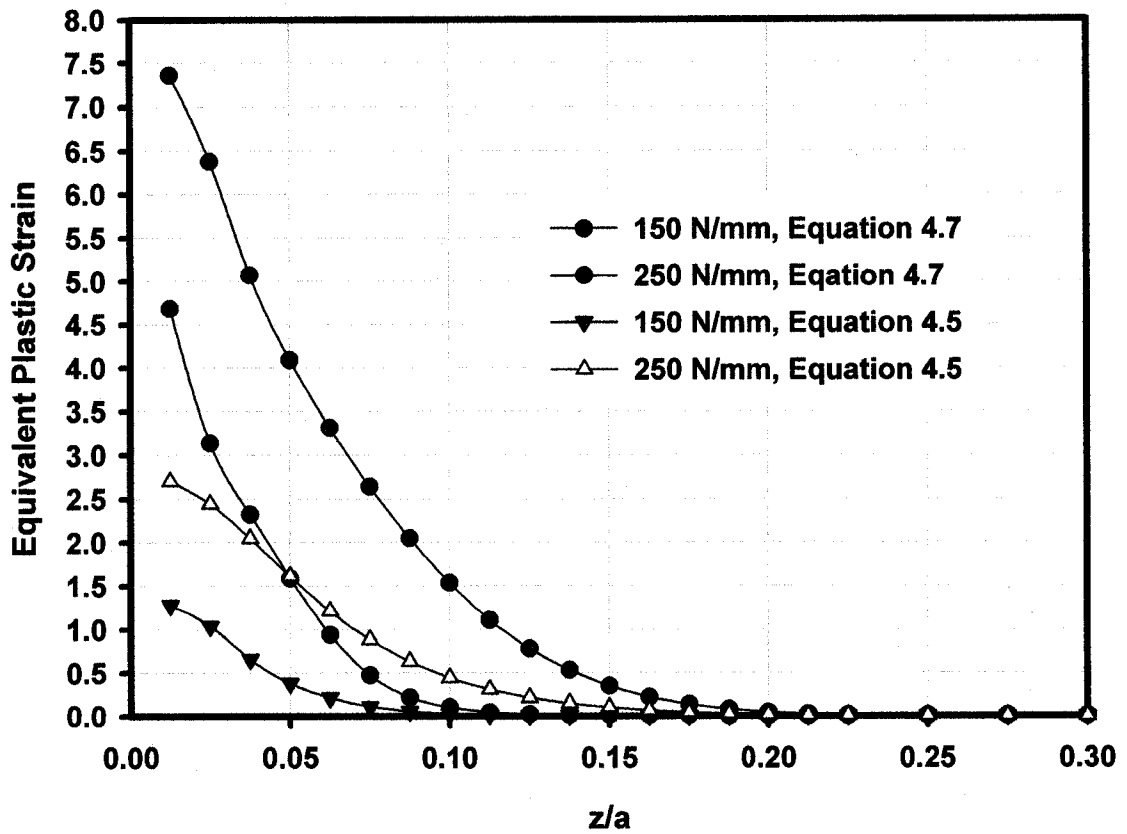


Figure 7.25: Effect of the normal load on the distribution of the subsurface strains (Results after the seventh contact) (Sliding velocity: 10 m/s, Lagrangian model).

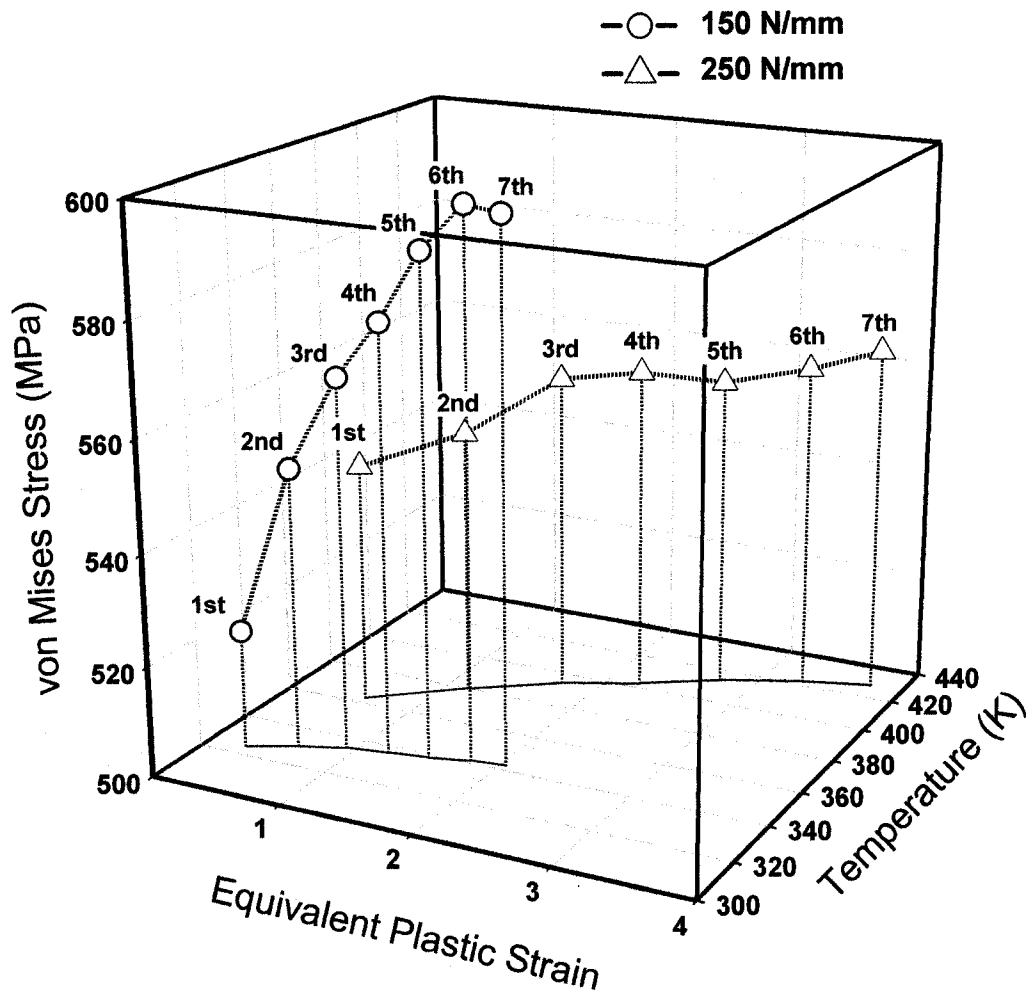


Figure 7.26: Effect of the normal load on the accumulation of the stresses, strains and temperature in the 356 Al half-space with increasing number of sliding contacts. (The order of the asperities, the resulting stresses, strains and temperatures are indicated. Results are taken from the mid-point of the 356 Al half-space close to the surface). (Sliding velocity: 10 m/s, Equation 4.5, Lagrangian model).

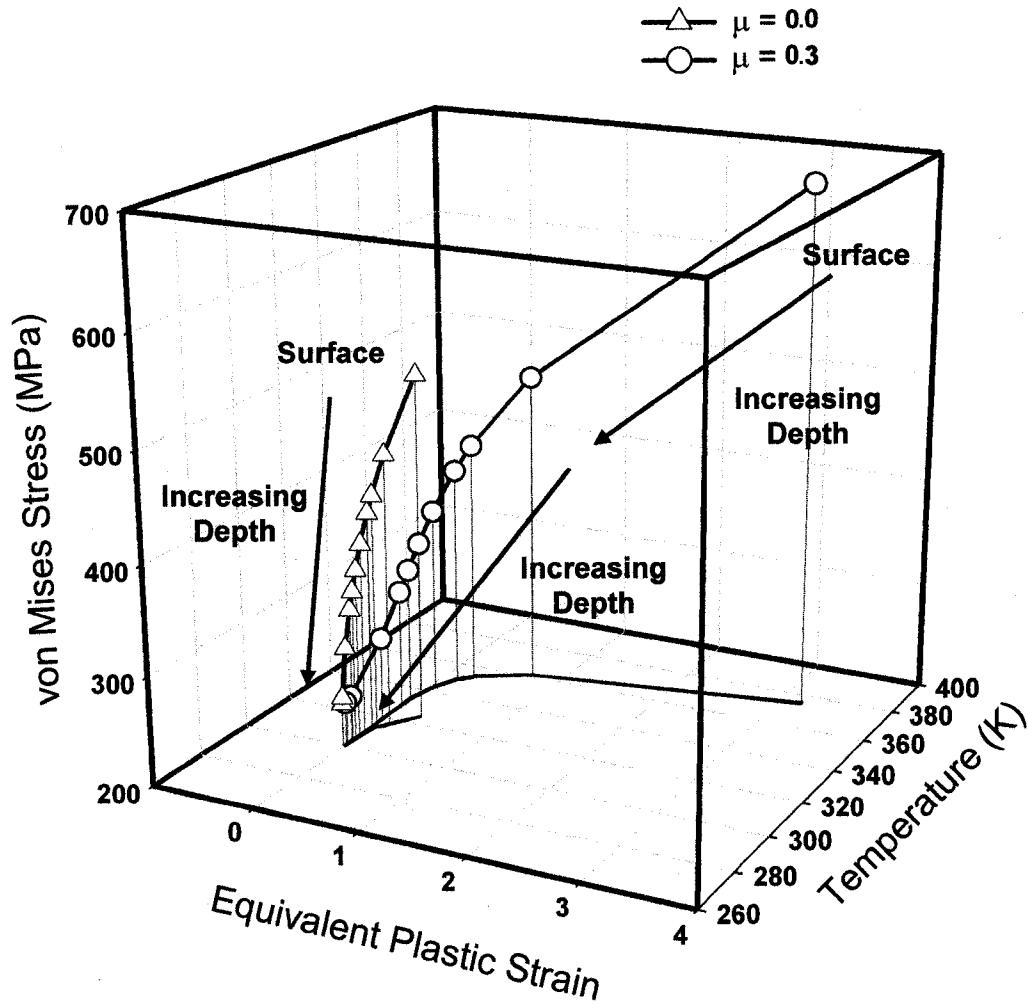


Figure 7.27: Effect of the friction on the accumulation of the stresses, strains and temperature in the 356 Al half-space after 3rd sliding contact. (The order of the asperities, the resulting stresses, strains and temperatures are indicated. Results are taken from the mid-point of the 356 Al half-space). (Sliding velocity: 10 m/s, Normal load: 150 N/mm, Equation 4.5, Lagrangian model).

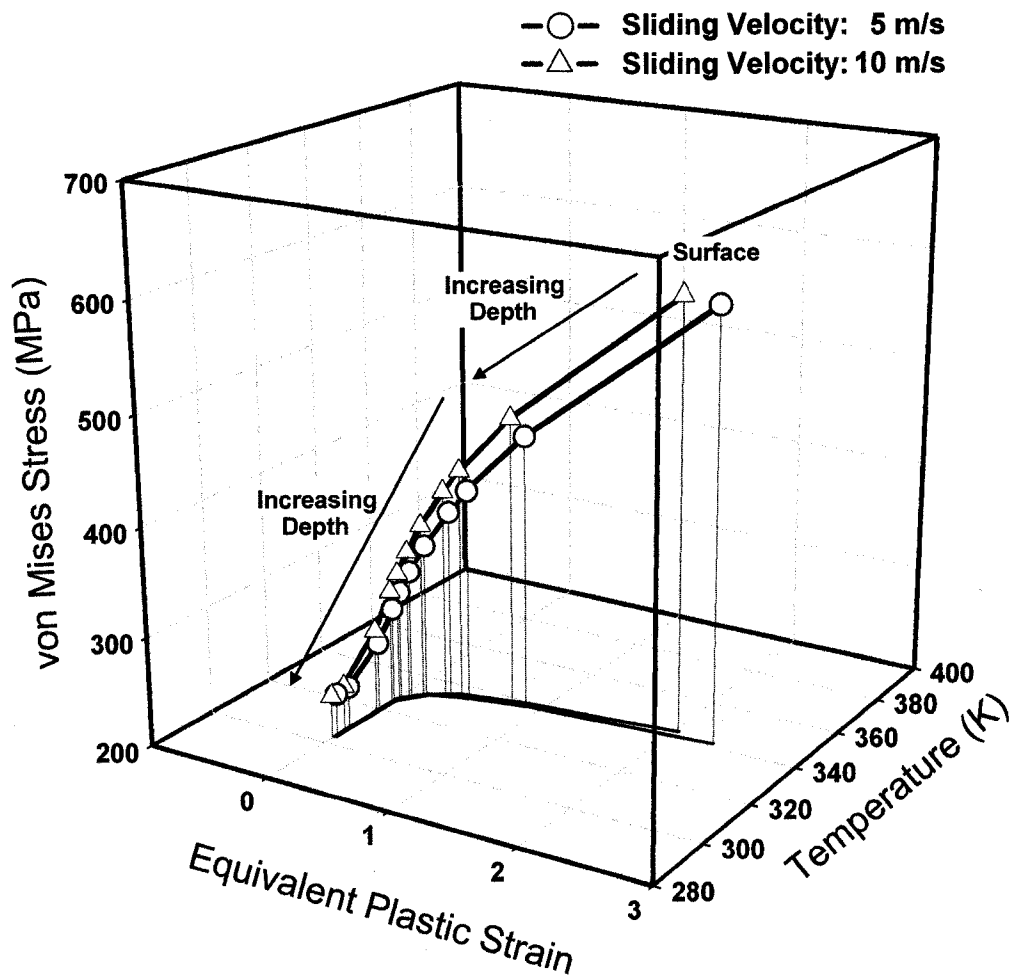


Figure 7.28: Effect of the sliding velocity on the accumulation of the subsurface stresses, strains and temperature in the 356 Al half-space after seventh sliding contact. (The order of increasing depth, and the resulting stresses, strains and temperatures are indicated. Results are taken from the mid-point of the 356 Al half-space). (Normal load: 150 N/mm, Equation 4.5, Lagrangian model).

Lagrangian elements proved a successful alternative for addressing the coupled thermo-mechanical analysis. In addition, the geometries of the models were similar, but not the same. The models had the same asperity diameter and aluminum alloy length, and width, but the Eulerian model had a finite third dimension while the Lagrangian model used a plane strain element formulation and its third dimension was assumed as infinite.

Despite the fact that the overall dimensions were different, the deformation predictions of both models can be compared in terms of unit thickness. Figure 7.29 shows the Eulerian and Lagrangian equivalent plastic strain predictions for different normal loads obtained with strain hardening material models (Equations 4.1 and 4.7). The plastic strain results, when extrapolated to the surface, show that maximum plastic strain was 7, 8, 10 and 17 for the normal loads of 150, 200, 250 and 300 N/mm, respectively. The models made similar predictions for the distribution of plastic strain below the surface, and the results from the Eulerian and Lagrangian models were compatible. However, the plastic strain predictions of the two models were the same for two different loads (200 and 250 N/mm) below the normalized depth of 0.075. Similarly, distributions of the von Mises stress at the mid-point of the 356 Al after the seventh sliding contact—obtained with the Eulerian and Lagrangian models—are presented in Figure 7.30. The maximum von Mises stress predicted at the surface was between 363 and 395 MPa for the loads of 150 to 300 N/mm.

Figure 7.31 illustrates the subsurface maximum stress and strain values observed after the passage of the first and last asperities for different normal loads. For comparison, the experimentally defined stress/strain relationship was also included (solid line in Figure 7.31). Figure 7.31 indicates that with an increasing normal load, subsurface stresses reach saturation (400 MPa) while subsurface plastic strains continue to increase. The increase in the plastic deformation at the surface of the 356 Al alloy after the passage of the last asperity was 15 % when the normal load was increased from 150 N/mm to 200 N/mm. The increase in the plastic deformation was 25 % and 70 % when the normal loads were increased from 200 N/mm to 250 N/mm and from 250 N/mm to 300 N/mm, respectively. This implies that the increase in the plastic deformation becomes more severe with higher normal loads. Figure 7.31 also proves that the developed Eulerian and Lagrangian models were consistent.

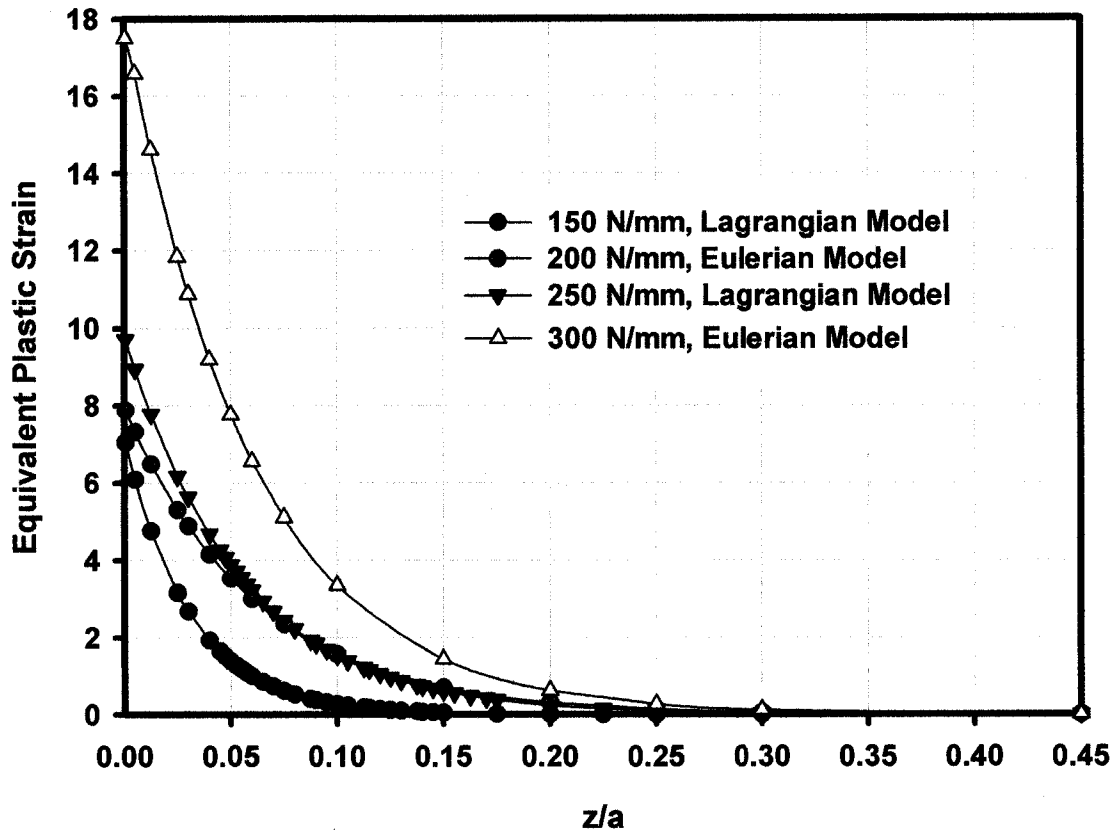


Figure 7.29: Distribution of the equivalent plastic strain at the center of the 356 Al after seventh sliding contact (Sliding velocity: 10 m/s, obtained with strain hardening material model (Equations 4.1 and 4.7)).

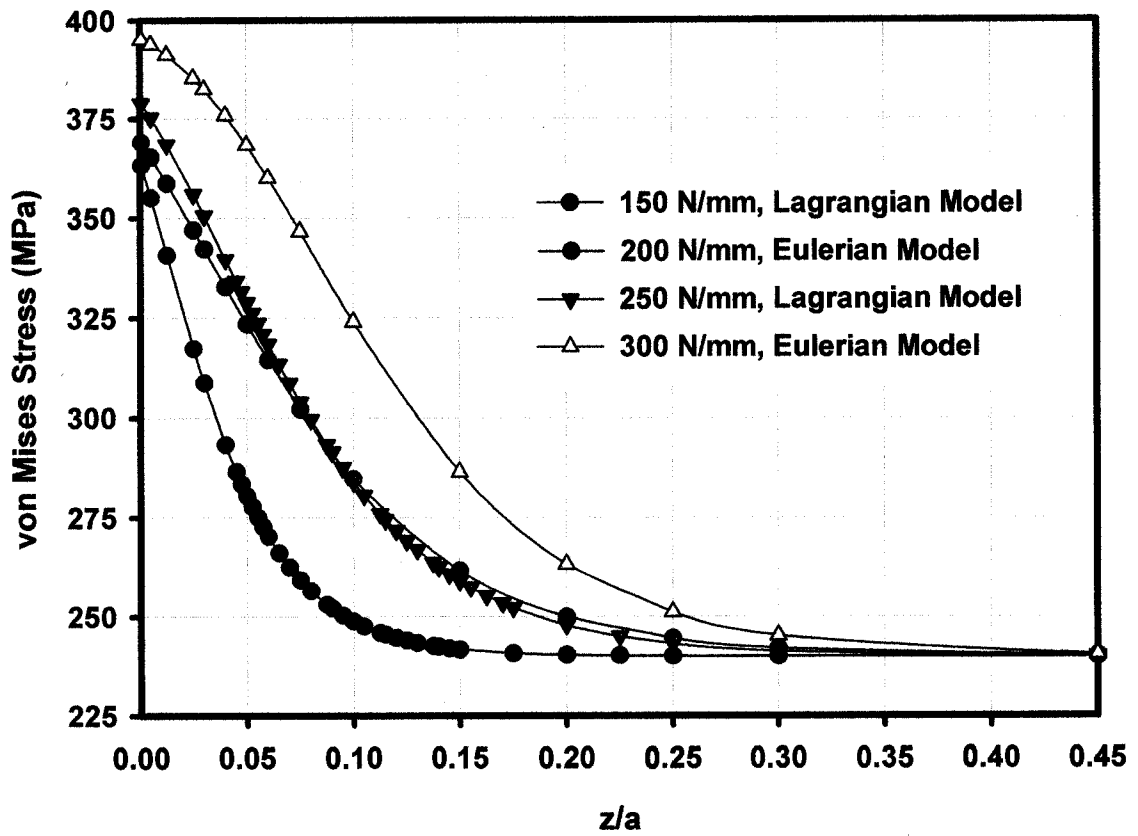


Figure 7.30: Distribution of the von Mises stress at the center of the 356 Al after seventh sliding contact (Sliding velocity: 10 m/s, obtained with strain hardening material model (Equations 4.1 and 4.7)).

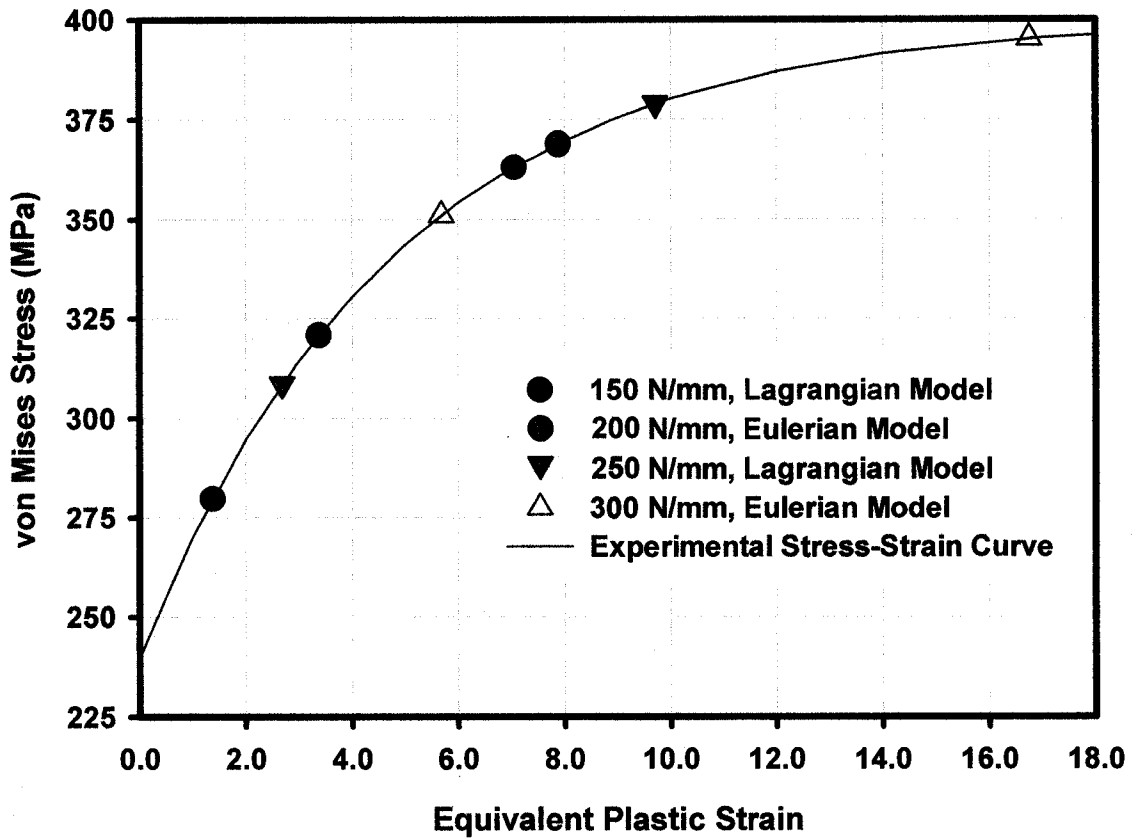


Figure 7.31: Maximum stress-strain values obtained from numerical simulations and comparison to the original experimental stress-strain curve (Results are given after first and seventh contacts at the surface). (Sliding velocity: 10 m/s, obtained with strain hardening material model (Equations 4.1 and 4.7)).

7.4. EFFECTS OF SECONDARY HARD PARTICLES ON THE SUBSURFACE DAMAGE

This section presents the results of the Lagrangian coupled thermal and structural finite element model, investigating the influence of the Si particles on subsurface damage. Details of the finite element model can be found in Section 4.4.

Figures 7.32 to 7.35 illustrate the von Mises stress distribution observed in the 356 Al half-space after the seventh sliding contact—obtained with the original model (no Si particle), as well as the models that considered Si particles—with different shapes for a sliding velocity of 10 m/s and a normal load of 250 N/mm. The maximum von Mises stress was observed at the surface in the original model, but the implementation of Si particles moved the position of the maximum von Mises stress to subsurface regions where Si particles were embedded. Interestingly, the maximum stress position was inside the Si particle, below the interface between the particle and the 356 Al matrix. Figure 7.32 suggests that before the implementation of Si particles inside the 356 Al half-space, the maximum von Mises stress was observed to be 575 MPa. With the consideration of square shaped Si particles, the maximum von Mises stress increased approximately 35 % to 775 MPa. A 36.5 % increase in the maximum von Mises stress was observed with the implementation of a higher aspect ratio rectangular Si particle. When the observations of square and circular shaped Si particles were compared where the subsurface positions and the aspect ratios of the particles were approximately the same, the results indicated that the shape of the Si particle did not influence the stress distribution inside the 356 Al alloy. However, the stresses inside the Si particles did appear to be influenced by the shape of the Si particles. The von Mises stress ranged between 600 MPa and 775 MPa in the square shaped Si particle, and ranged between 600 and 800 MPa for a circular shaped Si particle.

Figure 7.36 shows the distribution of the von Mises stress at the mid-point of the 356 Al half-space and Si particles against a normalized depth—a parameter defined as the ratio of depth below the surface and the asperity diameter. Figure 7.36 indicates that the implementation of subsurface Si particles causes a decrease in the von Mises stress at the subsurface positions above the Si particle. Due to elasticity, an increase in the von Mises stress inside the Si particles is observed. In addition, for higher aspect ratios of Si particle, the increase in the von Mises stress inside the Si particle is higher.

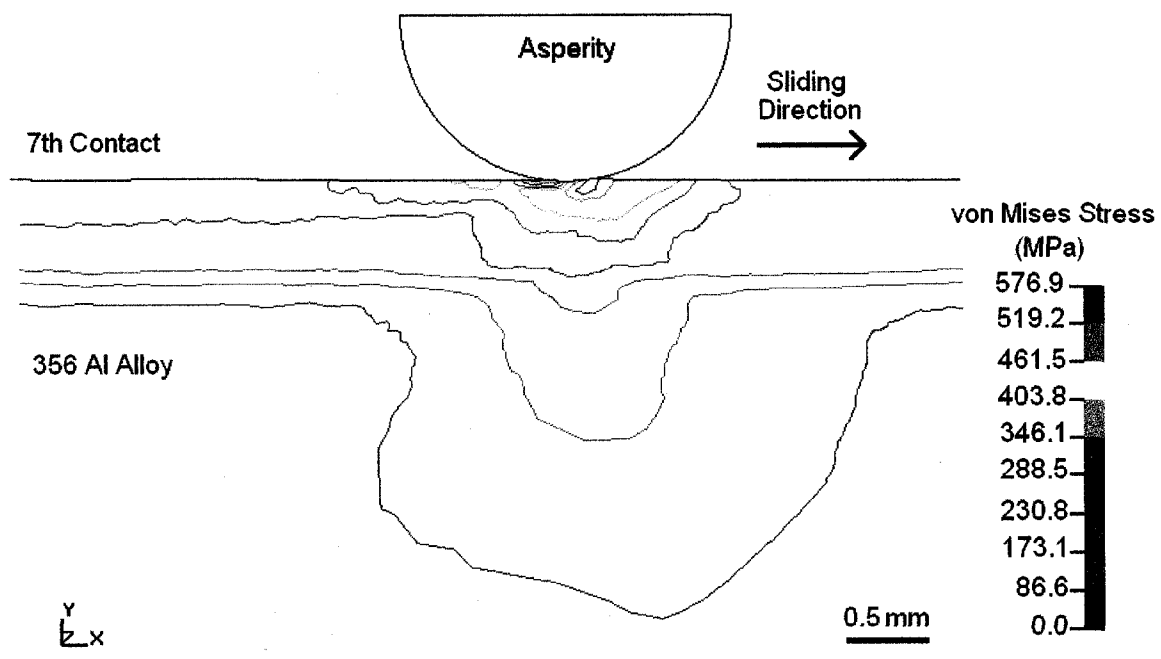


Figure 7.32: von Mises stress (MPa) distribution in the 356 Al half-space after seventh sliding contact (Sliding velocity: 10 m/s, Normal load: 250 N/mm, Equation 4.5).

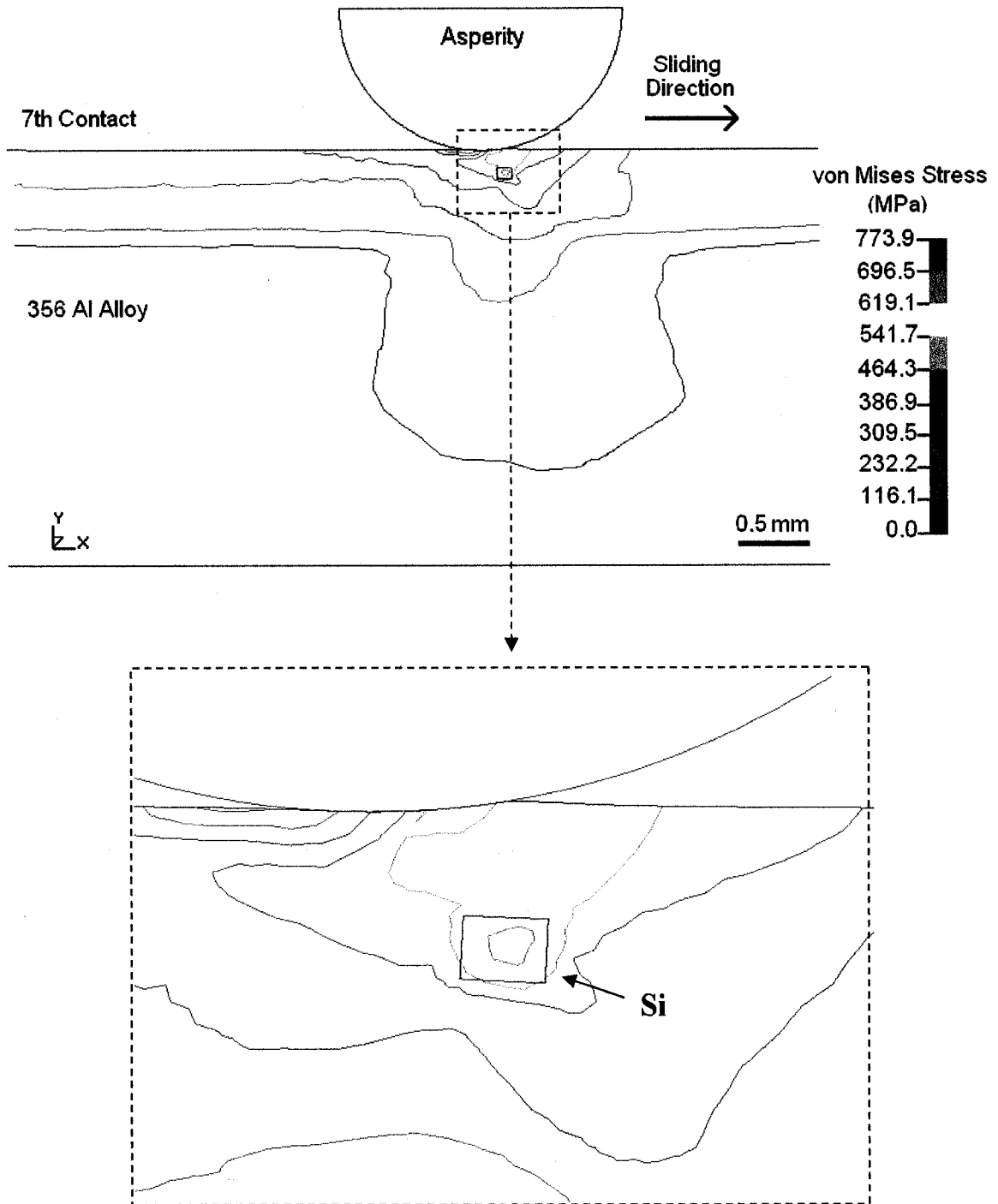


Figure 7.33: von Mises stress (MPa) distribution in the 356 Al half-space after seventh sliding contact with the implementation of a square shaped Si particle (Sliding velocity: 10 m/s, Normal load: 250 N/mm, Equation 4.5).

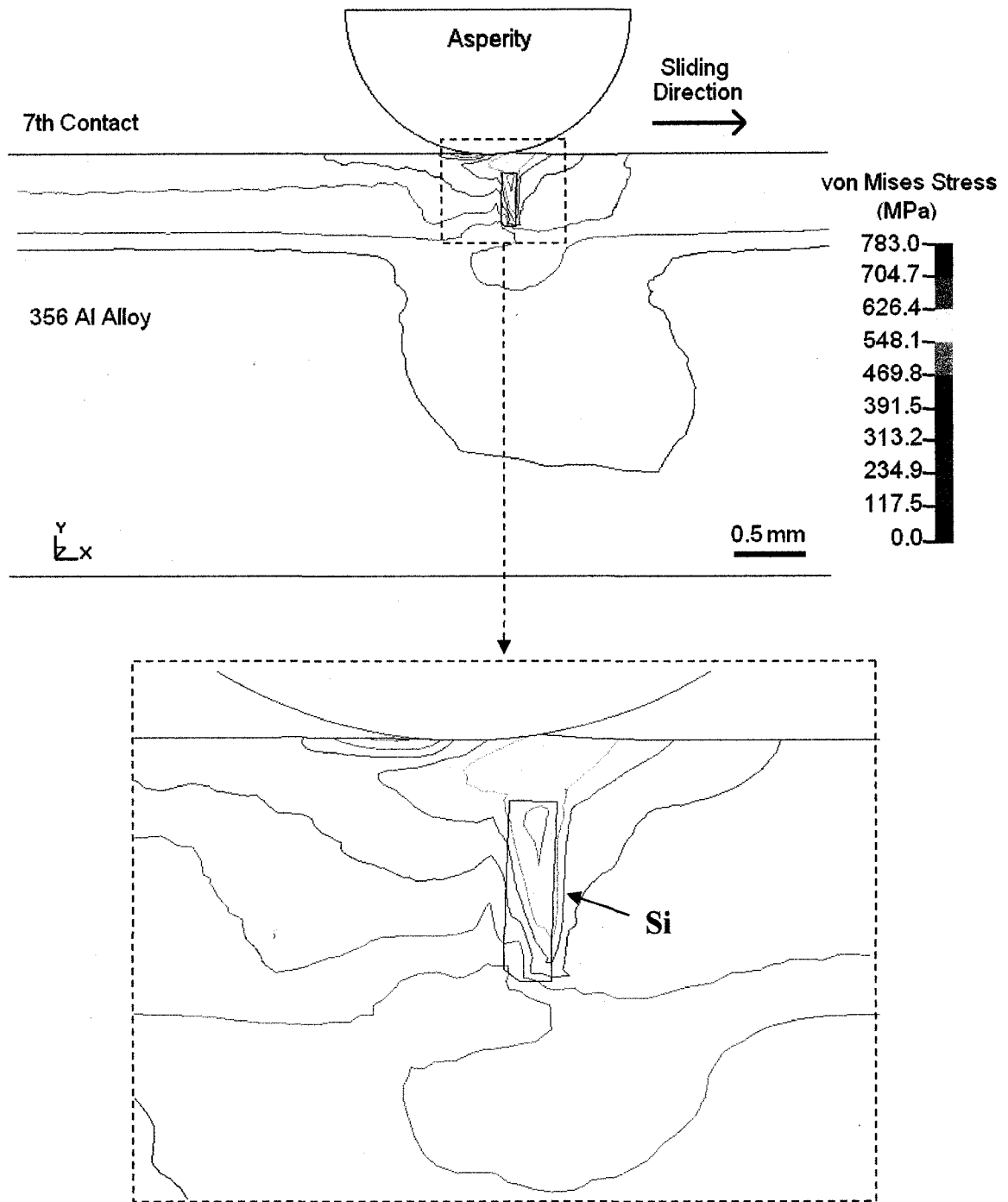


Figure 7.34: von Mises stress (MPa) distribution in the 356 Al half-space after seventh sliding contact with the implementation of a rectangular shaped Si particle (Sliding velocity: 10 m/s, Normal load: 250 N/mm, Equation 4.5).

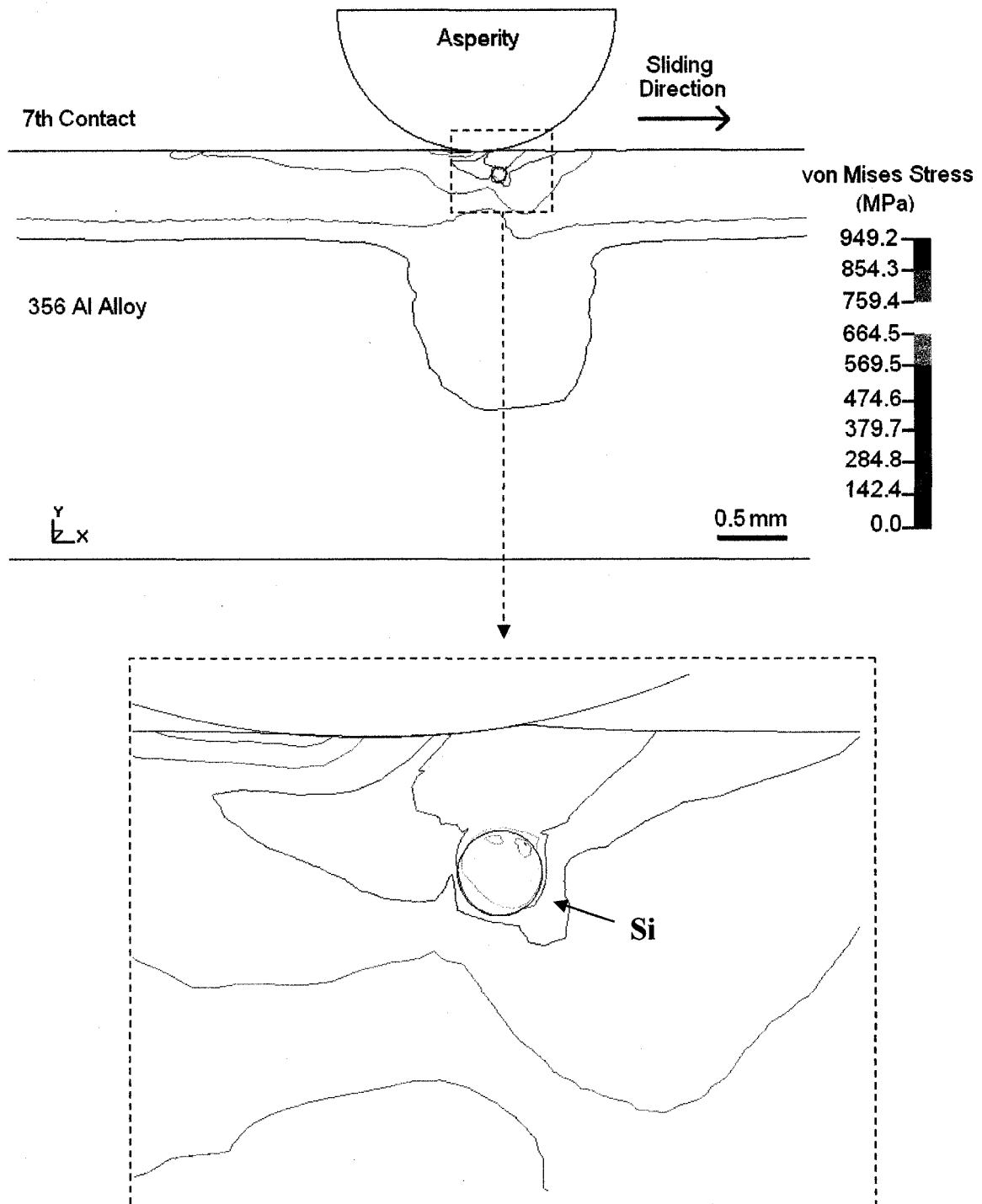


Figure 7.35: von Mises stress (MPa) distribution in the 356 Al half-space after seventh sliding contact with the implementation of a circular shaped Si particle (Sliding velocity: 10 m/s, Normal load: 250 N/mm, Equation 4.5).

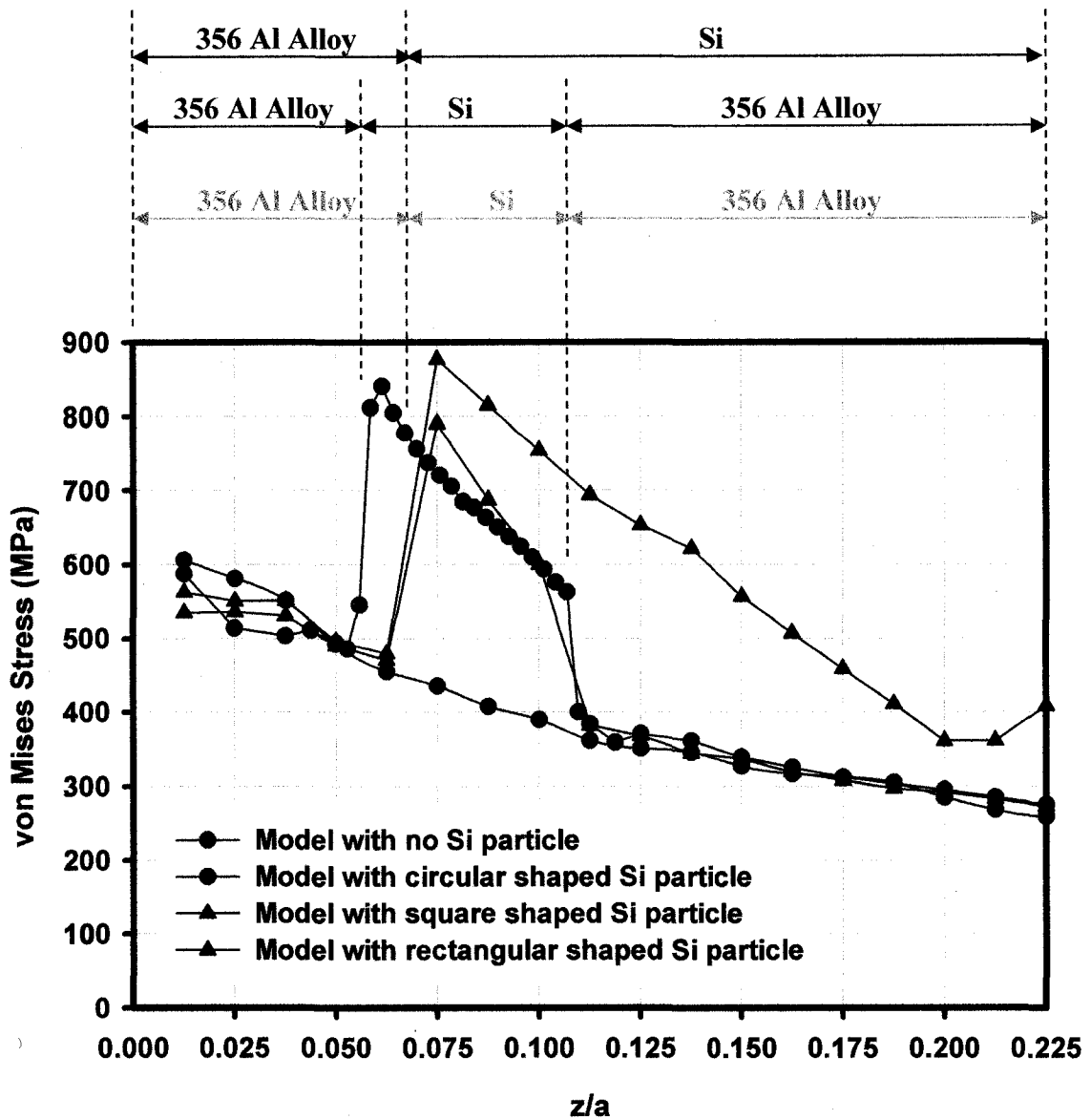


Figure 7.36: Subsurface von Mises stress (MPa) distribution at the mid-point of the 356 Al half-space after seventh sliding contact (Sliding velocity: 10 m/s, Normal load: 250 N/mm, Equation 4.5).

Figures 7.37. and 7.38 present the distribution of the equivalent plastic strain below the surface for models both with and without Si particles. The results indicate that the Si particles resisted penetration of the plastic deformation to the subsurface layers that are located below them, as expected. However, for the subsurface positions in close vicinity to the contact surface—specifically above the Si particles—an increase in the plastic deformation was observed. Figure 7.39 shows the distribution of subsurface plastic strain at the mid-point of the 356 Al half-space with a circular shaped Si particle. Figure 7.39 indicates that at a normalized depth of 0.0375 there is, approximately, a 4 % increase in the plastic strain with the implementation of a Si particle. Below a normalized depth of 0.0375 there was up to a 9% decrease in the plastic strain when the results were compared with the original model, which did not consider a Si particle. The results suggest that there was a 3.0 to 20.1 % decrease in the plastic strain in the positions below the Si particle.

Figure 7.40 displays the change in the distribution of subsurface hydrostatic pressure at the mid-point of the 356 Al half-space with a square shaped Si particle after the seventh asperity contact at a sliding velocity of 10 m/s and a normal load of 250 N/mm. Hydrostatic pressure was increased to 25 % and 19 % at the subsurface positions just before, and after the Si particle. The subsurface positions that corresponded to the Si particle showed a decrease in the hydrostatic pressure ranging between 17.5 to 26.5 % when results were compared with the predictions of the model that did not implement an Si particle.

The presence of elastic Si particles inside the 356 Al half-space caused a decrease in the predicted temperature. Figure 7.41 illustrates the change in the subsurface temperature distribution at the mid-point of the 356 Al half-space with the implementation of a Si particle below the surface at a sliding velocity of 10 m/s and a normal load of 250 N/mm. A 4 % decrease in the temperature at the surface was observed after the implementation of a square shaped Si particle, due to a decrease in the total plastic deformation.

In an effort to investigate the change of subsurface stresses and strains after the implementation of a Si particle below the surface of the 356 Al half-space, the subsurface regions surrounding the Si particle were categorized into nine regions and the subsurface characteristic predictions were compared with the original model that did not consider a Si particle. The subsurface regions adjacent to the square shaped Si

particle are illustrated in Figure 7.42. The subsurface positions over the Si particle were designated as regions above the Si particle (Regions 1, 2 and 3), and will be referred to accordingly. Similarly, the regions lower than the Si particles were defined as regions below the Si particle (Regions 7, 8 and 9). The regions at the same subsurface positions as the Si particles were identified as back (Region 4) and front (Region 6) edges. Region 5 represents the Si particles, themselves.

Distributions of the von Mises stress, hydrostatic pressure, equivalent plastic strain, strain rate and temperature were determined, both inside the Si particles and in the surrounding regions—up to three elements away from the Si particles—for seven sliding contacts. Changes in the subsurface distributions with the implementation of a Si particle are summarized as percentages for different shaped Si particles in Tables 7.1, 7.2 and 7.3. The values for these were taken when the asperities were at the top of the Si particle. Trends observed after the implementation of a Si particle were similar in all regions for the square and rectangular shaped Si particles. However, consideration of a higher aspect ratio of Si particle caused a higher decrease or increase in the subsurface values. Trends in the subsurface values followed a similar drift with the implementation of a circular shaped Si particle, or square shaped Si particle in some regions (Regions 1, 2, 4, 5, 7 and 8). However, there were significant differences in the trends observed for the other regions.

The results suggested that the implementation of an elastic Si particle caused a decrease in the predicted temperature in all subsurface regions surrounding the Si particle. This was an expected result since the temperature increase is calculated from the plastic deformations (Equation 4.6). When a Si particle was introduced into a 356 Al matrix, it prompted an increase in the von Mises stress, and a decrease in the hydrostatic pressure inside the Si particles (Region 5). The von Mises stress increase in Region 5 ranged between 53.0 % and 82.0 % for the square and circular shaped Si particles. However, up to 18.2 % decrease in hydrostatic pressure was observed for the circular shaped Si particle, while the reduction of hydrostatic pressure was approximately 26.5 % for the square shaped Si particle. As expected, there was no plastic deformation or corresponding strain rates in the elastic Si particles. The introduction of a Si particle prompted an increase in the von Mises stresses in the diagonal regions (Regions 1, 3, 7 and 9) and Region 8 (just below the Si particle).

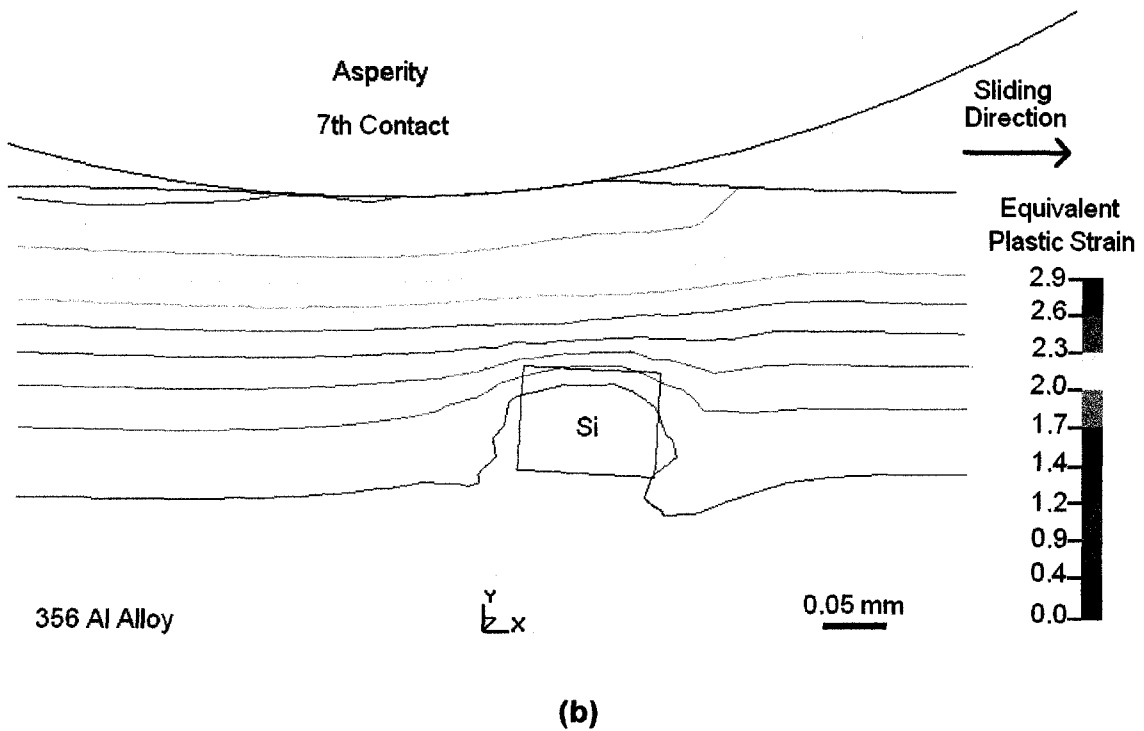
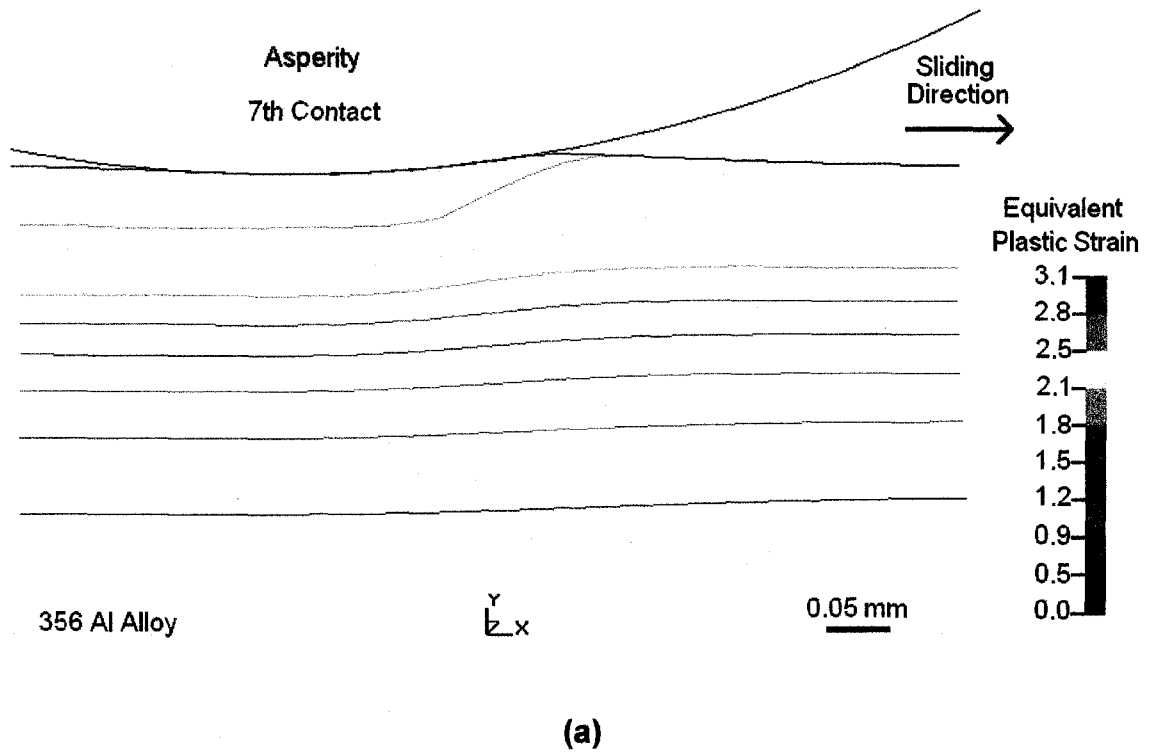


Figure 7.37: Equivalent plastic strain distribution in the 356 Al half-space after seventh sliding contact (Sliding velocity: 10 m/s, Normal load: 250 N/mm, Equation 4.5): (a) the model not considering a Si particle and (b) the model with square shaped Si particle.

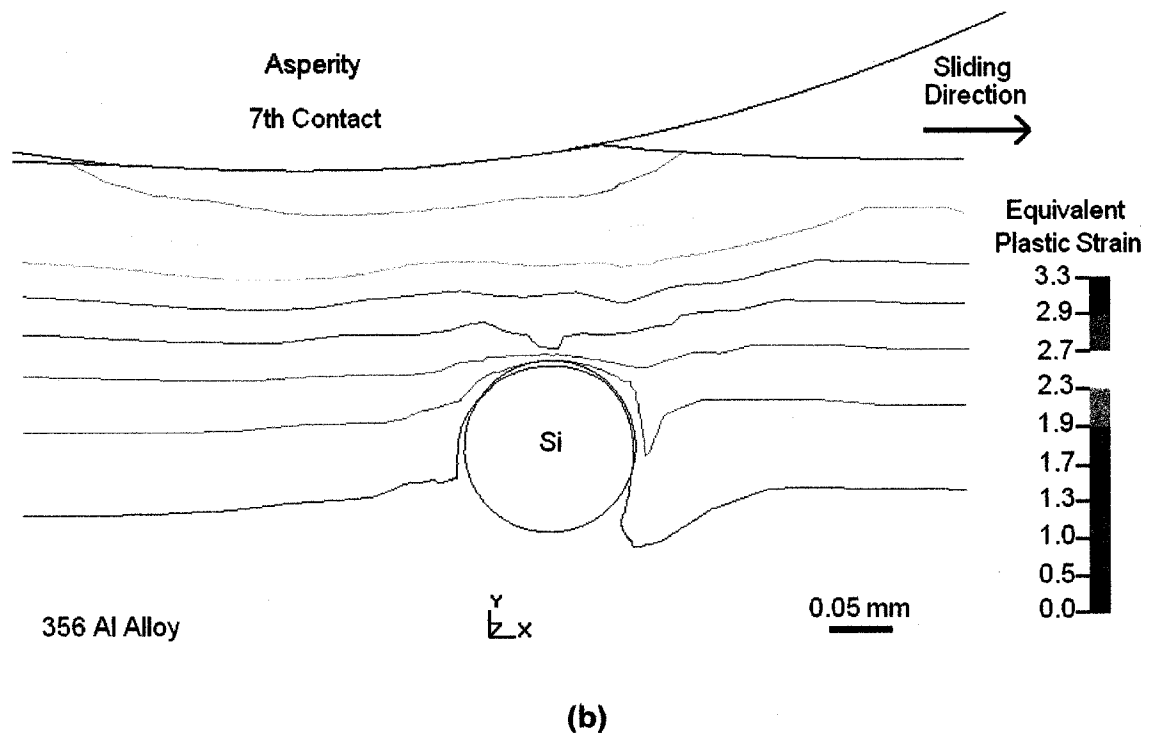
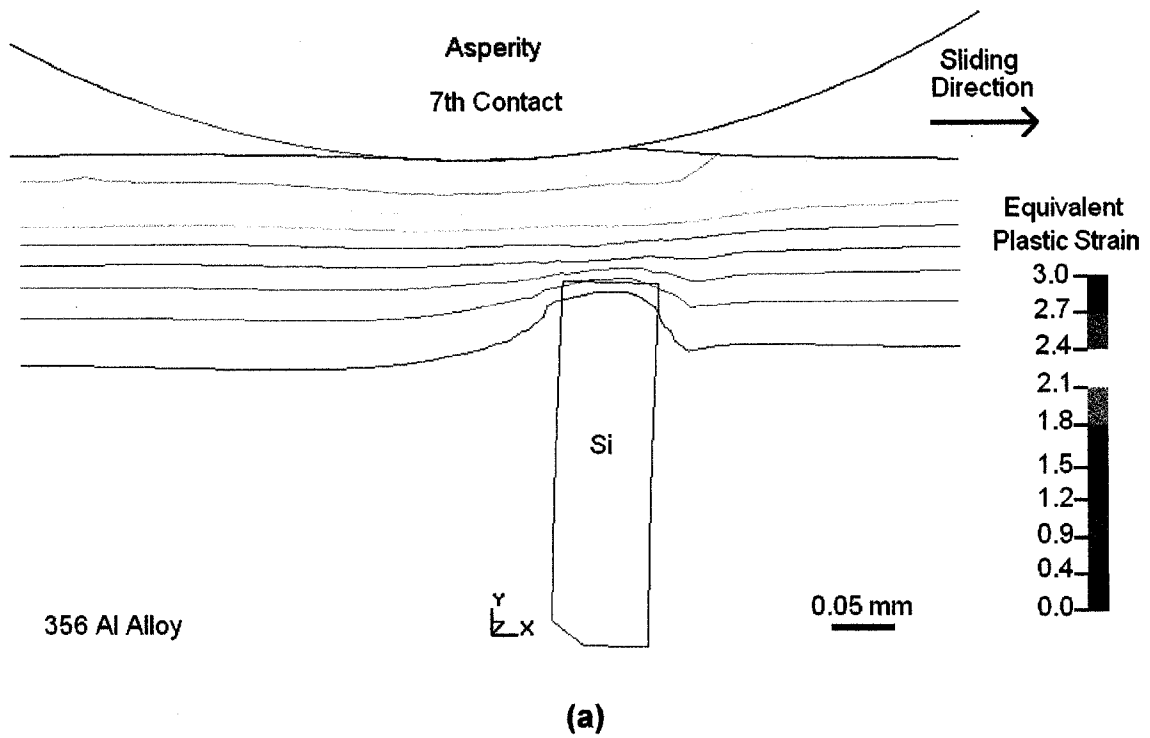


Figure 7.38: Equivalent plastic strain distribution in the 356 Al half-space after seventh sliding contact (Sliding velocity: 10 m/s, Normal load: 250 N/mm, Equation 4.5): (a) the model with rectangular shaped Si particle and (b) the model with circular shaped Si particle.

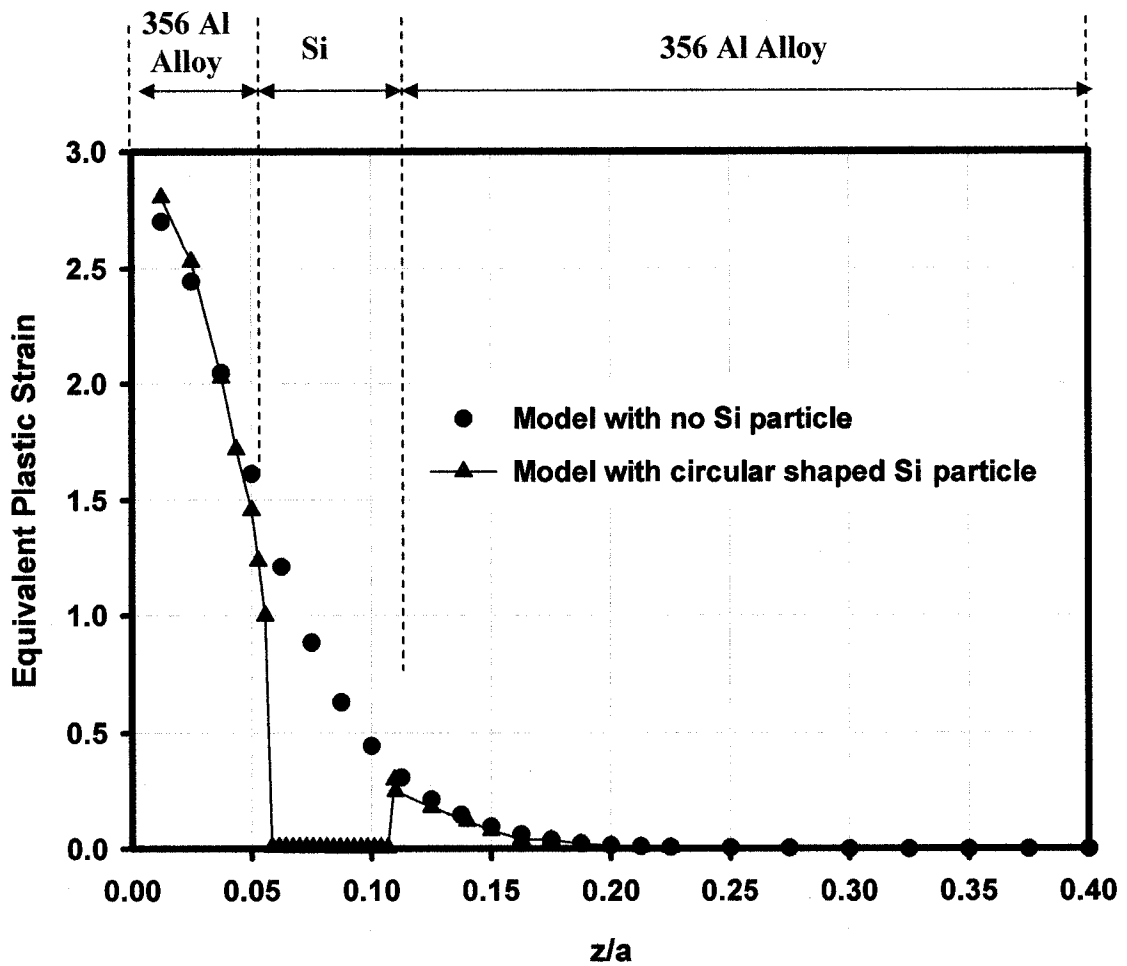


Figure 7.39: Equivalent plastic strain distribution at the mid-point of the 356 Al half-space after seventh sliding contact with and without the implementation of a Si particle (Sliding velocity: 10 m/s, Normal load: 250 N/mm, Equation 4.5).

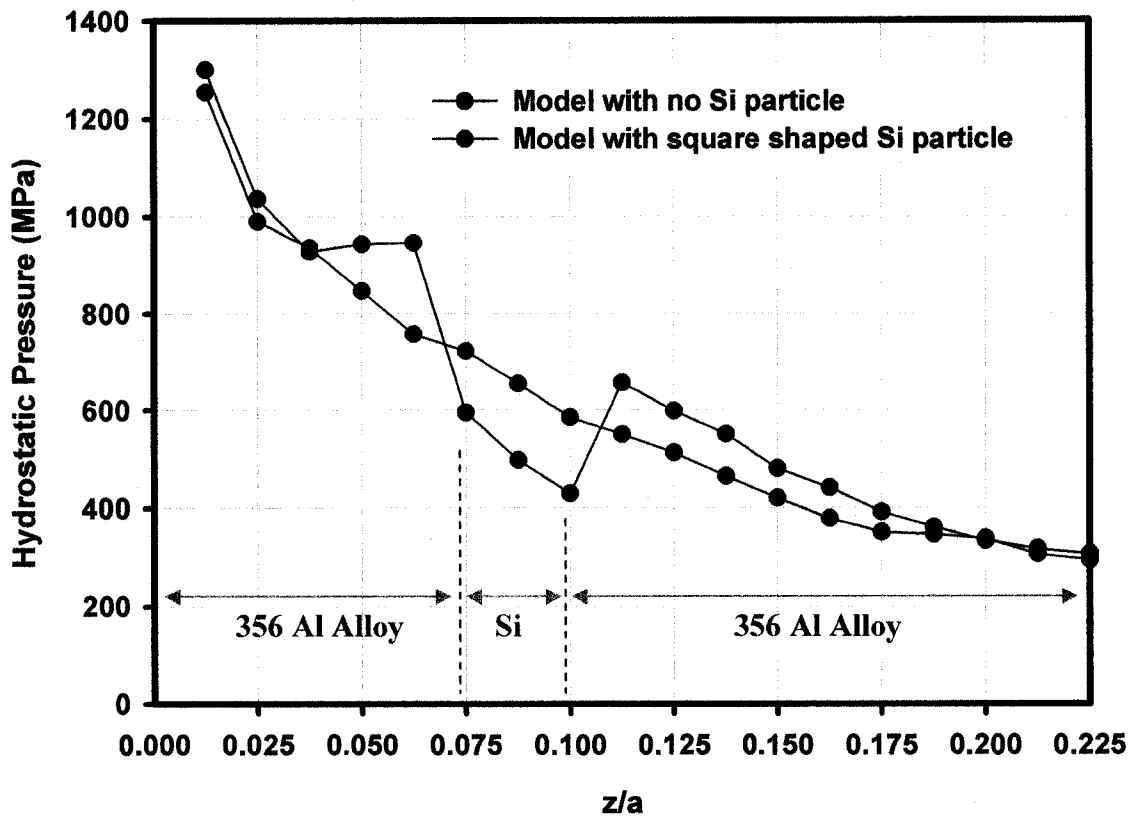


Figure 7.40: Hydrostatic pressure (in MPa units) distribution at the mid-point of the 356 Al half-space after seventh sliding contact with and without the implementation of a Si particle (Sliding velocity: 10 m/s, Normal load: 250 N/mm, Equation 4.5).

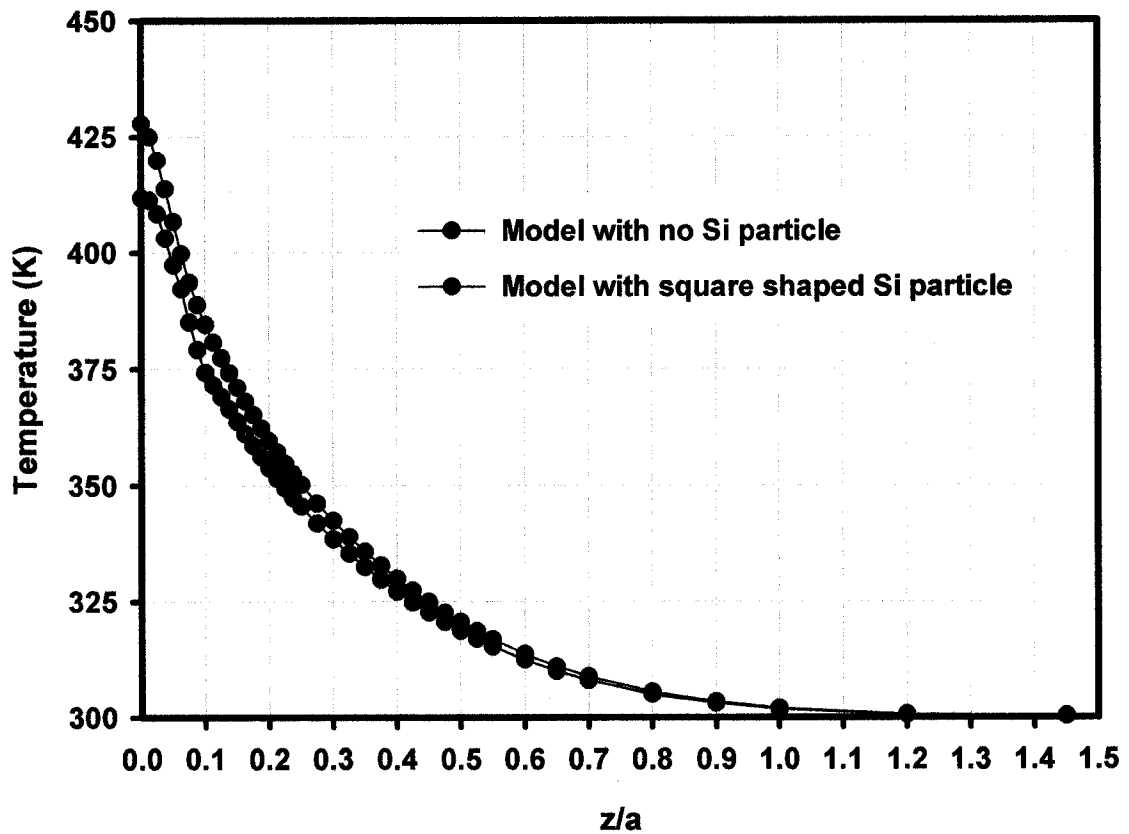


Figure 7.41: Change in the subsurface temperature distribution at the mid-point of the 356 Al half-space with the implementation of a Si particle below the surface (Sliding velocity: 10 m/s, Normal load: 250 N/mm, Equation 4.5).

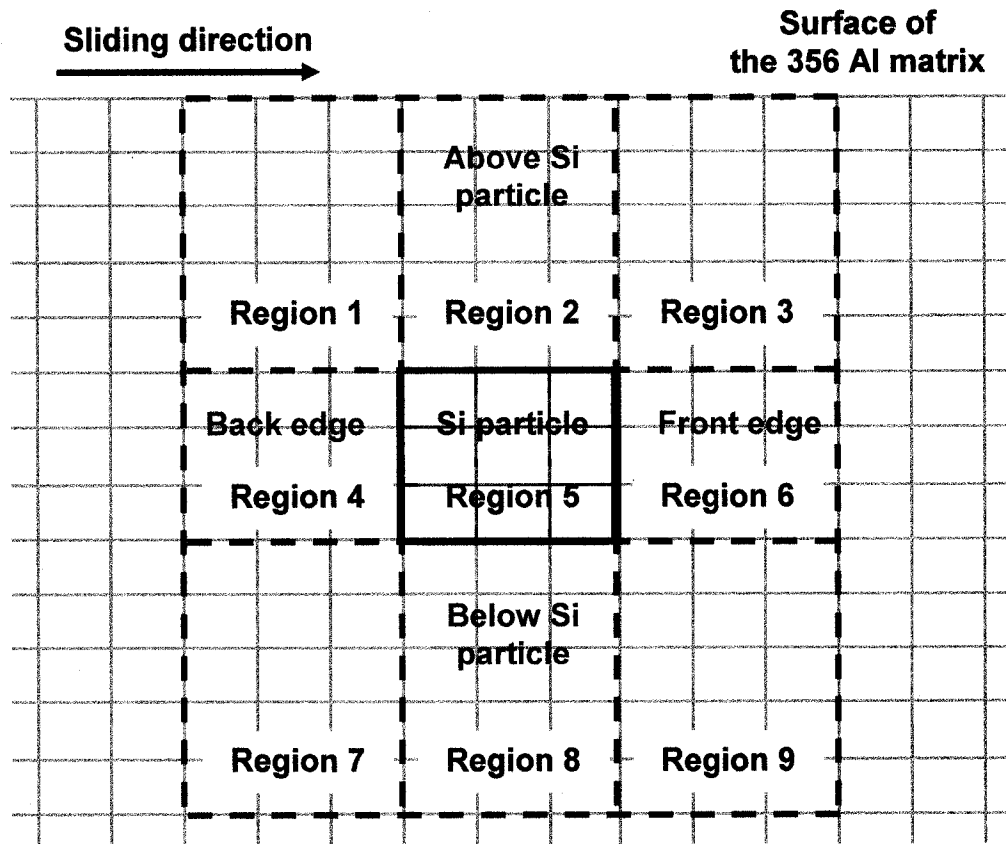


Figure 7.42: Subsurface regions adjacent to the square shaped Si particle.

Table 7.1: Change in the subsurface characteristics with the implementation of a square shaped Si particle in the 356 Al matrix for a sliding velocity of 10 m/s and normal load of 250 N/mm (\uparrow : increase, \downarrow : decrease).

Subsurface Position		von Mises Stress	Hydrostatic Pressure	Equiv. Plastic Strain	Strain Rate	Temperature
Above Si particle	Region 1	up to 8.5 % \uparrow	2.2 – 21.8 % \uparrow	0.4 – 12.3 % \uparrow	11.0 – 38.0 % \uparrow	1.6 – 2.6 % \downarrow
	Region 2	0.4 – 11.8 % \downarrow	7.5 – 25.0 % \uparrow	4.8 – 12.7 % \downarrow	0.7 – 3.8 % \uparrow	2.3 – 3.8 % \downarrow
	Region 3	2.5 – 11.5 % \uparrow	1.5 – 12.3 % \uparrow	4.8 – 9.2 % \downarrow	up to 29.3 % \uparrow	3.0 – 3.9 % \downarrow
Back edge	Region 4	4.1 – 5.7 % \downarrow	2.0 – 2.8 % \downarrow	18.7 – 44.5 % \downarrow	29.6 – 37.1 % \downarrow	1.8 – 2.1 % \downarrow
Si particle	Region 5	54.0 – 81.7 % \uparrow	17.5 – 26.5 % \downarrow	–	–	1.9 – 2.7 % \downarrow
Front edge	Region 6	up to 3.7 % \downarrow	4.4 – 14.9 % \downarrow	5.5 – 16.3 % \downarrow	8.7 – 20.2 % \downarrow	2.3 – 2.6 % \downarrow
Below Si particle	Region 7	3.9 – 7.7 % \uparrow	1.9 – 2.5 % \uparrow	2.7 – 24.4 % \uparrow	29.4 – 68.2 % \uparrow	1.7 – 2.0 % \downarrow
	Region 8	4.8 – 5.6 % \uparrow	16.8 – 19.2 % \uparrow	1.4 – 2.4 % \downarrow	up to 5.9 % \uparrow	2.1 – 2.4 % \downarrow
	Region 9	2.7 – 10.1 % \uparrow	3.7 – 9.2 % \uparrow	2.2 – 3.9 % \downarrow	29.1 – 68.1 % \uparrow	1.9 – 2.3 % \downarrow

Table 7.2: Change in the subsurface characteristics with the implementation of a rectangular shaped Si particle in the 356 Al matrix for a sliding velocity of 10 m/s and normal load of 250 N/mm (↑ : increase, ↓: decrease).

Subsurface Position		von Mises Stress	Hydrostatic Pressure	Equiv. Plastic Strain	Strain Rate	Temperature
Above Si particle	Region 1	1.3 – 9.3 % ↑	7.0 – 15.7 % ↑	0.9 – 12.8 % ↑	13.0 – 31.9 % ↑	0.6 – 1.2 % ↓
	Region 2	up to 7.2 % ↓	4.5 – 25.4 % ↑	1.2 – 14.4 % ↓	1.9 – 6.6 % ↑	1.3 – 2.2 % ↓
	Region 3	1.5 – 24.2 % ↑	3.0 – 39.0 % ↑	0.4 – 8.6 % ↓	up to 24.4 % ↑	2.5 – 3.6 % ↓
Back edge	Region 4	0.6 – 7.3 % ↓	3.0 – 8.8 % ↓	10.8 – 52.5 % ↓	12.0 – 48.0 % ↓	1.5 – 1.8 % ↓
Si particle	Region 5	26.7 – 101.3 % ↑	0.7 – 32.0 % ↓	–	–	1.2 – 1.9 % ↓
Front edge	Region 6	up to 3.0 % ↓	2.3 – 18.7 % ↓	2.2 – 12.8 % ↓	3.3 – 16.3 % ↓	1.9 – 2.0 % ↓
Below Si particle	Region 8	6.6 – 25.9 % ↑	7.0 – 11.2 % ↑	up to 2.5 % ↓	up to 7.0 % ↑	1.3 – 1.7 % ↓

Table 7.3: Change in the subsurface characteristics with the implementation of a circular shaped Si particle in the 356 Al matrix for a sliding velocity of 10 m/s and normal load of 250 N/mm (\uparrow : increase, \downarrow : decrease).

Subsurface Position		von Mises Stress	Hydrostatic Pressure	Equiv. Plastic Strain	Strain Rate	Temperature
Above Si particle	Region 1	2.1 – 8.4 % \uparrow	9.8 – 18.7 % \uparrow	3.2 – 9.9 % \uparrow	12.7 – 28.6 % \uparrow	1.7 – 2.2 % \downarrow
	Region 2	3.1 – 11.6 % \downarrow	2.7 – 3.2 % \uparrow	1.0 – 9.7 % \downarrow	1.8 – 7.7 % \downarrow	2.2 – 2.8 % \downarrow
	Region 3	0.5 – 3.4 % \uparrow	0.2 – 13.6 % \uparrow	up to 1.0 % \uparrow	10.2 – 17.5 % \downarrow	2.8 – 2.9 % \downarrow
Back edge	Region 4	3.1 – 3.3 % \downarrow	2.4 – 19.4 % \downarrow	14.8 – 38.6 % \downarrow	4.6 – 34.1 % \downarrow	1.9 – 2.4 % \downarrow
Si particle	Region 5	52.3 – 80.7 % \uparrow	12.4 – 18.2 % \downarrow	–	–	2.0 – 2.6 % \downarrow
Front edge	Region 6	3.0 – 19.2 % \uparrow	5.4 – 21.3 % \downarrow	6.3 – 22.4 % \uparrow	7.3 – 64.5 % \uparrow	2.4 – 2.8 % \downarrow
Below Si particle	Region 7	0.6 – 3.9 % \uparrow	1.5 – 7.7 % \uparrow	9.3 – 16.6 % \uparrow	2.3 – 42.3 % \uparrow	1.7 – 2.3 % \downarrow
	Region 8	2.6 – 6.3 % \uparrow	0.8 – 23.9 % \uparrow	3.1 – 20.1 % \downarrow	4.5 – 15.6 % \uparrow	0.9 – 1.9 % \downarrow
	Region 9	1.5 – 8.7 % \uparrow	6.5 – 20.4 % \uparrow	3.3 – 25.5 % \uparrow	37.8 – 64.3 % \uparrow	1.8 – 2.5 % \downarrow

Regions 2, 4 and 6 observed a decrease in the von Mises stresses with the implementation of square and rectangular shaped Si particles. An increase in the von Mises stress was observed at the front edge of the circular Si particle (Region 6). Trends in hydrostatic pressure changes were the same for all shapes of Si particles—with an increase in the hydrostatic pressure at the locations above and below the Si particles (Regions 1 to 3 and 7 to 9), and a decrease in the edge positions (Regions 4 and 6). Interestingly, considering a Si particle did not decrease the observed plastic deformation in all of the surrounding regions. There was an increase in the plastic strains at the back edge diagonal positions—13 % for Region 1 and 25 % for Region 7—with the consideration of square and rectangular shaped Si particles. The presence of a circular shaped Si particle prompted an increase in the plastic strains in all diagonal regions (Regions 1, 3, 7 and 9) and in the front edge region (Region 6). The highest increase in the equivalent plastic strain was observed in Region 9, reaching a 25.5 % increase with the circular shaped Si particle.

In summary, considering subsurface Si particles in the numerical model indicated that hard secondary particles help to resist the penetration of deformation below the surface of the 356 Al matrix, as expected. However, an increase in the stresses and plastic strains were observed in some locations adjacent the Si particles.

In the next section, a numerical investigation on a void growth model will be presented in an attempt to determine a damage gradient and a critical depth at which delamination cracks might initiate and propagate in an aluminum alloy during sliding contacts. The findings of the presented finite element models for subsurface distribution of stresses and strains will be used in the damage gradient analysis.

7.5. ANALYSIS OF SUBSURFACE DAMAGE ACCUMULATION PROCESS

7.5.1. NUMERICAL SUBSURFACE DAMAGE

This section proposes a model that examines void growth rate as a function of the number for the sliding contacts, in order to analyze the subsurface damage rate and predict the location of delamination cracks. In this model, the voids that nucleated at impurities and second phase particles were assumed to be present in the aluminum. It was assumed that the damage process progressed via the growth of voids that

coalesced and formed subsurface cracks parallel to the contact surface. The variation of the void growth rate beneath the contact surface—under the influence of stress gradients—was evaluated with respect to the subsurface depth, using Equation 1.1.

Non-linear regression analyses revealed that the variations in hydrostatic pressure (σ_H), plastic strain (ε), strain rate ($\dot{\varepsilon}$) and temperature (T) as a function of depth (z)—obtained by the coupled thermo-mechanical model—can be represented by the exponential relationships of the following forms (Figures 7.19, 7.17, 7.22 and 7.21):

$$\sigma_H = k_1 + [k_2 \exp(-k_3 z)] \quad (7.1)$$

$$\varepsilon = m_1 \exp(-m_2 z) \quad (7.2)$$

$$\dot{\varepsilon} = n_1 \exp(-n_2 z) \quad (7.3)$$

$$T = p_1 + [p_2 \exp(-p_3 z)] \quad (7.4)$$

where z has the units of mm. The coefficients in Equations 7.1 to 7.4 obtained for each sliding contact cycle are listed in Table 7.4 for a sliding velocity of 10 m/s and a normal load of 150 N/mm.

The flow strength of the aluminum as a function of the depth (z) was obtained by substituting Equations 7.2, 7.3 and 7.4 into Equation 4.5 as follows:

$$\sigma_f = \left[\sigma_s - (\sigma_s - \sigma_0) \exp\left(-\frac{m_1 \exp(-m_2 z)}{\varepsilon_c}\right) \right] \left[1 + \left(\frac{n_1 \exp(-n_2 z)}{D} \right)^{1/q} \right] \left[1 - \left(\frac{\{p_1 + [p_2 \exp(-p_3 z)]\} - T_{room}}{T_{melt} - T_{room}} \right)^m \right] \quad (7.5)$$

Then equations representing the hydrostatic pressure (Equation 7.1), flow stress (Equation 7.5) and strain rate (Equation 7.3) as a function of the depth were inserted into

Equation 1.1 to determine the void growth rate (\dot{R})—normalized with respect to the initial radius of the void (R):

$$\frac{\dot{R}}{R} = \left[\frac{5}{3} + \frac{\sqrt{3}}{2} \frac{[k_1 + [k_2 \exp(-k_3 z)]]}{\left[\sigma_s - (\sigma_s - \sigma_0) \exp\left(-\frac{m_1 \exp(-m_2 z)}{\varepsilon_c}\right) \right] \left[1 + \left(\frac{n_1 \exp(-n_2 z)}{D}\right)^{1/q} \right]} \right] \left[\frac{1}{\left[1 - \left(\frac{\{p_1 + [p_2 \exp(-p_3 z)]\} - T_{room}}{T_{melt} - T_{room}}\right)^m \right]} [n_1 \exp(-n_2 z)] \right] \quad (7.6)$$

Figure 7.43 illustrates how the change in damage rate acts as a function of normalized depth (z/a)—obtained using Equation 7.6 for a sliding velocity of 10 m/s and a normal load of 150 N/mm. The subsurface damage gradient remained constant after a finite number of sliding contacts. The maximum value of the normalized void growth rate (\dot{R}/R) was calculated as $8 \times 10^2 \text{ s}^{-1}$ after the first sliding contact, and $5 \times 10^2 \text{ s}^{-1}$ for the subsequent contacts. Figure 7.43 indicates that the location of the material layer where the maximum rate of damage accumulation occurred was at $z/a = 0.06$. The existing voids at this critical depth (z_c) below the surface corresponding to the maximum \dot{R}/R value will propagate faster than the voids at other subsurface positions, prompting subsurface fractures to occur at this depth. The \dot{R}/R at the close vicinity of the surface ($z/a < 0.03$) was negative. However, the predicted values for those subsurface regions might have no realistic foundation, due to the high strain rates discussed in Section 7.2.4.

In the proposed material model, the thermal softening and strain rate hardening effects were considered together, in addition to the strain hardening. However, an analysis of the changes in damage rate that considers each effect separately might provide a better understanding of the proposed model's ability to capture the influence of different material effects. The material model's influence on predicting the damage rate

below the contact surface after the seventh sliding contact is presented in Figure 7.44. For a strain hardening material model (Equation 4.7), the maximum rate of damage accumulation was calculated at a normalized depth of 0.10 (i.e. if the effects of surface heating and strain rate are ignored). When thermal softening of the material was considered with strain hardening (Equation 4.9), the position of the maximum rate of damage moved deeper, to a normalized depth of 0.13. In addition, the maximum \dot{R}/R value also decreased in magnitude. This result indicates that if the material softens during sliding contact because of a temperature increase, the void growth rate and possibility of producing or propagating a crack will decrease. This result is expected, since crack propagation will be slower in a ductile matrix. If the strain rate effects are considered in addition to the strain hardening (Equation 4.8), the results suggest that the hardening will prompt the maximum of the damage rate to move toward the surface (to $z/a = 0.05$), and the normalized void growth rate will increase. This result is also expected, because increasing strain rate will make material more brittle. When the thermal condition of the material is considered together with the strain and strain rate hardening (Equation 4.5), the position of the maximum rate of damage was at $z/a = 0.06$. These results indicate that the developed finite element model accurately captured the subsurface deformation characteristics of the 356 Al alloy, with changes in the material properties. In summary, Figure 7.44 shows the significance of the used material model in the prediction of subsurface damage in the 356 Al alloy.

Figure 7.45 illustrates the effects of load and sliding velocity on the damage rate below the contact surface. An increase in the applied load from 150 N/mm to 250 N/mm shifted the position of the maximum damage rate to a deeper location (i.e. from $z/a = 0.060$ to 0.085). The maximum normalized void growth rate value (\dot{R}/R) increased simultaneously. When a high sliding velocity of 10 m/s was issued—compared to 5 m/s—the critical material depth where the damage rate reached its maximum increased from $z/a = 0.050$ to 0.060. Meanwhile, the value of the maximum normalized damage rate almost doubled.

Considering excessive friction in the sliding contact completely changed the distribution of the subsurface damage rate. The damage rate below the surface of the 356 Al half-space is presented in Figure 7.46 for the frictionless condition ($\mu=0.0$), and the high friction condition ($\mu=0.3$). The maximum growth rate was observed at the surface with $\mu=0.3$ and the magnitude of the normalized growth rate increased more

Table 7.4: Pre-exponential and exponential coefficients in Equations 7.1 to 7.4
(Sliding velocity: 10 m/s, Normal load: 150 N/mm).

Contact Cycle	Coefficients				
	k_1 (MPa)	m_1 (mm/mm)	n_1 (1/s)	p_1 (K)	k_2 (MPa)
1st asperity	28.56	0.29	1.3×10^4	299.99	1257.07
2nd asperity	36.49	0.62	1.6×10^4	300.33	1359.12
3rd asperity	29.37	0.94	1.7×10^4	300.62	1194.46
4th asperity	40.06	1.24	1.6×10^4	300.78	1329.27
5th asperity	43.06	1.54	1.6×10^4	300.91	1289.70
6th asperity	47.78	1.82	1.5×10^4	301.17	1381.05
7th asperity	43.06	2.08	1.5×10^4	301.00	1220.65
Contact Cycle	Coefficients				
	m_2 (1/mm)	n_2 (1/mm)	p_2 (K)	k_3 (1/mm)	p_3 (1/mm)
1st asperity	15.66	17.20	24.32	7.09	6.12
2nd asperity	16.74	20.44	29.84	6.97	4.60
3rd asperity	17.01	20.55	33.74	5.91	3.73
4th asperity	17.00	20.06	35.76	6.87	3.08
5th asperity	16.98	20.29	37.52	6.95	2.65
6th asperity	16.93	20.00	40.25	7.50	2.42
7th asperity	16.73	18.29	41.53	6.54	2.10

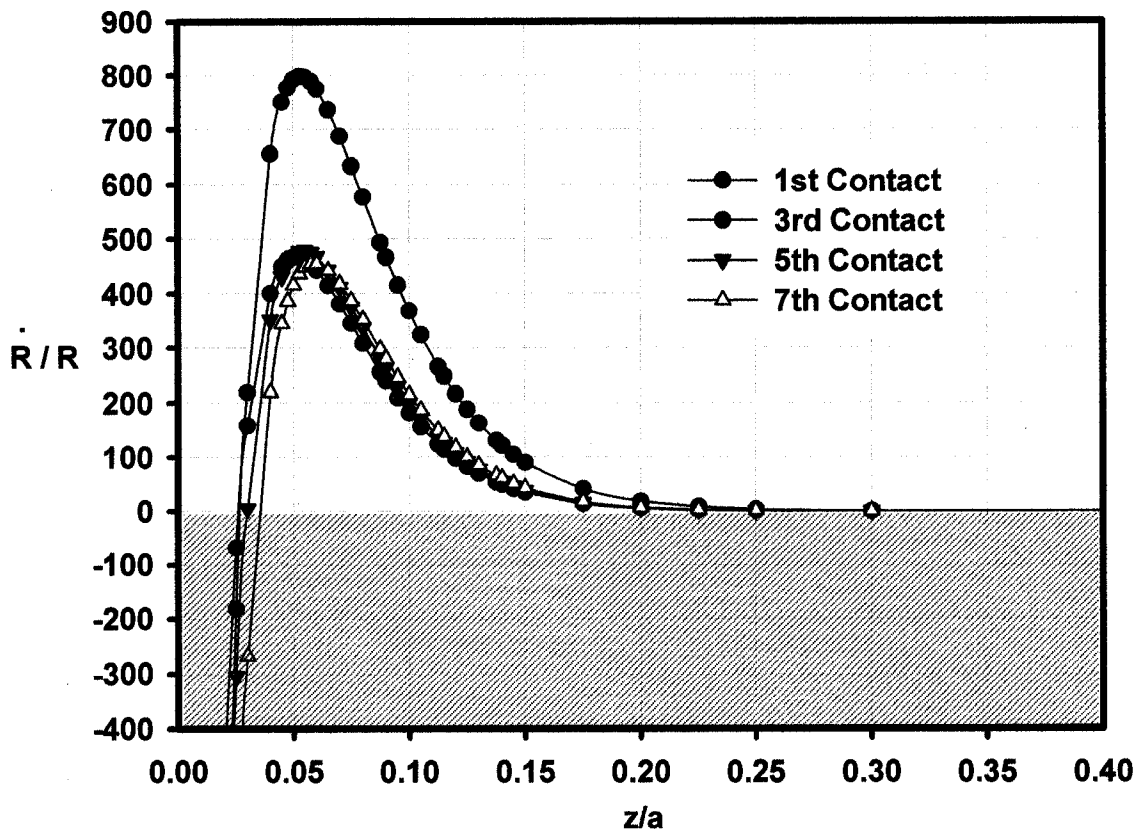


Figure 7.43: Change in the damage rate with the depth below the contact surface with increasing number of sliding contacts (Sliding velocity: 10 m/s and Normal load: 150 N/mm).

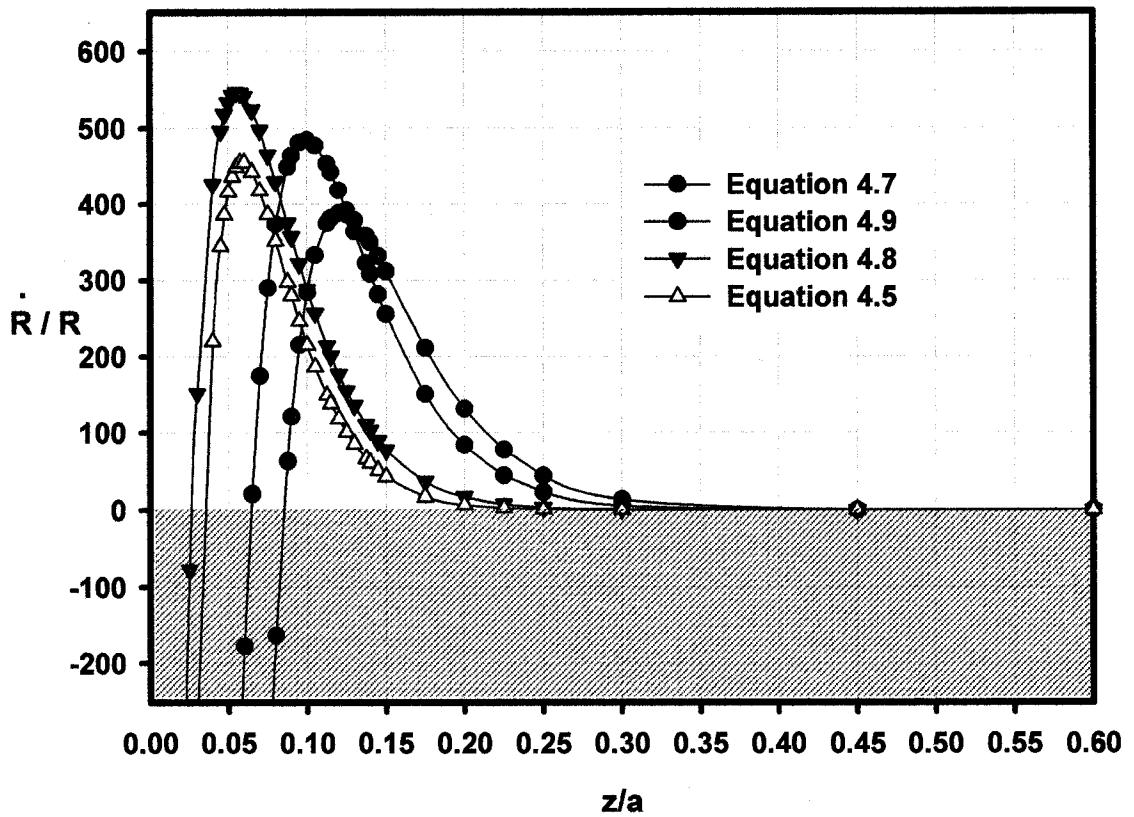


Figure 7.44: Effect of the material model on the damage rate below the contact surface after seventh sliding contact (Sliding velocity: 10 m/s and Normal load: 150 N/mm).

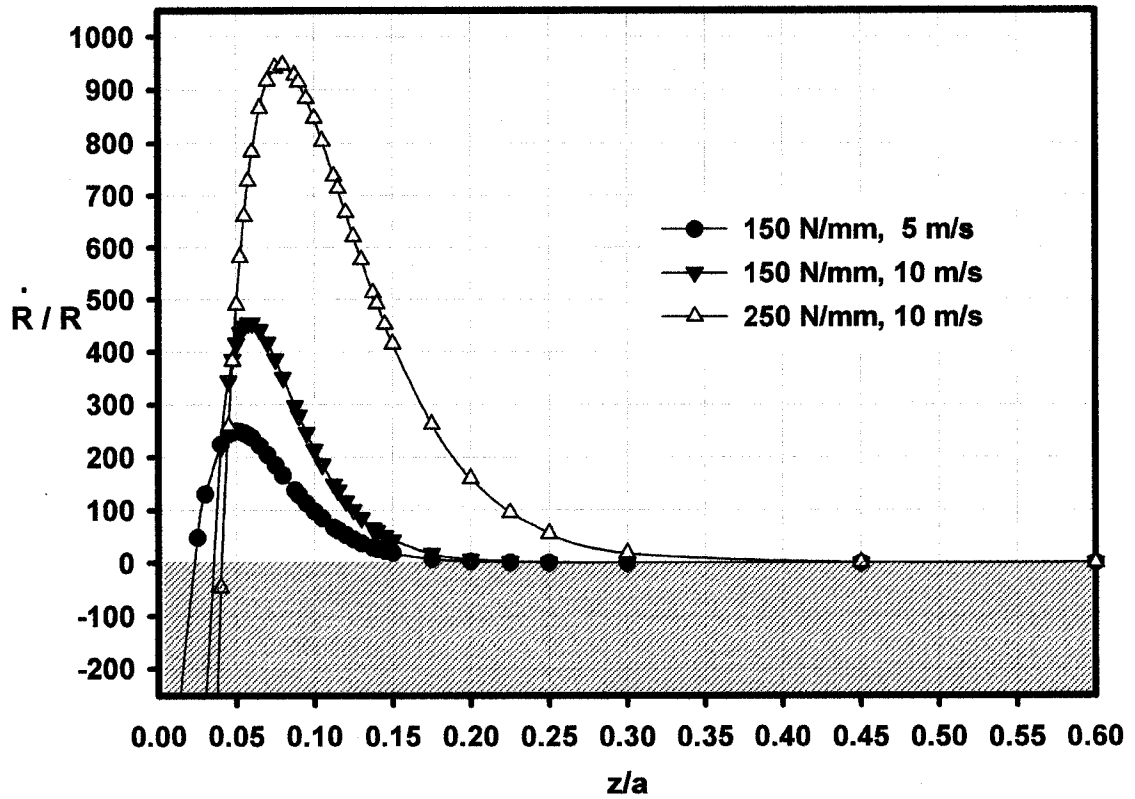


Figure 7.45: Effect of the normal load and the sliding velocity on the damage rate below the contact surface after seventh sliding contact obtained with Equation 4.5.

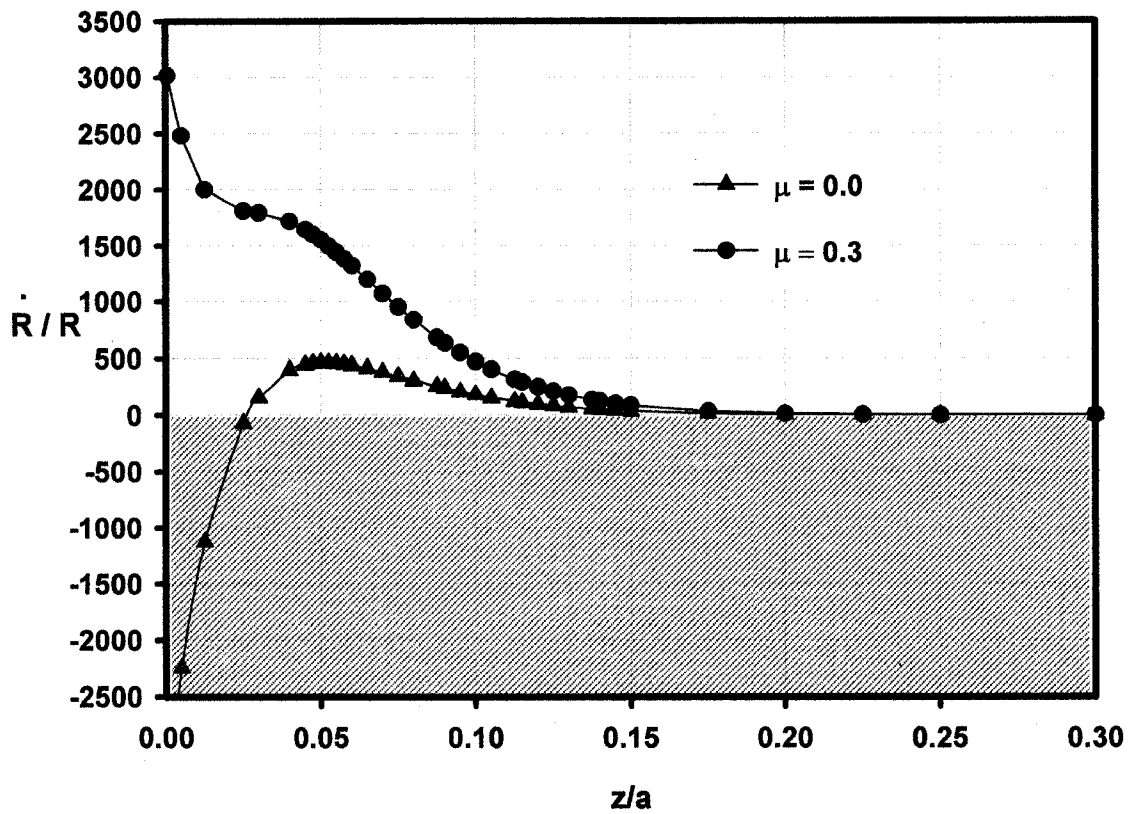


Figure 7.46: Effect of the friction on the damage rate below the contact surface after third sliding contact (Sliding velocity: 10 m/s, Normal load: 150 N/mm, obtained with Equation 4.5).

than six times. This change in the damage gradient was prompted by the overall effect of the changes in variables in Equation 7.6. The plastic strains, the strain rate and the flow stress increased with the friction between the 356 Al half-space and the asperities. However, the increase in the contact area due to friction forces resulted in a small decrease in the hydrostatic pressure. The overall effect of these variables is an increase in the normalized damage rate calculated by Equation 7.6, with the maximum \dot{R}/R value moving to the surface.

7.5.2. INFLUENCE OF SI PARTICLES ON SUBSURFACE DAMAGE GRADIENT

In Section 7.4, the change in the subsurface deformation characteristics in the 356 Al alloy with the implementation of a Si particle was investigated. This section explores the influence of the Si particles on the subsurface damage rate. The subsurface damage rate at the mid-point of the 356 Al half-space was calculated by using Equation 7.6, after the consideration of differently shaped Si particles. In addition, subsurface damage rate was also investigated along the lines that pass through the sides of the Si particles (back and front edges). Figure 7.47 illustrates the subsurface lines used for the investigation of the damage rate for the square shaped Si particle. Since the Si/Al interface was assumed to be infinitely strong in the finite element model, and the ductile void growth equation proposed by Rice and Tracey is applicable to the hardening materials, the void growth rate was not calculated for the subsurface positions where the Al/Si interface and the elastic Si particles were present. Void growth rate analysis was completed only for the regions surrounding the Si particles.

Figure 7.48 shows the change in the subsurface damage rate at the mid-point of the 356 Al half-space with the implementation of differently shaped Si particles at a sliding velocity of 10 m/s and a normal load of 250 N/mm after the seventh sliding contact. In Figure 7.48, the subsurface damage rate distribution for the model that did not consider a Si particle is also included, for comparison purposes. The maximum value of the normalized void growth rate for the original model that does not consider the hard particles was approximately 950 s^{-1} at the normalized depth of 0.085, after seven sliding contacts. The results indicate that the implementation of Si particles below the surface of the 356 Al alloy decreased the damage rate for the subsurface positions below the Si

particles—for all considered Si shapes. However, an increase in the growth rate was observed for the positions above the hard particles. The highest increase in the normalized growth rate was found in the model with circular shaped Si particles reaching to 1820 s^{-1} at the normalized depth of 0.045, which corresponds to half the distance between the surface and the Si particle. Similarly, for the square shaped Si particle, the maximum normalized growth rate was at a normalized depth of 0.0375 with a value of 200 s^{-1} . For the rectangular shaped Si particle, the position of the highest growth rate was observed to be at the surface. The void growth rate at the upper interface, between the Si particle and the 356 Al alloy, was calculated as negative values for all Si shapes.

Figure 7.49 illustrates the changes in the subsurface damage rate at the back edge of the Si particle. Discontinuous points in the damage rate curves correspond to the interfaces between different regions: Regions 1 and 4, and Regions 4 and 7 (for the subsurface regions surrounding the Si particles, please refer to Figure 7.42). The implementation of the square and rectangular shaped Si particles decreased the damage rate in Regions 4 and 7, but the void growth rate increased in Region 1. The maximum growth rate was at the interface between Regions 1 and 4, which corresponds to the subsurface level next to the upper boundary of the Si particle. Interestingly, circular shaped Si particles revealed a different effect on the damage rate at the back edge of the Si particle than those with square and rectangular shapes. An increase of approximately three times was observed in the maximum damage rate of Region 4 with the implementation of a circular shaped Si particle.

Figure 7.50 shows the change in the subsurface damage rate at the front edge of the Si particle for a sliding velocity of 10 m/s and a normal load of 250 N/mm. With consideration of the square and rectangular shaped Si particles, the maximum damage rate moved to the interface between Regions 3 and 6, which correspond to the positions next to the upper boundary of the Si particle. The maximum growth rate was observed in Region 6 with the circular shaped Si particle. In addition, there was an increase in the growth rate observed in Region 3 for the circular shaped Si particle.

In summary, the results indicate that Si particles placed below the surface help to protect the subsurface layers of the 356 Al alloy positioned below the Si particles. Although the Si particles resist the penetration of plastic deformation below the surface of the 356 Al, they create a reverse effect for the subsurface layers above the hard particles. For the same amount of loading, deformation concentrates between the

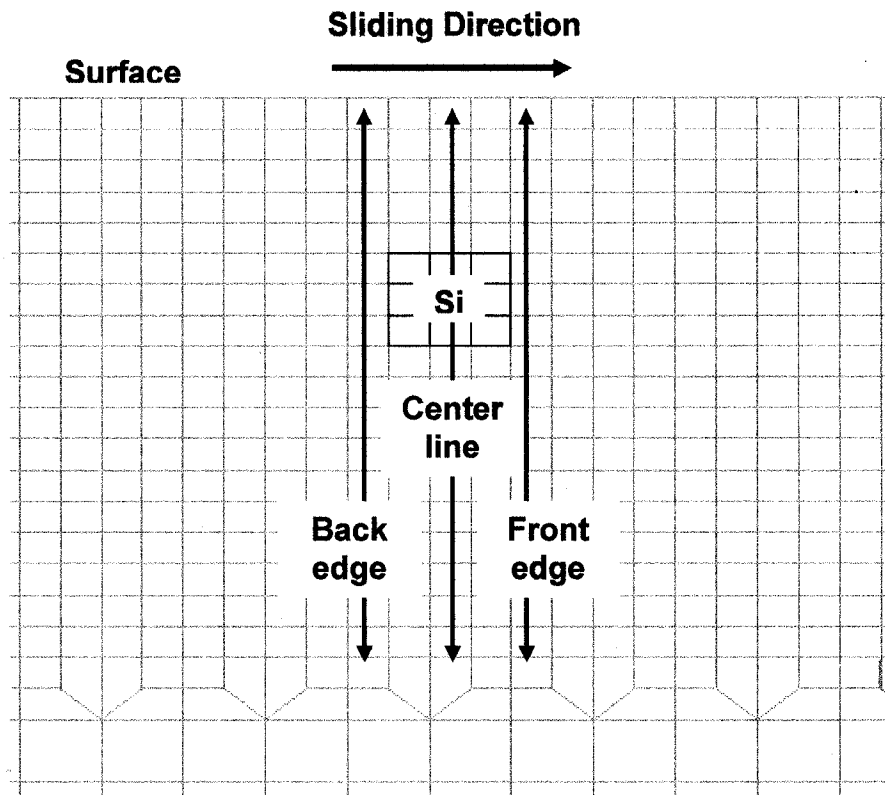


Figure 7.47: Position of the subsurface lines used for the damage rate calculations in the 356 Al half-space.

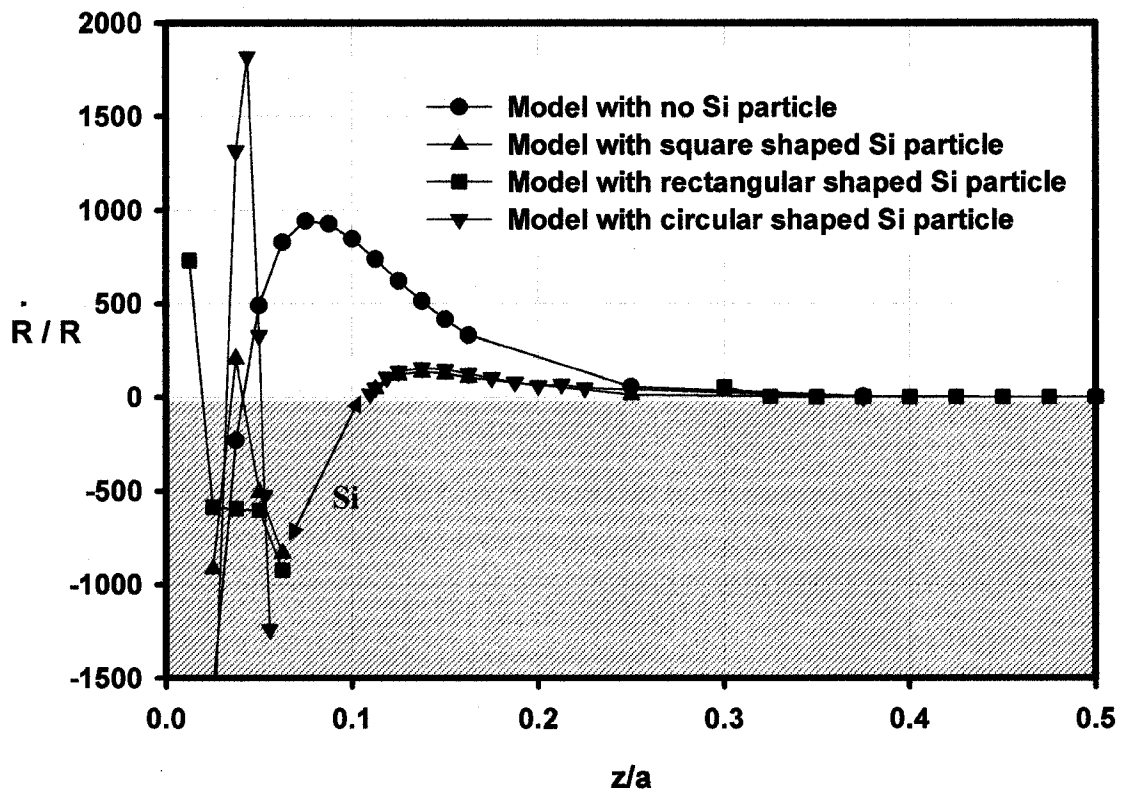


Figure 7.48: Change in the subsurface damage rate at the mid-point of the 356 Al half-space with the implementation of Si particles (Sliding velocity: 10 m/s, Normal load: 250 N/mm, Results after seventh sliding contact).

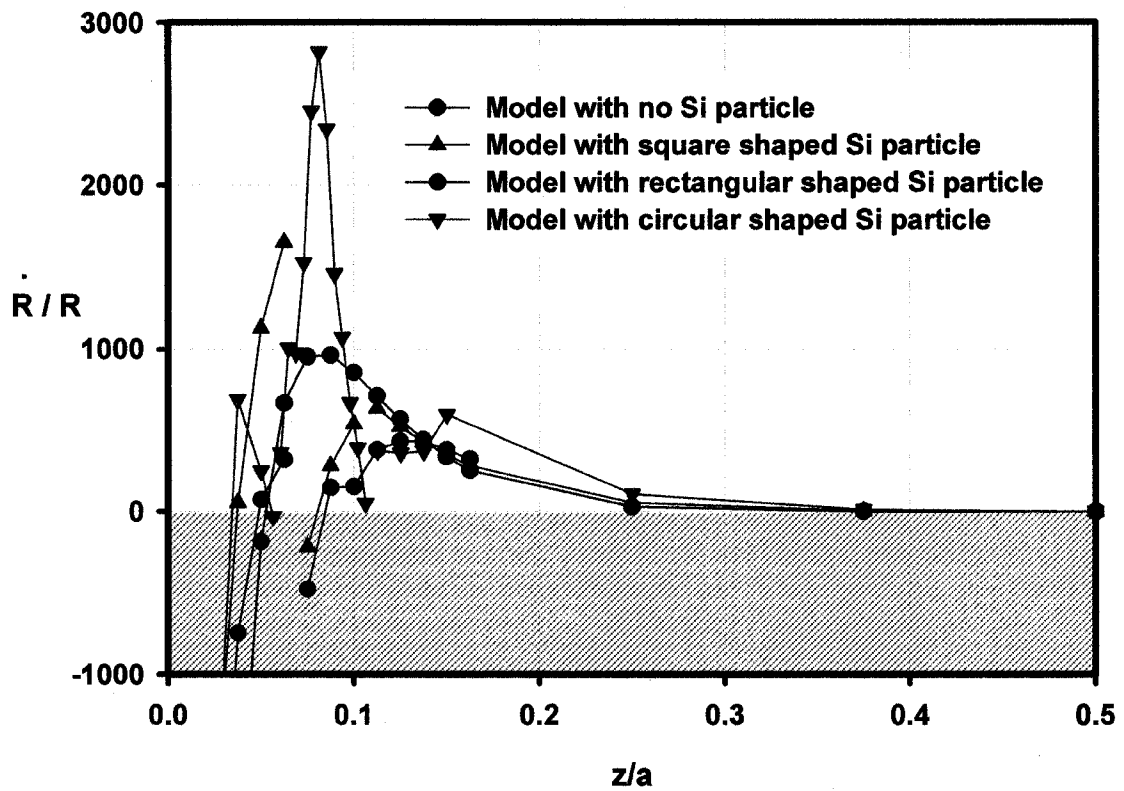


Figure 7.49: Change in the subsurface damage rate at the back edge of the Si particle (Sliding velocity: 10 m/s, Normal load: 250 N/mm, Results after seventh sliding contact).

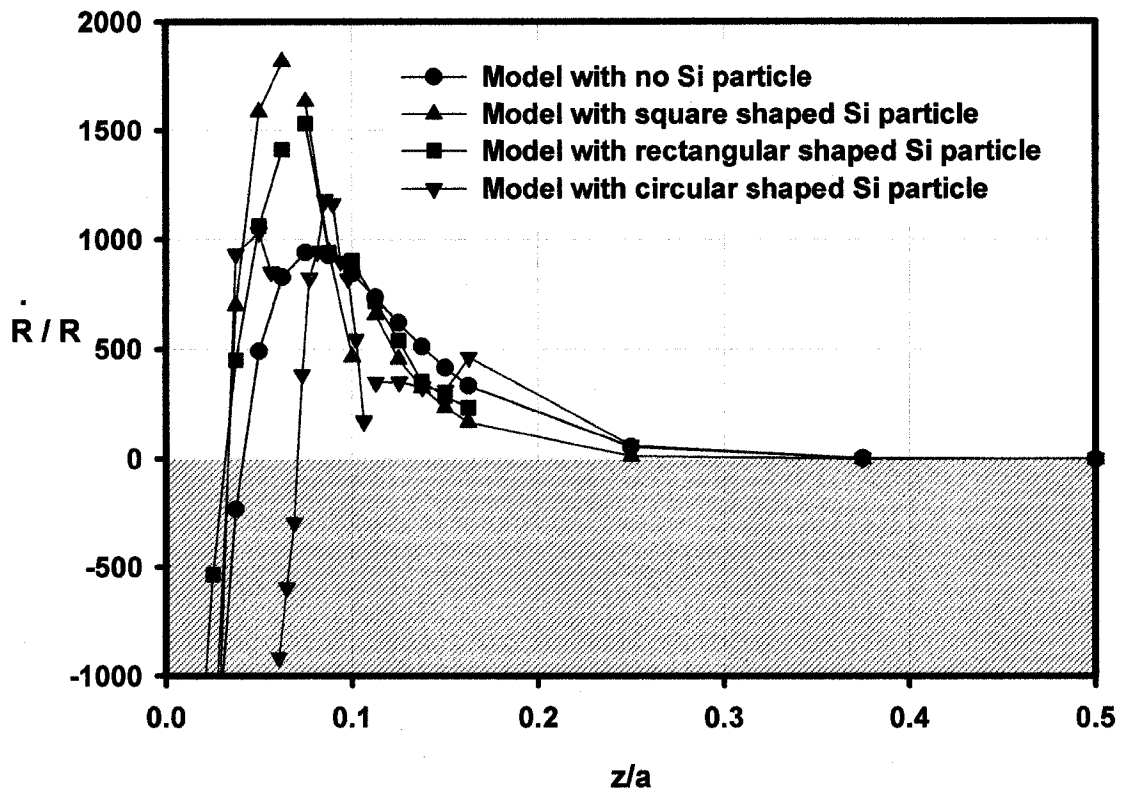


Figure 7.50: Change in the subsurface damage rate at the front edge of the Si particle (Sliding velocity: 10 m/s, Normal load: 250 N/mm, Results after seventh sliding contact).

surface and the Si particle, causing the damage rate to increase in those regions. This means that the layers above the Si particles will wear quickly, until the subsurface Si particles reach the surface and carry the loads.

7.5.3. EXPERIMENTAL SUBSURFACE CRACK GROWTH OBSERVATIONS AND COMPARISON WITH NUMERICAL DAMAGE GRADIENT

Sliding contact tests were performed with 356 Al alloy samples and M2 tool steels and details of the experimental sliding tests, utilizing a reciprocating sliding wear machine, are covered in Chapter 5. This section presents the results of the metallographic observations—used to gain experimental insight into the proposed subsurface damage model.

A metallographic investigation was performed on the longitudinal sections after the sliding contact tests (i.e. on a plane normal to the sliding wear surface and parallel to the sliding direction of the Al samples) using a scanning electron microscope (SEM). These SEM investigations revealed that the delamination of the subsurface layers contributes to the wear of the 356 Al alloy. Evidence of subsurface crack growth (i.e. cracks approximately 140 to 200 μm long) was found at subsurface depths of 5 to 20 μm . Figures 7.51 to 7.55 show subsurface crack propagation in the 356 Al alloy after seven sliding contact cycles with an M2 tool steel. In Figure 7.51, particle fracture and interface decohesion events, as well as subsurface crack propagation, are observed. Debris formation in the 356 Al alloy is illustrated in Figures 7.52 and 7.53, where 15-20 μm thick debris formation can be seen. Figure 7.55 displays the details of a damaged subsurface region—characterized by a series of cracks extending parallel to each other, although the main damage appears to occur at 20 μm below the surface.

The findings of the void growth model are consistent with the SEM observations of the cross-sections below the contact surface. Specifically, the propagation of subsurface cracks should occur at a critical depth (Figures 7.51 to 7.55). Moreover, according to Figure 7.43, there exists a damage gradient below the surface; hence there should be secondary cracks below and above the critical depth. Figures 7.52 to 7.55 confirm the presence of the secondary cracks above and below the main crack. The minor length of the secondary cracks correlates with a slower growth rate.

Figure 7.56 shows the experimental and numerical maximum damage depths (z_c) normalized by the counterface diameter for different sliding velocities and for a normal load of 250 N/mm. The experimental maximum damage depth observations (Figure 7.51 to 7.55) are given as a range. The numerical maximum damage depth given for a sliding velocity of 0.15 m/s was calculated after only two sliding cycles (due to long processing times). The results indicate that the relationship between the maximum damage depth and the sliding velocity is not linear. In summary, the damage rate calculations, according to the proposed model, provide a good estimation of the subsurface crack propagation depth.

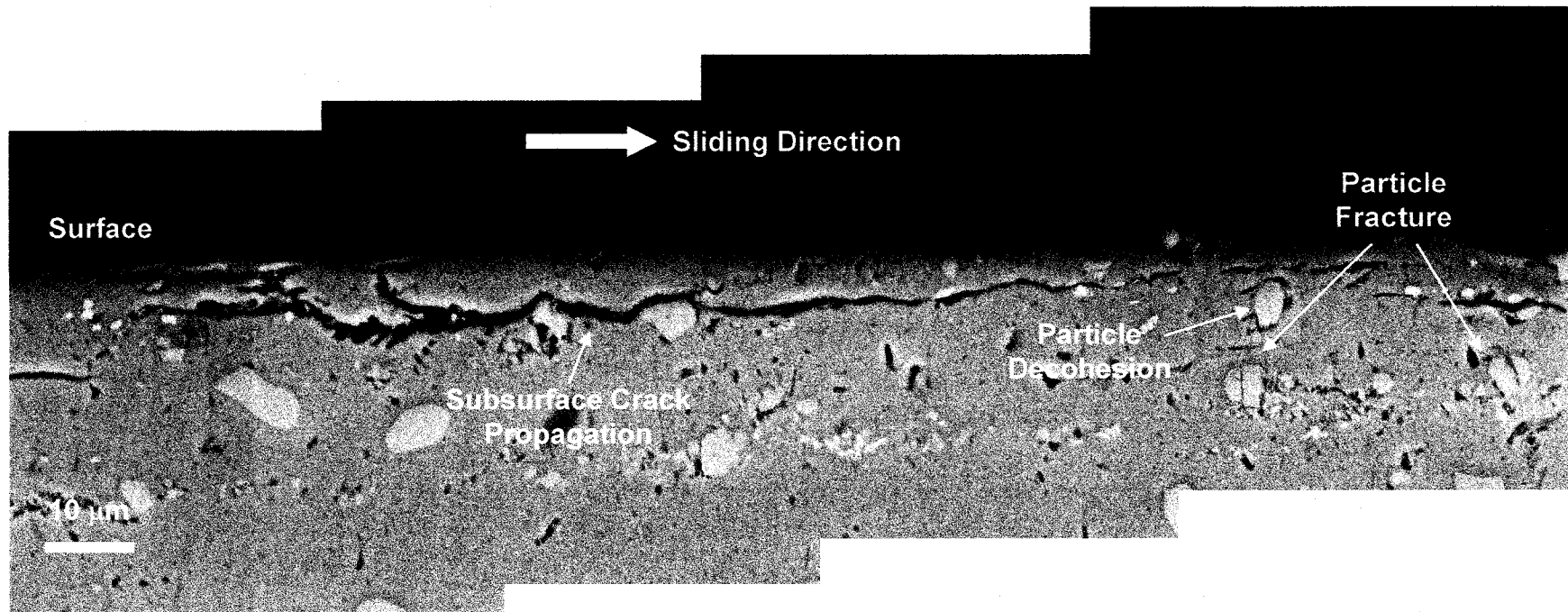


Figure 7.51: Subsurface crack propagation in the 356 Al alloy after seven sliding contacts with a M2 tool steel (Sliding velocity: 0.15 m/s and Normal load: 250 N/mm) (SEM Back-Scattered Electron Image (BEI)).

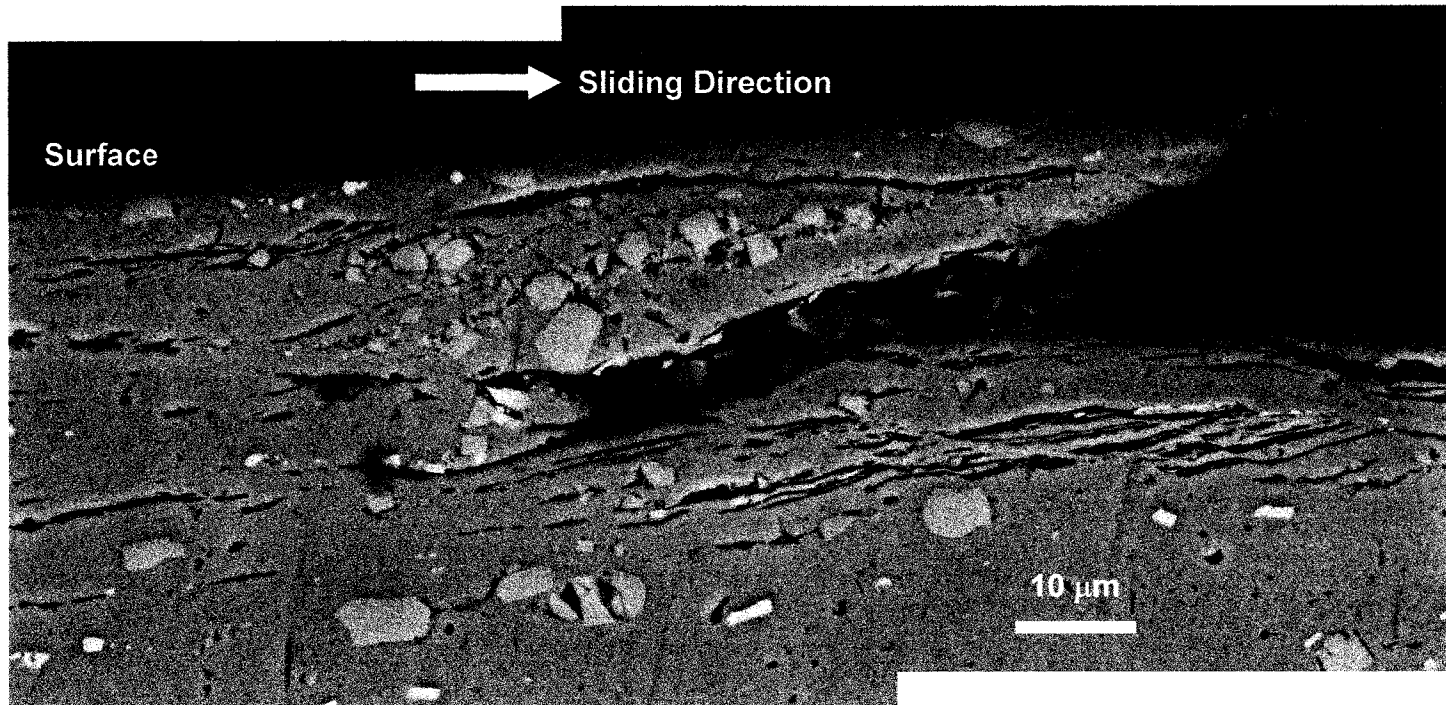


Figure 7.52: Plate-like wear debris formation in the 356 Al alloy after seven sliding contacts with a M2 tool steel (Sliding velocity: 0.15 m/s and Normal load: 250 N/mm) (SEM BEI).

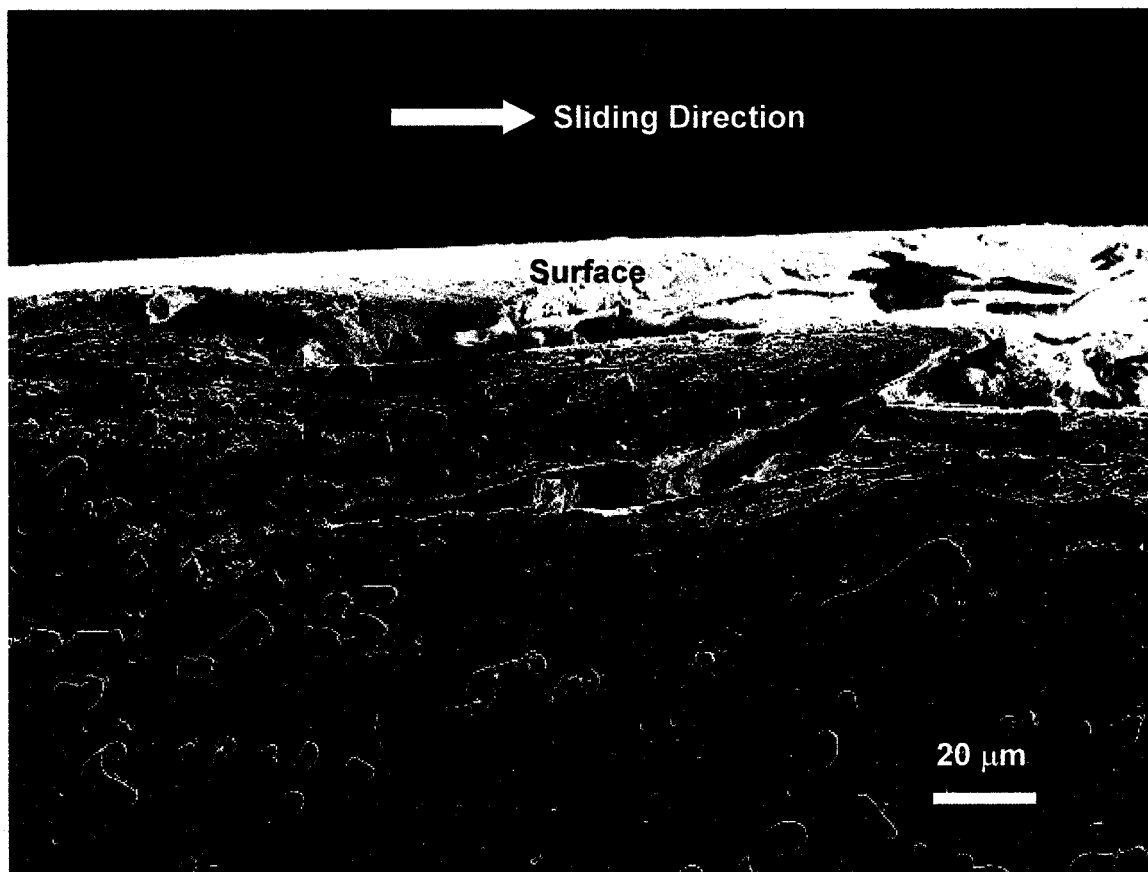


Figure 7.53: Debris formation in the 356 Al alloy after seven sliding contacts with a M2 tool steel (Sliding velocity: 0.15 m/s and Normal load: 250 N/mm) (SEM Secondary Electron Image (SEI)).

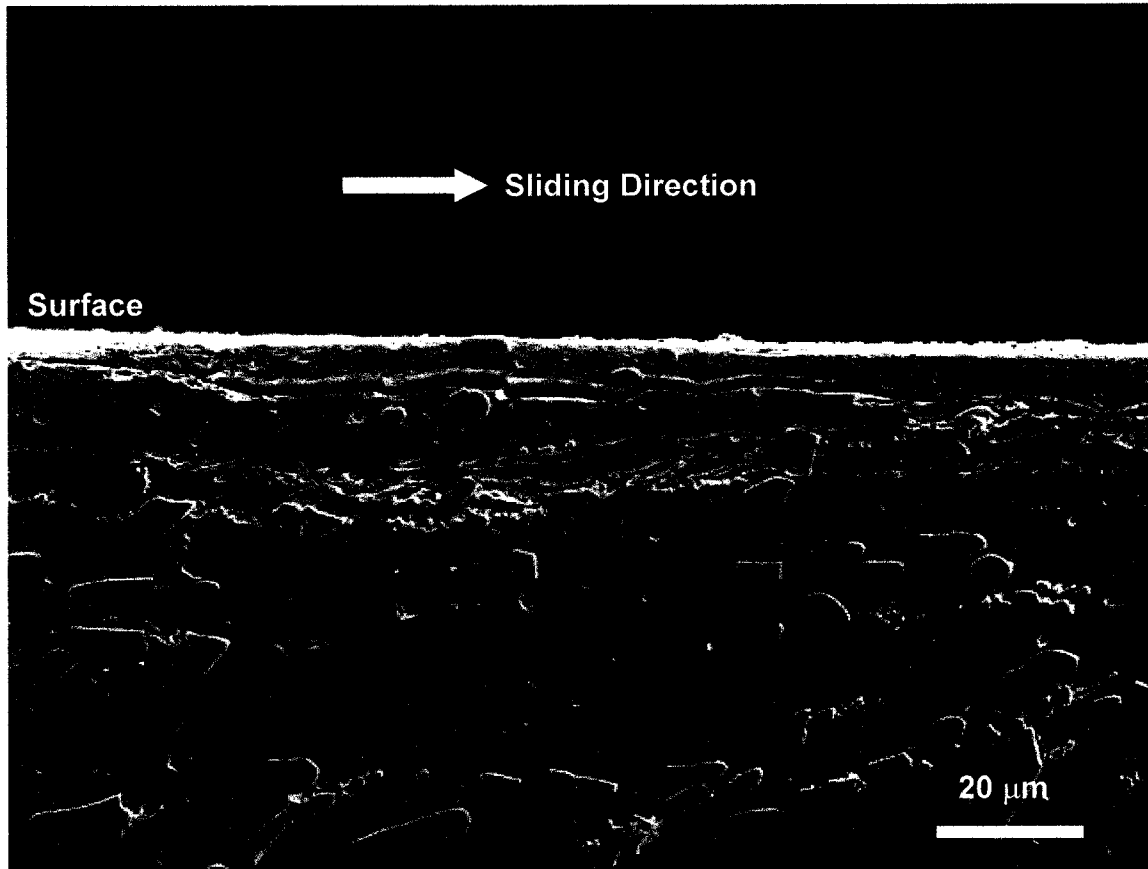


Figure 7.54: Propagation of a subsurface crack in the 356 Al alloy parallel to the surface (Sliding velocity: 0.15 m/s and Normal load: 250 N/mm) (SEM SEI).

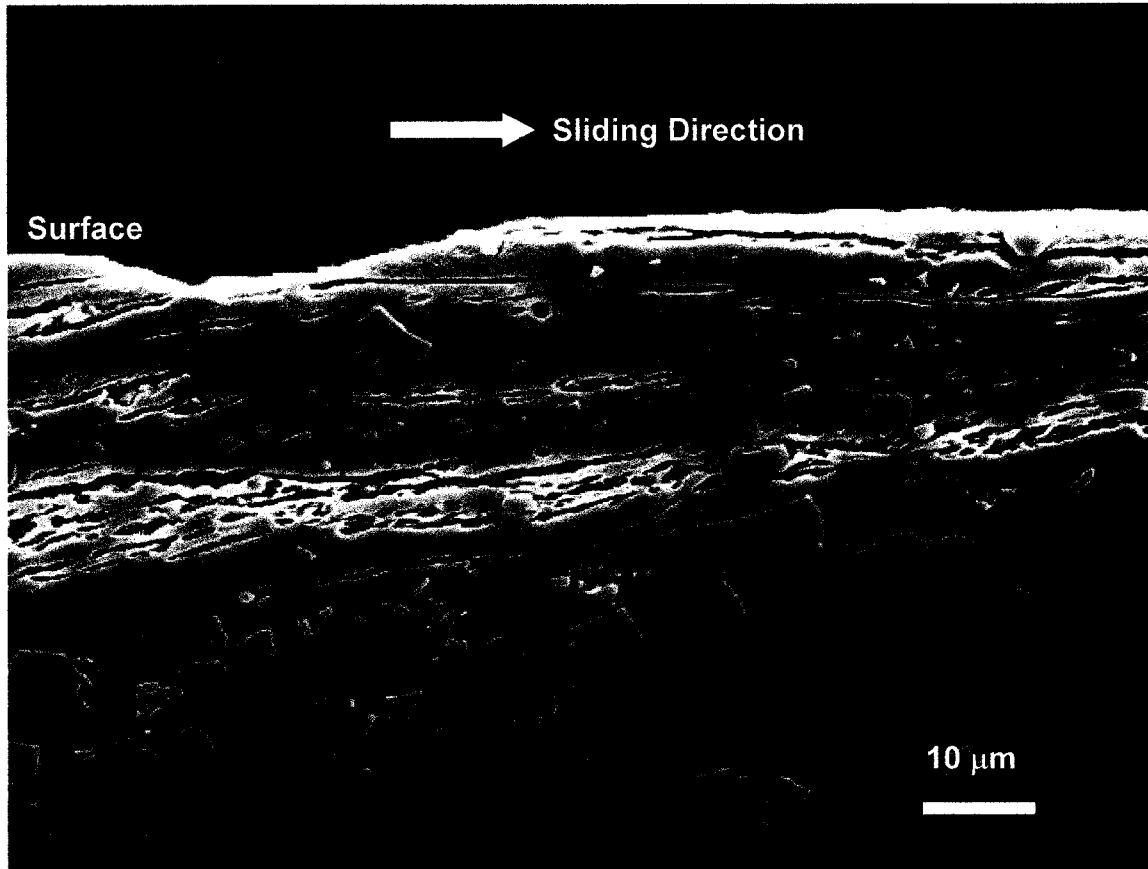


Figure 7.55: Propagation and joining of surface cracks in the 356 Al alloy (Sliding velocity: 0.15 m/s and Normal load: 250 N/mm) (SEM SEI).

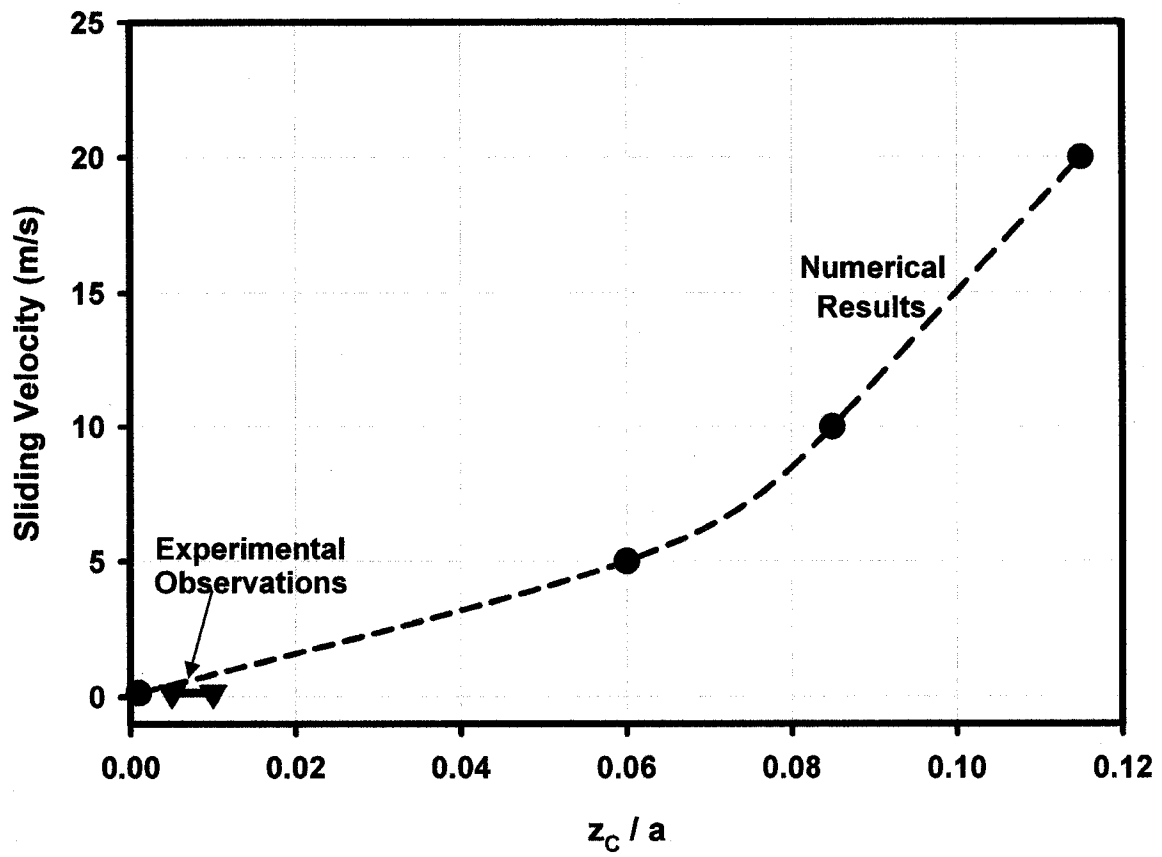


Figure 7.56: Comparison of the experimental and numerical maximum damage depths (z_c) in the 356 Al alloy for different sliding velocities (Normal load: 250 N/mm).

CHAPTER 8

SUMMARY AND CONCLUSIONS

The purpose of this study was to identify and interpret the subsurface deformation and damage accumulation events that are observed in aluminum alloys during sliding contact. The investigations were initiated by normal contact analysis, and directed to include more complex sliding contact conditions. Finite element analysis tools were used to model the deformation of an aluminum alloy during sliding contact, utilizing the stress-strain behavior of the 356 Al alloy—determined directly from analyzing the deformation state of subsurfaces generated during sliding wear tests. Strain rate and thermal softening effects were taken into account in a constitutive equation where the Voce-type exponential stress-strain equation was combined with a Cowper-Symonds-type strain rate, and Johnson-Cook-type temperature equations. The main results and conclusions of this study can be summarized as follows:

1. In order to simulate the large deformation behaviour of the 356 Al alloy in sliding wear conditions, an Eulerian model—capable of accounting for large strain accumulation during asperity contacts—was developed. The Eulerian element formulation successfully modeled the high deformation observed in the aluminum alloys under the application of high normal loads when a solution could not be obtained with a Lagrangian element formulation, due to excessive element distortion. The Eulerian element formulation identified large plastic strains ($\epsilon_p=20$) in the 356 Al structure, but the Eulerian model was not successful in an investigation that coupled thermal and mechanical analyses. The FE model utilizing Lagrangian elements was an acceptable alternative for the thermo-mechanical analysis.

2. The finite element model developed for this study was tested and validated by comparing the numerical results with normal contact and sliding contact experiments. The finite element model predicted the plastic zone depth and width with an accuracy of 20%, and the contact depth and length with an accuracy of 10% during normal contacts. A comparison of experimental and numerical results for sliding contacts showed that the finite element model successfully captured the distribution of subsurface plastic strains in

the 356 Al alloy. The difference between the experimental and numerical plastic strains for a specific depth was less than 20%.

3. Subsurface strains and stresses initially revealed rapid increases when the number of contact cycles was increased. At that point the stresses reached a constant value after a finite number of sliding contacts. The von Mises stress and the equivalent plastic strain at the contact surface were 514 MPa and 0.19, respectively after the first contact cycle for a sliding velocity of 10 m/s and a normal load of 150 N/mm. After the fourth cycle, the stress at the contact surface increased to 586 MPa and the strain to 0.78. Only a 2% increase occurred in the stress between the fourth and seventh (last) cycles, while the plastic strain continued to increase to 1.3.

4. The subsurface distribution of hydrostatic pressure, strain rate and temperature—all of which are difficult to characterize experimentally or theoretically for work hardening materials—was determined for different loading conditions during sliding contacts. The hydrostatic pressure at the contact surface was 1150 ± 100 MPa between the first and seventh contacts for a sliding velocity of 10 m/s and a normal load of 150 N/mm. A 45 K temperature increase was observed at the surface after seven sliding contacts.

5. Regression analyses showed that exponential curves of type $A = c_1 + [c_2 \exp(-c_3 z)]$ represent the distributions of hydrostatic pressure, strain rate and temperature as a function of depth z below the surface.

6. A model of the subsurface damage accumulation process was presented. The model revealed the presence of a damage gradient that reached a maximum value at a critical depth where the voids propagated at the highest rate. The predictions of the proposed damage model confirmed the presence of the critical crack growth depth, and were consistent with the metallographic observations.

7. The position of the highest damage was calculated to be at a normalized depth of 0.060 for a sliding velocity of 10 m/s and a normal load of 150 N/mm. The effects of the contact characteristics and loading conditions on the damage gradient were determined. An increase in the sliding velocity and normal load prompted an increase in the maximum damage rate, in turn causing the location of the maximum damage to sink deeper—further away from the contact surface. When the normal load was increased from 150 N/mm to 250 N/mm, the position of the maximum damage rate shifted from a

normalized depth of 0.060 to 0.085, leading to the formation of thicker debris. High friction (coefficient of friction ≥ 0.3) changed the subsurface damage gradient completely, moving the location of the maximum damage rate to the surface.

8. A stepwise comparison of the effects of the material properties on the subsurface damage accumulation revealed that significant differences in the prediction of the subsurface damage might be observed if strain rate and thermal softening effects are not considered in the material model. When thermal softening of the material was considered along with strain hardening, the void growth rate and the possibility of producing or propagating a crack decreased. While the strain rate effects were considered with the strain hardening, the maximum damage rate moved toward the surface, due to material hardening, and the void growth rate increased in a relatively more brittle matrix.

9. The effects of hard particles on the distribution of subsurface stresses, strains and the damage gradient were also investigated. Si particles embedded in the aluminum matrix helped to resist the penetration of deformation below the surface of the 356 Al alloy. However, an increase in the stresses and plastic strains were observed in some locations adjacent the Si particles. As a result, the presence of Si particles below the surface of the aluminum matrix moved the maximum damage rate to the layers positioned above the Si particles.

CHAPTER 9

SUGGESTIONS FOR FUTURE WORK

This investigation's shortcomings originate in two areas: numerical limitations, and experimental causes. The main numerical weakness is the lack of thermal-mechanical coupling for the Eulerian element formulation. The Eulerian element formulation has proven that it has great potential in the modeling of large deformation processes. However, experimental findings show that the temperature increase observed in contacting solids might be significant during high plastic deformation applications—possibly changing the deformation characteristics. The FE model utilizing Lagrangian elements was an acceptable alternative for the thermo-mechanical analysis, despite the excessive element distortion, which restricted the Lagrangian element formulation's ability to model the high deformation observed in aluminum alloys.

The material model used by the current sliding wear analysis is based on the experimentally determined stress-strain curve of a 356 Al alloy. The stress-strain behaviour was obtained directly from an analysis of the deformation state of the material layers below the contact surface that was subjected to sliding wear. Additionally, temperature and strain rate effects were taken into account, using a constitutive equation based on published literature. The experimental findings of this research indicated that the thermal softening equation based on the work of Johnson and Cook was acceptable for representing the influence of the thermal softening processes on the mechanical behaviour of the aluminum alloys, as observed during sliding wear. However, measuring the real strain rates during sliding wear conditions is a challenge that has yet to be addressed, and the issue of "how well the strain rate constitutive equations given in the literature reflect the deformation characteristics of the sliding wear conditions" is still open for investigation.

The influence of the hard particles on the distribution of subsurface stresses and strains in the aluminum matrix was also investigated in this study, by modeling different sized Si particles embedded below the 356 Al surface. Due to computational and time constraints, only a single Si particle below the surface was considered, although the interaction of many Si particles should also be studied. In addition, the interface between

the aluminum matrix and the Si particles was assumed to be infinitely strong, due to the limitations in the current engineering knowledge. Interface failure and particle fracture events should also be considered in future in order to model subsurface deformation completely.

REFERENCES

1. Hertz H., "Miscellaneous papers by Hertz", Eds. Jones and Schott, London, Macmillan, 1896.
2. Rigney D.A. and Hirth J.P., "Plastic deformation and sliding friction of metals", *Wear*, 1979, vol.53, pp.345-370.
3. Dautzenberg J.H. and Zaat H., "Quantitative determination of deformation by sliding wear", *Wear*, 1973, vol.23, pp.9-19.
4. Moore M.A. and Douthwaite R.M., "Plastic deformation below worn surfaces", *Metallurgical Transactions A*, 1976, vol. 7A, pp.1833-1839.
5. ZumGahr K.H., *Microstructure and wear of materials*, Elsevier, Amsterdam, 1987, pp.1-7, 48-53, 351-477.
6. Gurland J, and Plateau J., "The mechanism of ductile rupture of metals containing inclusions", *Transactions of the ASM*, 1963, vol.56, pp.442-454.
7. Voight R.C., and Bye D.R., "Microstructural aspects of fracture in A356", *AFS Transactions*, 1991, vol.99, pp.33-50.
8. Samuel A.M., and Samuel F.H., "Metallographic study of porosity and fracture behaviour in relation to the tensile properties in 319.2 end chill castings", *Metallurgical and Materials Trans. A*, 1995, vol.26A, pp.2359-2372.
9. Yeh J.W., and Liu W.P., "The cracking mechanism of silicon particles in an A357 aluminum alloy", *Metallurgical and Materials Trans. A*, 1996, vol.27A, pp.3558-3568.
10. Suh N.P., "The delamination theory of wear", *Wear*, vol.25, 1973, pp.111-124.
11. Suh N.P., "Overview of the delamination theory of wear", *Wear*, vol.44, 1977, pp.1-6.
12. Fleming J.R. and Suh N.P., "Mechanics of crack propagation in delamination wear", *Wear*, vol.44, 1977, pp.39-56.
13. Jahanmir S. and Suh N.P., "Mechanics of subsurface void nucleation in delamination wear", *Wear*, vol.44, 1977, pp.17-38.
14. Suh N.P., Saka N., and Jahanmir S., "Implications of the delamination theory on wear minimization", *Wear*, vol.44, 1977, pp.127-134.

15. Fleming J.R. and Suh N.P., "Relationship between crack propagation rates and wear rates", *Wear*, vol.44, 1977, pp.57-64.
16. Scott D., "Introduction to tribology", in *Fundamental of Tribology*, Suh N.P and Saka N. eds., The MIT Press, Cambridge, 1981, pp.1-13.
17. Zhang, J., and Alpas A.T., "Delamination wear in ductile materials containing second phase particles", *Materials Science and Eng. A*, 1993, vol.A160, pp.25-35.
18. Rosenfield A.R., "A Fracture Mechanics Approach to Wear", *Wear*, 1980, vol.61, pp.125-132.
19. Ritchie R.O, *Fundamentals of tribology*, eds. Suh N.P. and Saka N, MIT, Cambridge, MA, 1978, pp.127-134.
20. Hills D.A., and Ashelby D.W., "Combined mode fatigue crack propagation predictions using mode one data", *Eng. Fract. Mech.*, 1980, vol.13, pp.589-597.
21. Hearle A.D., and Johnson K.L., "Mode II stress intensity factors for a crack parallel to the surface of an elastic half-space subjected to a moving point load", *J. Mech. Phys. Solids*, 1985, vol.33, pp.61-81.
22. Kimura Y., *Fundamentals of friction and wear of materials*, ed. Rigney D.A., ASM, 1981, pp.187-221.
23. Tierlinck D, Zok F., Embury J.D., and Ashby M.F., "Fracture mechanism maps in stress space", *Acta Met.*, 1988, vol.36, pp.1213-1228.
24. Johnson K.L., "The mechanics of plastic deformation of surface and subsurface layers in rolling and sliding contact", in *The Role of Subsurface Zones in the Wear of Materials*, Solecki R. ed., Trans Tech Publications, Switzerland, 1988, pp.17-33.
25. Rice J.R., and Tracey D.M., "On the ductile enlargement of voids in triaxial stress fields", *J. Mech. Phys. Solids*, 1969, vol.17, pp.201-217.
26. "Standard terminology relating to erosion and wear", G 40, *Annual Book of ASTM Standards*, ASTM.
27. *ASM Handbook, Friction, lubrication and wear technology*, ASM International, vol.18, pp.175-183, 741-778.
28. Rigney D.A., "Viewpoint set on materials aspects of wear-Introduction plastic deformation and sliding friction of metals", *Scripta Metall.*, 1990, vol.24, pp.799-803.

29. Hutchings I.M., Tribology friction and wear of engineering materials, CRC Press, London, 1992, pp.4-21, 77-132.
30. Archard J.F., "Contact and rubbing of flat surfaces", Journal of Applied Physics, vol.24, 1953, pp.981-988.
31. Archard J.F., "Wear theory and mechanisms", in Wear Control Handbook, Peterson M.B. and Winer W.O. eds., ASME, New York, 1980, pp.35-80.
32. Suh N. P., Tribophysics, Prentice-Hall Inc., New Jersey, 1986, pp.11-18, 130-136, 195-221.
33. Quinn T.J.F., "Review of oxidatinal wear", Tribology International, vol.16, 1983, pp.257-271, 305-315.
34. Ohmae N., Tsukizoe T., and Akiyama F., "On the microscopic processes involved in metallic friction", Philosophical Magazine A, vol.40, 1979, pp.803-810.
35. Rigney D.A, Naylor M.G.S., Divakar R., and Ives L.K., "Low energy dislocation structures caused by sliding and by particle impact", Material Science and Engineering, vol.81, 1986, pp.409-425
36. Heilmann P., Clark W.A.T., and Rigney D.A., "Orientation determination of subsurface cells generated by sliding", Acta Metall., vol.31, 1983, pp.1293-1305.
37. Callister W.D., Materials science and Engineering, John Wiley and Sons Inc., New York, 1994, pp.183-184.
38. Tanaka K., Mori T., and Nakamura T., "Cavity formation at the interface of a spherical inclusion in a plastically deformed matrix", Philos. Magazine, 1970, vol.21, pp.267-279.
39. Argon A.S., Im J., and Safoglu R., "Cavity formation from inclusion in ductile fracture", Metallurgical and Materials Trans. A, 1975, vol.6A, pp.825-837.
40. Argon A.S. and Im J., "Seperation of second phase particles in spherodized 1045 steel, Cu-0.6 % Cr alloy, and maraging steel in plastic straning", Metallurgical and Materials Trans. A, 1975, vol.6A, pp.839-851.
41. Argon A.S., "Formation of cavities from non-deformable second phase particles in low temperature ductile fracture", Journal of Eng. Mater. Tech., 1976, vol. 98, pp. 60-68.

42. Le Roy G., Embury J. D., Edward G., and Ashby M.F., "A model of ductile fracture based on the nucleation and growth of voids", *Acta Metallurgica*, 1981, vol.29, pp.1509-1522.
43. French J. A. and Weinrich P. F., "Influence of hydrostatic pressure on the tensile deformation of a spheroidised 0.5 % C steel, *Scr. Metall.*, 1974, vol.8, pp.87-90.
44. Rogers H.C., *Trans. Metall. Soc., AIME*, vol.218, 1960, p.498.
45. Gurland J, and Plateau J., "The mechanism of ductile rupture of metals containing inclusions", *Transactions of the ASM*, 1963, vol.56, pp.442-454.
46. Beachem C.D., *Trans. Am. Soc. Metals*, vol.56, 1963, p.318.
47. Thomason P.F., *Ductile fracture of metals*, Pergamon Press, Exeter, 1990, pp.30-55.
48. McClintock F.A., "A criterion for ductile fracture by the growth of holes", *Journal of Applied Mechanics*, vol.35, 1968, pp.363-371.
49. Johnson K.L., "*Contact Mechanics*", Cambridge University Press, New York, 1985, pp.45-104.
50. Hamilton G.M., Goodman L.E, The stress field created by a circular sliding contact, *ASME Journal of Applied Mechanics*, 1966, June, pp.371-376.
51. Merwin J. E. and Johnson K.L., "An analysis of plastic deformation in rolling contact", *Proc. of the Institution of Mechanical Engineers*, 1963, vol.177, pp.676-690.
52. Ohmae N. and Tsukizoe T., "Analysis of a wear process using the finite element method", *Wear*, 1980, Vol.61, pp.333-339.
53. Sin H.C., Suh N.P., "Subsurface crack propagation due to surface traction in sliding wear", *Journal of Applied Mechanics*, 1984, Vol.51, pp.317-323.
54. Bhargava V., Hahn G.T., and Rubin C.A., "An elastic-plastic finite element model of rolling contact part 1: Analysis of single contacts", *ASME Journal of Applied Mechanics*, 1985, Vol.52, pp.67-74.
55. Komvopoulos K., "Elastic-plastic finite element analysis of indented layered media", *Journal of Tribology*, 1989, Vol.111, pp.430-439.
56. Tang K.C., Faulkner A., Schwarzer N., Arnell R.D., and Richter F., "Comparison between an elastic-perfectly plastic finite element model and a purely elastic analytical

model for a spherical indenter on a layered substrate", *Thin Solid Films*, 1997, Vol.300, pp.177-188.

57. Kral E.R., Komvopoulos K., and Bogy D.B., "Finite element analysis of repeated indentation of an elastic-plastic layered medium by a rigid sphere, part I: Surface results", *Journal of Applied Mechanics*, 1995, Vol.62, pp.20-28.

58. Bhargava V., Hahn G.T., and Rubin C.A., "An elastic-plastic finite element model of rolling contact part 2: Analysis of repeated contacts", *ASME Journal of Applied Mechanics*, 1985, Vol.52, pp.75-82.

59. Ohmae N., "Analysis of the large plastic deformation involved in wear processes using the finite element method with an updated Lagrangian formulation," *Journal of Tribology*, 1987, Vol.109, pp.330-337.

60. Komvopoulos K. , Saka N., and Suh N.P., "The role of hard layers in lubricated and dry sliding", *Journal of Tribology*, 1987, Vol.109, pp.223-231.

61. King R.B., O'Sullivan T.C., "Sliding contact stresses in a two-dimensional layered elastic half-space", *International Journal of Solids and Structures*, 1987, Vol.23, pp.581-597.

62. Tian H., Saka J., "Finite element analysis of an elastic-plastic two-layer half-space: Sliding contact", *Wear*, 1991, Vol.148, pp.261-285.

63. Bailey D.M., Sayles R.S., "Effect of roughness and sliding friction on contact stresses", *Journal of Tribology*, 1991, Vol.113, pp.729-738.

64. Tian H., Saka J., "Finite element analysis of interface cracking in sliding contacts", *Wear*, 1992, Vol.155, pp.163-182.

65. Djabella H., Arnell R.D., "Finite element analysis of the contact stresses in elastic coating/substrate under normal and tangential load", *Thin Solid Films*, 1993, Vol.223, pp.87-97.

66. Djabella H., Arnell R.D., "Two-dimensional finite-element analysis of elastic stresses in double-layer systems under combined surface normal and tangential loads", *Thin Solid Films*, 1993, Vol.226, pp.65-73.

67. Komvopoulos K., Cho S.S., "Finite element analysis of subsurface crack propagation in a half-space due to a moving asperity contact", *Wear*, 1997, Vol.209, pp.57-68.

68. Põdra P., Andersson S., "Simulating sliding wear with finite element method", *Tribology International*, 1999, Vol.32, pp.71-81.
69. Hamblí R., "Blanking tool wear modeling using the finite element method", *International Journal of Machine Tools & Manufacture*, 2001, Vol.41, pp.1815-1829.
70. Molinari J.F., Ortiz M., Radovitsky R., and Repetto E.A., "Finite element modeling of dry sliding wear in metals", *Engineering Computations*, 2001, Vol.18, No:3/4, pp.592-609.
71. Lancaster J., "The formation of surface films at the transition between mild and severe metallic wear", *Proceedings of Royal Society A*, 1963, Vol.273, pp.466-483.
72. Sevillano J. G., van Houtte P., and Aernoudt E., "Large strain work hardening and textures", *Progress in Materials Science*, 1981, vol.25, pp.69-412.
73. Hollomon J. H., *Trans AIME*, 1945, vol.162, p.268.
74. Ludwik P., *Elemente der Technologische Mechanik*, Springer Verlag, Berlin, 1909, p.32.
75. Voce E., "The relationship between stress and strain for homogeneous deformation", *J. Inst. Met.*, vol.74, pp.537-562.
76. Bridgman P.W., *Studies in large plastic flow and fracture*, Harvard University Press, Cambridge, Massachusetts, 1953 (1964).
77. Bridgman P.W., "The effect of pressure on the tensile properties of several metals and other materials", *Journal of Applied Physics*, 1953, Vol.24, p 560.
78. Pugh H.L.D. and Green D., "The effect of hydrostatic pressure on the plastic flow and fracture of metals", *Proc. Instn. Mech. Engrs.*, 1964-1965, Vol.179, pp. 415-437.
79. Hauser F.E., "Techniques for measuring stress-strain relations at high strain rates", *Experimental Mechanics*, 1966, Vol.6, pp.395-402.
80. Tsao M.C.C. and Campbell J.D., *Plastic shear properties of metals and alloys at high strain rates*, Oxford University, Department of Engineering Science Report No. 1055/73, 1973.
81. Ng D.H.Y., Delich M., and Lee L.H.N., "Yielding of 6061-T6 aluminum tubings under dynamic biaxial loadings", *Experimental Mechanics*, 1979, Vol.19, pp.200-206.

82. Cowper G.R. and Symonds P.S., Strain hardening and strain rate effects in the impact loading of cantilever beams, Brown University Division of Applied Mathematics Report No. 28, 1957.
83. Symonds P.S and Jones N., "Impulsive loading of fully clamped beams with finite plastic deflections and strain rate sensitivity", International Journal of Mechanical Sciences, 1972, Vol.14, pp.49-69.
84. Jones N., Structural Impact, Cambridge University Press, 1989, pp. 333-352.
85. Johnson G.R., and Cook W.H., "A Constitutive Model and Data for Metals Subjected to Large Strains, High Strain Rates and High Temperatures", presented at the Seventh International Symposium on Ballistics, The Hague, The Netherlands, April 1983, pp.541-547.
86. Johnson G.R., Hoegfeldt J.M., Lindholm U.S., and Nagy A., "Response of various metals to large torsional strains over a large range of strain rates- Part 2: less ductile metals", Journal of Engineering Materials and Technology, 1983, Vol.105, pp.48-53.
87. Follansbee P.S. and Kocks U. F., "A constitutive description of the deformation of copper based on the use of mechanical threshold stress as an internal state variable", Acta Metall., 1988, vol.36, pp.81-93.
88. Rule W. K. and Jones S. E., "A revised form for the Johnson-Cook strength model", Int. J. Impact Eng., 1998, vol.21, pp.609-624.
89. Ek D. R. and Asay J. R., Sandia National Laboratory Report, SAND 85-0156C, 1985.
90. Salzmann D., Gilath I., Givon M., and Noy T.B., "Measurement of the tensile strength of aluminum at a strain rate of $2 \times 10^7 \text{ s}^{-1}$ ", J. Phys. D: Appl. Phys., 1989, vol.22, pp.1271-1274.
91. Metals Handbook, Ninth Edition, vol. 2, Properties and Selection: Nonferrous alloys and pure metals, ASTM, pp.164-167.
92. Singh J., Elevated temperature wear of an aluminum matrix composite Al6061-20 % Al₂O₃ and an intermetallic alloy Ti₅₀Ni₄₇Fe₃, Master of Applied Science Thesis, University of Windsor, 1995.
93. Blaz L. and Evangelista E., "Strain rate sensitivity of hot deformed Al and AlMgSi alloy", Materials Science and Engineering A, 1996, Vol. A207, pp.195-201.

94. Stuwe H.P. and Les P., "Strain rate sensitivity of flow stress at large strains", *Acta Mater.*, 1998, Vol.46, pp.6375-6380.
95. Zerilli F.J. and Armstrong R.W., "Dislocation-mechanics-based constitutive relations for material dynamics calculations", *Journal of Applied Physics*, 1987, Vol. 61, pp.1816-1825.
96. LS-DYNA, *Keyword Users Manual*, March 2001, Version 970, Livermore Software Technology Corporation.
97. Altan T., *Tube hydroforming, Determination of formability of tubular materials using bulge test*, The Engineering Research Center for Net Shape Manufacturing, Internal Report, Columbus, Ohio, 2002.
98. Hill R., "A theory of plastic bulging of a metal diaphragm by lateral pressure", *Phil. Mag.*, 1950, Vol.41, pp.1133-1142.
99. Mellor P.B., "Stretch forming under fluid pressure", *J. Mech. Phys. Solids*, 1956, Vol.5, pp.41-56.
100. Ahmed M. and Hashmi M.S.J., "Finite element analysis of bulge forming applying pressure and in-plane compressive load", *Journal of Materials Processing Tech.*, 1998, Vol. 77, pp. 95-102.
101. Raczky A., Elmadagli M., Altenhof W.J., and Alpas A.T., "An Eulerian finite element model for determination of deformation state of a copper subjected to orthogonal cutting", *Metallurgical and Materials Trans. A*, 2004, Vol.35A, pp.2393-2400.
102. LS-DYNA, *Keyword Users Manual*, April 2003, Version 970, Livermore Software Technology Corporation.
103. D. J. Steinberg, "Equation of state and strength properties of selected materials", Lawrence Livermore National Laboratory, Livermore, CA, 1996.
104. Meyers M.A., *Dynamic Behaviour of Materials*, John Wiley and Sons, Inc., New York, 1994, pp.323-381.
105. Komanduri R. and Hou Z.B., "A review of the experimental techniques for the measurement of heat and temperatures generated in some manufacturing processes and tribology", *Tribology International*, 2001, vol.34, pp.653-682.

106. Mason J.J., Rosakis A.J., and Ravichandran G., "On the Strain and Strain Rate Dependence of the Fraction of Plastic Work Converted to Heat: an Experimental Study Using High Speed Infrared Detectors and the Kolsky Bar," *Mechanics of Materials*, 1994, vol.17, pp.135-145.
107. CRC handbook of chemistry and physics, Ed. Lide D.R., 79th Edition, CRC Press, Boca Raton, FL, 1998.
108. CRC handbook of chemistry and physics, Ed. Weast R.C., 62nd Edition, CRC Press, Boca Raton, FL, 1981.
109. Ross R.B., *Metallic materials specification handbook*, Fourth Edition, Chapman & Hall, London, 1992.
110. Gall K., Horstemeyer M.F., Schilfgaarde M.V., and Baskes M.I., "Atomistic simulations on the tensile debonding of an aluminum-silicon interface", *Journal of the Mechanics and Physics of Solids*, 2000, vol.48, pp.2138-2212.
111. Bowden F.P, and Tabor D., *The friction and lubrication of solids*, Part II, Oxford University Press, London, 1986, pp.10-14.
112. Zienkiewics O.C. and Taylor R.L., *The finite element method in structural and continuum mechanics*, Butterworth-Heinemann, Oxford, Fifth edition, 2000.
113. Flaherty J.E., *Finite element analysis*, Lecture notes, Departments of Computer Science and Mathematical Sciences, Rensselaer Polytechnic Institute, Troy, New York, 2000.
114. Moaveni S., *Finite element analysis*, Prentice Hall, New Jersey, 1999.
115. Wriggers P., *Computational Contact Mechanics*, John Wiley & Sons Ltd, 2002.
116. Altenhof W. and Zamani N, "An investigation into the axial buckling behavior of food cans using explicit and implicit finite element methods", *Proceedings of NAFEMS World Congress 2001*, Vol. 1, Lake Como, Italy, 2001, pp.11-22.
117. Maker B., *Implicit finite element method*, FEA Information, Livermore Software Technology Corporation, November 2001.
118. Benson D.J., *A brief introduction to explicit finite element methods*, FEA Information, Livermore Software Technology Corporation, June 2001.

119. Benson D.J., *Multimaterial Eulerian hydrodynamics*, FEA Information, Livermore Software Technology Corporation, September 2001.
120. Bala S., *Contact modeling in LS-DYNA*, FEA Information, Livermore Software Technology Corporation, December 2001.
121. Belytschko T., Liu W. K. and Moran B., *Nonlinear finite elements for continua and structures*, John Wiley and Sons Ltd., West Sussex, England, 1994.
122. Du Bois P. A., *Crashworthiness Engineering Course Notes*, Livermore Software Technology Corporation, Livermore, California, 2004, pp.3.1-3.48.
123. Cheng Y.T. and Cheng C.M., "Scaling, dimensional analysis, and indentation measurements", *Materials Science and Engineering Reports*, 2004, vol.44, pp.91-149.
124. Barenblatt G. I., "Scaling, self-similarity, and intermediate asymptotics", Cambridge University Press, 1996.
125. Bridgman P. W., "Dimensional analysis", Yale University Press, 1937.
126. Langhaar H. L., "Dimensional analysis and theory of models", Wiley, 1951.
127. Boucher and Alves, "Dimensionless numbers", *Chem. Eng. Progress*, 1960, vol.55, pp.55-64.
128. Buckingham E., "On physically similar systems: Illustrations of the use of dimensional analysis", *Phys. Rev*, 1914, vol.4, p.345.
129. Klinkenberg A., *Chem. Eng. Science*, 1955, vol.4, pp.130-140, 167-177.
130. Rayleigh L., "The principle of similitude", *Nature*, 1915, vol.95, pp.66-68.
131. Silberberg I. H. and McKetta J. J., "Learning how to use dimensional analysis", *Petrol. Refiner*, 1953, vol.32, pp.101, 129, 147, 179.
132. Van Driest, E. R., "On dimensional analysis and the presentation of data in fluid flow problems", *J. App. Mech*, March 1946, vol.68, A-34.
133. Perry J. H. et al., "Standard system of nomenclature for chemical engineering unit operations", *Trans. Am. Inst. Chem. Engrs.*, 1944, vol.40, p.251.
134. Moody L. F., "Friction factors for pipe flow", *Trans. Am. Soc. Mech. Engrs.*, 1944, vol.66, p.671.

APPENDIX A

FINITE ELEMENT ANALYSIS BASICS

In this appendix section fundamentals of finite element analysis (FEA) method will be presented. The aim of this section is not to explain or discuss the FEA method completely, but give a very short summary from a point of view that it covers the numerical approaches used in this study. A detailed information and discussion about the FEA method can be found in the following references: [96, 102, 112-121].

Finite element method (FEM) can be described as a general discretization procedure of continuum problems posed by mathematically defined statements [112]. The FEM is a computational technique for obtaining solutions to the partial differential equations that arise in scientific and engineering applications [113]. This method can be used to obtain solutions to a large class of steady, transient, linear or nonlinear problems involving stress analysis, heat transfer, fluid flow and electromagnetism [114]. The FEM utilizes a variational problem that involves an integral of the differential equation over the problem domain. This domain is divided into a finite number of subdomains called finite elements which are connected to each other at junction points called nodes. The solution of the partial differential equation is approximated by a simpler polynomial function (shape function) on each element. Then, these polynomials are collected together and the variational integral is evaluated as a sum of contributions from each finite element [113].

There are three basic steps involved in every finite element analysis [113, 114]:

1- Preprocessing

- A. Create and discretize the problem domain into finite number of elements or subdivide the problem domain into nodes and elements.**
- B. Assume a shape function to represent the physical behaviour of an element.**
- C. Develop differential equations for an element.**
- D. Assemble the elements to construct the global matrices.**
- E. Apply loading, boundary and initial conditions.**

2- Processing

F. Solve the equations to obtain nodal results, such as displacements or temperatures.

3- Postprocessing

G. Obtain needed information; principal stresses, strains, heat flux, etc.

Steps C, D and F are generally covered by commercially available finite element codes and the users only follow the steps A, B, E and G.

A.1. TIME INTEGRATION METHODS

After the spatial discretization has been performed in a FEA, the general form of the discrete equations of motion or the governing equation of motion is given by:

$$[M]\{\ddot{u}\} + [C]\{\dot{u}\} + [K]\{u\} = \{F_{external}\} \quad (A.1)$$

where $[M]$ is the mass matrix, $\{\ddot{u}\}$ is the nodal accelerations vector, $[C]$ is the damping matrix, $\{\dot{u}\}$ is the nodal velocities vector, $[K]$ is the stiffness matrix, $\{u\}$ is the nodal displacements vector and $\{F_{external}\}$ is the force vector including all forces, pressures, and body loads acting upon the finite element mesh.

There are two distinct methods for the solution of the Equation A.1 in a FEA; explicit and implicit time integration methods (schemes). In the FEA of time dependent problems, the central difference scheme is mostly applied in the explicit method, while the Newmark's method is used in the implicit scheme.

In the central difference algorithm [115, 116], the nodal velocities (\dot{u}) and accelerations (\ddot{u}) are approximated by

$$\dot{u}_n = \frac{u_{n+1} - u_{n-1}}{2\Delta t} \quad (\text{A.2})$$

$$\ddot{u}_n = \frac{u_{n+1} - 2u_n + u_{n-1}}{\Delta t^2} \quad (\text{A.3})$$

where the subscript notation n represents the present time step, $n-1$ and $n+1$ represent the previous and next time steps respectively. Δt is the duration of the time step interval. When Equations A.2 and A.3 are substituted into the governing equation of motion (Equation A.1), the following expression is obtained:

$$\left[\frac{[M]}{\Delta t^2} + \frac{[C]}{2\Delta t} \right] u_{n+1} = f([M], [C], [K], \{u_n\}, \{u_{n-1}\}, \{F_n\}, \Delta t) \quad (\text{A.4})$$

Equation A.4 indicates that in order to solve for u_{n+1} , the mass matrix and damping matrix must be inverted, or their transpose must be calculated. By lumping the mass and damping matrices, and assuming the rigid body accelerations and velocities, the matrices become diagonal and simple to invert. In the explicit time integration method, there is a condition of stability that the time step should not be larger than the time it takes an elastic wave to travel through the smallest element, or:

$$\Delta t_c = S \frac{l_c}{c} \quad (\text{A.5})$$

where Δt_c is the critical time step, S is the safety factor (0.9 by default in LS-DYNA), l_c is the smallest finite element length and c is the wave propagation velocity defined as a function of material density (ρ), Young's Modulus (E) and Poisson's ratio (ν) by the following equations:

$$c = \sqrt{\frac{E}{\rho}} \quad \text{for 1-D truss elements} \quad (\text{A.6})$$

$$c = \sqrt{\frac{E}{\rho(1-\nu)^2}} \quad \text{for 2-D shell elements} \quad (\text{A.7})$$

$$c = \sqrt{\frac{E(1-\nu)}{\rho(1+\nu)(1-2\nu)}} \quad \text{for 3-D solid elements} \quad (\text{A.8})$$

In the Newmark's method, the nodal displacements (u) and velocities (\dot{u}) are approximated by the following equations:

$$u_{n+1} = u_n + \Delta t \dot{u}_n + \Delta t^2 \left[\left(\frac{1}{2} - \beta \right) \ddot{u}_n + \beta \ddot{u}_{n+1} \right] \quad (\text{A.9})$$

$$\dot{u}_{n+1} = \dot{u}_n + \Delta t \left[(1-\gamma) \ddot{u}_n + \gamma \ddot{u}_{n+1} \right] \quad (\text{A.10})$$

where β and γ are the empirical coefficients with $0 \leq \beta \leq 0.5$ and $0 \leq \gamma \leq 1.0$. The governing equation of the implicit scheme (Equation A.11) is obtained once the equations A.9 and A.10 are substituted into the equation of motion (Equation A.1):

$$\left[\frac{4[M]}{\Delta t^2} + \frac{2[C]}{\Delta t} + [K] \right] u_{n+1} = f \left([M], [C], [K], \{u_n\}, \{\dot{u}_n\}, \{\ddot{u}_n\}, \{F_{n+1}\}, \Delta t \right) \quad (\text{A.11})$$

The explicit time integration method is easy to implement, since the solution at time t_{n+1} depends only upon known variables at time t_n (Equation A.4). This method is extremely efficient when the mass and the damping matrices are approximated by lumped diagonal matrices. The explicit time integration technique has the benefit over

the implicit method that a solution is guaranteed if a critical time step is selected. The main disadvantage behind the use of the explicit scheme is the size of the critical time step, which is generally very small, compared to the time step used in the implicit approach. This generally results in long processing times. The implicit time integration scheme approximates time derivatives by quantities which also depend upon the last time step t_n and upon the still unknown values at time t_{n+1} (Equation A.11). The implicit method requires a solution of a nonlinear equation at each time step. The obtained displacements are tested to verify that they satisfy the governing equations of motion. If equilibrium is not satisfied, an iterative procedure is applied until the equilibrium is achieved. Successful convergence of these iterations is not guaranteed and can be very difficult in practice. However, the implicit approach can be applied with a far bigger time step than explicit approach. Hence the total computational time can be very much smaller than that of an explicit simulation. Another disadvantage of the implicit approach is that the stiffness matrix must be inverted in addition to the mass and damping matrices. Since the stiffness matrix is not diagonal finding the transpose of it can be a time consuming process [115-118].

In this study, LS-DYNA FE software program developed by Livermore Software Technology Corporation (LSTC) was used. Both the implicit and explicit time integration methods were used in the modeling of quasi-static normal contacts, while only the explicit scheme was employed for the sliding contact studies.

A.2. ELEMENT FORMULATIONS

Two element types, Lagrangian and Eulerian elements, were utilized in this study. The Lagrangian finite element formulation uses a computational mesh that follows the material boundaries and moves with the material deformations. This approach is computationally efficient and accurate for moderate deformation problems. When the elements are distorted, they will have low accuracy and their stable time step size will be reduced. In the Eulerian finite element method, the mesh is fixed in space and the materials flow through the mesh. Since the mesh is fixed in space, the numerical difficulties associated with the distortion of the elements are eliminated [119].

Lagrangian time integration method was presented in the previous section (Section A.1). Eulerian elements have two main time steps: the Lagrangian step and the Eulerian advection step. The Lagrangian step, performed first, advances the solution in time, while the Eulerian step accounts for the transport between the elements. The Lagrangian step in the Eulerian element formulation is very similar to the explicit time step in Lagrangian element formulations. There are two main algorithmic differences between the Lagrangian step in an Eulerian calculation and the time step in a Lagrangian calculation:

1- Absence of contact algorithms in the Eulerian formulation.

2- The interactions between adjacent materials are handled by the mixture theory. The mixture theory distributes the strain increment of an element among the materials in an element and calculates the element stress from the stresses in the materials.

After the Lagrangian step, the mesh is remapped to its original spatial coordinates, referred as advection step or the Eulerian step. Since the mesh is brought back to the original position, in postprocessing it appears stationary. However, the material is not remapped to the original position and it moves throughout the mesh. Therefore, a void air mesh must surround the original mesh to provide space for the flow of deformed material.

A.3. CONTACT ALGORITHMS

Contact algorithms prevent surfaces from interpenetrating. Contact occurs when two or more surfaces come together and their interaction must be computed. Contact algorithms can be categorized by their 1) contact search strategy, 2) contact and release conditions and 3) contact force calculation. The contact search is a significant cost for the most contact algorithms [118].

There are a large number of contact types in LS-DYNA and they can be grouped in to the following categories: penalty based contacts, tied contacts and constrained based contacts. The penalty based contact method has proven to be the most versatile and robust method for contact with separation and slip in LS-DYNA [118]. In LS-DYNA, a contact is defined by identifying (via parts, part sets, segment sets and/or node sets)

what locations are checked for potential penetration of a slave node through a master segment [120]. When a penetration is found, in the penalty method linear tension-only springs are added to the model between penetrating nodes and contact surfaces, with a stiffness based on geometric and material properties of the contacting entities. The contact spring stiffness is defined as the product of the user defined penalty factor and a stiffness determined from the master segment, or the slave node [122]:

$$k = C_{user} \cdot K \cdot \frac{A}{\max(D_1, D_2)} \quad \text{for shell elements} \quad (\text{A.12})$$

$$k = C_{user} \cdot K \cdot \frac{A^2}{V} \quad \text{for solid (brick) elements} \quad (\text{A.13})$$

where C_{user} is the user defined scale factor, K is the bulk modulus equal to $\frac{E}{3(1-2\nu)}$, A is the face area of the element in contact, V is the volume of the element and D_1 and D_2 are the shell element diagonals. With tension only springs, a force (f) proportional to the penetration depth (p) is applied to resist, and ultimately eliminate the penetration:

$$f = kp \quad (\text{A.14})$$

Ideally the contact spring stiffness should be very high in order to prevent penetrations and add realism to the simulation. However, in reality the value of k is limited by the stability condition for the contact spring. Contact springs with stiffness is attributed for part of the mass of slave node and master segment and time step size for the springs Δt_{sc} is calculated by the following equation:

$$\Delta t_{sc} = \sqrt{\frac{4m_s m_m}{k(m_s + m_m)}} \quad (\text{A.15})$$

where m_s and m_m are the mass of slave node and master segment, respectively. To guarantee stability the user must ensure that Δt_{sc} is larger than the critical time step of the simulation:

$$\Delta t_{sc} \geq \Delta t_c \quad (\text{A.16})$$

A.4. ENERGIES AND EXTERNAL WORK

In order to confirm the validity of a numerical simulation, the energy and external work analysis is the first criterion that a researcher should refer. If there is no energy formation process modeled in a finite element model, the total energy should be always equal to the initial energy of the system. Types of energies that contribute to the total energy of the system are: internal energy, kinetic energy, sliding interface energy, hourglass energy, external work, etc. These energy types incorporated in the energy analysis of a system should be monitored carefully.

Usage of elements with under integration (single point Gaussian quadrature) in a simulation may lead zero energy modes of deformation (hourglassing), which refers to the deformation of elements in a finite element analysis without production of strain energy. So, this type of energy should be monitored and kept under 10 % of the total energy [121]. In addition, hourglass control might be used to eliminate this type of energy modes. When hourglass control is activated, artificial forces are placed on the nodes to eliminate deformation associated with this type of energy modes.

Another type of energy that contributes to the total energy of the system is sliding interface energy which is a result of the contact between the master and slave entities. During contact kinetic energy of the impacting body is typically converted in deformation energy of both colliding objects. This energy is numerically buffered in the linear contact springs that have potential energy:

$$E_{sie} = \sum_{springs} \int f dp = \sum_{springs} \frac{kp^2}{2} \quad (\text{A.17})$$

This non-physical energy is called sliding interface energy (E_{sie}) and should ideally remain very small compared to the physical energies in the system during normal contacts and frictionless contacts [122]. Therefore, sliding interface energy should also be monitored and kept under 10 % of the total energy of the system [121]. Friction will cause an increase in the interface forces and may result in positive sliding interface energy which is acceptable. Negative sliding interface energy indicates penetration and should be avoided [102].

APPENDIX B

SAMPLE NORMAL CONTACT ANALYSIS INPUT FILE

```

*KEYWORD
$-----1-----2-----3-----4-----5-----6-----7-----8
$
      (1) TITLE CARD.
$-----1-----2-----3-----4-----5-----6-----7-----8
*TITLE
MODEL
$-----1-----2-----3-----4-----5-----6-----7-----8
$
      (2) CONTROL CARDS.
$-----1-----2-----3-----4-----5-----6-----7-----8
*CONTROL_TERMINATION
$  ENDTIM  ENDCYC  DTMIN  ENDNEG  ENDMAS
   .100E-02    0    .000    .000    .000
*CONTROL_TIMESTEP
$  DTINIT  SCFT  ISDO  TSLIMIT  DT2MS  LCTM  ERODE  MS1ST
   .000    .900    0    -0.90E-10
*CONTROL_HOURLASS
$  IHQ  QH
   1    .100
*CONTROL_BULK_VISCOSITY
$  Q2  Q1
   1.500  .060
*CONTROL_SHELL
$  WRPANG  ITRIST  IRNXX  ISTUPD  THEORY  BWC  MITER
   20.000  2    -1    0    2    2    1
*CONTROL_CONTACT
$  SLSFAC  RWPNAL  ISLCHK  SHLTHK  PENOPT  THKCHG  ORIEN
   .100
$  USRSTR  USRFAC  NSBCS  INTERM  XPENE
   0    0    10    0    4.000
*CONTROL_ENERGY
$  HGEN  RWEN  SLNTEN  RYLEN
   2    2    1    1
*CONTROL_DAMPING
$  NRCYCK  DRTOL  DRFCTR  DRTERM  TSSFDR  IRELAL  EDTTL  IDRFLG
   250  .001  .995
*CONTROL_OUTPUT
$  NPOPT  NEECHO  NREFUP  IACCOP  OPIFS  IPNINT  IKEDIT
   0    0    0    0    .000  0    100
$-----1-----2-----3-----4-----5-----6-----7-----8
$
      (3) DATABASE CONTROL CARDS - ASCII HISTORY FILE
$-----1-----2-----3-----4-----5-----6-----7-----8
*DATABASE_HISTORY_SHELL_SET
$  ID1  ID2  ID3  ID4  ID5  ID6  ID7  ID8
   2
$-----1-----2-----3-----4-----5-----6-----7-----8
$
      (4) DATABASE CONTROL CARDS FOR ASCII FILE
$-----1-----2-----3-----4-----5-----6-----7-----8
*DATABASE_ELOUT
   .100E-05
*DATABASE_GLSTAT
   .100E-05
*DATABASE_MATSUM
   .100E-05
*DATABASE_RCFORC
   .100E-05
*DATABASE_SLEOUT
   .100E-05
$-----1-----2-----3-----4-----5-----6-----7-----8

```

```

$ (5) DATABASE CONTROL CARDS FOR BINARY FILE
$-----1-----2-----3-----4-----5-----6-----7-----8
*DATABASE_BINARY_D3PLOT
$ DT/CYCL LCDT NOBEAM
.500E-04
*DATABASE_BINARY_D3THDT
$ DT/CYCL LCDT NOBEAM
.500E-04
$-----1-----2-----3-----4-----5-----6-----7-----8
*DATABASE_EXTENT_BINARY
0 0 3 0 1 1 1
0 0 0 0 0 0 1
$-----1-----2-----3-----4-----5-----6-----7-----8
$ (6) DEFINE PARTS CARDS
$-----1-----2-----3-----4-----5-----6-----7-----8
*PART
$HEADING
PART PID = 1 PART NAME :BODY
$ PID SID MID EOSID HGID GRAV ADOPT TMID
1 1 1
*PART
$HEADING
PART PID = 2 PART NAME :ASPERITY
$ PID SID MID EOSID HGID GRAV ADOPT TMID
2 1 2 1
*PART
$HEADING
PART PID = 3 PART NAME :HRGLASS
$ PID SID MID EOSID HGID GRAV ADOPT TMID
3 1 1 1
$-----1-----2-----3-----4-----5-----6-----7-----8
$ (7) HOURGLASS CONTROL
$-----1-----2-----3-----4-----5-----6-----7-----8
*HOURGLASS
$ HGID IHQ QM IBQ
1 4 0.05
$-----1-----2-----3-----4-----5-----6-----7-----8
$ (8) MATERIAL CARDS
$-----1-----2-----3-----4-----5-----6-----7-----8
*MAT_ELASTIC
$MATERIAL NAME:A356
$ MID RO E PR DA DB
1 2.669E-06 7.240E+07 3.300E-01 0.000E+00 0.000E+00
*MAT_ELASTIC
$MATERIAL NAME:RIGID ST
$ MID RO E PR DA DB
2 7.800E-06 4.000E+08 3.000E-01 0.000E+00 0.000E+00
$-----1-----2-----3-----4-----5-----6-----7-----8
$ (9) SECTION CARDS
$-----1-----2-----3-----4-----5-----6-----7-----8
*SECTION_SHELL
$PROPERTY NAME:SHELL
$ SID ELFORM SHRF NIP PROPT QR/IRID ICOMP SETYP
1 13 .100E+01 2 .000E+00 .000E+00 0 1
$ T1 T2 T3 T4 NLOC
.100E+01 .100E+01 .100E+01 .100E+01 .000E+00
$-----1-----2-----3-----4-----5-----6-----7-----8
$ (10) NODAL POINT CARDS
$-----1-----2-----3-----4-----5-----6-----7-----8
*NODE
$ NODE X Y Z TC RC
1 .000000000E+00 .941666800E-01 .000000000E+00
2 .000000000E+00 .933333500E-01 .000000000E+00
3 .833333500E-03 .933333500E-01 .000000000E+00
...
... (cont'd)
8126 .575000000E-01 .954166800E-01 .000000000E+00

```

```

8127 .570833300E-01 .954166800E-01 .000000000E+00
8128 .579166600E-01 .954166800E-01 .000000000E+00
$-----1-----2-----3-----4-----5-----6-----7-----8
$
      (11) SHELL ELEMENT CARDS
$-----1-----2-----3-----4-----5-----6-----7-----8
*ELEMENT_SHELL
$   EID   PID      N1      N2      N3      N4
    1     1        1        2        3        4
    2     1        2        5        6        3
    3     1        5        7        8        6
    ...
    ... (cont'd)
    7862     3    6464    6850    6845    6462
    7863     3    6845    6848    6463    6462
    7864     3    6848    6847    8095    6463
$-----1-----2-----3-----4-----5-----6-----7-----8
$
      (12) DEFINE SET CARDS
$-----1-----2-----3-----4-----5-----6-----7-----8
*SET_NODE_LIST
$   SID      DA1      DA2      DA3      DA4
    1
$   NID1     NID2     NID3     NID4     NID5     NID6     NID7     NID8
    3631     3632     3673     3694     3715     3736     3757     3778
    3799     3820     3841     3862     3883     3904     3925     3946
    3967     3988     4009     4030     4051     4912     4913     4952
    4972     4992     5012     5032     5052     5072     5092     5112
    5132     5152     5172     5192     5212     5232     5252     5272
    5292     5312     5332     5352     5372     5392     5412     5432
    5452     5472     5492     5512     5532     5552     5572     5592
    5612     5632     5652     5672     5692     5712     5732     5752
    5772     5792     5812     5832     5852     5872     5892     5912
    5932     5952     5972     5992     6012     6032     6052     6072
    6092
$-----1-----2-----3-----4-----5-----6-----7-----8
$
      (13) LOADING CONDITIONS
$-----1-----2-----3-----4-----5-----6-----7-----8
*LOAD_NODE_SET
$   NSID     DOF      LCID      SF      CID      M1      M2      M3
    1         2         2         1
*DEFINE_CURVE
$   LCID     SIDR      SFA      SFO      OFFA     OFFO     DATTYP
    2         0         1.0     -1.0     0.0     0.0     0
$
      A1 (TIME)          O1 (FORCE)
      0.0                0.0
      0.0003             0.407E+02
      0.001              0.407E+02
$-----1-----2-----3-----4-----5-----6-----7-----8
*SET_SHELL_LIST
$   SID      NUM      DA1      DA2      DA3      DA4
    2         48
$   EIDS     EID2     EID3     EID4     EID5     EID5     EID7     EID8
    7135     7136     7138     7139     7151     7152     7154     7155
    7167     7168     7170     7171     7180     7181     7781     6641
    6640     7835     6240     1712     1713     1714     1715     1716
    1717     1718     1719     1720     1721     1722     1723     1724
    1725     1726     1727     1728     1729     1730     1731     1732
    1733     1734     1735     1736     1737     1738     1739     1740
$-----1-----2-----3-----4-----5-----6-----7-----8
$
      (14) BOUNDARY CONDITION CARDS
$-----1-----2-----3-----4-----5-----6-----7-----8
*BOUNDARY_SPC_NODE
$   NID/NSID  CID      DOFX     DOFY     DOFZ     DOFRX     DOFRY     DOFRZ
    59         0        1        1        1        1        1        1
    60         0        1        1        1        1        1        1
    90         0        1        1        1        1        1        1
    ...
    ... (cont'd)

```


6109	0	1	0	1	1	1	1	1
6110	0	1	0	1	1	1	1	1
6111	0	1	0	1	1	1	1	1

```

$-----1-----2-----3-----4-----5-----6-----7-----8
$
(15) DEFINE SET CARDS
$-----1-----2-----3-----4-----5-----6-----7-----8
*SET_PART_LIST
$   SID
   1
$   PID1   PID2
   3       1
*SET_PART_LIST
$   SID
   2
$   PID1
   2
$-----1-----2-----3-----4-----5-----6-----7-----8
$
(16) DEFINE CONTACT SURFACE
$-----1-----2-----3-----4-----5-----6-----7-----8
*CONTACT_2D_AUTOMATIC_NODE_TO_SURFACE
$   PSIDS   PSIDM   SFACT   FREQ   FS   FD   DC   MEMBS
   1       2       8.0     50  0.000E-01 0.000E-01 0.0   6
$   TBIRTH  TDEATH  SOS     SOM     NDS   NDM  IPF/COF  INIT
   0.0  1.000E+20  1.0     1.0     0     0    1       0
$-----1-----2-----3-----4-----5-----6-----7-----8
*END

```

APPENDIX C

SAMPLE SLIDING CONTACT ANALYSIS INPUT FILE

```

*KEYWORD
$-----1-----2-----3-----4-----5-----6-----7-----8
$
$ NOTE THE FOLLOWING SET OF UNITS: MM,KG,SEC,
$ ALL OTHER UNITS ARE DERIVED FROM THIS BASE SET
$
$-----1-----2-----3-----4-----5-----6-----7-----8
$
$ (1) TITLE CARD.
$-----1-----2-----3-----4-----5-----6-----7-----8
*TITLE
7ASP.SLG.CON
$-----1-----2-----3-----4-----5-----6-----7-----8
$
$ (2) CONTROL CARDS.
$-----1-----2-----3-----4-----5-----6-----7-----8
*CONTROL_TERMINATION
$ ENDTIM ENDCYC DTMIN ENDNEG ENDMAS
8.40E-03 0 .000 .000 .000
*CONTROL_TIMESTEP
$ DTINIT SCFT ISDO TSLIMIT DTMS LCTM ERODE MS1ST
.000 .900 0
*CONTROL_ENERGY
$ HGEN RWEN SLNTEN RYLEN
2 2 1 1
*CONTROL_ALE
$ DCT NADV METH AFAC BFAC CFAC DFAC EFAC
2 1 2 -1
$ START END AAFAC VFACT VLIMIT EBC
$-----1-----2-----3-----4-----5-----6-----7-----8
$
$ (3) DATABASE CONTROL CARDS - ASCII HISTORY FILE
$-----1-----2-----3-----4-----5-----6-----7-----8
$*DATABASE_HISTORY_OPTION
$ ID1 ID2 ID3 ID4 ID5 ID6 ID7 ID8
$
$OPTION : BEAM BEAM_SET NODE NODE_SET
$ SHELL SHELL_SET SOLID SOLID_SET
$ TSHELL TSHELL_SET
$-----1-----2-----3-----4-----5-----6-----7-----8
$
$ (4) DATABASE CONTROL CARDS FOR ASCII FILE
$-----1-----2-----3-----4-----5-----6-----7-----8
$*DATABASE_HISTORY_SOLID_SET
$ ID1 ID2 ID3 ID4 ID5 ID6 ID7 ID8
8
*DATABASE_ELOUT
1.00E-05
*DATABASE_GLSTAT
1.00E-05
*DATABASE_MATSUM
1.00E-05
*DATABASE_RCFORC
1.00E-05
*DATABASE_SLEOUT
1.00E-05
*DATABASE_FSI
1.00E-05
$ DBFSI_ID SID SIDTYPE
1 2 1

```

```

      2      4      1
      3      5      1
      4      6      1
      5      7      1
      6      8      1
      7      9      1
$-----1-----2-----3-----4-----5-----6-----7-----8
$
      (5) DATABASE CONTROL CARDS FOR BINARY FILE
$-----1-----2-----3-----4-----5-----6-----7-----8
*DATABASE_BINARY_D3PLOT
$ DT/CYCL      LCDT      NOBEAM
  1.00E-04
*DATABASE_BINARY_D3THDT
$ DT/CYCL      LCDT      NOBEAM
  1.00E-04
$-----1-----2-----3-----4-----5-----6-----7-----8
*DATABASE_EXTENT_BINARY
      0      0      3      0      1      1      1      1
      0      0      0      0      0      0      0      0
$-----1-----2-----3-----4-----5-----6-----7-----8
$
      (6) DEFINE PARTS CARDS
$-----1-----2-----3-----4-----5-----6-----7-----8
*PART
$HEADING
PART PID =      1 PART NAME :SOLID
$   PID      SID      MID      EOSID      HGID      GRAV      ADPOPT      TMID
      1      1      1      1
*PART
$HEADING
PART PID =      2 PART NAME :ASP
$   PID      SID      MID      EOSID      HGID      GRAV      ADPOPT      TMID
      2      2      2
*PART
$HEADING
PART PID =      3 PART NAME :AIRMESH
$   PID      SID      MID      EOSID      HGID      GRAV      ADPOPT      TMID
      3      3      1      1
*PART
$HEADING
PART PID =      4 PART NAME :ASP2
$   PID      SID      MID      EOSID      HGID      GRAV      ADPOPT      TMID
      4      2      2
*PART
$HEADING
PART PID =      5 PART NAME :ASP3
$   PID      SID      MID      EOSID      HGID      GRAV      ADPOPT      TMID
      5      2      2
*PART
$HEADING
PART PID =      6 PART NAME :ASP4
$   PID      SID      MID      EOSID      HGID      GRAV      ADPOPT      TMID
      6      2      2
*PART
$HEADING
PART PID =      7 PART NAME :ASP5
$   PID      SID      MID      EOSID      HGID      GRAV      ADPOPT      TMID
      7      2      2
*PART
$HEADING
PART PID =      8 PART NAME :ASP6
$   PID      SID      MID      EOSID      HGID      GRAV      ADPOPT      TMID
      8      2      2
*PART
$HEADING
PART PID =      9 PART NAME :ASP7
$   PID      SID      MID      EOSID      HGID      GRAV      ADPOPT      TMID
      9      2      2

```

```

$-----1-----2-----3-----4-----5-----6-----7-----8
$              (7) INITIAL VOID DEFINITIONS
$-----1-----2-----3-----4-----5-----6-----7-----8
*INITIAL_VOID_PART
$   PID
$     3
$-----1-----2-----3-----4-----5-----6-----7-----8
$              (8) MATERIAL CARDS
$-----1-----2-----3-----4-----5-----6-----7-----8
*MAT_ELASTIC_PLASTIC_HYDRO
$MATERIAL_NAME:A356
$   MID      RO      G      SIGY      EH      PC      FS
$     1 2.669E-06 2.720E+07 2.400E+05
$   EPS1      EPS2      EPS3      EPS4      EPS5      EPS6      EPS7      EPS8
$ 0.00E+00 0.10E+01 0.20E+01 0.30E+01 0.40E+01 0.50E+01 0.60E+01 0.70E+01
$   EPS9      EPS10     EPS11     EPS12     EPS13     EPS14     EPS15     EPS16
$ 0.80E+01 0.90E+01 0.10E+02 0.12E+02 0.14E+02 0.17E+02 0.20E+02 0.40E+02
$   ES1      ES2      ES3      ES4      ES5      ES6      ES7      ES8
$ 2.400E+05 2.701E+05 2.946E+05 3.145E+05 3.306E+05 3.437E+05 3.543E+05 3.629E+05
$   ES9      ES10     ES11     ES12     ES13     ES14     ES15     ES16
$ 3.698E+05 3.755E+05 3.802E+05 3.869E+05 3.914E+05 3.954E+05 3.975E+05 3.999E+05
$-----1-----2-----3-----4-----5-----6-----7-----8
*MAT_RIGID
$MATERIAL_NAME:RIGID ST
$   MID      RO      E      PR      N      COUPLE      M      ALIAS
$     2 7.800E-06 2.070E+08 3.000E-01      0.0
$   CMO      CON1      CON2
$     1.0      3      7
$ OPTIONAL BLANK CARD
$-----1-----2-----3-----4-----5-----6-----7-----8
*EOS_GRUNEISEN
$   EOSID      C      S1      S2      S3      GAMMO      A      E0
$     1 0.535E+07      1.338      0.0      0.0      1.97      0.48      0
$   VO
$     1
$-----1-----2-----3-----4-----5-----6-----7-----8
$              (9) SECTION CARDS
$-----1-----2-----3-----4-----5-----6-----7-----8
*SECTION_SOLID
$PROPERTY_NAME:SOLID1
$   SID      ELFORM      AET
$     1      12
*SECTION_SOLID
$PROPERTY_NAME:SOLID3
$   SID      ELFORM      AET
$     3      12
*SECTION_SOLID
$PROPERTY_NAME:SOLID2
$   SID      ELFORM      AET
$     2      1
$-----1-----2-----3-----4-----5-----6-----7-----8
$              (10) EULERIAN/LAGRANGIAN CONTACT COUPLING
$-----1-----2-----3-----4-----5-----6-----7-----8
*CONSTRAINED_LAGRANGE_IN_SOLID
$   SLAVE      MASTER      SSTYP      MSTYP      NQUAD      CTYPE      DIREC      MCOUP
$     2      1      0      0      4      5      2
$   START      END      PFAC      FRIC      FRCMIN      NORM
$           3.0      0.0
$   CQ      HMIN      HMAX
$
*SET_PART_LIST
$   PSID
$     2
$   PID1      PID2      PID3      PID3      PID5      PID6      PID7
$     2      4      5      6      7      8      9
*SET_PART_LIST

```

```

$ PSID
  1
$ PID1 PID2
  1 3
$-----1-----2-----3-----4-----5-----6-----7-----8
$ (11) NODAL POINT CARDS
$-----1-----2-----3-----4-----5-----6-----7-----8
*NODE
$ NODE X Y Z TC RC
  1 -.833295700E-02 .680000000E+01 .540000000E+01
  2 -.416666400E+00 .679999900E+01 .540000100E+01
  3 -.416666400E+00 .639999800E+01 .540000100E+01
  ...
  ... (cont'd)
  41992 .235410200E+00 .963748900E+01 .550000100E+01
  41993 .235410200E+00 .957499000E+01 .550000100E+01
  41994 .235410800E+00 .951248900E+01 .550000100E+01
$-----1-----2-----3-----4-----5-----6-----7-----8
$ (12) SOLID ELEMENT CARDS
$-----1-----2-----3-----4-----5-----6-----7-----8
*ELEMENT_SOLID
$ EID PID N1 N2 N3 N4 N5 N6 N7 N8
  1 1 1 2 3 4 5 6 7 8
  2 1 3 2 9 10 7 6 11 12
  3 1 13 14 15 16 17 18 19 20
  ...
  ... (cont'd)
  33353 9 41992 41840 41841 41993 41674 41522 41523 41675
  33354 9 41993 41841 41842 41994 41675 41523 41524 41676
  33355 9 41994 41842 41726 41885 41676 41524 41408 41567
$-----1-----2-----3-----4-----5-----6-----7-----8
$ (13) BOUNDARY CONDITION CARDS
$-----1-----2-----3-----4-----5-----6-----7-----8
*BOUNDARY_SPC_NODE
$ NID/NSID CID DOFX DOFY DOFZ DOFRX DOFRY DOFRZ
  5 0 0 0 1 1 1 0
  6 0 0 0 1 1 1 0
  7 0 0 0 1 1 1 0
  ...
  ... (cont'd)
  30544 0 0 0 1 1 1 0
  30545 0 0 0 1 1 1 0
  30546 0 0 0 1 1 1 0
$-----1-----2-----3-----4-----5-----6-----7-----8
$ (14) DEFINE SET CARDS
$-----1-----2-----3-----4-----5-----6-----7-----8
*SET_NODE_LIST
$ SID DA1 DA2 DA3 DA4
  1
$ NID1 NID2 NID3 NID4 NID5 NID6 NID7 NID8
  14195 14196 14201 14205 14209 14213 14290 14306
  14322 14338 14354 14370 14386 14402 14515 14518
  14522 14526 14530 14534 14609 14625 14641 14657
  14673 14689 14705 14191 14192 14199 14203 14207
  14211 14288 14304 14320 14336 14352 14368 14384
  14400 14511 14514 14520 14524 14528 14532 14607
  14623 14639 14655 14671 14687 14703 14773 14774
  14777 14779 14781 14783 14822 14830 14838 14846
  14854 14862 14870 14878 14933 14936 14938 14940
  14942 14944 14981 14989 14997 15005 15013 15021
  15029 15091 15092 15095 15097 15099 15101 15140
  15148 15156 15164 15172 15180 15188 15196 15251
  15254 15256 15258 15260 15262 15299 15307 15315
  15323 15331 15339 15347 15409 15410 15413 15415
  15417 15419 15458 15466 15474 15482 15490 15498

```

15506	15514	15569	15572	15574	15576	15578	15580
15617	15625	15633	15641	15649	15657	15665	15727
15728	15731	15733	15735	15737	15776	15784	15792
15800	15808	15816	15824	15832	15887	15890	15892
15894	15896	15898	15935	15943	15951	15959	15967
15975	15983						

\$-----1-----2-----3-----4-----5-----6-----7-----8
 \$ (15) LOADING CONDITIONS

\$-----1-----2-----3-----4-----5-----6-----7-----8
 *LOAD_NODE_SET
 \$ NSID DOF LCID SF CID M1 M2 M3
 1 2 1 1
 *DEFINE_CURVE
 \$ LCID SIDR SFA SFO OFFA OFFO DATYTP
 1 0 1.0 -1.0 0.0 0.0 0
 \$ A1 (TIME) O1 (FORCE)
 0.00 0.0
 0.0002 0.092593E+04
 0.0011 0.092593E+04
 0.0012 0.0
 0.0084 0.0

\$-----1-----2-----3-----4-----5-----6-----7-----8
 *SET_NODE_LIST

\$ SID DA1 DA2 DA3 DA4
 2
 \$ NID1 NID2 NID3 NID4 NID5 NID6 NID7 NID8
 30655 30656 30659 30660 30663 30665 30667 30669
 30671 30673 30675 30677 30752 30754 30768 30770
 30784 30786 30800 30802 30816 30818 30832 30834
 30848 30850 30864 30866 30975 30978 30979 30982
 30984 30986 30988 30990 30992 30994 30996 30998
 31071 31073 31087 31089 31103 31105 31119 31121
 31135 31137 31151 31153 31167 31169 31237 31238
 31241 31243 31245 31247 31286 31294 31302 31310
 31318 31326 31334 31342 31397 31400 31402 31404
 31406 31408 31445 31453 31461 31469 31477 31485
 31493 31555 31556 31559 31561 31563 31565 31604
 31612 31620 31628 31636 31644 31652 31660 31715
 31718 31720 31722 31724 31726 31763 31771 31779
 31787 31795 31803 31811 31873 31874 31877 31879
 31881 31883 31922 31930 31938 31946 31954 31962
 31970 31978 32033 32036 32038 32040 32042 32044
 32081 32089 32097 32105 32113 32121 32129 32191
 32192 32195 32197 32199 32201 32240 32248 32256
 32264 32272 32280 32288 32296 32351 32354 32356
 32358 32360 32362 32399 32407 32415 32423 32431
 32439 32447

\$-----1-----2-----3-----4-----5-----6-----7-----8
 \$ (15) LOADING CONDITIONS

\$-----1-----2-----3-----4-----5-----6-----7-----8
 *LOAD_NODE_SET
 \$ NSID DOF LCID SF CID M1 M2 M3
 2 2 2 1
 *DEFINE_CURVE
 \$ LCID SIDR SFA SFO OFFA OFFO DATYTP
 2 0 1.0 -1.0 0.0 0.0 0
 \$ A1 (TIME) O1 (FORCE)
 0.00 0.0
 0.0012 0.0
 0.0014 0.092593E+04
 0.0023 0.092593E+04
 0.0024 0.0
 0.0084 0.0

\$-----1-----2-----3-----4-----5-----6-----7-----8
 *SET_NODE_LIST

\$ SID DA1 DA2 DA3 DA4
 3

\$	NID1	NID2	NID3	NID4	NID5	NID6	NID7	NID8
	32563	32564	32567	32568	32571	32573	32575	32577
	32579	32581	32583	32585	32660	32662	32676	32678
	32692	32694	32708	32710	32724	32726	32740	32742
	32756	32758	32772	32774	32883	32886	32887	32890
	32892	32894	32896	32898	32900	32902	32904	32906
	32979	32981	32995	32997	33011	33013	33027	33029
	33043	33045	33059	33061	33075	33077	33145	33146
	33149	33151	33153	33155	33194	33202	33210	33218
	33226	33234	33242	33250	33305	33308	33310	33312
	33314	33316	33353	33361	33369	33377	33385	33393
	33401	33463	33464	33467	33469	33471	33473	33512
	33520	33528	33536	33544	33552	33560	33568	33623
	33626	33628	33630	33632	33634	33671	33679	33687
	33695	33703	33711	33719	33781	33782	33785	33787
	33789	33791	33830	33838	33846	33854	33862	33870
	33878	33886	33941	33944	33946	33948	33950	33952
	33989	33997	34005	34013	34021	34029	34037	34099
	34100	34103	34105	34107	34109	34148	34156	34164
	34172	34180	34188	34196	34204	34259	34262	34264
	34266	34268	34270	34307	34315	34323	34331	34339
	34347	34355						

\$-----1-----2-----3-----4-----5-----6-----7-----8
 \$ (15) LOADING CONDITIONS

*LOAD_NODE_SET

\$	NSID	DOF	LCID	SF	CID	M1	M2	M3
	3	2	3	1				

*DEFINE_CURVE

\$	LCID	SIDR	SFA	SFO	OFFA	OFFO	DATTYP
	3	0	1.0	-1.0	0.0	0.0	0

\$

	A1 (TIME)	O1 (FORCE)
	0.00	0.0
	0.0012	0.0
	0.0024	0.0
	0.0026	0.092593E+04
	0.0035	0.092593E+04
	0.0036	0.0
	0.0084	0.0

\$-----1-----2-----3-----4-----5-----6-----7-----8

*SET_NODE_LIST

\$	SID	DA1	DA2	DA3	DA4
	4				

\$	NID1	NID2	NID3	NID4	NID5	NID6	NID7	NID8
	34471	34472	34475	34476	34479	34481	34483	34485
	34487	34489	34491	34493	34568	34570	34584	34586
	34600	34602	34616	34618	34632	34634	34648	34650
	34664	34666	34680	34682	34791	34794	34795	34798
	34800	34802	34804	34806	34808	34810	34812	34814
	34887	34889	34903	34905	34919	34921	34935	34937
	34951	34953	34967	34969	34983	34985	35053	35054
	35057	35059	35061	35063	35102	35110	35118	35126
	35134	35142	35150	35158	35213	35216	35218	35220
	35222	35224	35261	35269	35277	35285	35293	35301
	35309	35371	35372	35375	35377	35379	35381	35420
	35428	35436	35444	35452	35460	35468	35476	35531
	35534	35536	35538	35540	35542	35579	35587	35595
	35603	35611	35619	35627	35689	35690	35693	35695
	35697	35699	35738	35746	35754	35762	35770	35778
	35786	35794	35849	35852	35854	35856	35858	35860
	35897	35905	35913	35921	35929	35937	35945	36007
	36008	36011	36013	36015	36017	36056	36064	36072
	36080	36088	36096	36104	36112	36167	36170	36172
	36174	36176	36178	36215	36223	36231	36239	36247
	36255	36263						

\$-----1-----2-----3-----4-----5-----6-----7-----8
 \$ (15) LOADING CONDITIONS

```

$-----1-----2-----3-----4-----5-----6-----7-----8
*LOAD_NODE_SET
$   NSID      DOF      LCID      SF      CID      M1      M2      M3
   4          2          4          1
*DEFINE_CURVE
$   LCID      SIDR      SFA      SFO      OFFA      OFFO      DATYP
   4          0          1.0      -1.0      0.0      0.0      0
$           A1 (TIME)      O1 (FORCE)
           0.00            0.0
           0.0012          0.0
           0.0024          0.0
           0.0036          0.0
           0.0038            0.092593E+04
           0.0047            0.092593E+04
           0.0048          0.0
           0.0084          0.0
$-----1-----2-----3-----4-----5-----6-----7-----8
*SET_NODE_LIST
$   SID      DA1      DA2      DA3      DA4
   5
$   NID1      NID2      NID3      NID4      NID5      NID6      NID7      NID8
  36379      36380      36383      36384      36387      36389      36391      36393
  36395      36397      36399      36401      36476      36478      36492      36494
  36508      36510      36524      36526      36540      36542      36556      36558
  36572      36574      36588      36590      36699      36702      36703      36706
  36708      36710      36712      36714      36716      36718      36720      36722
  36795      36797      36811      36813      36827      36829      36843      36845
  36859      36861      36875      36877      36891      36893      36961      36962
  36965      36967      36969      36971      37010      37018      37026      37034
  37042      37050      37058      37066      37121      37124      37126      37128
  37130      37132      37169      37177      37185      37193      37201      37209
  37217      37279      37280      37283      37285      37287      37289      37328
  37336      37344      37352      37360      37368      37376      37384      37439
  37442      37444      37446      37448      37450      37487      37495      37503
  37511      37519      37527      37535      37597      37598      37601      37603
  37605      37607      37646      37654      37662      37670      37678      37686
  37694      37702      37757      37760      37762      37764      37766      37768
  37805      37813      37821      37829      37837      37845      37853      37915
  37916      37919      37921      37923      37925      37964      37972      37980
  37988      37996      38004      38012      38020      38075      38078      38080
  38082      38084      38086      38123      38131      38139      38147      38155
  38163      38171
$-----1-----2-----3-----4-----5-----6-----7-----8
$
(15) LOADING CONDITIONS
$-----1-----2-----3-----4-----5-----6-----7-----8
*LOAD_NODE_SET
$   NSID      DOF      LCID      SF      CID      M1      M2      M3
   5          2          5          1
*DEFINE_CURVE
$   LCID      SIDR      SFA      SFO      OFFA      OFFO      DATYP
   5          0          1.0      -1.0      0.0      0.0      0
$           A1 (TIME)      O1 (FORCE)
           0.00            0.0
           0.0012          0.0
           0.0024          0.0
           0.0036          0.0
           0.0048          0.0
           0.0050            0.092593E+04
           0.0059            0.092593E+04
           0.0060          0.0
           0.0084          0.0
$-----1-----2-----3-----4-----5-----6-----7-----8
*SET_NODE_LIST
$   SID      DA1      DA2      DA3      DA4
   6
$   NID1      NID2      NID3      NID4      NID5      NID6      NID7      NID8
  38287      38288      38291      38292      38295      38297      38299      38301

```


38303	38305	38307	38309	38384	38386	38400	38402
38416	38418	38432	38434	38448	38450	38464	38466
38480	38482	38496	38498	38607	38610	38611	38614
38616	38618	38620	38622	38624	38626	38628	38630
38703	38705	38719	38721	38735	38737	38751	38753
38767	38769	38783	38785	38799	38801	38869	38870
38873	38875	38877	38879	38918	38926	38934	38942
38950	38958	38966	38974	39029	39032	39034	39036
39038	39040	39077	39085	39093	39101	39109	39117
39125	39187	39188	39191	39193	39195	39197	39236
39244	39252	39260	39268	39276	39284	39292	39347
39350	39352	39354	39356	39358	39395	39403	39411
39419	39427	39435	39443	39505	39506	39509	39511
39513	39515	39554	39562	39570	39578	39586	39594
39602	39610	39665	39668	39670	39672	39674	39676
39713	39721	39729	39737	39745	39753	39761	39823
39824	39827	39829	39831	39833	39872	39880	39888
39896	39904	39912	39920	39928	39983	39986	39988
39990	39992	39994	40031	40039	40047	40055	40063
40071	40079						

\$-----1-----2-----3-----4-----5-----6-----7-----8

(15) LOADING CONDITIONS

\$-----1-----2-----3-----4-----5-----6-----7-----8

*LOAD_NODE_SET

NSID	DOF	LCID	SF	CID	M1	M2	M3
6	2	6	1				

*DEFINE_CURVE

LCID	SIDR	SFA	SFO	OFFA	OFFO	DATTYP
6	0	1.0	-1.0	0.0	0.0	0

\$

A1 (TIME)	O1 (FORCE)
0.00	0.0
0.0012	0.0
0.0024	0.0
0.0036	0.0
0.0048	0.0
0.0060	0.0
0.0062	0.092593E+04
0.0071	0.092593E+04
0.0072	0.0
0.0084	0.0

\$-----1-----2-----3-----4-----5-----6-----7-----8

*SET_NODE_LIST

SID	DA1	DA2	DA3	DA4
7				

NID1	NID2	NID3	NID4	NID5	NID6	NID7	NID8
40195	40196	40199	40200	40203	40205	40207	40209
40211	40213	40215	40217	40292	40294	40308	40310
40324	40326	40340	40342	40356	40358	40372	40374
40388	40390	40404	40406	40515	40518	40519	40522
40524	40526	40528	40530	40532	40534	40536	40538
40611	40613	40627	40629	40643	40645	40659	40661
40675	40677	40691	40693	40707	40709	40777	40778
40781	40783	40785	40787	40826	40834	40842	40850
40858	40866	40874	40882	40937	40940	40942	40944
40946	40948	40985	40993	41001	41009	41017	41025
41033	41095	41096	41099	41101	41103	41105	41144
41152	41160	41168	41176	41184	41192	41200	41255
41258	41260	41262	41264	41266	41303	41311	41319
41327	41335	41343	41351	41413	41414	41417	41419
41421	41423	41462	41470	41478	41486	41494	41502
41510	41518	41573	41576	41578	41580	41582	41584
41621	41629	41637	41645	41653	41661	41669	41731
41732	41735	41737	41739	41741	41780	41788	41796
41804	41812	41820	41828	41836	41891	41894	41896
41898	41900	41902	41939	41947	41955	41963	41971
41979	41987						

\$-----1-----2-----3-----4-----5-----6-----7-----8

```

*LOAD_NODE_SET
$  NSID      DOF      LCID      SF      CID      M1      M2      M3
   7         2         7         1
*DEFINE_CURVE
$  LCID      SIDR      SFA      SFO      OFFA      OFFO      DATYYP
   7         0         1.0      -1.0     0.0       0.0       0
$           A1 (TIME)      O1 (FORCE)
           0.00           0.0
           0.0012         0.0
           0.0024         0.0
           0.0036         0.0
           0.0048         0.0
           0.0060         0.0
           0.0072         0.0
           0.0074         0.092593E+04
           0.0083         0.092593E+04
           0.0084         0.0
$-----1-----2-----3-----4-----5-----6-----7-----8
*BOUNDARY_PRESCRIBED_MOTION_RIGID
$  PARTID    DOF      VAD      LCID      SF      VID      DEATH      BIRTH
   2         1         0         8         1.0     0       1.E+28     0.0
*DEFINE_CURVE
$  LCID      SIDR      SFA      SFO      OFFA      OFFO      DATYYP
   8         0         1.0      1.0      0.0       0.0       0
$           A1 (TIME)      O1 (VELOCITY)
           0           0.0
           0.0002         0.0
           0.0003         10.0E+03
           0.0011         10.0E+03
           0.0012         10.0E+03
           0.0084         10.0E+03
$-----1-----2-----3-----4-----5-----6-----7-----8
*BOUNDARY_PRESCRIBED_MOTION_RIGID
$  PARTID    DOF      VAD      LCID      SF      VID      DEATH      BIRTH
   4         1         0         9         1.0     0       1.E+28     0.0
*DEFINE_CURVE
$  LCID      SIDR      SFA      SFO      OFFA      OFFO      DATYYP
   9         0         1.0      1.0      0.0       0.0       0
$           A1 (TIME)      O1 (VELOCITY)
           0           0.0
           0.0014         0.0
           0.0015         10.0E+03
           0.0023         10.0E+03
           0.0024         10.0E+03
           0.0084         10.0E+03
$-----1-----2-----3-----4-----5-----6-----7-----8
*BOUNDARY_PRESCRIBED_MOTION_RIGID
$  PARTID    DOF      VAD      LCID      SF      VID      DEATH      BIRTH
   5         1         0         10        1.0     0       1.E+28     0.0
*DEFINE_CURVE
$  LCID      SIDR      SFA      SFO      OFFA      OFFO      DATYYP
  10         0         1.0      1.0      0.0       0.0       0
$           A1 (TIME)      O1 (VELOCITY)
           0           0.0
           0.0026         0.0
           0.0027         10.0E+03
           0.0035         10.0E+03
           0.0036         10.0E+03
           0.0084         10.0E+03
$-----1-----2-----3-----4-----5-----6-----7-----8
*BOUNDARY_PRESCRIBED_MOTION_RIGID
$  PARTID    DOF      VAD      LCID      SF      VID      DEATH      BIRTH
   6         1         0         11        1.0     0       1.E+28     0.0
*DEFINE_CURVE
$  LCID      SIDR      SFA      SFO      OFFA      OFFO      DATYYP
  11         0         1.0      1.0      0.0       0.0       0
$           A1 (TIME)      O1 (VELOCITY)

```

```

0
0.0038 0.0
0.0039 10.0E+03
0.0047 10.0E+03
0.0048 10.0E+03
0.0084 10.0E+03
$-----1-----2-----3-----4-----5-----6-----7-----8
*BOUNDARY_PRESCRIBED_MOTION_RIGID
$ PARTID DOF VAD LCID SF VID DEATH BIRTH
7 1 0 12 1.0 0 1.E+28 0.0
*DEFINE_CURVE
$ LCID SIDR SFA SFO OFFA OFFO DATYTP
12 0 1.0 1.0 0.0 0.0 0
$ A1 (TIME) O1 (VELOCITY)
0 0.0
0.0050 0.0
0.0051 10.0E+03
0.0059 10.0E+03
0.0060 10.0E+03
0.0084 10.0E+03
$-----1-----2-----3-----4-----5-----6-----7-----8
*BOUNDARY_PRESCRIBED_MOTION_RIGID
$ PARTID DOF VAD LCID SF VID DEATH BIRTH
8 1 0 13 1.0 0 1.E+28 0.0
*DEFINE_CURVE
$ LCID SIDR SFA SFO OFFA OFFO DATYTP
13 0 1.0 1.0 0.0 0.0 0
$ A1 (TIME) O1 (VELOCITY)
0 0.0
0.0062 0.0
0.0063 10.0E+03
0.0071 10.0E+03
0.0072 10.0E+03
0.0084 10.0E+03
$-----1-----2-----3-----4-----5-----6-----7-----8
*BOUNDARY_PRESCRIBED_MOTION_RIGID
$ PARTID DOF VAD LCID SF VID DEATH BIRTH
9 1 0 14 1.0 0 1.E+28 0.0
*DEFINE_CURVE
$ LCID SIDR SFA SFO OFFA OFFO DATYTP
14 0 1.0 1.0 0.0 0.0 0
$ A1 (TIME) O1 (VELOCITY)
0 0.0
0.0074 0.0
0.0075 10.0E+03
0.0083 10.0E+03
0.0084 10.0E+03
$-----1-----2-----3-----4-----5-----6-----7-----8
*SET_SOLID
$ SID NUM
8 90
$ K1 K2 K3 K4 K5 K6 K7 K8
10679 10684 1655 1660 1661 1663 1664 1700
1701 1703 1704 1712 1713 1715 1716 1764
1765 1891 3911 3916 3917 3919 3920 3956
3957 3959 3960 3968 3969 3971 3972 4020
4021 4147 6167 6172 6173 6175 6176 6212
6213 6215 6216 6224 6225 6227 6228 6276
6277 6403 8423 8428 8429 8431 8432 8468
8469 8471 8472 8480 8481 8483 8484 8532
8533 8659 10685 10687 10688 10724 10725 10727
10728 10736 10737 10739 10740 10788 10789 10915
1939 4195 6451 8707 10963 1963 4219 6475
8731 10987
$-----1-----2-----3-----4-----5-----6-----7-----8
*END

```

APPENDIX D

EOS ANALYSIS

In order to simulate the large deformation behaviour of the 356 Al alloy in sliding wear conditions, an Eulerian model—capable of accounting for large strain accumulation during asperity contacts—was developed and the details of the Eulerian sliding contact models are presented in Section 4.2. The material model prepared for the Eulerian sliding contact analysis must be accompanied by an equation of state (EOS) to account for any resistance to hydrostatic stresses. Two different EOS —named Gruneisen EOS and Linear Polynomial EOS—were employed to define the pressure-volume relationship of the 356 Al material. Details of the Gruneisen EOS are presented in Section 4.2.3. In this appendix, details of the Linear Polynomial EOS are presented and then the results of two simulations using two different EOS are compared.

The Linear Polynomial EOS is linear in internal energy [102]. The pressure (P) is given by:

$$P = C_0 + C_1\psi + C_2\psi^2 + C_3\psi^3 + (C_4 + C_5\psi + C_6\psi^2)E \quad (\text{D-1})$$

where E is the energy per unit volume, C_0 to C_6 are the polynomial equation coefficients. ψ is the compression defined as:

$$\psi = \frac{\rho}{\rho_0} - 1 \quad (\text{D-2})$$

where ρ is the density of the material and ρ_0 is the initial density. When the 1st polynomial equation coefficient, C_1 , is used by itself and the rest of the coefficients are

set to zero, it corresponds to the elastic bulk modulus of the material. However, the equation cannot be used in this shape for deformation beyond the elastic regime.

Figure D.1 illustrates pressure predictions of the Gruneisen EOS and Linear Polynomial EOS with changing compression (ψ). Figure D.1 indicates that pressure prediction of the two EOS shouldn't differ more than 10 % for the low values of ψ . Figure D.2 compares the results of two simulations using two different EOS for the 356 Al material used in this study. Figure D.2 reveals that the difference between two models using two different EOS was always less than 10% for the loading conditions studied and both EOS could be used in the simulations. The Gruneisen EOS was chosen to complete the simulations, since it is a full equation and the constants for the full equation are available from literature.

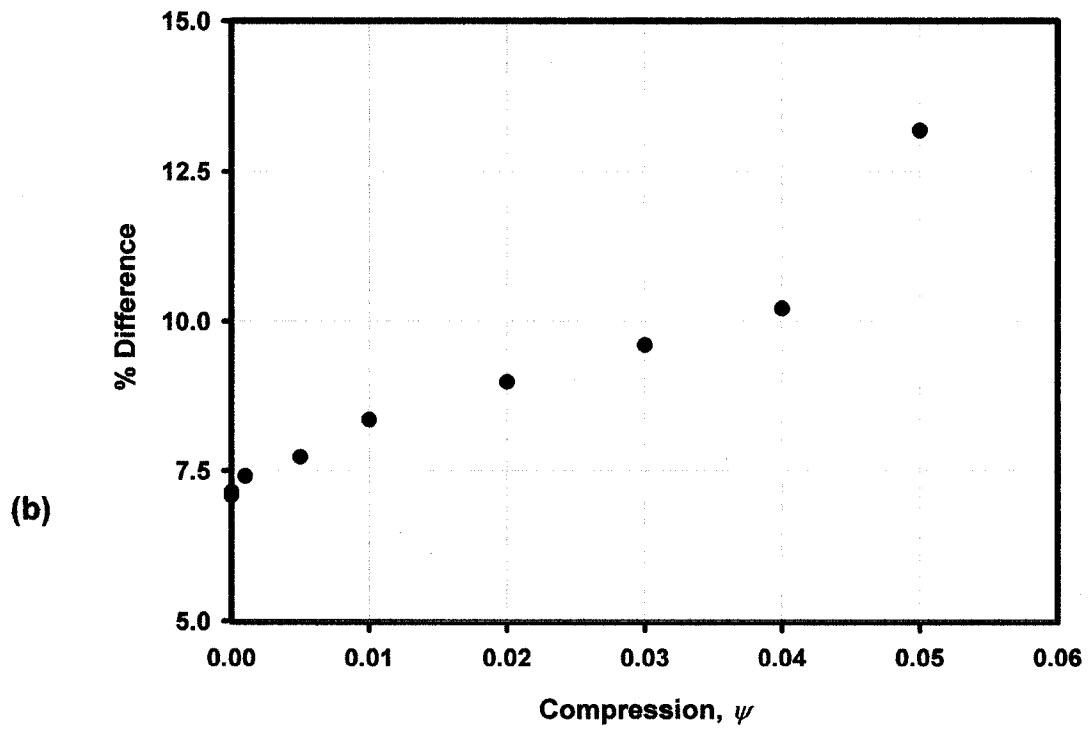
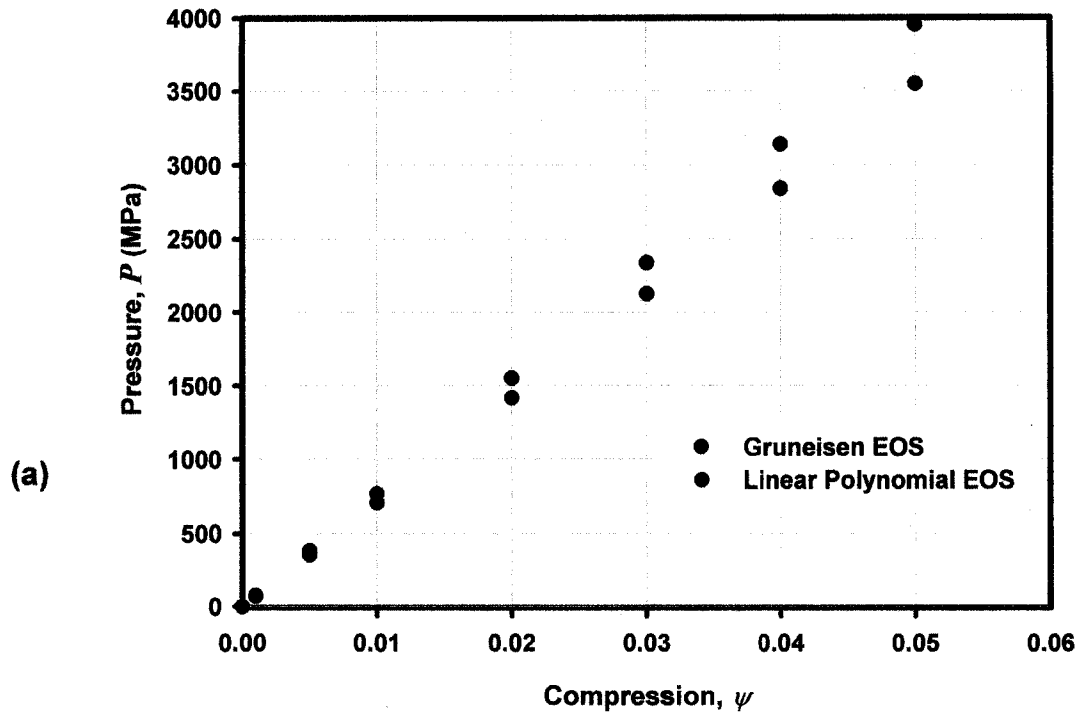


Figure D.1: (a) Pressure prediction by the Gruneisen EOS and Linear Polynomial EOS, (b) Pressure prediction difference between the Gruneisen EOS and Linear Polynomial EOS as percentage.

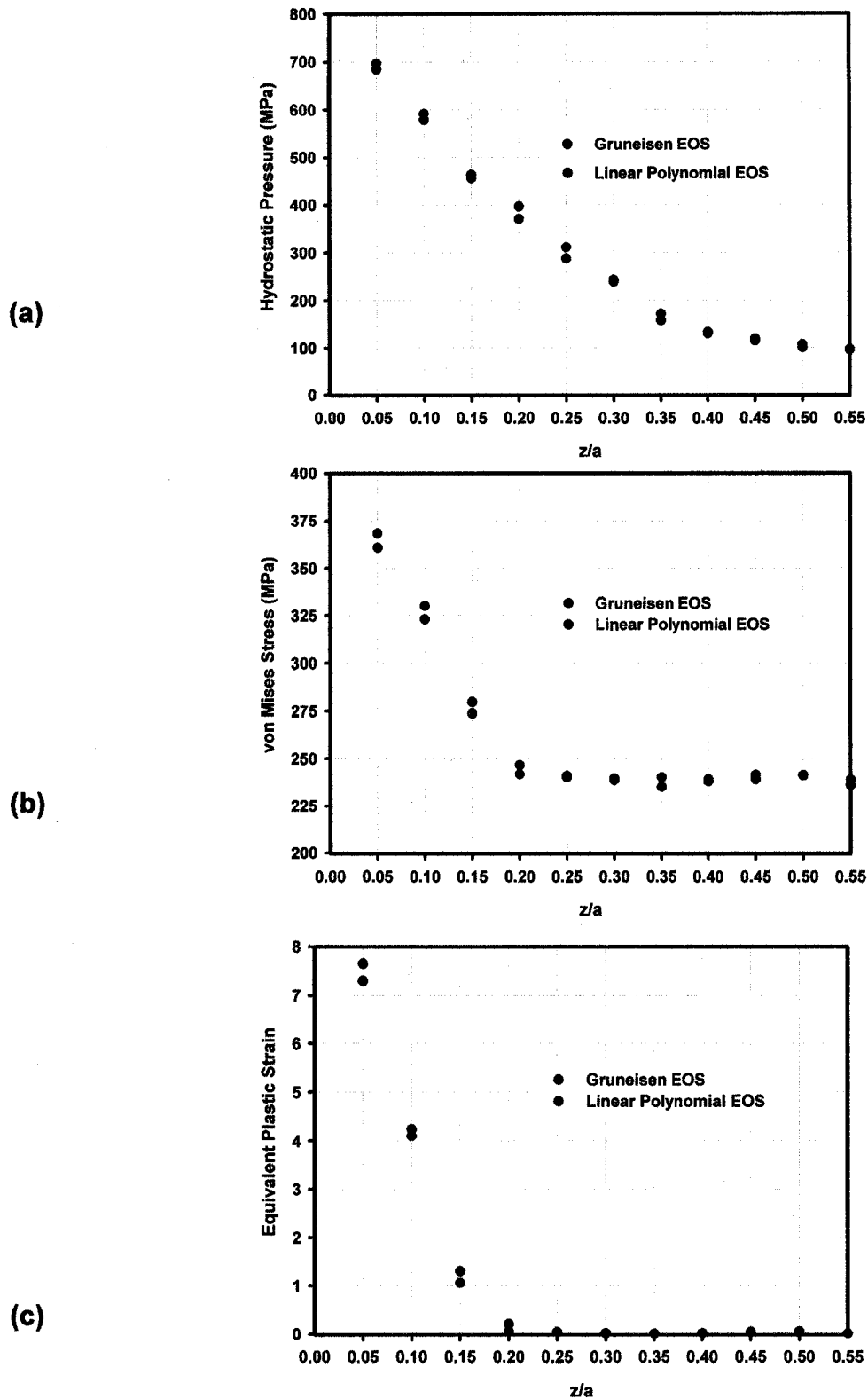


Figure D.2: Comparison of the predictions two simulations using two different EOS for the 356 Al material: (a) hydrostatic pressure, (b) von Mises stress and (c) equivalent plastic strain (Sliding velocity: 10 m/s, Normal load: 300 N/mm).

APPENDIX E

SAMPLE COUPLED THERMAL AND MECHANICAL SLIDING CONTACT ANALYSIS INPUT FILE

```

*KEYWORD
$-----1-----2-----3-----4-----5-----6-----7-----8
$
$ NOTE THE FOLLOWING SET OF UNITS: MM,KG,SEC,K
$ ALL OTHER UNITS ARE DERIVED FROM THIS BASE SET
$-----1-----2-----3-----4-----5-----6-----7-----8
$
$           (1) TITLE CARD.
$-----1-----2-----3-----4-----5-----6-----7-----8
*TITLE
7ASP.LAG.SLG,V:10M/S, FOR:150N/mm
$-----1-----2-----3-----4-----5-----6-----7-----8
$
$           (2) CONTROL CARDS.
$-----1-----2-----3-----4-----5-----6-----7-----8
*CONTROL TERMINATION
$  ENDTIM  ENDCYC  DTMIN  ENDNEG  ENDMAS
$    0.0084    0    .000    .000    .000
*CONTROL TIMESTEP
$  DTINIT  SCFT  ISDO  TSLIMIT  DTMS  LCTM  ERODE  MS1ST
$    .000    .800    0
*CONTROL SOLUTION
$  SOLN
$    2
*CONTROL THERMAL SOLVER
$  ATYPE  PTYPE  SOLVER  CGTOL  GPT  EQHEAT  FWORK  SBC
$    1    1    3  1.0E-04  8  1  0.95
*CONTROL THERMAL TIMESTEP
$  TS  TIP  ITS  TMIN  TMAX  DTEMP  TSCP
$    0  1.0  1.0E-04  0.0  0.0  0.0  0.5
*CONTROL ENERGY
$  HGEN  RWEN  SLNTEN  RYLEN
$    2    2    1    1
$-----1-----2-----3-----4-----5-----6-----7-----8
$
$           (3) DATABASE CONTROL CARDS - ASCII HISTORY FILE
$-----1-----2-----3-----4-----5-----6-----7-----8
*DATABASE HISTORY SHELL SET
$  ID1  ID2  ID3  ID4  ID5  ID6  ID7  ID8
$    8    9   10   11
$-----1-----2-----3-----4-----5-----6-----7-----8
$
$           (4) DATABASE CONTROL CARDS FOR ASCII FILE
$-----1-----2-----3-----4-----5-----6-----7-----8
$-----1-----2-----3-----4-----5-----6-----7-----8
*DATABASE RBDOUT
1.00E-05
*DATABASE SECFORC
1.00E-05
*DATABASE TPRINT
1.00E-05
*DATABASE ELOUT
1.00E-05
*DATABASE GLSTAT
1.00E-05
*DATABASE MATSUM
1.00E-05
*DATABASE RCFORC
1.00E-05
*DATABASE SLEOUT

```



```

1.00E-05
$-----1-----2-----3-----4-----5-----6-----7-----8
$              (5) DATABASE CONTROL CARDS FOR BINARY FILE
$-----1-----2-----3-----4-----5-----6-----7-----8
*DATABASE_BINARY_D3PLOT
$ DT/CYCL      LCDT      NOBEAM
1.00E-04
*DATABASE_BINARY_D3THDT
$ DT/CYCL      LCDT      NOBEAM
1.00E-04
$-----1-----2-----3-----4-----5-----6-----7-----8
*DATABASE_EXTENT_BINARY
      0          0          3          0          1          1          1          1
      0          0          0          0          0          0          0          0
$-----1-----2-----3-----4-----5-----6-----7-----8
$              (6) DEFINE PARTS CARDS
$-----1-----2-----3-----4-----5-----6-----7-----8
*PART
$HEADING
PART PID =          1 PART NAME :SOLID
$      PID      SID      MID      EOSID      HGID      GRAV      ADPOPT      TMID
      1          1          1          1          1          1          1          1
*PART
$HEADING
PART PID =          2 PART NAME :ASP
$      PID      SID      MID      EOSID      HGID      GRAV      ADPOPT      TMID
      2          2          2          2          2          2          2          2
*PART
$HEADING
PART PID =          3 PART NAME :ASP2
$      PID      SID      MID      EOSID      HGID      GRAV      ADPOPT      TMID
      3          2          2          2          2          2          2          3
*PART
$HEADING
PART PID =          4 PART NAME :ASP3
$      PID      SID      MID      EOSID      HGID      GRAV      ADPOPT      TMID
      4          2          2          2          2          2          2          4
*PART
$HEADING
PART PID =          5 PART NAME :ASP4
$      PID      SID      MID      EOSID      HGID      GRAV      ADPOPT      TMID
      5          2          2          2          2          2          2          5
*PART
$HEADING
PART PID =          6 PART NAME :ASP5
$      PID      SID      MID      EOSID      HGID      GRAV      ADPOPT      TMID
      6          2          2          2          2          2          2          6
*PART
$HEADING
PART PID =          7 PART NAME :ASP6
$      PID      SID      MID      EOSID      HGID      GRAV      ADPOPT      TMID
      7          2          2          2          2          2          2          7
*PART
$HEADING
PART PID =          8 PART NAME :ASP7
$      PID      SID      MID      EOSID      HGID      GRAV      ADPOPT      TMID
      8          2          2          2          2          2          2          8
$-----1-----2-----3-----4-----5-----6-----7-----8
$              (7) MATERIAL CARDS
$-----1-----2-----3-----4-----5-----6-----7-----8
*MAT_ELASTIC_VISCOPLASTIC_THERMAL
$MATERIAL NAME:A356
$      MID      RO          E          PR      SIGY      ALPHA      LCSS
      1 2.669E-06 7.24E+07      0.33 2.400E+05 23.5E-06      1
$      QR1      CR1      QR2      CR2      QX1      CX1      QX2      CX2
$      C          P          LCE      LCPR      LCSIGY      LCR      LCX      LCALPH

```

6500 4
\$ LCC LCP

10

\$-----1-----2-----3-----4-----5-----6-----7-----8

*DEFINE_CURVE

\$ STRESS/STRAIN DATA FROM FROM VOCE EQUATION

\$	LCID	SIDR	SFA	SFO	OFFA	OFFO	DATYYP
	1	0	1.0	1.0	0.0	0.0	

\$	STRAIN	STRESS
	0.0	2.40E+05
	1.0	2.7015E+05
	2.0	2.9461E+05
	3.0	3.1447E+05
	4.0	3.3059E+05
	5.0	3.4366E+05
	6.0	3.5429E+05
	7.0	3.6289E+05
	8.0	3.6988E+05
	9.0	3.7555E+05
	10.0	3.8016E+05
	11.0	3.8390E+05
	12.0	3.8693E+05
	13.0	3.8939E+05
	14.0	3.9139E+05
	15.0	3.9302E+05
	16.0	3.9433E+05
	17.0	3.9539E+05
	18.0	3.9627E+05
	19.0	3.9697E+05
	20.0	3.9754E+05
	21.0	3.9800E+05
	25.0	3.9838E+05
	30.0	3.9969E+05
	40.0	3.9996E+05

\$-----1-----2-----3-----4-----5-----6-----7-----8

*DEFINE_CURVE

\$ TEMP/STRESS SCALE

\$	LCID	SIDR	SFA	SFO	OFFA	OFFO	DATYYP
	10	0	1.0	1.0	0.0	0.0	

\$	TEMP (K)	STRESS SCALE
	300.0	1.0
	320.0	0.962121212
	330.0	0.943181818
	340.0	0.924242424
	350.0	0.905303030
	360.0	0.886363636
	370.0	0.867424242
	380.0	0.848484848
	390.0	0.829545455
	400.0	0.810606061
	410.0	0.791666667
	420.0	0.772727273
	430.0	0.753787879
	440.0	0.734848485
	450.0	0.715909091
	460.0	0.696969697
	470.0	0.678030303
	480.0	0.659090909
	490.0	0.640151515
	500.0	0.621212121
	550.0	0.526515152
	600.0	0.431818182
	650.0	0.337121212
	700.0	0.242424242
	750.0	0.147727273
	800.0	0.053030303

\$-----1-----2-----3-----4-----5-----6-----7-----8

```

*MAT_RIGID
$MATERIAL_NAME:RIGID ST
$      MID      RO      E      PR      N      COUPLE      M      ALIAS
      2 7.800E-06 2.070E+08 3.000E-01      0.0
$      CMO      CON1      CON2
      1.0      3      7
$ OPTIONAL BLANK CARD

```

```

$-----1-----2-----3-----4-----5-----6-----7-----8

```

```

*MAT_THERMAL_ISOTROPIC
$      TMID      TRO      TGRLC      TGMULT
      1      0.0      0.0      0.0
$      HC      TC
      9.63E+08 1.51E+05

```

```

$-----1-----2-----3-----4-----5-----6-----7-----8

```

```

*MAT_THERMAL_ISOTROPIC
$      TMID      TRO      TGRLC      TGMULT
      2      0.0      0.0      0.0
$      HC      TC
      9.63E+08 1.51E+05

```

```

$-----1-----2-----3-----4-----5-----6-----7-----8

```

```

*MAT_THERMAL_ISOTROPIC
$      TMID      TRO      TGRLC      TGMULT
      3      0.0      0.0      0.0
$      HC      TC
      9.63E+08 1.51E+05

```

```

$-----1-----2-----3-----4-----5-----6-----7-----8

```

```

*MAT_THERMAL_ISOTROPIC
$      TMID      TRO      TGRLC      TGMULT
      4      0.0      0.0      0.0
$      HC      TC
      9.63E+08 1.51E+05

```

```

$-----1-----2-----3-----4-----5-----6-----7-----8

```

```

*MAT_THERMAL_ISOTROPIC
$      TMID      TRO      TGRLC      TGMULT
      5      0.0      0.0      0.0
$      HC      TC
      9.63E+08 1.51E+05

```

```

$-----1-----2-----3-----4-----5-----6-----7-----8

```

```

*MAT_THERMAL_ISOTROPIC
$      TMID      TRO      TGRLC      TGMULT
      6      0.0      0.0      0.0
$      HC      TC
      9.63E+08 1.51E+05

```

```

$-----1-----2-----3-----4-----5-----6-----7-----8

```

```

*MAT_THERMAL_ISOTROPIC
$      TMID      TRO      TGRLC      TGMULT
      7      0.0      0.0      0.0
$      HC      TC
      9.63E+08 1.51E+05

```

```

$-----1-----2-----3-----4-----5-----6-----7-----8

```

```

*MAT_THERMAL_ISOTROPIC
$      TMID      TRO      TGRLC      TGMULT
      8      0.0      0.0      0.0
$      HC      TC
      9.63E+08 1.51E+05

```

```

$-----1-----2-----3-----4-----5-----6-----7-----8

```

```

$ (8) SECTION CARDS

```

```

$-----1-----2-----3-----4-----5-----6-----7-----8

```

```

*SECTION_SHELL
$PROPERTY_NAME:SHELL
$      SID      ELFORM      SHRF      NIP      PROPT      QR/IRID      ICOMP      SETYP
      1      13      1.0      4      0.0      0.0      0      1
$      T1      T2      T3      T4      NLOC
      1.0      1.0      1.0      1.0      0.0

```

```

*SECTION_SHELL
$PROPERTY_NAME:SHELL

```

```

$      SID      ELFORM      SHRF      NIP      PROPT      QR/IRID      ICOMP      SETYP
      2          13          1.0          4          0.0          0.0          0          1
$      T1         T2         T3         T4         NLOC
      1.0        1.0        1.0        1.0        0.0
$-----1-----2-----3-----4-----5-----6-----7-----8
$                                     (9) INITIAL DEFINITIONS
$-----1-----2-----3-----4-----5-----6-----7-----8
*INITIAL_TEMPERATURE_SET
      0          300.0
$-----1-----2-----3-----4-----5-----6-----7-----8
*CONTACT_2D_AUTOMATIC_NODE_TO_SURFACE_THERMAL
$      PSIDS      PSIDM      SFACT      FREQ      FS          FD          DC          MEMBS
      1          2          5.0          50         0.0          0.0          0.0          6
$      TBIRTH     TDEATH     SOS         SOM         NDS          NDM          IPF/COF      INIT
      0.0        1.000E+20  1.0          1.0          0            0            1            0
$      CF         FRAD       HTC         GCRIT       GMAX        CD_FACT
$-----1-----2-----3-----4-----5-----6-----7-----8
*SET_PART_LIST
$      PSID
      1
$      PID1
      1
*SET_PART_LIST
$      PSID
      2
$      PID1      PSID      PSID      PSID      PSID      PSID      PSID      PSID
      2          3          4          5          6          7          8
$-----1-----2-----3-----4-----5-----6-----7-----8
$                                     (10) NODAL POINT CARDS
$-----1-----2-----3-----4-----5-----6-----7-----8
*NODE
$      NODE      X          Y          Z          TC          RC
      1 -.585756800E+00 .889999900E+01 .580000200E+01
      2 -.618965100E+00 .890000000E+01 .580000200E+01
      3 -.618969400E+00 .887499700E+01 .580000300E+01
      ...
      ... (cont'd)
      22400 .744450600E+00 .952998400E+01 .580000200E+01
      22401 .744450500E+00 .949665100E+01 .580000200E+01
      22402 .744450600E+00 .946331800E+01 .580000300E+01
$-----1-----2-----3-----4-----5-----6-----7-----8
$                                     (11) SHELL ELEMENT CARDS
$-----1-----2-----3-----4-----5-----6-----7-----8
*ELEMENT_SHELL
$      EID      PID      N1      N2      N3      N4
      1          1          1          2          3          4
      2          1          4          3          5          6
      3          1          6          5          7          8
      ...
      ... (cont'd)
      21533      8      22141      22167      22169      22160
      21534      8      22169      22183      22180      22160
      21535      8      22183      22182      22189      22180
$-----1-----2-----3-----4-----5-----6-----7-----8
$                                     (12) BOUNDARY CONDITION CARDS
$-----1-----2-----3-----4-----5-----6-----7-----8
*BOUNDARY_SPC_NODE
$      NID/NSID      CID      DOFX      DOFY      DOFZ      DOFRX      DOFRY      DOFRZ
      9791          0          1          1          1          1          1          1
      9792          0          1          1          1          1          1          1
      9845          0          1          1          1          1          1          1
      ...
      ... (cont'd)
      10969          0          1          1          1          1          1          1
      11022          0          1          1          1          1          1          1
      11076          0          1          1          1          1          1          1
$-----1-----2-----3-----4-----5-----6-----7-----8

```

```

$ (13) DEFINE SET CARDS
$-----1-----2-----3-----4-----5-----6-----7-----8
*SET_NODE_LIST
$   SID      DA1      DA2      DA3      DA4
1
$   NID1     NID2     NID3     NID4     NID5     NID6     NID7     NID8
   11656    11657    11658    11659    11660    11661    11662    11663
   11670    11671    11672    11673    11674    11675    11676    11705
   11720    11735    11750    11765    11780    11795    11810    11825
   11840    11855    11870    11885    12466    12467    12468    12469
   12470    12471    12472    12473    12480    12481    12482    12483
   12484    12486    12501    12516    12531    12546    12561    12576
   12591    12606    12621    12636    12651    12666    12681
$-----1-----2-----3-----4-----5-----6-----7-----8
$ (14) LOADING CONDITIONS
$-----1-----2-----3-----4-----5-----6-----7-----8
*LOAD_NODE_SET
$   NSID     DOF     LCID     SF     CID     M1     M2     M3
   1         2       100     1
*DEFINE_CURVE
$   LCID     SIDR     SFA     SFO     OFFA     OFFO     DATTYP
   100       0        1.0    -1.0    0.0     0.0     0
$           A1 (TIME)           O1 (FORCE)
           0.00                0.0
           0.0002            0.272725E+04
           0.0011            0.272725E+04
           0.0012                0.0
           0.0084                0.0
$-----1-----2-----3-----4-----5-----6-----7-----8
*SET_NODE_LIST
$   SID      DA1      DA2      DA3      DA4
2
$   NID1     NID2     NID3     NID4     NID5     NID6     NID7     NID8
   13274    13275    13276    13277    13278    13279    13280    13281
   13288    13289    13290    13291    13292    13293    13294    13323
   13338    13353    13368    13383    13398    13413    13428    13443
   13458    13473    13488    13503    14084    14085    14086    14087
   14088    14089    14090    14091    14098    14099    14100    14101
   14102    14104    14119    14134    14149    14164    14179    14194
   14209    14224    14239    14254    14269    14284    14299
$-----1-----2-----3-----4-----5-----6-----7-----8
$ (14) LOADING CONDITIONS
$-----1-----2-----3-----4-----5-----6-----7-----8
*LOAD_NODE_SET
$   NSID     DOF     LCID     SF     CID     M1     M2     M3
   2         2       200     1
*DEFINE_CURVE
$   LCID     SIDR     SFA     SFO     OFFA     OFFO     DATTYP
   200       0        1.0    -1.0    0.0     0.0     0
$           A1 (TIME)           O1 (FORCE)
           0.00                0.0
           0.0012            0.0
           0.0014            0.272725E+04
           0.0023            0.272725E+04
           0.0024                0.0
           0.0084                0.0
$-----1-----2-----3-----4-----5-----6-----7-----8
*SET_NODE_LIST
$   SID      DA1      DA2      DA3      DA4
3
$   NID1     NID2     NID3     NID4     NID5     NID6     NID7     NID8
   14892    14893    14894    14895    14896    14897    14898    14899
   14906    14907    14908    14909    14910    14911    14912    14941
   14956    14971    14986    15001    15016    15031    15046    15061
   15076    15091    15106    15121    15702    15703    15704    15705
   15706    15707    15708    15709    15716    15717    15718    15719
   15720    15722    15737    15752    15767    15782    15797    15812

```

```

15827 15842 15857 15872 15887 15902 15917
$-----1-----2-----3-----4-----5-----6-----7-----8
$
(14) LOADING CONDITIONS
$-----1-----2-----3-----4-----5-----6-----7-----8
*LOAD_NODE_SET
$ NSID DOF LCID SF CID M1 M2 M3
3 2 300 1
*DEFINE_CURVE
$ LCID SIDR SFA SFO OFFA OFFO DATTYP
300 0 1.0 -1.0 0.0 0.0 0
$ A1 (TIME) O1 (FORCE)
0.00 0.0
0.0012 0.0
0.0024 0.0
0.0026 0.272725E+04
0.0035 0.272725E+04
0.0036 0.0
0.0084 0.0
$-----1-----2-----3-----4-----5-----6-----7-----8
*SET_NODE_LIST
$ SID DA1 DA2 DA3 DA4
4
$ NID1 NID2 NID3 NID4 NID5 NID6 NID7 NID8
16510 16511 16512 16513 16514 16515 16516 16517
16524 16525 16526 16527 16528 16529 16530 16559
16574 16589 16604 16619 16634 16649 16664 16679
16694 16709 16724 16739 17320 17321 17322 17323
17324 17325 17326 17327 17334 17335 17336 17337
17338 17340 17355 17370 17385 17400 17415 17430
17445 17460 17475 17490 17505 17520 17535
$-----1-----2-----3-----4-----5-----6-----7-----8
(14) LOADING CONDITIONS
$-----1-----2-----3-----4-----5-----6-----7-----8
*LOAD_NODE_SET
$ NSID DOF LCID SF CID M1 M2 M3
4 2 400 1
*DEFINE_CURVE
$ LCID SIDR SFA SFO OFFA OFFO DATTYP
400 0 1.0 -1.0 0.0 0.0 0
$ A1 (TIME) O1 (FORCE)
0.00 0.0
0.0012 0.0
0.0024 0.0
0.0036 0.0
0.0038 0.272725E+04
0.0047 0.272725E+04
0.0048 0.0
0.0084 0.0
$-----1-----2-----3-----4-----5-----6-----7-----8
*SET_NODE_LIST
$ SID DA1 DA2 DA3 DA4
5
$ NID1 NID2 NID3 NID4 NID5 NID6 NID7 NID8
18128 18129 18130 18131 18132 18133 18134 18135
18142 18143 18144 18145 18146 18147 18148 18177
18192 18207 18222 18237 18252 18267 18282 18297
18312 18327 18342 18357 18938 18939 18940 18941
18942 18943 18944 18945 18952 18953 18954 18955
18956 18958 18973 18988 19003 19018 19033 19048
19063 19078 19093 19108 19123 19138 19153
$-----1-----2-----3-----4-----5-----6-----7-----8
(14) LOADING CONDITIONS
$-----1-----2-----3-----4-----5-----6-----7-----8
*LOAD_NODE_SET
$ NSID DOF LCID SF CID M1 M2 M3
5 2 500 1
*DEFINE_CURVE

```

```

$   LCID      SIDR      SFA      SFO      OFFA      OFFO      DATYYP
$     500         0         1.0      -1.0         0.0         0.0         0
$           A1 (TIME)           O1 (FORCE)
$           0.00           0.0
$           0.0012         0.0
$           0.0024         0.0
$           0.0036         0.0
$           0.0048         0.0
$           0.0050         0.272725E+04
$           0.0059         0.272725E+04
$           0.0060         0.0
$           0.0084         0.0
$-----1-----2-----3-----4-----5-----6-----7-----8
*SET_NODE_LIST
$   SID      DA1      DA2      DA3      DA4
$     6
$   NID1     NID2     NID3     NID4     NID5     NID6     NID7     NID8
$  19746    19747    19748    19749    19750    19751    19752    19753
$  19760    19761    19762    19763    19764    19765    19766    19795
$  19810    19825    19840    19855    19870    19885    19900    19915
$  19930    19945    19960    19975    20556    20557    20558    20559
$  20560    20561    20562    20563    20570    20571    20572    20573
$  20574    20576    20591    20606    20621    20636    20651    20666
$  20681    20696    20711    20726    20741    20756    20771
$-----1-----2-----3-----4-----5-----6-----7-----8
$
$ (14) LOADING CONDITIONS
$-----1-----2-----3-----4-----5-----6-----7-----8
*LOAD_NODE_SET
$   NSID     DOF     LCID     SF     CID     M1     M2     M3
$     6         2         600         1
*DEFINE_CURVE
$   LCID      SIDR      SFA      SFO      OFFA      OFFO      DATYYP
$     600         0         1.0      -1.0         0.0         0.0         0
$           A1 (TIME)           O1 (FORCE)
$           0.00           0.0
$           0.0012         0.0
$           0.0024         0.0
$           0.0036         0.0
$           0.0048         0.0
$           0.0060         0.0
$           0.0062         0.272725E+04
$           0.0071         0.272725E+04
$           0.0072         0.0
$           0.0084         0.0
$-----1-----2-----3-----4-----5-----6-----7-----8
*SET_NODE_LIST
$   SID      DA1      DA2      DA3      DA4
$     7
$   NID1     NID2     NID3     NID4     NID5     NID6     NID7     NID8
$  21364    21365    21366    21367    21368    21369    21370    21371
$  21378    21379    21380    21381    21382    21383    21384    21413
$  21428    21443    21458    21473    21488    21503    21518    21533
$  21548    21563    21578    21593    22174    22175    22176    22177
$  22178    22179    22180    22181    22188    22189    22190    22191
$  22192    22194    22209    22224    22239    22254    22269    22284
$  22299    22314    22329    22344    22359    22374    22389
$-----1-----2-----3-----4-----5-----6-----7-----8
$
$ (14) LOADING CONDITIONS
$-----1-----2-----3-----4-----5-----6-----7-----8
*LOAD_NODE_SET
$   NSID     DOF     LCID     SF     CID     M1     M2     M3
$     7         2         700         1
*DEFINE_CURVE
$   LCID      SIDR      SFA      SFO      OFFA      OFFO      DATYYP
$     700         0         1.0      -1.0         0.0         0.0         0
$           A1 (TIME)           O1 (FORCE)
$           0.00           0.0

```

```

0.0012      0.0
0.0024      0.0
0.0036      0.0
0.0048      0.0
0.0060      0.0
0.0072      0.0
0.0074      0.272725E+04
0.0083      0.272725E+04
0.0084      0.0
$-----1-----2-----3-----4-----5-----6-----7-----8
*BOUNDARY_PRESCRIBED_MOTION_RIGID
$  PARTID      DOF      VAD      LCID      SF      VID      DEATH      BIRTH
   2          1          0          20        1.0        0        1.E+28        0.0
*DEFINE_CURVE
$  LCID      SIDR      SFA      SFO      OFFA      OFFO      DATYTP
   20          0          1.0        1.0        0.0        0.0        0
$          A1 (TIME)      O1 (VELOCITY)
   0          0.0
   0.0002      0.0
   0.0003      10.0E+03
   0.0011      10.0E+03
   0.0012      10.0E+03
   0.0084      10.0E+03
$-----1-----2-----3-----4-----5-----6-----7-----8
*BOUNDARY_PRESCRIBED_MOTION_RIGID
$  PARTID      DOF      VAD      LCID      SF      VID      DEATH      BIRTH
   3          1          0          21        1.0        0        1.E+28        0.0
*DEFINE_CURVE
$  LCID      SIDR      SFA      SFO      OFFA      OFFO      DATYTP
   21          0          1.0        1.0        0.0        0.0        0
$          A1 (TIME)      O1 (VELOCITY)
   0          0.0
   0.0014      0.0
   0.0015      10.0E+03
   0.0023      10.0E+03
   0.0024      10.0E+03
   0.0084      10.0E+03
$-----1-----2-----3-----4-----5-----6-----7-----8
*BOUNDARY_PRESCRIBED_MOTION_RIGID
$  PARTID      DOF      VAD      LCID      SF      VID      DEATH      BIRTH
   4          1          0          22        1.0        0        1.E+28        0.0
*DEFINE_CURVE
$  LCID      SIDR      SFA      SFO      OFFA      OFFO      DATYTP
   22          0          1.0        1.0        0.0        0.0        0
$          A1 (TIME)      O1 (VELOCITY)
   0          0.0
   0.0026      0.0
   0.0027      10.0E+03
   0.0035      10.0E+03
   0.0036      10.0E+03
   0.0084      10.0E+03
$-----1-----2-----3-----4-----5-----6-----7-----8
*BOUNDARY_PRESCRIBED_MOTION_RIGID
$  PARTID      DOF      VAD      LCID      SF      VID      DEATH      BIRTH
   5          1          0          23        1.0        0        1.E+28        0.0
*DEFINE_CURVE
$  LCID      SIDR      SFA      SFO      OFFA      OFFO      DATYTP
   23          0          1.0        1.0        0.0        0.0        0
$          A1 (TIME)      O1 (VELOCITY)
   0          0.0
   0.0038      0.0
   0.0039      10.0E+03
   0.0047      10.0E+03
   0.0048      10.0E+03
   0.0084      10.0E+03
$-----1-----2-----3-----4-----5-----6-----7-----8
*BOUNDARY_PRESCRIBED_MOTION_RIGID

```



```

$ PARTID      DOF      VAD      LCID      SF      VID      DEATH      BIRTH
   6          1          0          24       1.0      0       1.E+28      0.0
*DEFINE_CURVE
$ LCID        SIDR      SFA      SFO      OFFA      OFFO      DATTYP
   24         0         1.0      1.0      0.0      0.0      0
$           A1 (TIME)      O1 (VELOCITY)
           0              0.0
           0.0050          0.0
           0.0051          10.0E+03
           0.0059          10.0E+03
           0.0060          10.0E+03
           0.0084          10.0E+03
$-----1-----2-----3-----4-----5-----6-----7-----8
*BOUNDARY_PRESCRIBED_MOTION_RIGID
$ PARTID      DOF      VAD      LCID      SF      VID      DEATH      BIRTH
   7          1          0          25       1.0      0       1.E+28      0.0
*DEFINE_CURVE
$ LCID        SIDR      SFA      SFO      OFFA      OFFO      DATTYP
   25         0         1.0      1.0      0.0      0.0      0
$           A1 (TIME)      O1 (VELOCITY)
           0              0.0
           0.0062          0.0
           0.0063          10.0E+03
           0.0071          10.0E+03
           0.0072          10.0E+03
           0.0084          10.0E+03
$-----1-----2-----3-----4-----5-----6-----7-----8
*BOUNDARY_PRESCRIBED_MOTION_RIGID
$ PARTID      DOF      VAD      LCID      SF      VID      DEATH      BIRTH
   8          1          0          26       1.0      0       1.E+28      0.0
*DEFINE_CURVE
$ LCID        SIDR      SFA      SFO      OFFA      OFFO      DATTYP
   26         0         1.0      1.0      0.0      0.0      0
$           A1 (TIME)      O1 (VELOCITY)
           0              0.0
           0.0074          0.0
           0.0075          10.0E+03
           0.0083          10.0E+03
           0.0084          10.0E+03
$-----1-----2-----3-----4-----5-----6-----7-----8
*SET_SHELL_LIST
$ SID        NUM      DA1      DA2      DA3      DA4
   9         39
$ EIDS      EID2      EID3      EID4      EID5      EID5      EID7      EID8
  1181     1182     1183     1184     1185     1186     1187     1188
  1189     1190     1191     1192     1193     1194     1195     1196
  1197     1198     1199     1359     1360     1361     1362     1363
  1364     1365     1366     1397     9515     9516     9517     9518
  9560     9569     9561     9562     9571     9564     9565
$-----1-----2-----3-----4-----5-----6-----7-----8
*SET_SHELL_LIST
$ SID        NUM      DA1      DA2      DA3      DA4
   8         39
$ EIDS      EID2      EID3      EID4      EID5      EID5      EID7      EID8
  10135    10134    10141    10131    10132    10138    10122    10099
  10100    10101    10102    10127    5144     5145     5146     5147
   5148     5149     5150     5143     5053     5054     5055     5056
   5057     5058     5059     5060     5061     5062     5063     5064
   5065     5066     5067     5068     5069     5070     5151
$-----1-----2-----3-----4-----5-----6-----7-----8
*SET_SHELL_LIST
$ SID        NUM      DA1      DA2      DA3      DA4
  10         38
$ EIDS      EID2      EID3      EID4      EID5      EID5      EID7      EID8
  9849     9850     9856     9846     9847     9854     2748     2749
  2750     2751     2752     9800     9801     9802     9803     9845
  2745     2746     2747     2481     2482     2483     2484     2485

```

	2486	2487	2488	2489	2490	2491	2492	2493
	2494	2495	2496	2497	2498	2813		
\$	1	2	3	4	5	6	7	8
*SET_SHELL_LIST								
\$	SID	NUM	DA1	DA2	DA3	DA4		
	11	38						
\$	EIDS	EID2	EID3	EID4	EID5	EID5	EID7	EID8
	10420	10419	10426	10416	10417	10424	6509	6510
	6511	6512	10370	10371	10372	10373	10415	6505
	6506	6507	6508	6241	6242	6243	6244	6245
	6246	6247	6248	6249	6250	6251	6252	6253
	6254	6255	6256	6257	6258	6573		
\$	1	2	3	4	5	6	7	8
*END								

APPENDIX F

SAMPLE INPUT FILE FOR MODELING THE INFULENCE OF SECONDARY HARD PARTICLES

```

*KEYWORD
$-----1-----2-----3-----4-----5-----6-----7-----8
$
$ NOTE THE FOLLOWING SET OF UNITS: MM,KG,SEC,K
$ ALL OTHER UNITS ARE DERIVED FROM THIS BASE SET
$-----1-----2-----3-----4-----5-----6-----7-----8
$
$           (1) TITLE CARD.
$-----1-----2-----3-----4-----5-----6-----7-----8
*TITLE
7ASP.LAG.SLG,V:10M/S,FOR:250N/mm
$-----1-----2-----3-----4-----5-----6-----7-----8
$
$           (2) CONTROL CARDS.
$-----1-----2-----3-----4-----5-----6-----7-----8
*CONTROL_TERMINATION
$  ENDTIM      ENDCYC      DTMIN      ENDNEG      ENDMAS
$    0.0084      0          .000        .000        .000
*CONTROL_TIMESTEP
$  DTINIT      SCFT        ISDO      TSLIMIT      DTMS      LCTM      ERODE      MS1ST
$    .000      .500          0
*CONTROL_SOLUTION
$  SOLN
$    2
*CONTROL_THERMAL_SOLVER
$  ATYPE      PTYPE      SOLVER      CGTOL      GPT      EQHEAT      FWORK      SBC
$    1          1          3      1.0E-04      8          1          0.95
*CONTROL_THERMAL_TIMESTEP
$  TS         TIP         ITS         TMIN      TMAX      DTEMP      TSCP
$    0         1.0       1.0E-04    0.0       0.0       0.0       0.5
*CONTROL_ENERGY
$  HGEN      RWEN      SLNTEN      RYLEN
$    2         2          1          1
$-----1-----2-----3-----4-----5-----6-----7-----8
$
$           (3) DATABASE CONTROL CARDS - ASCII HISTORY FILE
$-----1-----2-----3-----4-----5-----6-----7-----8
*DATABASE_HISTORY_SHELL_SET
$  ID1      ID2      ID3      ID4      ID5      ID6      ID7      ID8
$    8         9       10       11       12
$-----1-----2-----3-----4-----5-----6-----7-----8
$
$           (4) DATABASE CONTROL CARDS FOR ASCII FILE
$-----1-----2-----3-----4-----5-----6-----7-----8
*DATABASE_RBDOUT
1.00E-05
*DATABASE_SECFORC
1.00E-05
*DATABASE_TPRINT
1.00E-05
*DATABASE_ELOUT
1.00E-05
*DATABASE_GLSTAT
1.00E-05
*DATABASE_MATSUM
1.00E-05
*DATABASE_RCFORC
1.00E-05
*DATABASE_SLEOUT
1.00E-05

```

```

$-----1-----2-----3-----4-----5-----6-----7-----8
$              (5) DATABASE CONTROL CARDS FOR BINARY FILE
$-----1-----2-----3-----4-----5-----6-----7-----8
*DATABASE_BINARY_D3PLOT
$ DT/CYCL      LCDT      NOBEAM
  0.50E-04
*DATABASE_BINARY_D3THDT
$ DT/CYCL      LCDT      NOBEAM
  0.50E-04
$-----1-----2-----3-----4-----5-----6-----7-----8
*DATABASE_EXTENT_BINARY
      0          0          3          0          1          1          1          1
      0          0          0          0          0          0          0          0
$-----1-----2-----3-----4-----5-----6-----7-----8
$              (6) DEFINE PARTS CARDS
$-----1-----2-----3-----4-----5-----6-----7-----8
*PART
$HEADING
PART PID =          1 PART NAME :SOLID
$   PID      SID      MID      EOSID      HGID      GRAV      ADOPT      TMID
      1          1          1
*PART
$HEADING
PART PID =          2 PART NAME :ASP
$   PID      SID      MID      EOSID      HGID      GRAV      ADOPT      TMID
      2          2          2
*PART
$HEADING
PART PID =          3 PART NAME :ASP2
$   PID      SID      MID      EOSID      HGID      GRAV      ADOPT      TMID
      3          2          2
*PART
$HEADING
PART PID =          4 PART NAME :ASP3
$   PID      SID      MID      EOSID      HGID      GRAV      ADOPT      TMID
      4          2          2
*PART
$HEADING
PART PID =          5 PART NAME :ASP4
$   PID      SID      MID      EOSID      HGID      GRAV      ADOPT      TMID
      5          2          2
*PART
$HEADING
PART PID =          6 PART NAME :ASP5
$   PID      SID      MID      EOSID      HGID      GRAV      ADOPT      TMID
      6          2          2
*PART
$HEADING
PART PID =          7 PART NAME :ASP6
$   PID      SID      MID      EOSID      HGID      GRAV      ADOPT      TMID
      7          2          2
*PART
$HEADING
PART PID =          8 PART NAME :ASP7
$   PID      SID      MID      EOSID      HGID      GRAV      ADOPT      TMID
      8          2          2
*PART
$HEADING
PART PID =          9 PART NAME :HARDPAR
$   PID      SID      MID      EOSID      HGID      GRAV      ADOPT      TMID
      9          2          3
$-----1-----2-----3-----4-----5-----6-----7-----8
$              (7) MATERIAL CARDS
$-----1-----2-----3-----4-----5-----6-----7-----8
*MAT_ELASTIC_VISCOPLASTIC_THERMAL
$MATERIAL NAME:A356
$   MID      RO      E      PR      SIGY      ALPHA      LCSS

```

```

      1 2.669E-06 7.24E+07 0.33 2.400E+05 23.5E-06 1
$   QR1      CR1      QR2      CR2      QX1      CX1      QX2      CX2
$   C        P        LCE      LCPR      LCSIGY      LCR      LCX      LCALPH
      6500      4
$   LCC      LCP

```

```

$-----1-----2-----3-----4-----5-----6-----7-----8

```

```

*DEFINE_CURVE

```

```

$ STRESS/STRAIN DATA FROM FROM VOCE EQUATION

```

```

$   LCID      SIDR      SFA      SFO      OFFA      OFFO      DAT TYP
      1          0          1.0      1.0      0.0      0.0

```

```

$   STRAIN      STRESS
      0.0          2.40E+05
      1.0          2.7015E+05
      2.0          2.9461E+05
      3.0          3.1447E+05
      4.0          3.3059E+05
      5.0          3.4366E+05
      6.0          3.5429E+05
      7.0          3.6289E+05
      8.0          3.6988E+05
      9.0          3.7555E+05
     10.0          3.8016E+05
     11.0          3.8390E+05
     12.0          3.8693E+05
     13.0          3.8939E+05
     14.0          3.9139E+05
     15.0          3.9302E+05
     16.0          3.9433E+05
     17.0          3.9539E+05
     18.0          3.9627E+05
     19.0          3.9697E+05
     20.0          3.9754E+05
     21.0          3.9800E+05
     25.0          3.9838E+05
     30.0          3.9969E+05
     40.0          3.9996E+05

```

```

$-----1-----2-----3-----4-----5-----6-----7-----8

```

```

*DEFINE_CURVE

```

```

$ TEMP/STRESS SCALE

```

```

$   LCID      SIDR      SFA      SFO      OFFA      OFFO      DAT TYP
      10          0          1.0      1.0      0.0      0.0

```

```

$   TEMP (K)      STRESS SCALE
      300.0          1.0
      320.0          0.962121212
      330.0          0.943181818
      340.0          0.924242424
      350.0          0.905303030
      360.0          0.886363636
      370.0          0.867424242
      380.0          0.848484848
      390.0          0.829545455
      400.0          0.810606061
      410.0          0.791666667
      420.0          0.772727273
      430.0          0.753787879
      440.0          0.734848485
      450.0          0.715909091
      460.0          0.696969697
      470.0          0.678030303
      480.0          0.659090909
      490.0          0.640151515
      500.0          0.621212121
      550.0          0.526515152
      600.0          0.431818182
      650.0          0.337121212

```

```

700.0      0.24242424
750.0      0.147727273
800.0      0.053030303
$-----1-----2-----3-----4-----5-----6-----7-----8
*MAT_RIGID
$MATERIAL NAME:RIGID ST
$      MID      RO      E      PR      N      COUPLE      M      ALIAS
      2 7.800E-06 2.070E+08 3.000E-01      0.0
$      CMO      CON1      CON2
      1.0      3      7
$ OPTIONAL BLANK CARD

$-----1-----2-----3-----4-----5-----6-----7-----8
*MAT_ELASTIC
$MATERIAL NAME:HARD Si
$      MID      RO      E      PR      DA      DB
      3 2.330E-06 1.127E+08 2.800E-01 0.000E+00 0.000E+00
$-----1-----2-----3-----4-----5-----6-----7-----8
*MAT_THERMAL_ISOTROPIC
$      TMID      TRO      TGRLC      TGMULT
      1      0.0      0.0      0.0
$      HC      TC
      9.63E+08 1.51E+05
$-----1-----2-----3-----4-----5-----6-----7-----8
*MAT_THERMAL_ISOTROPIC
$      TMID      TRO      TGRLC      TGMULT
      2      0.0      0.0      0.0
$      HC      TC
      9.63E+08 1.51E+05
$-----1-----2-----3-----4-----5-----6-----7-----8
*MAT_THERMAL_ISOTROPIC
$      TMID      TRO      TGRLC      TGMULT
      3      0.0      0.0      0.0
$      HC      TC
      9.63E+08 1.51E+05
$-----1-----2-----3-----4-----5-----6-----7-----8
*MAT_THERMAL_ISOTROPIC
$      TMID      TRO      TGRLC      TGMULT
      4      0.0      0.0      0.0
$      HC      TC
      9.63E+08 1.51E+05
$-----1-----2-----3-----4-----5-----6-----7-----8
*MAT_THERMAL_ISOTROPIC
$      TMID      TRO      TGRLC      TGMULT
      5      0.0      0.0      0.0
$      HC      TC
      9.63E+08 1.51E+05
$-----1-----2-----3-----4-----5-----6-----7-----8
*MAT_THERMAL_ISOTROPIC
$      TMID      TRO      TGRLC      TGMULT
      6      0.0      0.0      0.0
$      HC      TC
      9.63E+08 1.51E+05
$-----1-----2-----3-----4-----5-----6-----7-----8
*MAT_THERMAL_ISOTROPIC
$      TMID      TRO      TGRLC      TGMULT
      7      0.0      0.0      0.0
$      HC      TC
      9.63E+08 1.51E+05
$-----1-----2-----3-----4-----5-----6-----7-----8
*MAT_THERMAL_ISOTROPIC
$      TMID      TRO      TGRLC      TGMULT
      8      0.0      0.0      0.0
$      HC      TC
      9.63E+08 1.51E+05
$-----1-----2-----3-----4-----5-----6-----7-----8
*MAT_THERMAL_ISOTROPIC

```

```

$      TMID      TRO      TGRIC  TGMULT
      9          0.0      0.0      0.0
$      HC         TC
      6.78E+08 0.837E+05
$-----1-----2-----3-----4-----5-----6-----7-----8
$
      (8) SECTION CARDS
$-----1-----2-----3-----4-----5-----6-----7-----8
*SECTION SHELL
$PROPERTY NAME:SHELL
$      SID      ELFORM      SHRF      NIP      PROPT      QR/IRID      ICOMP      SETYP
      1          13          1.0      4          0.0      0.0          0          1
$      T1        T2          T3          T4          NLOC
      1.0        1.0          1.0        1.0        0.0
*SECTION SHELL
$PROPERTY NAME:SHELL
$      SID      ELFORM      SHRF      NIP      PROPT      QR/IRID      ICOMP      SETYP
      2          13          1.0      4          0.0      0.0          0          1
$      T1        T2          T3          T4          NLOC
      1.0        1.0          1.0        1.0        0.0
$-----1-----2-----3-----4-----5-----6-----7-----8
$
      (9) INITIAL DEFINITIONS
$-----1-----2-----3-----4-----5-----6-----7-----8
*INITIAL_TEMPERATURE_SET
      0          300.0
$-----1-----2-----3-----4-----5-----6-----7-----8
*CONTACT_2D_AUTOMATIC_NODE_TO_SURFACE_THERMAL
$      PSIDS      PSIDM      SFACT      FREQ      FS          FD          DC          MEMBS
      1          2          5.0      50          0.0      0.0          0.0          6
$      TBIRTH      TDEATH      SOS          SOM          NDS          NDM          IPF/COF      INIT
      0.0 1.000E+20 1.0          1.0          0          0          1          0
$      CF          FRAD          HTC          GCRIT      GMAX      CD_FACT
*SET_PART_LIST
$      PSID
      1
$      PID1
      1
*SET_PART_LIST
$      PSID
      2
$      PID1      PSID      PSID      PSID      PSID      PSID      PSID      PSID
      2          3          4          5          6          7          8
$-----1-----2-----3-----4-----5-----6-----7-----8
$
      (10) NODAL POINT CARDS
$-----1-----2-----3-----4-----5-----6-----7-----8
*NODE
$      NODE      X          Y          Z          TC          RC
      1  -.585756800E+00 .889999900E+01 .580000200E+01
      2  -.618965100E+00 .890000000E+01 .580000200E+01
      3  -.618969400E+00 .887499700E+01 .580000300E+01
      ...
      ... (cont'd)
      22400 .744450600E+00 .952998400E+01 .580000200E+01
      22401 .744450500E+00 .949665100E+01 .580000200E+01
      22402 .744450600E+00 .946331800E+01 .580000300E+01
$-----1-----2-----3-----4-----5-----6-----7-----8
$
      (11) SHELL ELEMENT CARDS
$-----1-----2-----3-----4-----5-----6-----7-----8
*ELEMENT_SHELL
$      EID      PID      N1      N2      N3      N4
      1          1          1          2          3          4
      2          1          4          3          5          6
      3          1          6          5          7          8
      ...
      ... (cont'd)
      21533      8  22141  22167  22169  22160
      21534      8  22169  22183  22180  22160

```

```

21535      8  22183  22182  22189  22180
$-----1-----2-----3-----4-----5-----6-----7-----8
$
      (12) BOUNDARY CONDITION CARDS
$-----1-----2-----3-----4-----5-----6-----7-----8
*BOUNDARY_SPC_NODE
$ NID/NSID      CID      DOFX      DOFY      DOFZ      DOFRX      DOFRY      DOFRZ
   9791         0         1         1         1         1         1         1
   9792         0         1         1         1         1         1         1
   9845         0         1         1         1         1         1         1
   ...
   ... (cont'd)
   10969        0         1         1         1         1         1         1
   11022        0         1         1         1         1         1         1
   11076        0         1         1         1         1         1         1
$-----1-----2-----3-----4-----5-----6-----7-----8
$
      (13) DEFINE SET CARDS
$-----1-----2-----3-----4-----5-----6-----7-----8
*SET_NODE_LIST
$   SID      DA1      DA2      DA3      DA4
   1
$   NID1     NID2     NID3     NID4     NID5     NID6     NID7     NID8
   11656    11657    11658    11659    11660    11661    11662    11663
   11670    11671    11672    11673    11674    11675    11676    11705
   11720    11735    11750    11765    11780    11795    11810    11825
   11840    11855    11870    11885    12466    12467    12468    12469
   12470    12471    12472    12473    12480    12481    12482    12483
   12484    12486    12501    12516    12531    12546    12561    12576
   12591    12606    12621    12636    12651    12666    12681
$-----1-----2-----3-----4-----5-----6-----7-----8
$
      (14) LOADING CONDITIONS
$-----1-----2-----3-----4-----5-----6-----7-----8
*LOAD_NODE_SET
$   NSID      DOF      LCID      SF      CID      M1      M2      M3
   1         2         100       1
*DEFINE_CURVE
$   LCID      SIDR      SFA      SFO      OFFA      OFFO      DATTYP
   100         0         1.0      -1.0     0.0      0.0      0
$
      A1 (TIME)      O1 (FORCE)
      0.00           0.0
      0.0002        0.454545E+04
      0.0011        0.454545E+04
      0.0012         0.0
      0.0084         0.0
$-----1-----2-----3-----4-----5-----6-----7-----8
*SET_NODE_LIST
$   SID      DA1      DA2      DA3      DA4
   2
$   NID1     NID2     NID3     NID4     NID5     NID6     NID7     NID8
   13274    13275    13276    13277    13278    13279    13280    13281
   13288    13289    13290    13291    13292    13293    13294    13323
   13338    13353    13368    13383    13398    13413    13428    13443
   13458    13473    13488    13503    14084    14085    14086    14087
   14088    14089    14090    14091    14098    14099    14100    14101
   14102    14104    14119    14134    14149    14164    14179    14194
   14209    14224    14239    14254    14269    14284    14299
$-----1-----2-----3-----4-----5-----6-----7-----8
$
      (14) LOADING CONDITIONS
$-----1-----2-----3-----4-----5-----6-----7-----8
*LOAD_NODE_SET
$   NSID      DOF      LCID      SF      CID      M1      M2      M3
   2         2         200       1
*DEFINE_CURVE
$   LCID      SIDR      SFA      SFO      OFFA      OFFO      DATTYP
   200         0         1.0      -1.0     0.0      0.0      0
$
      A1 (TIME)      O1 (FORCE)
      0.00           0.0
      0.0012         0.0

```



```

0.0014      0.454545E+04
0.0023      0.454545E+04
0.0024      0.0
0.0084      0.0
$-----1-----2-----3-----4-----5-----6-----7-----8
*SET_NODE_LIST
$      SID      DA1      DA2      DA3      DA4
      3
$      NID1      NID2      NID3      NID4      NID5      NID6      NID7      NID8
      14892      14893      14894      14895      14896      14897      14898      14899
      14906      14907      14908      14909      14910      14911      14912      14941
      14956      14971      14986      15001      15016      15031      15046      15061
      15076      15091      15106      15121      15702      15703      15704      15705
      15706      15707      15708      15709      15716      15717      15718      15719
      15720      15722      15737      15752      15767      15782      15797      15812
      15827      15842      15857      15872      15887      15902      15917
$-----1-----2-----3-----4-----5-----6-----7-----8
$
(14) LOADING CONDITIONS
$-----1-----2-----3-----4-----5-----6-----7-----8
*LOAD_NODE_SET
$      NSID      DOF      LCID      SF      CID      M1      M2      M3
      3          2          300      1          CID          M1      M2      M3
*DEFINE_CURVE
$      LCID      SIDR      SFA      SFO      OFFA      OFFO      DATTYP
      300      0          1.0      -1.0      0.0      0.0      0
$
      A1 (TIME)      O1 (FORCE)
      0.00          0.0
      0.0012        0.0
      0.0024        0.0
      0.0026        0.454545E+04
      0.0035        0.454545E+04
      0.0036        0.0
      0.0084        0.0
$-----1-----2-----3-----4-----5-----6-----7-----8
*SET_NODE_LIST
$      SID      DA1      DA2      DA3      DA4
      4
$      NID1      NID2      NID3      NID4      NID5      NID6      NID7      NID8
      16510      16511      16512      16513      16514      16515      16516      16517
      16524      16525      16526      16527      16528      16529      16530      16559
      16574      16589      16604      16619      16634      16649      16664      16679
      16694      16709      16724      16739      17320      17321      17322      17323
      17324      17325      17326      17327      17334      17335      17336      17337
      17338      17340      17355      17370      17385      17400      17415      17430
      17445      17460      17475      17490      17505      17520      17535
$-----1-----2-----3-----4-----5-----6-----7-----8
$
(14) LOADING CONDITIONS
$-----1-----2-----3-----4-----5-----6-----7-----8
*LOAD_NODE_SET
$      NSID      DOF      LCID      SF      CID      M1      M2      M3
      4          2          400      1          CID          M1      M2      M3
*DEFINE_CURVE
$      LCID      SIDR      SFA      SFO      OFFA      OFFO      DATTYP
      400      0          1.0      -1.0      0.0      0.0      0
$
      A1 (TIME)      O1 (FORCE)
      0.00          0.0
      0.0012        0.0
      0.0024        0.0
      0.0036        0.0
      0.0038        0.454545E+04
      0.0047        0.454545E+04
      0.0048        0.0
      0.0084        0.0
$-----1-----2-----3-----4-----5-----6-----7-----8
*SET_NODE_LIST
$      SID      DA1      DA2      DA3      DA4
      5

```

NID1	NID2	NID3	NID4	NID5	NID6	NID7	NID8
18128	18129	18130	18131	18132	18133	18134	18135
18142	18143	18144	18145	18146	18147	18148	18177
18192	18207	18222	18237	18252	18267	18282	18297
18312	18327	18342	18357	18938	18939	18940	18941
18942	18943	18944	18945	18952	18953	18954	18955
18956	18958	18973	18988	19003	19018	19033	19048
19063	19078	19093	19108	19123	19138	19153	

\$-----1-----2-----3-----4-----5-----6-----7-----8
 (14) LOADING CONDITIONS
 \$-----1-----2-----3-----4-----5-----6-----7-----8
 *LOAD_NODE_SET
 \$ NSID DOF LCID SF CID M1 M2 M3
 5 2 500 1
 *DEFINE_CURVE
 \$ LCID SIDR SFA SFO OFFA OFFO DATYYP
 500 0 1.0 -1.0 0.0 0.0 0
 \$ A1 (TIME) O1 (FORCE)
 0.00 0.0
 0.0012 0.0
 0.0024 0.0
 0.0036 0.0
 0.0048 0.0
 0.0050 0.454545E+04
 0.0059 0.454545E+04
 0.0060 0.0
 0.0084 0.0
 \$-----1-----2-----3-----4-----5-----6-----7-----8
 *SET_NODE_LIST
 \$ SID DA1 DA2 DA3 DA4
 6
 \$ NID1 NID2 NID3 NID4 NID5 NID6 NID7 NID8
 19746 19747 19748 19749 19750 19751 19752 19753
 19760 19761 19762 19763 19764 19765 19766 19795
 19810 19825 19840 19855 19870 19885 19900 19915
 19930 19945 19960 19975 20556 20557 20558 20559
 20560 20561 20562 20563 20570 20571 20572 20573
 20574 20576 20591 20606 20621 20636 20651 20666
 20681 20696 20711 20726 20741 20756 20771
 \$-----1-----2-----3-----4-----5-----6-----7-----8
 (14) LOADING CONDITIONS
 \$-----1-----2-----3-----4-----5-----6-----7-----8
 *LOAD_NODE_SET
 \$ NSID DOF LCID SF CID M1 M2 M3
 6 2 600 1
 *DEFINE_CURVE
 \$ LCID SIDR SFA SFO OFFA OFFO DATYYP
 600 0 1.0 -1.0 0.0 0.0 0
 \$ A1 (TIME) O1 (FORCE)
 0.00 0.0
 0.0012 0.0
 0.0024 0.0
 0.0036 0.0
 0.0048 0.0
 0.0060 0.0
 0.0062 0.454545E+04
 0.0071 0.454545E+04
 0.0072 0.0
 0.0084 0.0
 \$-----1-----2-----3-----4-----5-----6-----7-----8
 *SET_NODE_LIST
 \$ SID DA1 DA2 DA3 DA4
 7
 \$ NID1 NID2 NID3 NID4 NID5 NID6 NID7 NID8
 21364 21365 21366 21367 21368 21369 21370 21371
 21378 21379 21380 21381 21382 21383 21384 21413
 21428 21443 21458 21473 21488 21503 21518 21533

21548	21563	21578	21593	22174	22175	22176	22177
22178	22179	22180	22181	22188	22189	22190	22191
22192	22194	22209	22224	22239	22254	22269	22284
22299	22314	22329	22344	22359	22374	22389	

\$-----1-----2-----3-----4-----5-----6-----7-----8
\$ (14) LOADING CONDITIONS
\$-----1-----2-----3-----4-----5-----6-----7-----8
*LOAD_NODE_SET
\$ NSID DOF LCID SF CID M1 M2 M3
7 2 700 1
*DEFINE_CURVE
\$ LCID SIDR SFA SFO OFFA OFFO DATTYP
700 0 1.0 -1.0 0.0 0.0 0
\$ A1 (TIME) O1 (FORCE)
0.00 0.0
0.0012 0.0
0.0024 0.0
0.0036 0.0
0.0048 0.0
0.0060 0.0
0.0072 0.0
0.0074 0.454545E+04
0.0083 0.454545E+04
0.0084 0.0
\$-----1-----2-----3-----4-----5-----6-----7-----8
*BOUNDARY_PRESCRIBED_MOTION_RIGID
\$ PARTID DOF VAD LCID SF VID DEATH BIRTH
2 1 0 20 1.0 0 1.E+28 0.0
*DEFINE_CURVE
\$ LCID SIDR SFA SFO OFFA OFFO DATTYP
20 0 1.0 1.0 0.0 0.0 0
\$ A1 (TIME) O1 (VELOCITY)
0 0.0
0.0002 0.0
0.0003 10.0E+03
0.0011 10.0E+03
0.0012 10.0E+03
0.0084 10.0E+03
\$-----1-----2-----3-----4-----5-----6-----7-----8
*BOUNDARY_PRESCRIBED_MOTION_RIGID
\$ PARTID DOF VAD LCID SF VID DEATH BIRTH
3 1 0 21 1.0 0 1.E+28 0.0
*DEFINE_CURVE
\$ LCID SIDR SFA SFO OFFA OFFO DATTYP
21 0 1.0 1.0 0.0 0.0 0
\$ A1 (TIME) O1 (VELOCITY)
0 0.0
0.0014 0.0
0.0015 10.0E+03
0.0023 10.0E+03
0.0024 10.0E+03
0.0084 10.0E+03
\$-----1-----2-----3-----4-----5-----6-----7-----8
*BOUNDARY_PRESCRIBED_MOTION_RIGID
\$ PARTID DOF VAD LCID SF VID DEATH BIRTH
4 1 0 22 1.0 0 1.E+28 0.0
*DEFINE_CURVE
\$ LCID SIDR SFA SFO OFFA OFFO DATTYP
22 0 1.0 1.0 0.0 0.0 0
\$ A1 (TIME) O1 (VELOCITY)
0 0.0
0.0026 0.0
0.0027 10.0E+03
0.0035 10.0E+03
0.0036 10.0E+03
0.0084 10.0E+03
\$-----1-----2-----3-----4-----5-----6-----7-----8

```

$-----1-----2-----3-----4-----5-----6-----7-----8
*BOUNDARY_PRESCRIBED_MOTION_RIGID
$ PARTID      DOF      VAD      LCID      SF      VID      DEATH      BIRTH
   5          1          0         23       1.0      0       1.E+28      0.0
*DEFINE_CURVE
$ LCID      SIDR      SFA      SFO      OFFA      OFFO      DATTYP
   23          0         1.0       1.0       0.0       0.0       0
$          A1 (TIME)          O1 (VELOCITY)
          0          0.0
          0.0038          0.0
          0.0039          10.0E+03
          0.0047          10.0E+03
          0.0048          10.0E+03
          0.0084          10.0E+03
$-----1-----2-----3-----4-----5-----6-----7-----8
*BOUNDARY_PRESCRIBED_MOTION_RIGID
$ PARTID      DOF      VAD      LCID      SF      VID      DEATH      BIRTH
   6          1          0         24       1.0      0       1.E+28      0.0
*DEFINE_CURVE
$ LCID      SIDR      SFA      SFO      OFFA      OFFO      DATTYP
   24          0         1.0       1.0       0.0       0.0       0
$          A1 (TIME)          O1 (VELOCITY)
          0          0.0
          0.0050          0.0
          0.0051          10.0E+03
          0.0059          10.0E+03
          0.0060          10.0E+03
          0.0084          10.0E+03
$-----1-----2-----3-----4-----5-----6-----7-----8
*BOUNDARY_PRESCRIBED_MOTION_RIGID
$ PARTID      DOF      VAD      LCID      SF      VID      DEATH      BIRTH
   7          1          0         25       1.0      0       1.E+28      0.0
*DEFINE_CURVE
$ LCID      SIDR      SFA      SFO      OFFA      OFFO      DATTYP
   25          0         1.0       1.0       0.0       0.0       0
$          A1 (TIME)          O1 (VELOCITY)
          0          0.0
          0.0062          0.0
          0.0063          10.0E+03
          0.0071          10.0E+03
          0.0072          10.0E+03
          0.0084          10.0E+03
$-----1-----2-----3-----4-----5-----6-----7-----8
*BOUNDARY_PRESCRIBED_MOTION_RIGID
$ PARTID      DOF      VAD      LCID      SF      VID      DEATH      BIRTH
   8          1          0         26       1.0      0       1.E+28      0.0
*DEFINE_CURVE
$ LCID      SIDR      SFA      SFO      OFFA      OFFO      DATTYP
   26          0         1.0       1.0       0.0       0.0       0
$          A1 (TIME)          O1 (VELOCITY)
          0          0.0
          0.0074          0.0
          0.0075          10.0E+03
          0.0083          10.0E+03
          0.0084          10.0E+03
$-----1-----2-----3-----4-----5-----6-----7-----8
*SET_SHELL_LIST
$ SID      NUM      DA1      DA2      DA3      DA4
   9        39
$ EIDS     EID2     EID3     EID4     EID5     EID5     EID7     EID8
 1181     1182     1183     1184     1185     1186     1187     1188
 1189     1190     1191     1192     1193     1194     1195     1196
 1197     1198     1199     1359     1360     1361     1362     1363
 1364     1365     1366     1397     9515     9516     9517     9518
 9560     9569     9561     9562     9571     9564     9565
$-----1-----2-----3-----4-----5-----6-----7-----8
*SET_SHELL_LIST

```

\$	SID	NUM	DA1	DA2	DA3	DA4		
	8	15						
\$	EIDS	EID2	EID3	EID4	EID5	EID5	EID7	EID8
	10135	10134	10141	10131	10132	10138	10122	10099
	10100	10101	10102	10127	5148	5149	5150	
\$	1	2	3	4	5	6	7	8
*SET_SHELL_LIST								
\$	SID	NUM	DA1	DA2	DA3	DA4		
	10	38						
\$	EIDS	EID2	EID3	EID4	EID5	EID5	EID7	EID8
	9849	9850	9856	9846	9847	9854	2748	2749
	2750	2751	2752	9800	9801	9802	9803	9845
	2745	2746	2747	2481	2482	2483	2484	2485
	2486	2487	2488	2489	2490	2491	2492	2493
	2494	2495	2496	2497	2498	2813		
\$	1	2	3	4	5	6	7	8
*SET_SHELL_LIST								
\$	SID	NUM	DA1	DA2	DA3	DA4		
	11	38						
\$	EIDS	EID2	EID3	EID4	EID5	EID5	EID7	EID8
	10420	10419	10426	10416	10417	10424	6509	6510
	6511	6512	10370	10371	10372	10373	10415	6505
	6506	6507	6508	6241	6242	6243	6244	6245
	6246	6247	6248	6249	6250	6251	6252	6253
	6254	6255	6256	6257	6258	6573		
\$	1	2	3	4	5	6	7	8
*SET_SHELL_LIST								
\$	SID	NUM	DA1	DA2	DA3	DA4		
	12	420						
\$	EIDS	EID2	EID3	EID4	EID5	EID5	EID7	EID8
	4886	4887	4888	4889	4890	4891	4892	4893
	4894	4895	4896	4897	4898	4899	4900	4901
	4902	4903	4905	4906	4907	4908	4909	4910
	4911	4912	4913	4914	4915	4916	4917	4918
	4919	4920	4921	4922	4923	4924	4925	4926
	4927	4928	4929	4930	4931	4932	4933	4934
	4935	4936	4937	4938	4939	4940	4941	4942
	4943	4944	4945	4946	4947	4948	4949	4950
	4951	4952	4953	4954	4955	4956	4957	4958
	4960	4961	4962	4963	4964	4965	4966	4967
	4968	4969	4970	4971	4972	4973	4974	4975
	4976	4977	4979	4980	4981	4982	4983	4984
	4985	4986	4987	4988	4989	4990	4991	4992
	4993	4994	4995	4996	4997	4998	4999	5000
	5001	5002	5003	5004	5005	5006	5007	5008
	5009	5010	5011	5012	5013	5014	5015	5016
	5017	5018	5019	5020	5021	5022	5023	5024
	5025	5026	5027	5028	5029	5030	5031	5032
	4249	4250	4251	4252	4253	4254	4255	4256
	4257	4258	4259	4260	4261	4262	4263	4264
	4268	4269	4270	4271	4272	4273	4274	4275
	4276	4277	4278	4279	4280	4281	4282	4283
	4287	4288	4289	4290	4291	4292	4293	4294
	4295	4296	4297	4298	4299	4300	4301	4302
	4305	4306	4307	4308	4309	4310	4311	4312
	4313	4314	4315	4316	4317	4318	4319	4320
	4323	4324	4325	4326	4327	4328	4329	4330
	4331	4332	4333	4334	4335	4336	4337	4338
	4342	4343	4344	4345	4346	4347	4348	4349
	4350	4351	4352	4353	4354	4355	4356	4357
	4361	4362	4363	4364	4365	4366	4367	4368
	4369	4370	4371	4372	4373	4374	4375	4376
	4379	4380	4381	4382	4383	4384	4385	4386
	4387	4388	4389	4390	4391	4392	4393	4394
	4231	4232	4233	4234	4235	4236	4237	4238
	4239	4240	4241	4242	4243	4244	4245	4246
	4247	4248	4265	4266	4267	4284	4285	4286

4303	4304	4321	4322	4339	4340	4341	4358
4359	4360	4377	4378	4395	4396	4692	4693
4694	4695	4696	4697	4698	4699	4700	4904
4959	4978	5033	5034	5035	5036	5037	5038
5039	5040	5041	5042	5043	5044	5045	5046
5047	5048	5049	5050	5051	5052	5053	5054
5055	5056	5057	5058	5059	5060	5061	5062
5063	5064	5065	5066	5067	5068	5069	5070
5151	5152	5153	5154	5155	5156	5157	5158
5159	5160	4601	4602	4603	4604	4605	4609
4610	4611	4612	4613	4617	4618	4619	4620
4621	4625	4626	4627	4628	4629	4633	4634
4635	4636	4637	5111	5112	5113	5114	5115
5119	5120	5121	5122	5123	5127	5128	5129
5130	5131	5135	5136	5137	5138	5139	5143
5144	5145	5146	5147				

\$---+---1---+---2---+---3---+---4---+---5---+---6---+---7---+---8
*END

APPENDIX G

DIMENSIONAL ANALYSIS

The main objective of this study was to build a finite element model to analyze subsurface deformation that occurs in the aluminum alloys subjected to sliding contact. In the course of the project, sliding contact of an asperity and an aluminum alloy was planned to be investigated by using explicit finite element program LS-DYNA. However, because of the CPU requirements and costs, the asperity diameter and the size of the finite element model geometry had to be increased. A dimensional analysis was applied to choose the most appropriate the finite element geometry with minimum CPU costs. In this discussion, dimensional analysis will be used to show the possibility of application of the current finite element model results to different sized asperity contacts. Initially dimensional analysis and Buckingham π theorem will be introduced and briefly explained before discussion of the application to the sliding contact.

G.1. INTRODUCTION TO DIMENSIONAL ANALYSIS AND BUCKINGHAM π THEOREM

Dimensional analysis is a mathematical tool often applied in science and engineering to simplify a problem by reducing the number of variables to the smallest number of essential parameters. Systems which share these parameters are called similar and do not have to be studied separately. Dimensional analysis has broad applications. It plays an essential role for experimentalists from design of experiments to data analysis. It helps to establish equations and yield solutions to modelers [123]. Frequently researchers need small scale models to investigate complex structural systems which are difficult to analyze theoretically and numerically or experimentally. The dynamic response of underground structures, impact of nuclear fuel capsules, missile impact of nuclear power installations and collision protection of ships are several areas which have been studied with the aid of small scale models. Instead of full scale models of the system of interest, geometrically similar small scale prototypes are used in

the tests in order to obtain the response characteristics. This procedure known as scaling is governed by certain principles [84].

The dimension of a physical quantity is the type of unit needed to express it. For instance, the dimension of a speed is distance/time and the dimension of a force is (mass x distance / time²). In mechanics, every dimension can be expressed in terms of distance (which physicists often call "length"), time, and mass, or alternatively in terms of force, length and mass. Depending on the problem, it may be advantageous to choose one or the other set of fundamental units. Every unit is a product of (possibly fractional) powers of the fundamental units, and the units form a group under multiplication [123, 124].

In the most primitive form, dimensional analysis is used to check the correctness of algebraic derivations: in every physically meaningful expression, only quantities of the same dimension can be added or subtracted. The two sides of any equation must have the same dimensions. Furthermore, the arguments to exponential, trigonometric and logarithmic functions must be dimensionless numbers, which is often achieved by multiplying a certain physical quantity by a suitable constant of the inverse dimension.

The Buckingham π theorem is a key theorem in dimensional analysis. The theorem states that the functional dependence between a certain number (e.g.: n) of variables can be reduced by the number (e.g. k) of independent dimensions occurring in those variables to give a set of $p = n - k$ independent, dimensionless numbers. For the purposes of the experimenter, different systems which share the same description by dimensionless numbers are equivalent. Most importantly, it provides a method for computing sets of dimensionless parameters from the given variables, even if the form of the equation is still unknown. However, the choice of dimensionless parameters is not unique: Buckingham's theorem only provides a way of generating sets of dimensionless parameters, and will not choose the most physically meaningful [124-131]. Two systems for which these parameters coincide are called similar; they are equivalent for the purposes of the equation, and the experimentalist who wants to determine the form of the equation can choose the most convenient one.

A typical application example of dimensional analysis can be given in fluid dynamics. If a moving fluid meets an object, it exerts a force on the object, according to a complicated (and not completely understood) law. The variables involved are: the speed, density and viscosity of the fluid, the size of the body (expressed in terms of its

frontal area A), and the force. Using the algorithm of the π theorem, one can reduce these five variables to two dimensionless parameters: the drag coefficient and the Reynolds number [132-134].

$$f(F, u, A, \rho, \nu) = 0 \quad (\text{G-1})$$

where f is a function that takes five arguments. There are many ways of combining the five arguments of f to form dimensionless groups, but the Buckingham's theorem states that there will be two such groups. The most appropriate are the Reynolds number, given by:

$$\text{Re} = \frac{u\sqrt{A}}{\nu} \quad (\text{G-2})$$

and the drag coefficient, given by:

$$C_D = \frac{F}{\rho Au^2} \quad (\text{G-3})$$

Thus the original law involving a function of five variables may be replaced by one involving only two:

$$f\left(\frac{F}{\rho Au^2}, \frac{u\sqrt{A}}{\nu}\right) = 0 \quad (\text{G-4})$$

where f is a function of two arguments. The original law is then reduced to a law involving only these two numbers. Because the only unknown in the above equation is F , it is possible to express it as following:

$$\frac{F}{\rho Au^2} = f\left(\frac{u\sqrt{A}}{\nu}\right) \quad (\text{G-5})$$

or

$$F = \rho Au^2 f(\text{Re}) \quad (\text{G-6})$$

Dimensional analysis thus makes a complex problem (trying to determine the behaviour of a function of five variables) a very much simpler one: the determination of a function of one variable, the Reynolds number. The analysis also gives other information. The drag force will be proportional to the frontal area of the body and to the density of the fluid. This kind of information often proves to be extremely valuable, especially in the early stages of a research project. To empirically determine the Reynolds number dependence, instead of experimenting on huge bodies with fast flowing fluids (such as real-size airplanes in wind-tunnels), one may just as well experiment on small models with slow flowing, more viscous fluids, because these two systems are similar.

G.2. SLIDING OF AN ASPERITY OVER A DEFORMABLE MATERIAL

Before applying dimensional analysis to the developed finite element model, geometric scale factor must be defined. The geometric scale factor c is the ratio of a length unit of a scaled model to that of the original finite element model:

$$c = \frac{L_S}{L_0} \quad (\text{G-7})$$

where L_S is the length unit in the scaled model and L_0 refers to the length unit in the original model.

In Chapter 4.2, the contact between a rigid cylindrical asperity of diameter $2R$ and thickness W and a three-dimensional 356 Al surface was investigated. The steel asperity was indented on the 356 Al surface by applying a constant normal load of F . A constant sliding velocity V was assigned to the asperity to translate it over the 356 Al surface.

In summary, the input parameters consist of three principle types: geometrical characteristics (R and W), material properties (σ_0 , σ_S , ϵ_C) and external loads (F and V). Output parameters are strain (ϵ) and stress (σ_f).

To apply dimensional analysis, the recipe of dimensional analysis given by Cheng and Cheng [123] will be followed:

1- List independent variables and parameters:

$$F, \sigma_0, \sigma_S, \epsilon_C, V, R, W, t$$

2- List dependent variables and parameters:

$$\epsilon \text{ (or } \sigma_f)$$

3- Identify independent variables and parameters with independent dimensions:

$$\sigma_0, R, t$$

4- Form dimensionless quantities π terms:

$$\pi_1 = F / (R \cdot W \cdot \sigma_0)$$

$$\pi_2 = \sigma_S / \sigma_0$$

$$\pi_3 = \epsilon_C$$

$$\pi_4 = (V \cdot t) / R$$

$$\pi_5 = W / R$$

$$\pi_\alpha = \epsilon$$

$$\epsilon = f(F, \sigma_0, \sigma_S, \epsilon_C, V, R, W, t)$$

$$\pi_\alpha = \pi_\alpha(\pi_1, \pi_2, \pi_3, \pi_4, \pi_5)$$

If input parameters are scaled geometrically so that π terms are identical for the original finite element model and the scaled models, then the dimensionless response is also identical [84]. Let's examine the physical requirements associated with each of these π terms when they are made equal for the original and scaled finite element models:

π_1 : applied force must be scaled by the square of the geometric scale factor c , c^2 times.

π_2 : stress constant to bulk flow strength ratio must be the same, this condition is satisfied when the same material is used in the original and scaled models.

π_3 : material constants in the original model and scaled model must be the same.

π_4 : to satisfy this term, ratio of sliding velocity times sliding time divided by characteristic length must be kept constant. If sliding velocity is constant, sliding time (t) must be increased c times since the characteristic length R increases c times with geometric scaling.

π_5 : in a geometrically similar scaling this condition is already satisfied.

π_α : strains (or stresses) are identical in the original model and scaled model at scaled locations for scaled times.

To investigate the correctness of the above dimensional analysis, all dimensions of the original finite element model described in Chapter 4.2 were scaled up an order of magnitude ($c=10$). Accordingly, the asperity diameter was increased from 2 mm to 20 mm and the width was increased from 0.5 mm to 5 mm. According to the requirement of π_1 , applied normal load was increased from 150 N to 15 kN (c^2 times, 100 times). The sliding velocity was kept constant and to satisfy requirement of π_4 sliding time was increased 10 times since asperity radius (R) increases 10 times with scaling. The comparison of the results revealed that the stress and strain predictions did not differ more than 2-3% (Figure G.1), which might be attributed to the numerical errors and noise.

Similar reasoning, the developed finite element model may be applied to smaller asperity dimensions. As a result of this, all the predictions of the study presented in Chapters 4.2 and 5.1 might be assumed to be valid for 0.2 mm and/or 20 μm asperity diameters with the normal loads of 1.5 N and/or 15 mN, respectively.

G.3. STRAIN RATE AND THERMAL SOFTENING EFFECTS

Strain rate and thermal softening effects were taken in the consideration by using a Lagrangian coupled thermal and structural finite element model. In literature it has been shown that temperature and thermal effects can be scalable since temperature distribution is calculated from the deformation within the material [84, 125, 126]. However, strain rate sensitivity and strain rate effects will be different for the original model and the scaled models [84, 125, 126].

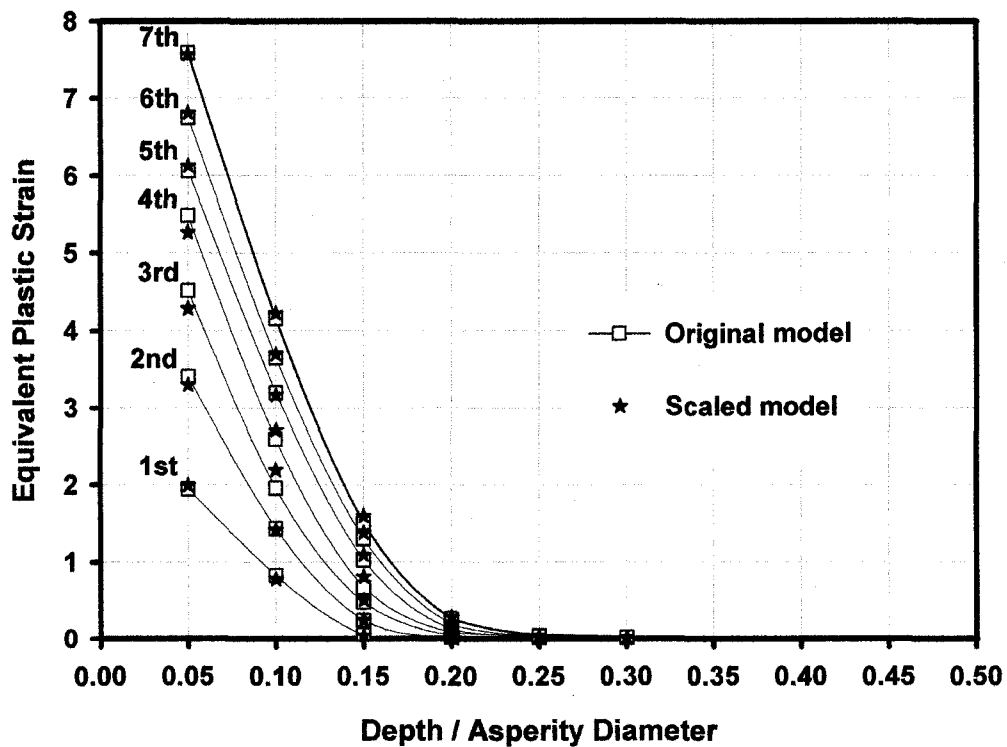


Figure G.1: The change of plastic strain against depth at the mid point of the finite element model.

VITA AUCTORIS

NAME: Semsettin Subutay Akarca

PLACE OF BIRTH: Besiri, Turkey

YEAR OF BIRTH: 1974

EDUCATION: University of Windsor, Windsor, ON
Department of Mechanical, Automotive and Materials Engineering
Ph.D., 2001-2005

Middle East Technical University, Ankara, TURKEY
Department of Metallurgical and Materials Engineering
M.Sc., 1997-2000

Middle East Technical University, Ankara, TURKEY
Department of Metallurgical and Materials Engineering
B.Sc., 1993-1997